Geochemical (major and trace elements and Sr-Nd-Hf-Pb isotopes) characterization of the upper oceanic crust (sediments to gabbros) at ODP/IODP Site 1256 in the eastern Central Pacific

DISSERTATION

zur Erlangung des Doktorgrades
der Mathematisch-Naturwissenschaftlichen Fakultät
der Christian-Albrechts-Universität zu Kiel

vorgelegt von

Tobias Walter Höfig

Kiel, im Juli 2014

Erster Gutachter: ……... Prof. Dr. Kaj Hoernle

Zweiter Gutachter: ……..…… Prof. Dr. Martin Frank

Tag der mündlichen Prüfung: ……14.07.2014

Zum Druck genehmigt: ……

……
Der Dekan

Eidesstattliche Erklärung

Hiermit versichere ich, dass ich die vorliegende Doktorarbeit selbständig und ohne Benutzung anderer als der angegebenen Quellen und Hilfsmittel angefertigt und die den benutzten Quellen wörtlich oder inhaltlich entnommenen Stellen als solche kenntlich gemacht habe. Sie stellt, abgesehen von der Beratung durch meinen Betreuer, nach Inhalt und Form meine eigene Arbeit dar. Diese Arbeit wurde weder ganz noch zum Teil in gleicher oder ähnlicher Form an einer anderen Hochschule im Rahmen eines Prüfungsverfahrens vorgelegt, veröffentlicht oder zur Veröffentlichung eingereicht. Ferner ist die vorliegende Arbeit unter Einhaltung der Regeln guter wissenschaftlicher Praxis der Deutschen Forschungsgemeinschaft entstanden.

Kiel, den .....

Tobias Walter Höfig

DANKSAGUNG

Die vorliegende Arbeit entstand im Rahmen der durch die Deutsche Forschungsgemeinschaft (DFG) geförderten Projekte HO1833/16-1 und 18-1 des Schwerpunktprogramms SPP 527 (International Ocean Discovery Program). Für die Ausarbeitung und das Stellen der Projektanträge möchte ich mich bei Prof. Dr. Kaj Hoernle, Dr. Jörg Geldmacher und Dr. Svend Duggen bedanken.

Mein größter Dank gilt meinem Betreuer Prof. Dr. Kaj Hoernle für die Vergabe dieser Arbeit und für Denkanstöße und interpretatorische Unterstützung in vielen fruchtbaren Diskussionen sowie die kritische Durchsicht meiner Manuskripte. Ferner danke ich ihm ganz besonders herzlich, dass er mir auch in schwierigen Zeiten stets das Vertrauen geschenkt und die Geduld entgegengebracht hat, die nötig gewesen sind, damit ich die vorliegende Arbeit erfolgreich abschließen konnte. Seine Zuversicht und sein Glauben in meine Fähigkeiten haben mich immer wieder gestärkt.

Ich danke Prof. Dr. Martin Frank sehr herzlich für seine essentielle Unterstützung im Rahmen der vorliegenden Arbeit. Sein wissenschaftlicher Input war eine große Bereicherung für mich und das Projekt insgesamt. In fruchtbaren Diskussionen hat er mir die Welt der Paläoozeanographie vertrauter werden lassen und mir dabei geholfen die Daten besser zu interpretieren. Auch gilt ihm mein Dank für die kritische Durchsicht meiner Manuskripte.

Einen ganz besonderen Dank möchte ich an Dr. Jörg Geldmacher richten für seine wissenschaftliche, logistische und moralische Unterstützung, die wesentlich dazu beigetragen hat, dass das Projekt „Site 1256“ erfolgreich gestaltet werden konnte. Seine Ideen und seine Denkanstöße im Zuge der Interpretation meiner Daten sowie die kritische Durchsicht von Manuskripten bildeten einen wichtigen Baustein für meine Arbeit.

Ich danke meinem Projektvorgänger Dr. Svend Duggen sehr herzlich für seine Hilfsbereitschaft und fruchtbare Diskussionen, dir mir es ermöglichten einen Einstieg in das Projekt zu finden.

Ein herzliches Dankeschön gilt Dr. Folkmar Hauff und Silke Hauff für die Durchführung der Isotopenanalysen, welche die Basis jeglicher Ideen gebildet haben. Darüber hinaus danke ich Dr. Folkmar Hauff für die kritische Durchsicht von Manuskripten.

Ein großes Dankeschön möchte ich auch an Dr. Dieter Garbe-Schönberg und Dipl.-Ing. Ulrike Westernströer richten für die Basement-Spurenelementanalytik sowie für die Unterstützung und Zusammenarbeit in ihren Laborräumen. Diese Zeit werde ich stets in sehr guter Erinnerung behalten.

Ich danke Dr. Andreas Klügel herzlich für die Spurenelementanalytik an den Sedimenten. Ferner danke ich sehr Dagmar Rau für die Hauptelementanalytik. Auch danke ich Jutta Heinze herzlich für die Unterstützung im Labor beim Entfernen der Fe-Mn Coatings.

Ich danke herzlich Frauke Rathjen für viele nette und positiv stimmende Gespräche und für die stete Hilfsbereitschaft während meiner Zeit am GEOMAR. Ich danke herzlich meiner Büronachbarin Antje für ein offenes Ohr zu jeder Zeit und für ihre Hilfsbereitschaft.

Einen freundschaftlichen und herzlichen Dank möchte ich an meine „GEOMAR-Mädels“ Andrea und Maren richten, die mich in vielen Situationen moralisch und praktisch unterstützt

und mir stets die positiven Dinge bewusst gemacht haben. Die gemeinsame Zeit mit ihnen ließ jeden grauen Kieler Tag sonnig werden.

Sonnig war auch die gemeinsame Kieler Zeit mit meiner guten Freundin und besten Mitbewohnerin Gabi. Sie hat immer darauf geachtet, dass ich auch auf mich Acht gebe. Ein Gespräch mit ihr hat jeden Tag zu einem angenehmen werden lassen. Ihr Zuspruch hat mich stärker gemacht. Für all dies danke ich ihr sehr herzlich.

Ein besonders herzliches Dankeschön gilt meinen lieben Freiberger Kolleginnen und Kollegen, die mich insbesondere in den letzten sechs Wochen der Fertigstellung der Arbeit sehr entlastet haben, damit ich das große Ziel vollenden konnte. Zudem waren sie eine stete Quelle des Zuspruchs. Ein ganz besonders wichtiger Dank richtet sich an meinen Kollegen Matthias Bauer, der mich als Formatierungs- und Zitationsassistent in den letzten Tagen der Arbeit tatkräftig unterstützt hat. Seine Hilfe hat wesentlich die pünktliche Abgabe der Arbeit ermöglicht. An dieser Stelle möchte ich auch Prof. Dr. Jens Gutzmer und Prof. Dr. Thomas Seifert sehr herzlich danken. Sie haben mir neue Perspektiven eröffnet und mir stets das Vertrauen geschenkt und mir Geduld entgegengebracht. In den letzten vier Wochen der Arbeit haben sie mich freigestellt. Ohne diese gewonnene Zeit hätte ich die vorliegende Arbeit nicht in dem vorgeschriebenen Zeitrahmen fertigstellen können.

Bedanken möchte ich mich auch ganz herzlich bei allen Freunden, Bekannten und Verwandten für ihren Zuspruch, ihren Glauben in meine Stärken und das stets positive Denken, das mir auf meinem Weg immer sehr geholfen hat. Obwohl viele Namen genannt werden müssten, möchte ich doch hier ganz besonders Rosi und Udo aus meiner Heimat Erfurt danken, die immer wieder an mich gedacht, mich mit Nervenrationen versorgt und mir ihre guten Wünsche über alle möglichen Medien mitgeteilt haben.

Von ganzem Herzen bedanke ich mich besonders bei meiner Familie für die moralische Unterstützung. Insbesondere danke ich aus tiefstem Herzen meiner Mutter, die mich auf meinem gesamten Weg stets so großartig und umfangreich unterstützt und gefördert hat, dass ich dafür kaum Worte finden und ihr gar nicht genug danken kann. Sie hat mir immer Kraft, Hoffnung, Glaube an meine Stärken und die Zuversicht gegeben, die mir es überhaupt erst ermöglicht haben den nicht immer einfachen Weg zu meistern.

Gewidmet meinen Großeltern

Anneliese und Walter Totzki

CONTENTS

DANKSAGUNG VII

ABSTRACT XIV

KURZFASSUNG XVI

INTRODUCTION XIX

CHAPTER I 1

From the lavas to the gabbros: 1.25 km of geochemical characterization of upper oceanic crust at ODP/IODP Site 1256, eastern equatorial Pacific 1

Abstract 1
1 Introduction 2
2 Geological background 3
2.1 Lithostratigraphy and observed alteration at Site 1256 3
2.2 Lithostratigraphy and observed alteration at Site 504 4
3 Sample preparation and analytical methods 5
4 Results 7
4.1 General geochemical characteristics of the Site 1256 basement composition 7
4.2 Alteration-insensitive trace elements (La, Nd, Th) 7
4.3 Alteration-sensitive trace elements (U, Pb, Rb, Sr) 8
4.4. Base metals (Cu, Zn) 8
4.5 Sr-Nd-Hf-Pb isotopes 9
5 Discussion 9
5.1 Constraining source-related heterogeneities 9
5.2 Alteration effects on the Rb-Sr isotope system 10
5.3 Alteration effects on the U-Th-Pb isotope system 11
5.4 Alteration effects on the mobility of base metals (Cu, Zn) 13
5.5 Could superfast spreading crust at Site 1256 evolve to a HIMU-type composition? 13
6 Conclusions 15
Acknowledgments 16
References 17
Figure 1 28
Figure 2 29
Figure 3 30
Figure 4 32
Figure 5 36
Figure 6 38
Figure 7 39
Figure 8 41
Figure 9 44
Figure 10 45
Figure 11 46
Table 1. 47
Table 2. 49

CHAPTER II 50

23 Ma history of hydrothermal and active margin sediment supply to the eastern equatorial Pacific: Geodynamic and paleoceanographic implications 50

Abstract 50
1 Introduction 50
2 Background 52
2.1 Geological setting 52
2.2 Atmospheric circulation 53
2.2 Oceanic circulation 54
3 Sample preparation and analytical methods 55
4 Results 56
5 Discussion 57
5.1 Identification of endmembers for eastern equatorial Pacific sediment compositions 57
5.2 Constraining transport pathways of Pb to the studied sites of deposition 60
5.3 Major drivers controlling Pb deposition in the Guatemala Basin through time 64
5.4 Paleoceanographic implications of continuous supply of hydrothermal Pb from the EPR 67
5.5 Why has Central America been insignificant for Pb input into the Guatemala Basin? 68
6 Conclusions 68
Acknowledgments 69
References 70
Figure captions 79
Figure 1 82
Figure 2 83
Figure 3 84
Figure 4 85
Figure 5 86
Table 1 87
Table 2 89

CHAPTER III 90

The geochemical evolution of Cocos Plate sedimentation and its paleoceanographic implications 90

Abstract 90
1 Introduction 90
2 Geological and oceanographic background 91
3 Sample preparation and analytical methods 93
4 Results 95
5 Discussion 97
6 Conclusions 102
Acknowledgments 102
References 103
Figure captions 110
Figure 1 112
Figure 2 113
Figure 3 114
Figure 4 115
Figure 5 116
Table 1 118
Table 2 121
Table 3 122
Table 4 126

APPENDICES 128

Appendix I (CHAPTER I) 128
Appendix Section A.1: 128
Detailed summary on observed alteration at ODP/IODP Site 1256 128
Appendix Section A.2: 129
On the applied isotopic modeling approach after Stracke et al. (2003) 129
References cited in Appendix I 130
Figure captions for Appendix I 132
Supplementary Figure A.1 (Appendix I) 134
Supplementary Figure A.2 (Appendix I) 135
Supplementary Figure A.3 (Appendix I) 136
Supplementary Figure A.4 (Appendix I) 137
Supplementary Table A.1 (Appendix I) 138
Supplementary Table A.2 (Appendix I) 139
Supplementary Table A.3 (Appendix I) 140
Supplementary Table A.4 (Appendix I) 141

Appendix II (CHAPTER II) 142
Appendix Section A.1: 142
Details on Pb isotopic database construction applied to the present study 142

Appendix III (CHAPTER III) 144
Supplementary Table A.1 (Appendix III) 144
Supplementary Table A.2 (Appendix III) 146
Supplementary Table A.3 (Appendix III) 147

ABSTRACT

Ocean Drilling Program (ODP) / Integrated Ocean Drilling Program (IODP) Site 1256, located on the Cocos Plate in the eastern Central Pacific, forms a notable exception in marine earth sciences, since it has been the first and, to date, the only drilling site that has intersected a complete in situ section of upper oceanic crust, penetrating the basement from the lavas to the uppermost gabbros. This took place during four research cruises between 2002 and 2011 (ODP Leg 206, IODP Expeditions 309, 312, 335), resulting in a current drilling depth of 1522 meters below seafloor (cf. Teagle et al., 2012: Scientific Drilling, no. 13, p. 28–34). In recent years, numerous studies were carried out addressing crustal accretion and alteration processes at Site 1256. However, none of those focused on the entire basement drilled with respect to both trace element and isotopic compositions. This gap is filled by the present study, employing most relevant radiogenic isotope systems (Rb-Sr, Nd-Sm, Lu-Hf, and U-Th-Pb). Furthermore, it addresses another major outcome of drilling at Site 1256: the recovery of a ~250 m thick sediment blanket, which has accumulated on the seafloor during ~15 million years of plate movement since the formation of the Site 1256 basement. This sediment package forms an excellent geochemical archive, which has been accessed using major and trace elements as well as Sr-Nd-Hf-Pb isotopes to decipher sediment sources and paleoceanographic processes in the eastern Central Pacific. Moreover, by adding new isotope data from the nearby Deep Sea Drilling Project (DSDP) Site 495 sedimentary succession, it has been possible to cover ~23 million years of marine sedimentation on the Cocos Plate tracking the entire pathway of this tectonic plate from its birth at the East Pacific Rise mid-ocean ridge spreading center to arrival at the Central American subduction zone.

The entire Site 1256 igneous basement reveals trace element and Sr-Nd-Hf-Pb (double spike) isotopic compositions similar to East Pacific Rise (EPR) normal mid-ocean ridge basalt. However, the mid-Miocene crustal accretion was geochemically slightly affected by the nearby Galápagos hotspot, confirming previous results for Site 1256 lavas (e.g., Geldmacher et al., 2013: Geology, v. 41, no. 2, p. 183–186). Despite the chemical enrichment, only narrow downhole variations in Nd-Hf-Pb isotope ratios have been revealed, probably pointing to small-scale magma source heterogeneities. In contrast, the Sr isotopic composition considerably varies downhole and, as expected, represents a sensitive tracer of seawater impact, resulting from seawater convection during crust formation at the spreading center. In particular, the dike-lava transition zone and the sheeted dikes have been affected by seawater alteration, which is most pronounced in a highly metal sulfide-enriched volcanic breccia layer of ~2.8 m thickness penetrated within the lithologic transition zone, showing the highest Sr isotope ratio of ~0.706. A comparison of alteration-related modification reflected by the Site 1256 superfast-spreading crust (20–22 cm/a full spreading rate) to alteration at Nazca Plate Site 504 intermediate-spreading crust (6–7 cm/a) has yielded that the overall intensity of seawater influence is lower at Site 1256. This is expressed by several proxies, such as lesser base metal mobility and variation of concentrations of trace elements susceptible to alteration

as well as overall less radiogenic Sr isotopic compositions at Site 1256. It is suggested that these differences between Sites 504 and 1256 likely reflect the significantly slower spreading at the Galápagos Spreading Center, where the Site 504 basement formed. Less enduring hydrothermal activity at Site 1256 did not allow either to produce a thicker sulfide-mineralized zone, which amounts to a thickness of ~18 m at Site 504. Therefore, the present study substantiates previous models obtained from surface scanning of present-day seafloor that strongly indicate a negative correlation of spreading rate and accumulation of metal sulfide (Hannington et al., 2011: Geology, v. 39, no. 12, p. 1155–1158), proving the spreading rate to potentially serve as an important mineral exploration proxy. Finally, Sr-Nd-Pb isotopic modeling additionally yielded that superfast-spreading crust of Site 1256 composition is not a suitable precursor to evolve to a HIMU (high μ = high $^{238}U/^{204}Pb$) mantle reservoir.

The first comprehensive geochemical characterization of sediments recovered from Sites 1256 and 495 has revealed that both sedimentary successions essentially form one geochemical record. This suggests that major changes in sedimentation occurred on a basin scale in the eastern equatorial Pacific (EEP). However, the investigated isotope systems show distinct differences in terms of sedimentary input pathways and driving forces over time. In addition, variations in provenance characterized the past ~23 million years covered by the present thesis. Bulk sediment Pb isotopic compositions have mainly varied in response to tectonic migration of the Cocos Plate away from the EPR toward Central America, which has been superimposed by changes in atmospheric circulation. Submarine mid-ocean ridge hydrothermal Pb and continental arc Pb have been continuously delivered from the EPR as well as Mexican (Trans-Mexican Volcanic Belt) and Andean (Northern Volcanic Zone, South Central Volcanic Zone) sources, respectively, suggesting deep-water flow and winds to form the most important pathways for Pb supply to the study area. Major changes in Pb isotopic evolution began at ~6 Ma, reflecting crossing of the Intertropical Convergence Zone and entering of the Northern Hemisphere circulation. However, Sr and Nd isotopic trends show profound inflections taking place c. 5 million years earlier at a time of major changes in the depositional setting in the EEP, reflecting a rapid decline of carbonate accumulation. In contrast, the Pb isotopic evolution has been independent of changes in sediment type. Nd and Sr have been derived from similar source areas compared to Pb, except for no significant impact of mid-ocean ridge hydrothermal sources on the bulk sediment Sr-Nd isotopic record. However, compared to eolian-dominated detrital Pb, there has been stronger emphasis on continental runoff and, most likely, exchange processes between ocean boundary currents and the continental margins. Both Pb and Sr-Nd isotopic records suggest stable deep-water flow patterns in the central and eastern Pacific over millions of years. Eastward deep-water currents have supplied the study area with hydrothermal matter and Central Pacific seawater for at least ~23 million years, despite any paleoceanographic changes, which may have occurred as a consequence of the Central American Seaway closure between the eastern Central Pacific and the Caribbean Sea. However, the termination of deep-water exchange through this gateway most likely resulted in formation of abyssal gyres at ~10.8 Ma, giving rise to remarkably well-mixed eastern equatorial Pacific seawater in the Guatemala Basin.

KURZFASSUNG

Die Ocean Drilling Program (ODP) / Integrated Ocean Drilling Program (IODP) Bohrungslokation (Site) 1256, welche sich auf der Cocos-Platte im östlichen Zentralpazifik befindet, bildet eine bemerkenswerte Ausnahme in den marinen Geowissenschaften, da sie die erste und bislang einzige Bohrung repräsentiert, die einen kompletten in situ Abschnitt der oberen ozeanischen Kruste erbohrt und dabei den gesamten oberen ozeanischen Krustenuntergrund von den Laven bis zu den obersten Gabbros durchdrungen hat. Dies fand im Rahmen von vier Forschungsausfahrten zwischen 2002 und 2011 statt (ODP Leg 206, IODP Expeditions 309, 312, 335), was in der momentanen Bohrungstiefe von 1522 m unterhalb des Meeresbodens mündete (cf. Teagle et al., 2012: Scientific Drilling, no. 13, p. 28–34). In den letzten Jahren wurden zahlreiche Studien durchgeführt, die sich mit den Akkretions- und Alterationsprozessen der ozeanischen Kruste von Site 1256 befasst haben. Jedoch hat sich keine dieser Studien auf die gesamte abgeteufte Kruste fokussiert hinsichtlich sowohl der Spurenelement- als auch der Isotopenzusammensetzungen. Diese Lücke wird von der vorliegenden Studie gefüllt, indem sie die relevantesten radiogenen Isotopensysteme (Rb-Sr, Nd-Sm, Lu-Hf und U-Th-Pb) anwendet. Darüber hinaus befasst sie sich mit einem weiteren Resultat der Bohrung von Site 1256: der Ausbringung einer ca. 250 m mächtigen Sedimentdecke, die sich seit der Bildung des Basements von Site 1256 im Laufe von etwa 15 Mio. Jahren Plattenbewegung auf dem Meeresboden akkumuliert hat. Dieses Sedimentpaket bildet ein hervorragendes geochemisches Archiv, das durch die Nutzung von Haupt- und Spurenelementen sowie Sr-Nd-Hf-Pb Isotopen zugänglich geworden ist, mit dem Ziel der Entschlüsselung der Sedimentquellen und paläoozeanographischen Prozesse im östlichen Zentralpazifik. Ferner ist es durch die Hinzunahme neu generierter Isotopendaten der nahegelegenen Deep Sea Drilling Project (DSDP) Site 495 möglich gewesen ca. 23 Mio. Jahre mariner Sedimentation auf der Cocos-Platte abzudecken und dabei den gesamten Pfad dieser tektonischen Platte von deren Entstehung am Spreizungszentrum des Ostpazifischen Rückens bis zur Ankunft an der zentralamerikanischen Subduktionszone zu verfolgen.

Das gesamte magmatische Basement von Site 1256 hat eine Spurenelement-zusammensetzung und Sr-Nd-Hf-Pb (double spike) Isotopensignatur offengelegt, welche der des Mittelozeanischen Rückenbasalts vom Ostpazifischen Rücken ähnlich ist. Die mittelmiozäne Krustenbildung war jedoch geochemisch affektiert durch den unweit gelegenen Galápagos Hotspot, was frühere Ergebnisse für die Laven von Site 1256 bestätigt (Geldmacher et al., 2013: Geology, v. 41, no. 2, p. 183–186). Trotz der chemischen Anreicherung haben die Untersuchungen nur geringe Variationen mit der Tiefe in den Zusammensetzungen der Nd-Hf-Pb Isotope gezeigt, was vermutlich auf kleinmaßstäbliche Heterogenitäten in der magmatischen Quelle hindeutet. Im Gegensatz dazu variiert die Sr-Isotopenzusammensetzung beträchtlich entlang der Teufe. Wie zu erwarten war, repräsentiert dieses Isotopenverhältnis einen empfindlichen Indikator für den Einfluss von Meerwasser (auf die chemische Zusammensetzung der Kruste), was aus der Konvektion von Meerwasser

während der Krustenbildung am Spreizungszentrum resultiert. Insbesondere sind die Übergangszone von Laven zu den magmatischen Gangintrusionen und die Gänge selbst davon beeinflusst worden. Dies drückt sich am stärksten in einer hochgradig mit Metallsulfiden angereicherten vulkanischen Brekzie aus, die mit einer Mächtigkeit von ca. 2,8 m innerhalb der lithologischen Übergangszone durchteuft worden ist und das höchste Sr-Isotopenverhältnis von etwa 0,706 zeigt. Ein Vergleich der alterationsbezogenen Modifikation der chemischen Zusammensetzung der Site 1256 Kruste, die während einer superschnell-spreizenden Phase (20–22 cm/a volle Spreizungsrate) entstanden ist, mit der Alteration der Site 504 (Nazca-Platte), die während einer intermediären Spreizung (6–7 cm/a) gebildet wurde, hat ergeben, dass insgesamt die Intensität des Meerwassereinflusses bei Site 1256 geringer ist. Dies drückt sich durch mehrere Proxys aus, wie der geringeren Mobilität von Buntmetallen und geringeren Variation von Spurenelementkonzentrationen, die anfällig für Alteration sind, sowie der durchschnittlich geringeren radiogenen Sr-Isotopen-zusammensetzung von Site 1256. Dies legt nahe, dass diese Unterschiede zwischen den Sites 504 und 1256 wahrscheinlich die signifikant langsamere Krustenspreizung am Galápagos-Spreizungszentrum, wo sich das Basement von Site 504 bildete, widerspiegeln. Weniger beständige hydrothermale Aktivität bei Site 1256 gestattete es nicht eine mächtigere sulfid-mineralisierte Zone zu generieren, die sich bei Site 504 auf ca. 18 m Mächtigkeit beläuft. Demzufolge untermauert die vorliegende Studie frühere Modelle, die von einem Oberflächenscan des heutigen Meeresbodens erhalten worden sind und nachhaltig eine negative Korrelation zwischen der Spreizungsrate und der Akkumulation von Metallsulfiden erkennen lassen (Hannington et al., 2011: Geology, v. 39, no. 12, p. 1155–1158). Dies beweist, dass die Spreizungsrate potentiell als Proxy für die Exploration dienen kann. Eine zusätzlich durchgeführte Sr-Nd-Pb Isotopenmodellierung hat letztlich ergeben, dass die superschnell spreizende Kruste mit der Zusammensetzung von Site 1256 keine geeignete Ausgangskruste darstellt, die sich zu einem Mantelreservoir mit HIMU (high μ = hohes $^{238}U/^{204}Pb$) Signatur entwickeln kann.

Die erste umfassende geochemische Charakterisierung der Sedimente, die von den Sites 1256 und 495 erhalten worden sind, hat offenbart, dass beide sedimentäre Abfolgen im Wesentlichen eine korrespondierende geochemische Aufzeichnung bilden. Dies legt nahe, dass bedeutende Veränderungen der Sedimentation beckenweit im östlichen Äquatorialpazifik auftraten. Die untersuchten Isotopensysteme zeigen jedoch klare Unterschiede hinsichtlich der sedimentären Eintragswege und treibenden Kräfte im Laufe der Zeit. Darüber hinaus haben Variationen in der Herkunft der Sedimente die letzten 23 Mio. Jahre gekennzeichnet, welche von der vorliegenden Arbeit abgedeckt werden. Gesamtsediment-Isotopenzusammen-setzungen von Pb haben hauptsächlich als Resonanz auf die tektonische Migration der Cocos-Platte weg vom Ostpazifischen Rücken hin zur zentralamerikanischen Subduktionszone variiert. Dies ist überlagert worden von Veränderungen in der atmosphärischen Zirkulation. Submarines hydrothermales Pb vom Mittelozeanischen Rücken und Pb von kontinentalen Bögen sind kontinuierlich vom Ostpazifischen Rücken bzw. von Mexiko (Transmexikanischer Vulkangürtel) und den Anden (Nördliche Vulkanzone, Südliche

Zentralvulkanzone) geliefert worden. Dies deutet auf Tiefenwasserströme (hydrothermales Pb) und Winde (kontinentales Pb) als wichtigste Transportpfade für das Untersuchungsgebiet hin. Große Veränderungen in der Evolution der Pb-Isotopie begannen vor etwa 6 Mio. Jahren, was eine Querung der Intertropischen Konvergenzzone und den Einzug in die Zirkulation der nördlichen Hemisphäre widerspiegelt. Jedoch zeigen die Isotopentrends von Sr und Nd tiefgreifende Wendungen bereits ca. 5 Mio. Jahre früher, zu einer Zeit von bedeutenden Veränderungen im Ablagerungsmilieu des östlichen Äquatorialpazifiks, was einen rapiden Abfall der Karbonat-Akkumulation widerspiegelt. Im Gegensatz dazu ist die Pb-Isotopenevolution stets weitestgehend unabhängig von Veränderungen des Sedimenttyps gewesen. Nd und Sr sind von ähnlichen Quellen geliefert worden wie Pb, mit der Ausnahme, dass kein signifikanter Einfluss von hydrothermalen Quellen auf die aufgezeichnete Gesamtgesteinsisotopenentwicklung von Sr und Nd sichtbar ist. Im Vergleich zum äolisch dominierten detritischen Pb liegt ein stärkerer Schwerpunkt auf dem kontinentalen Abflussregime und sehr wahrscheinlich auf chemischen Austauschprozessen zwischen ozeanischen Randströmungen und den Kontinentalrändern. Sowohl die Pb als auch die Sr-Nd Isotopie deuten stabile Tiefenwasserströme an, die das Untersuchungsgebiet mit hydrothermalem Material und zentralpazifischem Meerwasser über mindestens 23 Mio. Jahre versorgt haben, trotz jeglicher paläoozeanographischer Veränderungen, die sich als Konsequenz aus der Schließung der zentralamerikanischen Seeweges zwischen dem östlichen Zentralpazifik und dem Karibischen Meer vollzogen haben können. Allerdings führte die Beendigung des Tiefenwasseraustausches über den zentralamerikanischen Seeweg sehr wahrscheinlich zur Bildung eines abyssalen Kreislaufs vor ca. 10.8 Mio. Jahren im Guatemalabecken. Dies mündete in eine tiefgreifende Durchmischung des Meerwassers im östlichen Zentralpazifik.

INTRODUCTION

In the scientific ocean drilling community, there has been the long-term, ambitious quest for drilling an ultra-deep hole into the uppermost mantle through intact oceanic lithosphere since the initiation of the ocean drilling program series in the 1960s (cf. Ildefonse et al., 2010: Scientific Drilling, no. 10, p. 56–63). This shall provide valuable answers to fundamental questions associated with the interior structure and dynamics of our planet. In this regard, ODP/IODP Site 1256 is presently the favored location in fulfillment of this enduring goal.

Site 1256 was drilled on the Cocos Plate in the eastern Central Pacific into mid-Miocene oceanic crust, which formed during a period of superfast spreading. The present study was aimed at characterizing the igneous basement and the overlying sediment cover in order to address multiple aspects of hydrothermal alteration of oceanic crust and geochemical evolution of pelagic sediments over time, during transport on the moving Cocos Plate. The present dissertation has been written within the scope of the combined projects HO1833/16-1 and 18/1 funded by the German Research Foundation (DFG) Priority Program SPP 527 (International Ocean Discovery Program).

The present thesis is subdivided into three discrete chapters, which are either in review (Chapter I) or in preparation for submission (Chapters II and III). They are stratigraphically ordered, i.e., Chapter I addresses the igneous basement and the two following chapters shed light on the sedimentary pile of Site 1256 (and Site 495).

The first chapter provides a comprehensive Sr-Nd-Hf-Pb isotopic stratigraphy of the Site 1256 basement. Furthermore, a thorough comparison to alteration at nearby intermediate-spreading Site 504 is given. Lesser alteration at Site 1256 is suggested to reflect faster mid-Miocene spreading rates at the East Pacific Rise. A negative correlation of spreading rate and metal sulfide accumulation is substantiated. Finally, it is highlighted that altered Site 1256 basement cannot develop HIMU-type isotopic compositions through time.

The second chapter gives valuable insights into the long-term evolution of sedimentary Pb input into the eastern equatorial Pacific. It reveals the major driving forces of this evolution and fingerprints distinct source regions using Pb isotopes. Furthermore, major implications for the pattern and longevity of deep-water flow in the study area and its response to the gradual closure of the Central American Seaway are revealed.

The third chapter deals with the geochemical evolution of sedimentation in terms of major and trace element compositions and Sr-Nd-Hf isotopic records. It demonstrates the connectivity of changes in the depositional setting and the Sr-Nd isotopic evolution. Moreover, it provides constraints on sources and pathways of Nd and Sr input and shed light on changes in timing and extent of Guatemala Basin deep water circulation.

CHAPTER I

From the lavas to the gabbros: 1.25 km of geochemical characterization of upper oceanic crust at ODP/IODP Site 1256, eastern equatorial Pacific

Tobias W. Höfig [a,b], Jörg Geldmacher [a], Kaj Hoernle [a], Folkmar Hauff [a], Svend Duggen [a,c], and Dieter Garbe-Schönberg [d]

[a] *GEOMAR Helmholtz Centre for Ocean Research Kiel, Wischhofstr. 1-3, D-24148 Kiel, Germany*
[b] *New address: Department of Mineralogy, TU Bergakademie Freiberg, Brennhausgasse 14, D-09599 Freiberg, Germany*
[c] *New address: A. P. Møller Skolen, Fjordallee 1, D-24837 Schleswig, Germany*
[d] *Institute of Geosciences, Christian Albrechts University Kiel, Ludewig-Meyn-Str. 10, D-24118 Kiel, Germany*

in review

Abstract

Here we present trace element and Sr-Nd-Hf-Pb (double spike) isotopic data covering the entire igneous section of oceanic crust drilled at Ocean Drilling Program (ODP)/Integrated Ocean Drilling Program (IODP) Site 1256 on the Cocos Plate. The penetrated interval extends from the upper lavas through the sheeted dike complex to the gabbroic plutonic rocks, formed during superfast spreading at the mid-Miocene equatorial East Pacific Rise. The data are used to characterize the effects of chemical alteration, resulting from convection of seawater and hydrothermal fluids, on the trace element and isotopic composition of oceanic crust. Compared to normal mid-ocean-ridge basalt, the igneous basement of Site 1256 (Hole 1256C/D) is isotopically slightly enriched but shows only narrow downhole variations in Nd-Hf-Pb isotope ratios: $^{143}Nd/^{144}Nd = 0.513089 \pm 0.000028$ (2σ), $^{176}Hf/^{177}Hf = 0.283194 \pm 0.000033$ (2σ), $^{206}Pb/^{204}Pb = 18.61 \pm 0.11$ (2σ), $^{207}Pb/^{204}Pb = 15.521 \pm 0.014$ (2σ), $^{208}Pb/^{204}Pb = 38.24 \pm 0.15$ (2σ). We believe that this minor variability is mainly of primary (magmatic) origin. The Sr isotopic composition shows considerably larger variation and, as expected, serves as sensitive tracer of seawater influence, which is particularly pronounced in the dike-lava transition zone and the sheeted dikes. The seawater influence is most prominent in a highly metal sulfide-enriched breccia layer encountered in the transition zone with $^{87}Sr/^{86}Sr$ of ~0.706, indicating a maximum water-rock mixing ratio of ~12. However, compared to the igneous section drilled at Site 504 (Hole 504B), which formed at intermediate, i.e., slower spreading rates at the Galápagos Spreading Center and hosting a much thicker sulfide-rich stockwork zone, the average intensity of water-rock interaction is lower. This is expressed by lesser mobility of base metals, narrower variability of alteration-sensitive incompatible elements, and less radiogenic Sr isotopic compositions on average at Site 1256. The amount of metal sulfide precipitation seems to be positively correlated with the degree of hydrothermal overprint. The less intense alteration of the Site 1256 transition

zone, compared to Site 504, most likely reflects the impact of the higher supply rate of magma during superfast spreading, eventually leading to a shorter period of time of continuous exposure to hydrothermal convection at the ridge crest. The observed alteration-related modification of radiogenic parent/daughter concentration ratios in the Site 1256 rocks is ultimately not sufficient to develop time-integrative high $^{206}Pb/^{204}Pb$ and moderate $^{87}Sr/^{86}Sr$ ratios, as being characteristic of the HIMU (high μ = high $^{238}U/^{204}Pb$) mantle signature proposed to originate from altered subducted oceanic crust.

1 Introduction

Crustal accretion at mid-ocean ridges is intimately associated with the percolation of seawater-derived hydrothermal fluids through the newly formed oceanic crust. This leads to high fluid flux taking place in hydrothermal convection cells, which turns submarine ridge crests and their flanks into major sites of mass and energy exchange between seawater and seafloor (reviewed by Bach et al., 2013). Here we report trace element and Sr-Nd-Hf-Pb (double spike) isotopic data of in situ oceanic crust formed during a period of superfast spreading at the East Pacific Rise (EPR) in the Middle Miocene (Wilson, 1996), which has been drilled at Ocean Drilling Program/Integrated Ocean Drilling Program (ODP/IODP) Site 1256. Since approximately 50 % of the modern seafloor and thus 30 % of the Earth's surface formed at fast spreading rates (>80 mm/y full rate) (Teagle and Wilson, 2007; Wilson et al., 2003), studying such crust is critical to understand hydrothermal alteration and evolution of a major part of Earth's oceanic lithosphere. The present study provides the first comprehensive radiogenic isotope stratigraphy of the entire section of igneous oceanic crust penetrated at Site 1256. By comparing our data with results obtained from Deep Sea Drilling Project (DSDP)/ODP Site 504 (Bach et al., 2003; Kusakabe et al., 1989; Pedersen and Furnes, 2001; Shimizu et al., 1989), we assess the different extent of hydrothermal alteration during superfast (Site 1256) compared to intermediate (Site 504) spreading.

Extensive water-rock interaction at spreading ridges alters the geochemical composition of igneous oceanic crust, which eventually gets subducted into the mantle affecting the composition of melts extracted from it (e.g., Hofmann and White, 1982). The origin of isotopically distinct mantle endmembers is believed to arise from time-integrated fractionation of radioactive parent/daughter element pairs (e.g., Hofmann and White, 1982; Weaver, 1991). In this regard, strongly radiogenic Pb isotopic compositions found in ocean island basalts, defining the so-called HIMU component (high μ = high $^{238}U/^{204}Pb$) (Houtermans, 1953; Zindler and Hart, 1986), have been ascribed to alteration, subduction, and subsequent long-term storage of oceanic crust within the Earth's mantle (reviewed by Stracke et al., 2005). We therefore evaluate whether the observed alteration-related modifications of the Site 1256 oceanic crust can potentially develop to HIMU-type composition over time.

2 Geological background

Site 1256 is located in the eastern equatorial Pacific Guatemala Basin on the Cocos Plate (Fig. 1) and formed ~15.2 Ma ago at the East Pacific Rise (EPR) (Wilson et al., 2003). It was produced during a period of superfast spreading at full rates of ~200–220 mm/y lasting from ~22.5 to ~11 Ma (Geldmacher et al., 2013; Wilson, 1996). In comparison, the crust at nearby Site 504 formed at an intermediate spreading rate of ~70 mm/y at the Costa Rica Rift, as part of the eastern Galápagos Spreading Center (GSC), ~6.6 Ma ago (Bach et al., 2003; DeMets et al., 1990). Today, Site 504 is located ~200 km south of the GSC on the Nazca Plate (Fig. 1). For a better understanding, lithostratigraphy and observed alteration of both sites, 1256 and 504, are briefly outlined in the following.

2.1 Lithostratigraphy and observed alteration at Site 1256

Approximately 1.25 km of igneous basement, overlain by ~250 m of marine sediments, was penetrated at Site 1256 (Hole 1256C/D) during ODP Leg 206 (Wilson et al., 2003), and subsequent IODP Expeditions 309, 312 (Teagle et al., 2006), and 335 (Teagle et al., 2012) (Fig. 2). The upper part of the basement (~275 to 1004 meters below seafloor, mbsf) is made up of pillow and sheet flow lavas, also termed the volcanic zone (VZ) (Fig. 2). The lavas are generally described as aphyric to sparsely phyric (plagioclase and olivine) basalts often exhibiting glassy chilled margins (Wilson et al., 2003). The dike-lava transition zone (TZ), representing the transition from extrusive to intrusive magma emplacement, was identified between 1004 and 1061 mbsf. This zone is marked by a cataclastic massive unit in the upper part but is mostly made up of aphyric, cryptocrystalline basalt with the first subvertical intrusive contact detected at ~1018 mbsf (Teagle et al., 2006). A highly metal sulfide-mineralized zone of volcanic breccia and breccia intercalated with basaltic sheet flows form a remarkable layer of ~2.8 m thickness (Unit 1256D-42) beginning at ~1027.6 mbsf (Fig. 2). Subvertical intrusive contacts are common below ~1061 mbsf, characterizing a sheeted dike complex (SDC) of at least 346 m thickness (Teagle et al., 2006; Tominaga et al., 2009) (Fig. 2). The lowermost nearly ~60 m (~1348–1407 mbsf) of the SDC are contact-metamorphosed resulting in the appearance of granoblastic textures (Teagle et al., 2012). The plutonic section (PS) was entered at ~1407 mbsf (Fig. 2) and comprises two medium-grained gabbro units of different thickness, named Gabbro 1 (“upper gabbros”, ~52 m thick) and Gabbro 2 (“lower gabbros”, ~24 m thick), which are separated by a ~24 m thick, fine-grained, considerably recrystallized, metabasaltic dike screen (Dike screen 1) (Teagle et al., 2012). Both gabbroic sequences show a geochemical trend to less fractionated compositions downhole, whereas the Gabbro 1 unit (mostly oxide gabbro) generally appears to be less evolved than the Gabbro 2 unit (commonly gabbronorite) (Teagle et al., 2006). During Expedition 335, the plutonic section was drilled down to ~1522 mbsf, the current bottom of Hole 1256D, presently ending in another fine-grained dike screen (Dike screen 2) (Teagle et al., 2012).

Almost all lava flows were exposed to at least low-temperature alteration (<150 °C), which led to a slight overprint revealed by the presence of phyllosilicates and iron oxyhydroxides (Alt et al., 2010; Teagle et al., 2006). At ~981 mbsf, the first chlorite-smectite assemblage occurs representing the beginning of the hydrothermal alteration transition zone (Fig. 2), which is characterized by a gradually increasing degree of alteration downhole, leading to (sub)greenschist-facies conditions in the upper dikes at ~1028 mbsf, where the first green background alteration is observed (Alt et al., 2010; Teagle et al., 2006). The identification of greenschist facies manifests the upper boundary of the high-temperature hydrothermal alteration zone and corresponds well with the top of the highly metal sulfide-mineralized hyaloclastic breccia encountered in the TZ at ~1028 mbsf (Fig. 2). Hydrothermal alteration predominates from this sulfide-mineralized layer downward through the sheeted dikes to the gabbros.

The lowermost ~58 m of the SDC are made up of highly to completely hydrothermally altered rocks, which were transformed to granoblastic hornfels to variable extent at high temperatures (850–900 °C) through contact metamorphism (Alt et al., 2010; Koepke et al., 2008; Teagle et al., 2006). A more detailed summary on the alteration effects and secondary mineral parageneses of Site 1256 is given in the Appendix I (Section A.1).

2.2 Lithostratigraphy and observed alteration at Site 504

During seven DSDP and ODP legs, Site 504 (Hole 504B) was deepened to a total depth of ~2111 mbsf (Alt et al., 1993), including a 274.5 m thick sedimentary cover. The top of the basement consists of a lava section (Fig. 2), which comprises ~571.5 m of pillows and minor sheet lavas accompanied by subordinate hyaloclastites (down to ~846 mbsf) (Alt et al., 1993). Like at Site 1256, gradual transformation into an intrusive setting below is established by a 209 m thick dike-lava transition zone (TZ), encompassing strongly brecciated and altered pillow lavas, massive flows, and dikes (~846 to ~1055 mbsf) (Alt et al., 1986, 1993; Honnorez et al., 1985). However, in contrast to Site 1256, this TZ hosts a ~18 m thick stockwork-like metal sulfide-mineralized zone from ~910 down to ~928 mbsf (Honnorez et al., 1985). The TZ passes into a SDC of considerable thickness (>1056 m), comprising massive basalts sporadically bordered by chilled zones (Alt et al., 1993). The SDC of Site 504 extends down to the termination of the hole at ~2111 mbsf (Fig. 2). Thus, plutonic rocks have not been intersected at Site 504. The dikes are sparsely to moderately phyric, comprising plagioclase and olivine as prevalent phenocryst phases (Alt et al., 1993), similar to Site 1256.

Multiple phases of overprint related to fluid circulation affected the crustal section of Site 504 (Alt et al., 1986, 1996; Bach et al., 2003). Low-temperature alteration characterizes the lavas and upper part of the TZ. The upper 250–300 m of the lava section were exposed to near-axis circulation of relatively cold (<25–50 °C), oxidizing seawater leading to formation of iron oxyhydroxides, celadonite, and oxidized clay minerals, followed by off-axis precipitation of zeolites and carbonates (~60 °C). Below ~600 mbsf, the volcanic zone underwent low-temperature alteration at higher maximum temperatures (up to 150 °C) under

a reducing environment resulting in a gradually increasing abundance of pyrite (Alt et al., 1986, 1996). Thus, fluids acting in this zone were reducing rather than oxidizing as being the case above 600 mbsf (Honnorez et al., 1983). The underlying TZ and the upper ~450 m of the SDC show evidence of fluid mixing. Upwelling hydrothermal solutions interacted with cooler seawater leading to maximum alteration temperatures of 350–380 °C, which gave rise to growth of secondary greenschist-facies minerals (e.g., chlorite, actinolite, and epidote) (Alt et al., 1996). Although the greatest abundance of metal sulfides occurs in the ~18 m thick stockwork zone, sulfide-mineralized breccias and sulfide-impregnated massive basalts have been partially formed ubiquitously from the lower TZ (beginning at ~900 mbsf) downhole to the top of the SDC establishing a broad mineralization zone, which contains disseminated and replacive pyrite as a common mineral (Bach et al., 2003) (Fig. 2). The stockwork zone and other intervals of the TZ were affected by a complex alteration history including circulation of chemically different fluids at variable temperatures, leading to the formation of several generations of metal sulfides (chalcopyrite, pyrite, sphalerite, and accessory galena) (Bach et al., 2003; Honnorez et al., 1985). Down to ~1500 mbsf, variable alteration under greenschist-facies conditions continues, however, fracturing and alteration are generally less intense compared to the TZ (Alt et al., 1996; Bach et al., 2003). Below ~1500 mbsf, high-temperature hydrothermal alteration exceeding 400 °C, which gave rise to crystallization of secondary amphibole and Ca-rich plagioclase, affected the sheeted dikes (Alt et al., 1996).

3 Sample preparation and analytical methods

The present study used 44 representative igneous rock samples covering the entire igneous basement interval cored at Site 1256.

The samples were wrapped in polyethylene foil, carefully crushed with a hammer, followed by sieving and repeated washing in an ultrasonic bath comprising deionized water for removing dust-sized particles through decantation until a clear solution was obtained. Subsequently, the samples were dried overnight at 50 °C. Thereafter, 0.5–2 mm sized rock chips were handpicked under the binocular microscope to preclude visible potential compositional modification derived from shipboard treatment and sample preparation. Selected rock chips were then split into two fractions. One fraction was pulverized with an agate mortar for trace element analyses, whereas the other rock-chip subset was used for the Sr-Nd-Hf-Pb (double spike, DS) isotope analyses.

For trace element analyses, approximately 100 mg pulverized material from each sample taken from depths above 1260 mbsf underwent pressurized digestion by means of a multi-step procedure in sealed PFA vials using a concentrated HF–aqua regia solution overnight at 160 °C. After evaporation of the digest solution, another dissolution step was carried out with a 2 to 1 hot mixture of HNO_3 and ultrapure deionized water (DIW). The final residue, derived from a second evaporation stage, was then taken up with a HNO_3–DIW mixture at a ratio of 1:3, heated overnight, and made up to a final solution mass of 50 g. Pulverized samples from depths below 1260 mbsf underwent an additional pressure bomb step (Parr bombs; outlined in

John et al., 2008) to ensure complete dissolution of acid-resistant minerals (e.g., zircon), since it has been demonstrated on Site 1256 dike and gabbro samples from depths > 1260 mbsf that conventional acid digestion may not completely dissolve those mineral phases (Neo et al., 2009). Each obtained solution was then 10-fold diluted and spiked with 5 µg/l beryllium, indium, and rhenium for internal standardization prior to analysis. Trace element concentrations were determined on an "AGILENT 7500cs" inductively coupled plasma – mass spectrometer (ICP-MS) at the University of Kiel following the principles outlined in Garbe-Schönberg (1993). Determined trace element contents are provided in Table 1. Measurements of international rock standards (BHVO-2 and AGV-2) along with duplicates of individually digested samples and results for within-batch replicate analyses are shown in supplementary Tables A.1, A.2, and A.3 (Appendix I), respectively. The results for freshly digested BHVO-2 (n = 5) and for AGV-2 (n = 4) can be compared to compiled and recommended values (GeoReM online database: http://georem.mpch-mainz.gwdg.de/ – February 28, 2014; Jochum et al., 2005; see Tab. A.1). Relative differences among duplicate sample dissolutions are < 3 % for most elements (Tab. A.2). Based on repeated runs of the same sample solution, the instrument reproducibility is ≤ 1 % RSD for almost all elements except low concentrations of Rb, Sb, Cs, Ta, and partially Th (sample 206-1256D-30R-1, 44–59 cm) as well as some compatible elements (e.g., Sc, Cr, Ni; sample 309-1256D-128R-1, 80–91 cm), which range between 3 and 6 % RSD (Tab. A.3).

For Sr-Nd-Hf-Pb (DS) isotope analyses, the required ion-chromatographic separation and purification of Sr, Nd, Pb, and Hf was conducted according to the procedures outlined in Hoernle et al. (2008) (Sr, Nd, Pb) and Geldmacher et al. (2006) (Hf), respectively. Sr-Nd-Pb (DS) isotope analyses were obtained by thermal ionization mass spectrometry (TIMS) at GEOMAR on Finnigan MAT 262 RPQ^{2+} (Sr, Pb-DS) and Thermo Finnigan TRITON-TI (Sr, Nd), both operating in static multi-collection mode. Procedures for TIMS analyses, implemented for the present study, are extensively described by Hoernle et al. (2011). Within-run errors are given as $2\sigma / \sqrt{n-1}$ (n = number of scans passing the outlier test) and all external errors, such as the reproducibility of standards, are reported as 2σ of the mean (Tab. 2). Sr and Nd isotope ratios were mass bias corrected within-run to $^{86}Sr/^{88}Sr = 0.1194$ and $^{146}Nd/^{144}Nd = 0.7219$, respectively. The Sr isotope data are given relative to $^{87}Sr/^{86}Sr = 0.710250 \pm 0.000011$ (n = 49) for NBS987, whereas the Nd isotope data are reported relative to $^{143}Nd/^{144}Nd = 0.511850 \pm 0.000007$ (n = 65) for La Jolla. Total chemistry blanks were <100 pg for Sr and Nd. Pb isotope ratios were determined using the Pb-DS technique outlined in Hoernle et al. (2011). The long-term average DS corrected NBS981 values are $^{206}Pb/^{204}Pb = 16.9420 \pm 0.0030$, $^{207}Pb/^{204}Pb = 15.4998 \pm 0.0029$, $^{208}Pb/^{204}Pb = 36.7256 \pm 0.0072$, $^{207}Pb/^{206}Pb = 0.91487 \pm 0.00006$, and $^{208}Pb/^{206}Pb = 2.16772 \pm 0.00010$ (n = 139) over the course of the project (2006–2012). Total chemistry blanks are considered negligible, as they typically ranged from 6 to 20 pg Pb with one exception of 75 pg Pb. Hf isotope ratios were determined by means of multi-collector ICP-MS on a NU Plasma II instrument at GEOMAR, using static multi-collection mode. Within-run mass bias correction of Hf isotope ratios was carried out to $^{179}Hf/^{177}Hf = 0.7325$. An in-house SPEX Hf ICP

reference solution, normalized to JMC-475 ($^{176}Hf/^{177}Hf = 0.282163$; Blichert-Toft and Albarède, 1997), yielded an average value of $^{176}Hf/^{177}Hf = 0.282170 \pm 0.000008$ (n = 51) over the course of the measurement period (2011–2012). Sr-Nd-Hf-Pb (DS) isotope analyses of selected samples were replicated by means of a separate digestion within the external two sigma errors of the standard values (Tab. 2).

4 Results

4.1 General geochemical characteristics of the Site 1256 basement composition

The igneous basement of Site 1256 generally resembles normal mid-ocean-ridge basalt (N-MORB) composition (Fig. 3), except for one compositionally unusual SDC sample (312-1256D-189R-1, 71–89 cm) revealing trace element-enriched MORB (E-MORB)-like composition (Fig. 3c), as previously found in some of the uppermost (off-axis) lavas at this site (Geldmacher et al., 2013; Sadofsky et al., 2009) (Fig. 3a). Compared to the VZ and SDC, samples from the plutonic section show slightly more depleted incompatible element compositions (Fig. 3). However, this is only valid for the true gabbros, as the dike screen sample shows lesser depletion and appears to be more similar to the dikes above (Fig. 3d). In comparison to Site 1256, the igneous basement of Site 504 is generally more depleted, being akin to depleted MORB (D-MORB) (Fig. 3).

4.2 Alteration-insensitive trace elements (La, Nd, Th)

Analyses of trace elements being fairly insensitive to alteration (Nb, Ta, and all rare earth elements) basically show no significant differences in fresh N-MORB glasses (Geldmacher et al., 2013) and altered whole rocks in samples from the same lava unit in the volcanic zone (Fig. 3a and supplementary Fig. A.1, Appendix I), suggesting that these elements also reflect primary compositions in whole rock samples from the intrusive sections below. A comparison of downhole variations between Sites 1256 and 504 of indicative trace elements reveals that generally fluid-immobile La, Nd, and Th display analogous behavior, without any significant variations from the lavas down to the upper dikes (Figs. 4a-c). However, Nd tends to be slightly enriched in the lower Site 1256 dikes below ~1200 mbsf, whereas La and Th continue to show no variations down to the base of that sheeted dike complex. For those three elements, the pattern in the plutonic section is different, revealing moderate (La, Nd) to slight (Th) decrease in concentrations in the gabbroic rocks. All three elements display somewhat higher abundances at Site 1256 compared to 504. A Site 1256 off-axis lava flow shows pronounced negative Sr and Eu anomalies in the multielement diagram (Fig. 3a), most likely caused by plagioclase fractionation. This indicates considerable off-axis melt differentiation leading to an overall enrichment of incompatible trace elements. Regarding the transition zones, depletion of both La and Nd is indicated for the metal sulfide-rich levels at both sites

and minor La-Nd enrichment below (around 1000 mbsf) at Site 504, which is not seen in the Site 1256 TZ.

4.3 Alteration-sensitive trace elements (U, Pb, Rb, Sr)

Pb and Sr concentrations remain nearly constant downhole at Site 1256 with a couple of exceptions (Figs. 4e/g). The Sr values range mostly around ~85 ppm in the VZ and vary within the narrow range of their associated Site 1256 N-MORB-like glasses. However, they reveal a considerable scatter in the TZ with concentrations well above and below the narrow range of the lavas. Significant Sr depletion with values considerably <60 ppm (down to ~20 ppm) is shown by the metal sulfide-rich interval (Fig. 4g). The Sr values in the dikes and gabbros generally display lesser fluctuation. The same observations can be made for Pb, except that the scatter in the TZ generally extends only in the direction of (much) higher values, reflecting ~2- to ~50-fold increases in the metal sulfide-enriched rocks of the Site 1256 TZ compared to the average Pb concentration of the corresponding fresh Site 1256 N-MORB-like glasses (Figs. 3b, 4e). The Sr-Pb pattern at Site 504 is similar to 1256 with, however, more variation at lower concentration ranges (Figs. 4e/g). Nevertheless, the degree of Pb enrichment in the central part of the Site 504 TZ is much more pronounced compared to Site 1256, showing ~30–700-fold increases relative to the average Pb content of the associated volcanic zone (Figs. 3b, 4e). Moreover, alteration-related crustal uptake of Pb and U from seawater is indicated by comparison of slightly altered whole rock samples with their corresponding fresh glassy margins (supplementary Fig. A.1) and average composition of Site 1256 N-MORB glasses (Figs. 3a, 4d/e). Apart from a fairly slight decreasing trend indicated in the gabbros, U behaves similar to Sr and Pb (Figs. 4d/e/g). At Site 504, the U concentrations are quite uniform as well, however, the volcanic and transition zones are characterized by a significantly greater fluctuation of U values (Fig. 4d). Increases, as in case of U and Pb, or variations, similar to the Sr pattern, are not obvious for highly incompatible, fluid-mobile Rb at the TZ in either hole. Both sites show similar behavior for Rb, decreasing from ~2 ppm in the extrusive part to fairly constant values of <1 ppm below the TZ at Site 1256 (Fig. 4f). In general, it is obvious that Rb behaves differently downhole, being either enriched or depleted in the volcanic zone (with respect to fresh N-MORB), but constantly depleted from the transition zone down to the gabbros.

4.4. Base metals (Cu, Zn)

The contents of base metals Cu and Zn are largely constant in the volcanic zone at both sites (Figs. 4h/i). However, as expected, Cu and Zn show significantly elevated concentrations in the metal-sulfide-rich TZ of up to 112 and 144 ppm (Site 1256), respectively, reaching particularly high values in the stockwork zone at Site 504 (Cu: ~580 ppm, Zn: ~1650 ppm) and at some intervals in the underlying sheeted dike complex of both holes (Figs. 4h/i). Site 1256 Cu and Zn concentrations generally decrease from the TZ down to the Gabbro 2 unit,

apart from some exceptions in the Gabbro 1 unit. The overall variation of both base metals is considerably more pronounced at Site 504, particularly in the transition zone.

4.5 Sr-Nd-Hf-Pb isotopes

The $^{87}Sr/^{86}Sr$ isotope ratio of Site 1256 igneous basement rocks ranges from ~0.7028 to ~0.7060 (Fig. 5a). The lavas, uppermost TZ rocks, and gabbros show no significant deviation from the relatively tight Sr isotopic 2σ range of the fresh Site 1256 lava glasses (~0.7030 ± 0.0003; Geldmacher et al., 2013). In contrast, the Sr isotopic compositions of the dikes, observed for both SDC and dike screen samples, are somewhat shifted toward seawater Sr isotopic composition, reaching values up to ~0.7040 (Fig. 5a). However, the most radiogenic Sr isotopic composition of the entire Site 1256 basement is observed in the TZ showing a considerably increased $^{87}Sr/^{86}Sr$ of up to ~0.7060 measured in a sample from the highly sulfide-mineralized breccia layer at ~1028 mbsf (light orange-rimmed sample in Fig. 5a). This sample also has the lowest Sr concentration among all measured Site 1256 igneous rocks (see Fig. 4g). In general, there is, however, no difference in Sr concentration of whole rocks compared to their corresponding fresh glassy margins, as indicated by samples from the volcanic zone (supplementary Fig. A.1, Appendix I). Compared to Site 1256, the downhole variation in $^{87}Sr/^{86}Sr$ is generally larger at Site 504 and most values are shifted toward seawater compositions (Fig. 5a).

The Nd and Hf isotopic compositions of the igneous section at Site 1256 vary, without any systematic downhole trend, from 0.513037 to 0.513110 and 0.283132 to 0.283215 (Tab. 2), respectively, but broadly overlap with the 2σ range of the fresh Site 1256 lava glasses (Figs. 5b and 6). One exception is the incompatible-element-enriched dike sample 312-1256D-189R-1, 71–89 cm, which shows comparatively unradiogenic values (Figs. 5b, 6).

The range of Pb isotopic compositions at Site 1256 ($^{206}Pb/^{204}Pb$ = 18.53–18.76; $^{207}Pb/^{204}Pb$ = 15.51–15.54; $^{208}Pb/^{204}Pb$ = 38.14–38.49; see Tab. 2) is constant along the entire core and is far more limited than at Site 504 ($^{206}Pb/^{204}Pb$ = 17.90–18.82; $^{207}Pb/^{204}Pb$ = 15.43–15.56; $^{208}Pb/^{204}Pb$ = 37.63–38.46; Pedersen and Furnes, 2001) (Fig. 7). No clear correlations of Pb isotopic compositions with Th/Pb and U/Pb ratios are observed (cf. Figs. 7 and 8d/e). On thorogenic and uranogenic Pb isotope diagrams ($^{206}Pb/^{204}Pb$ versus $^{207}Pb/^{204}Pb$ and $^{208}Pb/^{204}Pb$, respectively), the Site 1256 data are broadly correlated, forming linear arrays, which plot above and roughly subparallel to the Northern Hemisphere Reference Line (NHRL) (supplementary Fig. A.2).

5 Discussion

5.1 Constraining source-related heterogeneities

As demonstrated by Pedersen and Furnes (2001), Site 504 Nd isotope ratios vary with Sm/Nd showing a relationship of high $^{143}Nd/^{144}Nd$ with high Sm/Nd (D-MORB) and low

$^{143}Nd/^{144}Nd$ with low Sm/Nd (N/E-MORB). Such a relationship is not observed for Site 1256 (cf. Figs. 5b and 8b). Considering the overall lower Sm/Nd ratios of the Site 1256 igneous rocks and their higher La/Sm ratios (Fig. 8a), representing fairly alteration-insensitive incompatible trace element pairs, it is obvious that the magma source of the Site 1256 rocks was slightly more geochemically enriched than the Site 504 source, which largely reflects D-MORB composition throughout. It is proposed that the upper mantle source at Site 1256 was more enriched in incompatible trace elements and enriched isotope ratios due to interaction with the nearby Galápagos hotspot during times of superfast spreading (Geldmacher et al., 2013; Park et al., 2008). This model is substantiated by Pb isotopic compositions of the present, more comprehensive study, tending toward radiogenic (higher) values consistent with a Galápagos plume signal, which is not observed at Site 504 (supplementary Fig. A.2).

The trace element-enriched E-MORB-like composition of some off-axis lava flows at Site 1256 is probably of primary (source) origin. Downhole source heterogeneity might have also led to compositional differences between Site 1256 off- and on-axis lavas possibly indicating a slightly lower degree of melting for the off-axis lavas, since the upper E-MORB-like lavas above 400 mbsf are, on average, more incompatible-element enriched in comparison to bulk rock samples of the lava section further downhole. Similarly enriched trace element patterns with E-MORB signatures can also be found in today's off-axis EPR lavas between 9° and 10° N (Fig. 3a), derived from a segment that is believed to be unaffected by any hotspot, and where predominantly (on-axis) N-MORB is produced (Sims et al., 2002; Waters et al., 2011). Our new data show that off-axis lavas with E-MORB composition occasionally formed at the EPR already ~15 m.y. ago in this area. Furthermore, small-scale source heterogneities are reflected by the small downhole Nd isotope variations at Site 1256, since there seems to be no correlation with seawater-derived elevated Sr isotope ratios (Fig. 5).

5.2 Alteration effects on the Rb-Sr isotope system

The most obvious deviations of trace element and isotopic composition from fresh glass compositions at Site 1256 can be found in the TZ and in individual units from the plutonic section. In contrast to Site 504, where even certain rare-earth-element ratios like La over Sm of TZ rocks are believed to have been fractioned by alteration-related mobilization (Bach et al., 2003), the compositional deviations in the TZ at Site 1256 are significantly less pronounced, indicating less intense alteration at the dike-lava interface.

One of the best indicators for (seawater) alteration processes in igneous rocks are elevated Sr isotope ratios [mid-Miocene seawater: $^{87}Sr/^{86}Sr = 0.708780$ (Hodell and Woodruff, 1994), c_{Sr} (present-day) = 7.6 ppm (Frank, 2002)]. Interestingly, Sr isotopic enrichment (Fig. 5a) does not generally correlate with elevated Sr concentrations (Fig. 4g) confirming studies by Kirchner and Gillis (2012), who demonstrated that Sr isotopic exchange through seawater-rock interaction does not necessarily result in Sr uptake or loss but is principally governed by the replacement of igneous minerals (low $^{87}Sr/^{86}Sr$) by hydrothermal minerals (higher $^{87}Sr/^{86}Sr$). The observed downhole variation in Rb/Sr (Fig. 8f) must therefore be mainly

controlled by gain or loss of Rb due to its higher fluid mobility. Interestingly, the range of the Rb/Sr ratio in the TZ and across the SDC is fairly limited and generally depleted (resulting from Rb loss; see Fig. 4f) compared to the overlying VZ, which, in contrast, displays a large scatter of up to ~0.1 (Fig. 8f), although these samples have primary (low) $^{87}Sr/^{86}Sr$ ratios (Fig. 9). Thus, the observed increase of the average Sr isotopic composition in the TZ and upper dike section took place without any considerable enhancement of the Rb/Sr ratios (Fig. 9). In contrast, the comparatively more altered volcanic rocks from Site 504 tend to display increasing Sr isotope ratios with enhanced Rb/Sr (Fig. 9). The interval of elevated Sr isotopic compositions, culminating at ~0.706 in the TZ-hosted pyrite-rich breccia layer (~1028 mbsf) at Site 1256 (Fig. 5a), coincides with the upper limit of the high-temperature hydrothermal alteration zone (cf. Fig. 2). This interval is proposed to show the maximum water-rock interaction, which is constrained by the calculated mixing line in Fig. 10. Most samples display a narrow scatter around primary MORB $^{87}Sr/^{86}Sr$ ratios of ~0.703 with some samples shifted toward radiogenic, mid-Miocene seawater-like Sr isotope values without any significant change in $^{143}Nd/^{144}Nd$. Due to the low concentration of Nd in average seawater (<100 pmol/kg; Chen et al., 2013, and references therein), water-rock ratios of 10^5 to 10^6 would be required to change the Nd isotopic composition of the lavas toward seawater values. A maximum water-rock ratio of ~12 is inferred for the sulfide-mineralized breccia of the Site 1256 TZ (Fig. 10). Unfortunately, the lack of combined Sr-Nd isotopic data measured on the same sample from Site 504 TZ rocks preclude a direct comparison with Site 1256. Nevertheless, the most radiogenic Sr isotopic compositions of <0.705 for Site 504 (Bach et al., 2003) suggest a maximum water-rock ratio below 10 for individual samples (cf. Fig. 10). However, the significantly greater downhole variability and higher mean values of $^{87}Sr/^{86}Sr$ for Site 504 volcanics (in comparison to both Site 1256 rocks and fresh GSC MORB values associated with 504; Fig. 5a) reflect, on average, more pervasive seawater-rock interaction (alteration) at Site 504 compared to Site 1256. The systematic downhole decrease of Sr isotope ratios from peak values in the TZ to MORB-like ratios in the upper dikes (Fig. 5a) might reflect diminishing influence of seawater with depth and suggests that the TZ plays an important role as barrier for downwelling seawater encountering upwelling hydrothermal fluids.

5.3 Alteration effects on the U-Th-Pb isotope system

Compared to the Rb-Sr isotope system, the U-Th-Pb isotope system displays a more complex behavior. Though Th may be somewhat mobilized under high-temperature hydrothermal conditions (e.g., Valsami-Jones and Ragnarsdóttir, 1997), it is commonly considered to be insoluble in geologic fluids (e.g., Langmuir and Herman, 1980). In contrast, Pb is highly mobile in hydrothermal systems (e.g., Chauvel et al., 1995) and U (as uranyl ion, UO_2^{2+}) is extremely mobile under oxidizing conditions even at low temperature (e.g., Duff et al., 2002; Langmuir, 1978; Shock et al., 1997). Although most Site 1256 samples have Pb contents narrowly ranging around unaltered N-MORB, considerable mobilization of Pb is

evident close to and in the sulfide-cemented volcanic breccia layer of the Site 1256 TZ through a 2- to 51-fold enrichment (with up to 17.2 ppm Pb; Figs. 3b and 4e), compared to the average composition of Site 1256 N-MORB-like glasses (0.34 ppm; Geldmacher et al., 2013). Such pattern is similarly reported from galena-free greenschist-altered basement rocks from other eastern Pacific ridges showing 10–20-fold increase in Pb concentrations relative to unaltered MORB (Mühe et al., 1997). Besides incorporation by calcium carbonate, Pb is a substituting trace metal in pyrite and subordinate chalcopyrite (Hawley and Nichol, 1961), forming the common sulfide assemblage in the TZ of Site 1256. Generally, the whole rock Pb enrichment in the TZ of Site 504 is far more pronounced (up to ~266 ppm; Bach et al., 2003) than at Site 1256, reflecting presence of accessory galena (Honnorez et al., 1985) and more vigorous hydrothermal activity. In the lava section at both sites, whole rock Pb concentration peaks are revealed [relative to the average content of 0.34 ppm (Site 1256 N-MORB-like glasses) and 0.37 ppm (Site 504 volcanic zone), respectively] (see Figs. 3a and 4e), implying crustal Pb uptake from seawater through incorporation by secondary carbonates, since Pb is primarily complexed with CO_3^{2-} in oxidized seawater (Chester, 1990). Secondary carbonate minerals have been identified throughout in the lava section at both sites (1256: Alt et al., 2010; Wilson et al., 2003; 504: Alt et al., 1996; Honnorez et al., 1983).

Principally, seafloor volcanic rocks often show an uptake of U from seawater during low-temperature alteration (e.g., Hart and Staudigel, 1982), as already documented for some oxidatively altered volcanic units of Sites 504 (Bach et al., 2003) and 1256 (Sadofsky et al., 2009; this study) (Figs. 3a, 4d, and A.1). It has been suggested that U co-precipitates with secondary iron oxyhydroxides and carbonates, which have been supposed to be the major hosts to U in such an altered crustal environment (e.g., Kelley et al., 2005; Krolikowska-Ciaglo et al., 2007). Consequently, the upper part of the Site 1256 crust (volcanic and transition zone rocks) is characterized by low Th/U ratios compared to fresh MORB glasses from this site (caused by U uptake). Notably, compared to the average content in Site 1256 N-MORB glasses (0.06 ppm; Geldmacher et al., 2013), U is 18-fold enriched in the lower greenschist-facies sulfide-mineralized breccia (1.07 ppm) of the Site 1256 TZ, revealing that crustal uptake of U does not only occur at low temperature. This observation confirms the results obtained for the Site 504 TZ (Bach et al., 2003).

The sulfide-cemented breccia sample shows both the highest contents in Pb and U among all igneous rocks studied at Site 1256. Likewise at Site 504, the TZ samples of the stockwork zone are among those rocks with the most elevated U and Pb contents (Figs. 4d/e). The comparatively thin metal sulfide-rich breccia layer in the Site 1256 TZ is thus not regarded as an outlier but rather reflects an analogy to the thick stockwork-like zone of Site 504. It has been speculated that carbonates may primarily govern the U distribution in the TZ (Bach et al., 2003). However, metal sulfides may additionally form hosts to uranium, as demonstrated by experimental studies showing aqueous uptake of the uranyl ion through chemical reduction and precipitation on the surface of pyrite crystals under both anoxic (Wersin et al., 1994) and oxidized (Scott et al., 2007) conditions at room temperature. Adsorption of U by metal sulfides may also take place within the upper oceanic crustal mixing zone of seawater-derived

and hydrothermal fluids at the dike-lava interface. Such an uptake of U under lower greenschist-facies conditions has been suggested for Site 504 by Bach et al. (2003) and is also indicated for Site 1256 by the present study. Therefore, extraction of U from fluids by secondary sulfide and carbonate minerals turns the dike-lava transition zone into a further sink (besides the volcanic zone) for this element in the upper oceanic crust, being a likely additional explanation for the essential lack of uranium in mid-ocean ridge vent fluids (e.g., Michard et al., 1983) and seafloor hydrothermal sulfide deposits (e.g., Zeng et al., 2010). Subsurface formation of secondary minerals and related U-Pb uptake from fluids is reflected in variable Th/U, Th/Pb, and U/Pb, relative to N- and E-MORB, seen at both sites (Figs. 8c-e) with the considerably larger range in Th/U ratios at Site 504, being consistent with stronger seawater alteration.

5.4 Alteration effects on the mobility of base metals (Cu, Zn)

Distinct zones of base metal enrichment and depletion, respectively, point to a considerable metal mobility throughout the basement of both holes. In particular, the sulfide-rich rocks found in the Site 1256 TZ (and partly uppermost dikes) reveal significantly elevated contents of Cu and Zn, particularly in the sulfide-rich hyaloclastite breccia at ~1028 mbsf, whereas the lower sheeted dike and plutonic sections are much depleted in these elements. However, a strong fractionation of Zn/Cu ratios, as shown by the stockwork zone of Site 504, is lacking at the Site 1256 TZ (Fig. 8g). Higher Cu and Zn contents in the stockwork zone of the Site 504 TZ reflect more abundant Cu-Zn sulfides. In the Site 1256 dike section, sporadically occurring sulfide-bearing veins, described for moderately to strongly fractured dikes (Teagle et al., 2006), result only in local Cu-Zn enrichments, as partly revealed by the upper dikes (Figs. 4h/i). However, the general decrease in base metal concentrations below the TZ down to the lower gabbros (Figs. 4h/i) indicates loss of metals, suggested to be caused by high-temperature (>350 °C) hydrothermal leaching processes in the lower sheeted dikes and upper plutonic rocks (Alt et al., 2010).

5.5 Could superfast spreading crust at Site 1256 evolve to a HIMU-type composition?

The comprehensive geochemical characterization of the entire Site 1256 oceanic basement sequence of ~1.25 km thickness provides the opportunity to use the present data for an assessment whether this oceanic crust segment could develop HIMU-type isotopic composition over time. HIMU-type ocean island basalts (OIB) are characterized by radiogenic Pb ($^{206}Pb/^{204}Pb > 20$), relatively low $^{87}Sr/^{86}Sr$ (0.7027–0.7033) as well as intermediate $^{143}Nd/^{144}Nd$ (0.5128–0.5130) isotopic compositions and are believed to reflect ancient, subducted (variably altered) oceanic crust (e.g., Hart, 1988; Zindler and Hart, 1986). For the present study, both the upper oceanic crust package as an entity and its distinct ignous units (lavas, transition zone, sheeted dikes, plutonic section) have been modeled separately. Given a calculated initial isotopic composition of ancient MORB as starting composition

(being consistently less radiogenic with increasing age), we used the Site 1256 chemical compositions of the Rb-Sr, Sm-Nd, and U-Th-Pb systems to investigate whether the isotopic evolution during recycling of this superfast-spreading crust would yield the present-day HIMU-type signature for a given recycling age (0.5, 1, 1.5, 2, 2.5, and 3 Ga). For this purpose, we followed the modeling approach and calculations of Stracke et al. (2003). The compositional evolution of the oceanic crust was modeled in two different ways: 1) assuming no significant modification of the parent-daughter ratios during subduction (Fig. 11a, supplementary Fig. A.3, Appendix I) and, in contrast, 2) taking into account subarc fractionation processes (Fig. 11b, supplementary Fig. A.4), using estimated element mobility coefficients of Kogiso et al. (1997) and Stracke et al. (2003) (supplementary Tab. A.4, Appendix I). Details of the applied modeling approach are provided in the Appendix I (Section A.2).

Evolution models of aging Site 1256 oceanic crust, assuming no modification by subduction processes (Figs. 11a, A.3), reveal that neither the defined crustal sections nor the composite crust developed an isotopic composition (over a recycling time of 0.5–3 Ga), which led to a modern HIMU-type composition in all three isotope systems considered. The transition zone evolved to more depleted and the gabbros and composite crust evolved to somewhat more enriched Pb isotopic compositions, relative to the present-day (unmodified) MORB source, the SDC remained largely in the MORB field (except at recycling ages >1.5 Ga), and the lavas evolved to $^{206}Pb/^{204}Pb$ similar to HIMU OIB after 2 Ga, but resulting Sr and Nd isotope ratios were too high and $^{208}Pb/^{204}Pb$ too low for HIMU OIB. Therefore, it becomes obvious that the alteration-related in situ increase in Rb/Sr and U/Pb as well as slight decrease in Th/Pb are not sufficient to make the Site 1256 rocks a suitable precursor for the HIMU mantle component without involving additional fractionation during subduction processes. Bach et al. (2003) came to a similar conclusion for the even more alteration-affected upper oceanic crust of Site 504. However, considerably long aging of the oceanic crust on the seafloor may also be taken into account as option to generate HIMU-type isotopic signatures prior to subduction. This has been addressed by Hoernle (1998), who showed that altered Jurassic MORB xenoliths (~178 Ma), found in volcanic deposits from the Canary Islands, have developed HIMU-like trace element as well as Sr, Nd, and uranogenic Pb isotopic compositions (similar to basalts from St. Helena) even before subduction, due to extremely high U/Pb ratios. One problem related to some of the sub-Canarian samples is that the thorogenic Pb isotopic composition was much more radiogenic than found in St. Helena HIMU-type. Thus, a lower time-integrated Th/U ratio (2.5 instead of 3.8) would be required to generate the appropriate $^{208}Pb/^{204}Pb$ HIMU-type ratio within 170–180 Ma (Hoernle, 1998). Given the fairly immobile behavior of Th during seafloor alteration, this would call for more intense alteration-related modification of the crust to enhance the content of variably fluid-mobile U, particularly for the strongly seawater-affected parts of the basement, i.e., volcanic and transitional rocks. However, this, in turn, would give rise to an enhanced U/Pb ratio. Consequently, it is questionable whether such elevated U/Pb would yield uranogenic Pb isotope ratios still plotting in the HIMU field and not being much higher. Instead, a less

enriched primary composition, reducing the concentration of fairly fluid-immobile Th, would be another possibility to obtain lower Th/U ratios.

Alternatively, subduction processes can reduce the Th concentration (Pearce and Peate, 1995). Indeed, several OIB studies have recently called for additional fractionation of relevant isotope systems, e.g., U-Th-Pb, during the subduction process for developing time-integrative HIMU-like isotope signatures (e.g., Kawabata et al., 2011; Kelley et al., 2005; Kogiso et al., 1997; Stracke et al., 2003). Thus, the subarc evolution of the oceanic crust gets very complex, since U and Pb are also lost through subduction-related dehydration with a higher mobility indicated for Pb compared to U (Kelley et al., 2005). However, even additional subduction-related element fractionation, estimating similar mobility of Pb and U as modeled prerequisite for HIMU generation (Stracke et al., 2003), did not yield isotopic compositions similar to HIMU-type basalt using the Site 1256 basement as a protolith (Fig. 11b). Solely the altered lava section, additionally modified by modeled subduction-related partial chemical removal (dehydration) of elements, evolved to compositions closest to HIMU in terms of similarly radiogenic $^{206}Pb/^{204}Pb$ and unradiogenic $^{87}Sr/^{86}Sr$ for ages >2 Ga, however, its $^{143}Nd/^{144}Nd$ and $^{208}Pb/^{204}Pb$ became much too radiogenic (Figs. 11b, A.4), similar to the sub-Canarian MORB (i.e., sample B9117.3) with a $^{208}Pb/^{204}Pb$ ratio being much more radiogenic than at St. Helena (Hoernle, 1998). One possible explanation for this mismatch is that element modifications during the subduction process are quantitatively poorly constrained, since the degrees of chemical enrichments/depletions are largely unknown (Stracke et al., 2003). In summary, we were not able to attain a HIMU-like composition simply by alteration-caused chemical modification and seafloor aging, even with subsequent subduction modification, for any of the Site 1256 igneous basement units separately or as an entity and independent of the permitted time frame.

6 Conclusions

The present study is the first comprehensive geochemical characterization of the entire upper igneous oceanic basement penetrated at superfast-spreading Site 1256 in terms of most relevant radiogenic isotope systems.

The recovered basaltic rocks from Site 1256 show trace element and isotopic compositions similar to EPR N-MORB, however, being slightly influenced by the nearby Galápagos hotspot (Geldmacher et al., 2013; Park et al., 2008). In general, the Sm-Nd, Lu-Hf, U-Pb, and Th-Pb isotope systems in the Site 1256 rocks do not appear to be significantly affected by low- to high-temperature hydrothermal alteration, showing no systematic downhole variations. However, compared to fresh lava glasses from this site, U in whole rock samples is enriched in some low-temperature altered lavas in the volcanic zone (VZ) and high-temperature altered rocks in the transition zone (TZ). This suggests that U was extracted both directly from cooler seawater in the VZ and further downhole from a hybrid fluid, reflecting mixing of upwelling hot fluids and descending colder seawater in the TZ (Alt et al., 2010). In the same interval, Pb displays a high degree of hydrothermal mobilization by a maximum

~50-fold increase in concentration (relative to the fresh Site 1256 N-MORB-like lava glasses), reflecting significant crustal uptake from seawater into secondary carbonates and sulfides. The significant seawater imprint on the transition zone rocks is also recorded by their comparatively high Sr isotope ratios. These high ratios, however, are not caused by radiogenic ingrowth (since the transition zone rocks possess the lowest Rb/Sr ratios), but most likely result from direct replacement of igneous by seawater-derived Sr. In contrast, the Sr-isotopic overprint is minor or even virtually absent in the highly to completely altered gabbros at the base of the core indicating significantly lesser influence of seawater-derived fluids. This supports recent fluid inclusion and thermometric data, demonstrating lesser impact of seawater and thus favoring the role of hydrothermal magmatic and/or evolved fluids during high-temperature alteration of the plutonic rocks at Site 1256 (Alt et al., 2010).

Compared to Site 1256, alteration-related modification of the elemental and crustal composition is more pronounced at nearby Site 504, particularly in the TZ and across the VZ. We suggest that these differences may reflect the significantly slower spreading rate at the Galápagos Spreading Center, where the Site 504 oceanic crust was formed, relative to superfast spreading Site 1256. It has previously been demonstrated that the activity of hydrothermal systems is rather persistent at slow- and intermediate-spreading centers. This has been attributed to the lower supply rate of magma, which favors the tectonically controlled upwelling of hydrothermal fluids giving rise to less frequent disruption of fluid conduits by magmatic pulses (e.g., Hannington et al., 2005). Therefore, superfast spreading at Site 1256 simply did not allow for sustained alteration that could generate a thick mineralization zone as observed at Site 504. Consequently, the spreading rate represents a key proxy for exploration of ancient and, possibly, modern in situ volcanic-hosted massive sulfide deposits (and related stockwork sulfide mineralization), whose formation is closely linked to hydrothermal convection at submarine spreading systems. By adding a third (downhole) dimension, the present study thus corroborates previous two-dimensional models (based on surface scanning of present-day seafloor) that suggest a negative correlation of spreading rate and metal sulfide accumulation (Hannington et al., 2011).

Finally, the alteration-related modification of superfast spreading crust, as demonstrated at Site 1256, also appears to be insufficient to create high enough U/Pb and low enough Rb/Sr ratios to develop time-integrated isotopic compositions required for the proposed HIMU-type mantle endmember. Additional mobilization and loss of Pb, occurring during subduction of the oceanic crust, may be required to transform oceanic lithosphere into the HIMU mantle reservoir.

Acknowledgments

We are grateful to S. Hauff and U. Westernströer for valuable analytical support. This research used samples provided by the Integrated Ocean Drilling Program (IODP). The present study and T.W.H. were funded by the Deutsche Forschungsgemeinschaft (DFG) IODP/ODP priority program grants HO1833/16-1 and 18-1.

References

Alt, J.C., Honnorez, J., Laverne, C., Emmerman, R., 1986. Hydrothermal alteration of a 1 km section through the upper oceanic crust, Deep Sea Drilling Project Hole 504B: Mineralogy, chemistry and evolution of seawater-basalt interactions. Journal of Geophysical Research 91 (B10), 10309. 10.1029/JB091iB10p10309.

Alt, J.C., Kinoshita, H., Stokking, L.B., et al., 1993. Proceedings of the Ocean Drilling Program, Initial Reports, Volume 148. Ocean Drilling Program, College Station, TX.

Alt, J.C., Laverne, C., Coggon, R.M., Teagle, D.A.H., Banerjee, N., Morgan, S., Smith-Duque, C.E., Harris, M., Galli, L., 2010. Subsurface structure of a submarine hydrothermal system in ocean crust formed at the East Pacific Rise, ODP/IODP Site 1256. Geochemistry, Geophysics, Geosystems 11 (10). 10.1029/2010GC003144.

Alt, J.C., Laverne, C., Vanko, D., Tartarotti, P., Teagle, D.A.H., Bach, W., Zuleger, E., Erzinger, J., Honnorez, J., Pezard, P., Becker, K., Salisbury, M., Wilkens, R., 1996. Hydrothermal Alteration of a Section of Upper Oceanic Crust in the Eastern Equatorial Pacific: A Synthesis of Results from Site 504 (DSDP Legs 69, 70, and 83, and ODP Legs 111, 137, 140, and 148), in: Alt, J.C., Kinoshita, H., Stokking, L.B., Michael, P.J. (Eds.), Proceedings of the Ocean Drilling Program, Scientific Results, Volume 148. Ocean Drilling Program, College Station, TX, pp. 417–434.

Bach, W., Jöns, N., Klein, F., 2013. Metasomatism Within the Ocean Crust, in: Harlov, D.E., Austrheim, H. (Eds.), Metasomatism and the Chemical Transformation of Rock. Springer Berlin Heidelberg, Berlin, New York, pp. 253–288.

Bach, W., Peucker-Ehrenbrink, B., Hart, S.R., Blusztajn, J.S., 2003. Geochemistry of hydrothermally altered oceanic crust: DSDP/ODP Hole 504B - Implications for seawater-crust exchange budgets and Sr- and Pb-isotopic evolution of the mantle. Geochemistry, Geophysics, Geosystems 4 (3). 10.1029/2002GC000419.

Blichert-Toft, J., Albarède, F., 1997. The Lu-Hf isotope geochemistry of chondrites and the evolution of the mantle-crust system. Earth and Planetary Science Letters 148 (1-2), 243–258. 10.1016/S0012-821X(97)00040-X.

Broecker, W., Peng, T.H., Beng, Z., 1982. Tracers in the Sea. Lamont-Doherty Geological Observatory, Columbia University, Palisades, NY.

Chauvel, C., 1995. Hydration and dehydration of oceanic crust controls Pb evolution in the mantle. Chemical Geology 126 (1), 65–75. 10.1016/0009-2541(95)00103-3.

Chen, T.-Y., Rempfer, J., Frank, M., Stumpf, R., Molina-Kescher, M., 2013. Upper ocean vertical supply: A neglected primary factor controlling the distribution of neodymium concentrations of open ocean surface waters? Journal of Geophysical Research: Oceans 118 (8), 3887–3894. 10.1002/jgrc.20288.

Chester, R., 1990. Trace elements in the oceans, in: Chester, R. (Ed.), Marine Geochemistry. Springer Netherlands, Dordrecht, pp. 346–421.

DeMets, C., Gordon, R., Argus, D., Stein, S., 1990. Current plate motions. Geophysical Journal International 101 (2), 425–478. 10.1111/j.1365-246X.1990.tb06579.x.

Duff, M.C., Coughlin, J.U., Hunter, D.B., 2002. Uranium co-precipitation with iron oxide minerals. Geochimica et Cosmochimica Acta 66 (20), 3533–3547. 10.1016/S0016-7037(02)00953-5.

Farrell, J.W., Clemens, S., Gromet, P., 1995. Improved chronostratigraphic reference curve of late Neogene seawater 87Sr/86Sr. Geology 23 (5), 403–406.

Faure, G., Mensing, T.M., 2005. Isotopes: principles and applications. John Wiley & Sons, Inc., Hoboken, New Jersey.

Frank, M., 2002. Radiogenic isotopes: Tracers of past ocean circulation and erosional input. Reviews of Geophysics 40 (1). 10.1029/2000RG000094.

Garbe-Schönberg, D., 1993. Simultaneous determination of thirty-seven trace elements in twenty-eight international rock standards by ICP-MS. Geostandards Newsletter 17 (1), 81–97. 10.1111/j.1751-908X.1993.tb00122.x.

Geldmacher, J., Hoernle, K., Klügel, A., van den Bogaard, P., Wombacher, F., Berning, B., 2006. Origin and geochemical evolution of the Madeira-Tore Rise (eastern North Atlantic). Journal of Geophysical Research 111 (B9). 10.1029/2005JB003931.

Geldmacher, J., Höfig, T.W., Hauff, F., Hoernle, K., Garbe-Schönberg, D., Wilson, D.S., 2013. Influence of the Galápagos hotspot on the East Pacific Rise during Miocene superfast spreading. Geology 41 (2), 183–186. 10.1130/G33533.1.

Goss, A., Perfit, M., Ridley, W., Rubin, K., Kamenov, G., Soule, S.A., Fundis, A., Fornari, D., 2010. Geochemistry of lavas from the 2005-2006 eruption at the East Pacific Rise, 9°46′N-9°56′N: Implications for ridge crest plumbing and decadal changes in magma chamber compositions. Geochemistry, Geophysics, Geosystems 11 (5). 10.1029/2009GC002977.

Hannington, M.D., Jamieson, J., Monecke, T., Petersen, S., Beaulieu, S., 2011. The abundance of seafloor massive sulfide deposits. Geology 39 (12), 1155–1158. 10.1130/G32468.1.

Hannington, M.D., Ronde, C. de, Petersen, S., 2005. Sea-floor tectonics and submarine hydorthermal systems, in: Hedenquist, J., Thompson, J., Goldfarb, R., Richards, J. (Eds.), Economic Geology. One hundredth anniversary volume: 1905-2005. Society of Economic Geologists, Inc., Littleton, CO, pp. 111–141.

Hart, S.R., Staudigel, H., 1982. The control of alkalies and uranium in seawater by ocean crust alteration. Earth and Planetary Science Letters 58 (2), 202–212. 10.1016/0012-821X(82)90194-7.

Hart, S.R., 1988. Heterogeneous mantle domains: signatures, genesis and mixing chronologies. Earth and Planetary Science Letters 90 (3), 273–296. 10.1016/0012-821X(88)90131-8.

Hawley, J.E., Nichol, I., 1961. Trace elements in pyrite, pyrrhotite and chalcopyrite of different ores. Economic Geology 56 (3), 467–487. 10.2113/gsecongeo.56.3.467.

Hodell, D.A., Woodruff, F., 1994. Variations in the strontium isotopic ratio of seawater during the Miocene: Stratigraphic and geochemical implications. Paleoceanography 9 (3), 405–426. 10.1029/94PA00292.

Hoernle, K., 1998. Geochemistry of Jurassic Oceanic Crust beneath Gran Canaria (Canary Islands): Implications for Crustal Recycling and Assimilation. Journal of Petrology 39 (5), 859–880. 10.1093/petroj/39.5.859.

Hoernle, K., Abt, D.L., Fischer, K.M., Nichols, H., Hauff, F., Abers, G.A., van den Bogaard, P., Heydolph, K., Alvarado, G., Protti, M., Strauch, W., 2008. Arc-parallel flow in the mantle wedge beneath Costa Rica and Nicaragua. Nature 451 (7182), 1094–1097. 10.1038/nature06550.

Hoernle, K., Hauff, F., Kokfelt, T.F., Haase, K., Garbe-Schönberg, D., Werner, R., 2011. On- and off-axis chemical heterogeneities along the South Atlantic Mid-Ocean-Ridge (5–11°S): Shallow or deep recycling of ocean crust and/or intraplate volcanism? Earth and Planetary Science Letters 306 (1-2), 86–97. 10.1016/j.epsl.2011.03.032.

Hofmann, A.W., White, W.M., 1982. Mantle plumes from ancient oceanic crust. Earth and Planetary Science Letters 57 (2), 421–436. 10.1016/0012-821X(82)90161-3.

Hofmann, A.W., 1988. Chemical differentiation of the Earth: the relationship between mantle, continental crust, and oceanic crust. Earth and Planetary Science Letters 90 (3), 297–314. 10.1016/0012-821X(88)90132-X.

Honnorez, J., Alt, J.C., Honnorez-Guerstein, B.-M., Laverne, C., Muehlenbachs, K., Ruiz, J., Saltzman, E., 1985. Stockwork-Like Sulfide Mineralization in Young Oceanic Crust: Deep Sea Drilling Project Hole 504B, in: Anderson, R., Honnorez, J., Becker, K. (Eds.), Initial Reports of the Deep Sea Drilling Project, Volume 83. U.S. Government Printing Office.

Honnorez, J., Laverne, C., Hubberten, H.-W., Emmerman, R., Muehlenbachs, K., 1983. Alteration Processes in Layer 2 Basalts from Deep Sea Drilling Project Hole 504B, Costa Rica Rift, in: Cann, J., Langseth, M., Honnorez, J., Herzen, R.P. von, White, S. (Eds.), Initial Reports of the Deep Sea Drilling Project, Volume 69. U.S. Government Printing Office, Washington, DC, pp. 509–546.

Houtermans, F., 1953. Determination of the age of the earth from the isotopic composition of meteoritic lead. Il Nuovo Cimento 10 (12), 1623–1633. 10.1007/BF02781658.

Ildefonse, B., Abe, N., Blackman, D.K., Canales, J., Isozaki, Y., Kodaira, S., Myers, G., Nakamura, K., Nedimovic, M., Skinner, A.C., Seama, N., Takazawa, E., Teagle, D.A.H., Tominaga, M., Umino, S., Wilson, D.S., Yamao, M., 2010. The MoHole: A Crustal Journey and Mantle Quest, Workshop in Kanazawa, Japan, 3—5 June 2010. Scientific drilling (10), 56–63. 10.2204/iodp.sd.10.07.2010.

Ito, E., White, W.M., Göpel, C., 1987. The O, Sr, Nd and Pb isotope geochemistry of MORB. Chemical Geology 62 (3-4), 157–176. 10.1016/0009-2541(87)90083-0.

Jochum, K.P., Nohl, U., Herwig, K., Lammel, E., Stoll, B., Hofmann, A.W., 2005. GeoReM: A New Geochemical Database for Reference Materials and Isotopic Standards. Geostandards and Geoanalytical Research 29 (3), 333–338. 10.1111/j.1751-908X.2005.tb00904.x.

John, T., Klemd, R., Gao, J., Garbe-Schönberg, C.-D., 2008. Trace-element mobilization in slabs due to non steady-state fluid–rock interaction: Constraints from an eclogite-facies

transport vein in blueschist (Tianshan, China). Lithos 103 (1-2), 1–24. 10.1016/j.lithos.2007.09.005.

Kawabata, H., Hanyu, T., Chang, Q., Kimura, J.-I., Nichols, A., Tatsumi, Y., 2011. The Petrology and Geochemistry of St. Helena Alkali Basalts: Evaluation of the Oceanic Crust-recycling Model for HIMU OIB. Journal of Petrology 52 (4), 791–838. 10.1093/petrology/egr003.

Kelley, K.A., Plank, T., Farr, L., Ludden, J., Staudigel, H., 2005. Subduction cycling of U, Th, and Pb. Earth and Planetary Science Letters 234 (3-4), 369–383. 10.1016/j.epsl.2005.03.005.

Kirchner, T.M., Gillis, K.M., 2012. Mineralogical and strontium isotopic record of hydrothermal processes in the lower ocean crust at and near the East Pacific Rise. Contributions to Mineralogy and Petrology 164 (1), 123–141. 10.1007/s00410-012-0729-5.

Koepke, J., Christie, D., Dziony, W., Holtz, F., Lattard, D., Maclennan, J., Park, S., Scheibner, B., Yamasaki, T., Yamazaki, S., 2008. Petrography of the dike-gabbro transition at IODP Site 1256 (equatorial Pacific): The evolution of the granoblastic dikes. Geochemistry, Geophysics, Geosystems 9 (7). 10.1029/2008GC001939.

Kogiso, T., Tatsumi, Y., Nakano, S., 1997. Trace element transport during dehydration processes in the subducted oceanic crust: 1. Experiments and implications for the origin of ocean island basalts. Earth and Planetary Science Letters 148 (1-2), 193–205. 10.1016/S0012-821X(97)00018-6.

Krolikowska-Ciaglo, S., Deyhle, A., Hauff, F., Hoernle, K., 2007. Boron isotope geochemistry and U–Pb systematics of altered MORB from the Australian Antarctic Discordance (ODP Leg 187). Chemical Geology 242 (3-4), 455–469. 10.1016/j.chemgeo.2007.05.004.

Kusakabe, M., Shibata, T., Yamamoto, M., Mayeda, S., Kagami, H., Honma, H., Masuda, H., Sakai, H., 1989. Petrology and isotope characteristics (H, O, S, Sr and Nd) of basalts from ocean drilling program Hole 504B, Leg 111, Costa Rica Rift, in: Becker, K., Sakai, H. (Eds.), Proceedings of the Ocean Drilling Program, 111 Scientific Reports, vol. 111. Ocean Drilling Program, College Station, TX, pp. 47–60.

Langmuir, D., 1978. Uranium solution-mineral equilibria at low temperatures with applications to sedimentary ore deposits. Geochimica et Cosmochimica Acta 42 (6), 547–569. 10.1016/0016-7037(78)90001-7.

Langmuir, D., Herman, J.S., 1980. The mobility of thorium in natural waters at low temperatures. Geochimica et Cosmochimica Acta 44 (11), 1753–1766. 10.1016/0016-7037(80)90226-4.

Ling, H.F., Burton, K.W., O'Nions, R.K., Kamber, B., Blanckenburg, F. von, Gibb, A., Hein, J.R., 1997. Evolution of Nd and Pb isotopes in Central Pacific seawater from ferromanganese crusts. Earth and Planetary Science Letters 146 (1-2), 1–12. 10.1016/S0012-821X(96)00224-5.

McCulloch, M., Gregory, R., Wasserburg, G.J., Taylor, Jr., H.P., 1980. A neodymium, strontium, and oxygen isotopic study of the Cretaceous Samail ophiolite and implications for the petrogenesis and seawater-hydrothermal alteration of oceanic crust. Earth and Planetary Science Letters 46 (2), 201–211. 10.1016/0012-821X(80)90006-0.

Michard, A., Albarède, F., Michard, G., Minster, J.F., Charlou, J., 1983. Rare-earth elements and uranium in high-temperature solutions from East Pacific Rise hydrothermal vent field (13 °N). Nature 303 (5920), 795–797. 10.1038/303795a0.

Mühe, R., Peucker-Ehrenbrink, B., Devey, C., Garbe-Schönberg, D., 1997. On the redistribution of Pb in the oceanic crust during hydrothermal alteration. Chemical Geology 137 (1-2), 67–77. 10.1016/S0009-2541(96)00151-9.

Neo, N., Yamazaki, S., Miyashita, S., 2009. Data report: bulk rock compositions of samples from the IODP Expedition 309/312 sample pool, ODP Hole 1256D, in: Teagle, D., Alt, J., Umino, S., Miyashita, S., Banerjee, N., Wilson, D. (Eds.), Proceedings of the IODP, 309/312, 309/312. Integrated Ocean Drilling Program.

Park, S., Maclennan, J., Teagle, D.A.H., Hauff, F., 2008. Did the Galápagos plume influence the ancient EPR? : A geochemical study of basaltic rocks from Hole 1256D. Eos Transactions AGU, Fall Meeting Supplement 89 (53), Abstract V51F-2097.

Pearce, J.A., Peate, D.W., 1995. Tectonic implications of the composition of volcanic arc magmas. Annual Review of Earth and Planetary Sciences 23 (1), 251–285. 10.1146/annurev.ea.23.050195.001343.

Pedersen, R.B., Furnes, H., 2001. Nd- and Pb-isotopic variations through the upper oceanic crust in DSDP/ODP Hole 504B, Costa Rica Rift. Earth and Planetary Science Letters 189 (3-4), 221–235. 10.1016/S0012-821X(01)00349-1.

Perfit, M., Fornari, D., Malahoff, A., Embley, R.W., 1983. Geochemical studies of abyssal lavas recovered by DSRV Alvin from Eastern Galapagos Rift, Inca Transform, and Ecuador Rift: 3. Trace element abundances and petrogenesis. Journal of Geophysical Research 88 (B12), 10551. 10.1029/JB088iB12p10551.

Saal, A., Kurz, M., Hart, S.R., Blusztajn, J.S., Blichert-Toft, J., Liang, Y., Geist, D., 2007. The role of lithospheric gabbros on the composition of Galapagos lavas. Earth and Planetary Science Letters 257 (3-4), 391–406. 10.1016/j.epsl.2007.02.040.

Sadofsky, S., Hoernle, K., Duggen, S., Hauff, F., Werner, R., Garbe-Schönberg, D., 2009. Geochemical variations in the Cocos Plate subducting beneath Central America: implications for the composition of arc volcanism and the extent of the Galápagos Hotspot influence on the Cocos oceanic crust. International Journal of Earth Sciences 98 (4), 901–913. 10.1007/s00531-007-0289-5.

Schilling, J.-G., Fontignie, D., Blichert-Toft, J., Kingsley, R., Tomza, U., 2003. Pb-Hf-Nd-Sr isotope variations along the Galápagos Spreading Center (101°-83°W): Constraints on the dispersal of the Galápagos mantle plume. Geochemistry, Geophysics, Geosystems 4 (10). 10.1029/2002GC000495.

Scott, T., Riba Tort, O., Allen, G., 2007. Aqueous uptake of uranium onto pyrite surfaces; reactivity of fresh versus weathered material. Geochimica et Cosmochimica Acta 71 (21), 5044–5053. 10.1016/j.gca.2007.08.017.

Shimizu, H., Mori, K., Masuda, A., 1989. REE, Ba, and Sr Abundances and Sr, Nd, and Ce Isotopic Ratios in Hole 504B Basalts, ODP Leg 111, Costa Rica Rift, in: Becker, K., Sakai, H. (Eds.), Proceedings of the Ocean Drilling Program, 111 Scientific Reports, vol. 111. Ocean Drilling Program, College Station, TX, pp. 77–83.

Shock, E.L., Sassani, D.C., Betz, H., 1997. Uranium in geologic fluids: Estimates of standard partial molal properties, oxidation potentials, and hydrolysis constants at high temperatures and pressures. Geochimica et Cosmochimica Acta 61 (20), 4245–4266. 10.1016/S0016-7037(97)00240-8.

Sims, K.W., Blichert-Toft, J., Fornari, D., Perfit, M., Goldstein, S., Johnson, P., DePaolo, D., Hart, S.R., Murrell, M., Michael, P.J., Layne, G., Ball, L., 2003. Aberrant youth: Chemical and isotopic constraints on the origin of off-axis lavas from the East Pacific Rise, 9°-10°N. Geochemistry, Geophysics, Geosystems 4 (10). 10.1029/2002GC000443.

Sims, K.W., Goldstein, S., Blichert-Toft, J., Perfit, M., Kelemen, P., Fornari, D., Michael, P.J., Murrell, M., Hart, S.R., DePaolo, D., Layne, G., Ball, L., Jull, M., Bender, J., 2002. Chemical and isotopic constraints on the generation and transport of magma beneath the East Pacific Rise. Geochimica et Cosmochimica Acta 66 (19), 3481–3504. 10.1016/S0016-7037(02)00909-2.

Smith, W., 1997. Global Sea Floor Topography from Satellite Altimetry and Ship Depth Soundings. Science 277 (5334), 1956–1962. 10.1126/science.277.5334.1956.

Stracke, A., Bizimis, M., Salters, V., 2003. Recycling oceanic crust: Quantitative constraints. Geochemistry, Geophysics, Geosystems 4 (3). 10.1029/2001GC000223.

Stracke, A., Hofmann, A.W., Hart, S.R., 2005. FOZO, HIMU, and the rest of the mantle zoo. Geochemistry, Geophysics, Geosystems 6 (5). 10.1029/2004GC000824.

Sun, S.-s., McDonough, W.F., 1989. Chemical and isotopic systematics of oceanic basalts: implications for mantle composition and processes. Geological Society, London, Special Publications 42 (1), 313–345. 10.1144/GSL.SP.1989.042.01.19.

Teagle, D.A.H., Alt, J.C., Umino, S., Miyashita, S., Banerjee, N., Wilson, D.S., et al., 2006. Expedition 309/312 summary, in: Teagle, D.A.H., Alt, J.C., Umino, S., Miyashita, S., Banerjee, N., Wilson, D.S. (Eds.), Proceedings of the IODP, Volume 309/312. Integrated Ocean Drilling Program, Washington, DC, pp. 1–127.

Teagle, D.A.H., Ildefonse, B., Blum, P., 2012. IODP Expedition 335: Deep Sampling in ODP Hole 1256D. Scientific drilling 13, 28–34.

Teagle, D.A.H., Wilson, D.S., 2007. Leg 206 synthesis: initiation of drilling an intact section of upper oceanic crust formed at a superfast spreading rate at Site 1256 in the eastern equatorial Pacific, in: Teagle, D.A.H., Wilson, D.S., Acton, G., Vanko, D. (Eds.), Proceedings of the Ocean Drilling Program, Scientific Results, Volume 206. Ocean Drilling Program, College Station, TX, pp. 1–15.

Tominaga, M., Teagle, D.A.H., Alt, J.C., Umino, S., 2009. Determination of the volcanostratigraphy of oceanic crust formed at superfast spreading ridge: Electrofacies analyses of ODP/IODP Hole 1256D. Geochemistry, Geophysics, Geosystems 10 (1). 10.1029/2008GC002143.

Valsami-Jones, E., Ragnarsdóttir, K.V., 1997. Controls on uranium and thorium behaviour in ocean-floor hydrothermal systems: examples from the Pindos ophiolite, Greece. Chemical Geology 135 (3-4), 263–274. 10.1016/S0009-2541(96)00121-0.

Waters, C., Sims, K.W., Perfit, M., Blichert-Toft, J., Blusztajn, J.S., 2011. Perspective on the Genesis of E-MORB from Chemical and Isotopic Heterogeneity at 9-10 N East Pacific Rise. Journal of Petrology 52 (3), 565–602. 10.1093/petrology/egq091.

Weaver, B.L., 1991. The origin of ocean island basalt end-member compositions: trace element and isotopic constraints. Earth and Planetary Science Letters 104 (2-4), 381–397. 10.1016/0012-821X(91)90217-6.

Werner, R., Hoernle, K., Barckhausen, U., Hauff, F., 2003. Geodynamic evolution of the Galápagos hot spot system (Central East Pacific) over the past 20 m.y.: Constraints from morphology, geochemistry, and magnetic anomalies. Geochemistry, Geophysics, Geosystems 4 (12). 10.1029/2003GC000576.

Wersin, P., Hochella, M.F., Persson, P., Redden, G., Leckie, J.O., Harris, D.W., 1994. Interaction between aqueous uranium (VI) and sulfide minerals: Spectroscopic evidence for sorption and reduction. Geochimica et Cosmochimica Acta 58 (13), 2829–2843. 10.1016/0016-7037(94)90117-1.

White, W.M., McBirney, A.R., Duncan, R.A., 1993. Petrology and geochemistry of the Galápagos Islands: Portrait of a pathological mantle plume. Journal of Geophysical Research 98 (B11), 19533. 10.1029/93JB02018.

Wilson, D.S., 1996. Fastest known spreading on the Miocene Cocos-Pacific Plate Boundary. Geophysical Research Letters 23 (21), 3003–3006. 10.1029/96GL02893.

Wilson, D.S., Teagle, D.A.H., Acton, G., 2003. Proceedings of the Ocean Drilling Program, Initial Reports, Volume 206. Ocean Drilling Program, College Station, TX.

Zeng, Z., Chen, D., Yin, X., Wang, X., Zhang, G., Wang, X., 2010. Elemental and isotopic compositions of the hydrothermal sulfide on the East Pacific Rise near 13°N. Science China Earth Sciences 53 (2), 253–266. 10.1007/s11430-010-0013-3.

Zindler, A., Hart, S.R., 1986. Chemical Geodynamics. Annual Review of Earth and Planetary Sciences 14 (1), 493–571. 10.1146/annurev.ea.14.050186.002425.

Figure captions

Figure 1. Tectonic map of the eastern equatorial Pacific Ocean showing the locations of ODP/IODP Site 1256 (Hole 1256C/D) and DSDP/ODP Site 504 (Hole 504B). The crustal ages of Cocos and northern Nazca Plates as well as reconstructed tectonic tracks of displayed ocean drilling sites have been calculated with the software GPlates (http://www.gplates.org). Small black dots along the tracks mark 1 Ma and small black ticks label 5 Ma increments. Isochrons of seafloor magnetic lineations are shown in 5 Ma increments. Labeled gray-shaded areas on either side of the Galápagos Spreading Center (GSC; also known as Cocos-Nazca Spreading Center) refer to distinct features of the Galápagos hotspot track (e.g., GI = Galápagos Islands). Dashed black lines mark the boundary between crust formed at the GSC and the East Pacific Rise (EPR) (based on Smith and Sandwell, 1997).

Figure 2. Simplified stratigraphic columns of Sites 1256 (Hole 1256C/D) and 504 (Hole 504B) drilled upper oceanic crust segments, showing both lithologic and alteration zones (mbsf = meters below seafloor). Lithostratigraphy: Site 1256 – Teagle et al. (2006), Tominaga et al. (2009), Wilson et al. (2003); Site 504 – Bach et al. (2003). TZ = lithological (dike-lava) transition zone. PS = plutonic section. Alteration zones: Site 1256 – Alt et al. (2010), Teagle et al. (2006); Site 504 – Alt et al. (1986, 1996). ATZ = alteration transition zone. afc = amphibolite-facies conditions, gfc = greenschist-facies conditions. MZ = mineralization zone. Granoblastic d. = dikes.

Figure 3. Multielement plots depicting trace element patterns normalized to normal mid-ocean-ridge basalt (N-MORB) values of Sun and McDonough (1989) for both Site 1256 and 504 igneous basements. (a) lavas (volcanic zone), (b) (dike-lava) transition zone, including orange-rimmed sulfide-mineralized breccia sample 309-1256D-122R-1, 67–79 cm (~1028 mbsf), (c) sheeted dike complex, including orange-rimmed enriched MORB (E-MORB)-like dike sample 312-1256D-189R-1, 71–89 cm (~1335 mbsf), (d) plutonic section, including blue-rimmed dike screen sample 312-1256D-227R-1, 113–126 cm (~1470 mbsf). Whole rock and glass data from the Site 1256 volcanic zone, derived from previous studies (Geldmacher et al., 2013; Sadofsky et al., 2009), are shown for comparison in Fig. 3a. The yellow patterns in Figs. 3a-c represent the average composition of Site 1256 N-MORB lava glasses and an E-MORB-type off-axis glass sample (206-1256C-14R-1, 139–142 cm, ~361 mbsf), respectively (data from Geldmacher et al., 2013). Extremely rarely occurring off-axis E-MORB-like lavas from the upper ~150 m of the Site 1256 basement have not been accounted for the mean value calculation of Site 1256 lavas shown in Fig. 3a. Site 504 data source: Bach et al. (2003). Average present-day East Pacific Rise (EPR) N-MORB (9–10°N) pattern derived from compilation of different data sources: Goss et al. (2010), Sims et al. (2002, 2003). Average modern EPR E-MORB (9–10°N) pattern derived from Waters et al. (2011).

Figure 4. Downhole variation of trace elements of Sites 1256 (left panels) and 504 (right panels) from the lavas of the volcanic zone across the dike-lava transition zone (TZ) through the sheeted dike complex (SDC) to the plutonic section (PS) (mbsf = meters below seafloor), including lava whole rock data from Sadofsky et al. (2009) and lava glass data from Geldmacher et al. (2013) for Site 1256. Site 504 igneous basement trace element data (reflecting ICP-MS results, except for Th und U determined by means of isotope dilution) from Bach et al. (2003) and Pedersen and Furnes (2001). (a) La, (b) Nd, (c) Th, (d) U, (e) Pb, (f) Rb, (g) Sr, (h) Cu, (i) Zn. E- and N-MORB values are taken from Sun and McDonough (1989), except for N-MORB Cu value taken from Hofmann (1988). Insets of different scale are used to show extreme compositions. Borehole stratigraphic divisions are the same as in Fig. 2. Note that the horizontal, light orange lines refer to the corresponding highly sulfide-mineralized layers within the TZ at both sites (1256: 2.8 m thick volcanic breccia, 504: 18 m thick stockwork zone) and light orange-rimmed symbols mark samples taken from these intervals.

Figure 5. $^{87}Sr/^{86}Sr$ (a) and $^{143}Nd/^{144}Nd$ (b) isotope ratios, respectively, versus depth comparing Sites 1256 (left panels) and 504 (right panels) across all drilled upper oceanic crust sections (mbsf = meters below seafloor). TZ = (dike-lava) transition zone. Rimless green circles within the volcanic zone (lavas) represent whole rock samples (Geldmacher et al., 2013; Sadofsky et al., 2009). Gray vertical boxes in each diagram identify the corresponding ±2σ range of the average Sr-Nd isotopic compositions of fresh lava glasses obtained from Site 1256 and the Galápagos Spreading Center (GSC) mid-ocean-ridge basalt (MORB), representing a present-day ridge segment proximal to Site 504, respectively. Data sources: Site 504 (Bach et al., 2003; Kusakabe et al., 1989; Pedersen and Furnes, 2001; Shimizu et al., 1989), fresh Site 1256 MORB glasses (Geldmacher et al., 2013), fresh GSC MORB glasses (0.5–2.0° N, 85–86° W) (Ito et al., 1987; Perfit et al., 1983; Schilling et al., 2003). Sr isotopic compositions of present-day seawater (Broecker et al., 1982), 14.6 Ma seawater (Hodell and Woodruff, 1994), and 6.0 Ma seawater (Farrell et al., 1995) are displayed as dashed vertical lines with the latter ones reflecting seawater composition shortly after igneous basement formation at the respective sites. Errors are within symbol size for Site 1256 Sr-Nd isotope data. Borehole stratigraphic divisions are the same as in Fig. 2. See the Fig. 4 caption for explanation of the horizontal orange lines and light orange-rimmed symbols.

Figure 6. $^{176}Hf/^{177}Hf$ isotope ratio versus depth (mbsf = meters below seafloor) for fresh lava glasses (diamond symbols) and basaltic whole rock samples (circles) at Site 1256. TZ = (dike-lava) transition zone. The gray vertical box refers to the ±2σ range of the average Hf isotopic composition of pristine Site 1256 lava glasses. Errors are within symbol size. Borehole stratigraphic divisions as in Fig. 2. See the Fig. 4 caption for explanation of the horizontal orange line.

Figure 7. $^{206}Pb/^{204}Pb$ (a), $^{207}Pb/^{204}Pb$ (b), and $^{208}Pb/^{204}Pb$ (c) isotope ratios versus depth (mbsf = meters below seafloor) of Sites 1256 (top) and 504 (bottom) igneous basements, respectively. TZ = (dike-lava) transition zone. Rimless circles within the Site 1256 volcanic zone (lavas) represent whole rock Pb isotopic compositions from Sadofsky et al. (2009) (conventional, gray) and Geldmacher et al. (2013) (double spike, green). Errors are within symbol size for Site 1256 $^{206}Pb/^{204}Pb$ and $^{208}Pb/^{204}Pb$, whereas the $^{207}Pb/^{204}Pb$ error bar marks the 2σ external reproducibility. The gray vertical boxes define the ±2σ range of average fresh Site 1256 lava glass Pb isotopic composition obtained from Geldmacher et al. (2013). Site 504 data source: Pedersen and Furnes (2001). Borehole stratigraphic divisions as in Fig. 2. See the Fig 4 caption for explanation of the horizontal orange lines and light orange-rimmed symbols.

Figure 8. Trace element ratios versus depth (mbsf = meters below seafloor) for Site 1256 basaltic rocks from the lavas across the dike-lava transition zone (TZ) through the sheeted dike complex down to the plutonic section (PS) (left panels). Site 504 variation of igneous basement trace element ratios is shown for comparison (right panels). (a) La/Sm, (b) Sm/Nd, (c) Th/U, (d) Th/Pb, (e) U/Pb, (f) Rb/Sr, (g) Zn/Cu. Site 1256 lava whole rock data from Sadofsky et al. (2009) and lava glass data from Geldmacher et al. (2013) are displayed as well. Site 504 data sources: Bach et al. (2003), Pedersen and Furnes (2001). E- and N-MORB values are taken from Sun and McDonough (1989). Borehole stratigraphic divisions are the same as in Fig. 2. See the Fig. 4 caption for explanation of the horizontal orange lines and light orange-rimmed symbols.

Figure 9. Rb/Sr versus $^{87}Sr/^{86}Sr$ isotope ratios for both Site 1256 (circles and diamond symbols) and Site 504 (rimless squares). The light orange-rimmed circle represents the highly sulfide-mineralized breccia of the Site 1256 transition zone (TZ) sampled at ~1028 meters below seafloor. The horizontal dark gray arrow identifies a range of elevated Rb/Sr ratios corresponding to low radiogenic Sr isotopic compositions (Site 1256 lavas and gabbros). The sloped light gray arrow refers to those Site 504 lavas, which tend to show positive correlation of Rb/Sr and $^{87}Sr/^{86}Sr$. The vertical black arrow along the left border of the diagram marks increasing Sr isotopic compositions without any significant change of the Rb/Sr ratio (TZ and dike samples of both holes). Data sources: Site 1256 lava glasses (Geldmacher et al., 2013), Site 504 rocks (Bach et al., 2003).

Figure 10. $^{87}Sr/^{86}Sr$ versus $^{143}Nd/^{144}Nd$ [adapted from Faure and Mensing (2005) and McCulloch et al. (1980)] for Site 1256 basaltic rocks covering the complete upper oceanic crustal sequence drilled. The light orange-rimmed circle represents a sample taken from the highly sulfide-mineralized breccia intersected at ~1028 meters below seafloor, hosted by the Site 1256 dike-lava transition zone. Values for water-rock mixing ratios (W/R) at a given point in the Sr-Nd isotopic space can be calculated according to McCulloch et al. (1980) [$W/R = {}^{87}Sr/^{86}Sr_{MORB(initial)} - {}^{87}Sr/^{86}Sr_{MORB(final)} \diagup {}^{87}Sr/^{86}Sr_{MORB(final)} - {}^{87}Sr/^{86}Sr_{sw} \cdot (c_{Sr/MORB} \diagup$

$c_{Sr/sw}$)]. The following variables were integrated: fresh Site 1256 mid-ocean-ridge basalt (MORB) average ($^{143}Nd/^{144}Nd_{initial}$ = 0.513068, $c(Nd_{MORB})$ = 9.28 ppm, $^{87}Sr/^{86}Sr_{initial}$ = 0.702983, $c(Sr_{MORB})$ = 83.2 ppm); average (past eastern Pacific) seawater (sw) composition ($^{143}Nd/^{144}Nd_{sw}$ = 0.512435, $c(Nd_{sw}) = 4 \cdot 10^{-6}$ ppm, $^{87}Sr/^{86}Sr_{sw}$ = 0.708780, $c(Sr_{sw})$ = 7.6 ppm). Data sources: glass data from Geldmacher et al. (2013) included in the Site 1256 lava dataset (= average MORB data used for W/R calculation), East Pacific Rise (EPR) MORB (9–11° N) (Sims et al., 2002; Waters et al., 2011), Galápagos Islands (Saal et al., 2007; Werner et al., 2003; White et al., 1993), (past eastern Pacific) seawater composition [Frank, 2002 (average Sr and Nd concentrations in seawater); Hodell and Woodruff, 1994 (Sr isotopic composition); Ling et al., 1997 (regional Nd isotopic composition)]. Errors are within symbol size.

Figure 11. Modeled present-day uranogenic ($^{206}Pb/^{204}Pb$) and thorogenic ($^{208}Pb/^{204}Pb$) isotopic compositions of recycled igneous oceanic crust of Site 1256 basaltic rock composition as a function of the recycling age (0.5–3 Ga, with 0.5 Ga increments) and the age-dependent calculated initial isotopic composition of mid-ocean-ridge basalt (MORB). For example, the 3 Ga points show the modeled present-day isotopic compositions for a crustal segment that was modified (altered) 3 billion years ago. Modeling was implemented (a) irrespective of any possible isotopic modification of the recycled oceanic crust during subduction and (b) taking into account compositional modification during subduction processes ("subd") by applying element mobility coefficients from Kogiso et al. (1997) and Stracke et al. (2003) (see supplementary Tab. A.4). Modeled crustal sections depicted: lavas (volcanic zone; whole rocks), dike-lava transition zone (TZ), sheeted dike complex (SDC), gabbros (plutonic section) and a composite crust composed of 25 % altered MORB (whole rock data of lavas, transition zone, and sheeted dikes) and 75 % gabbros according the estimated proportions at Site 1256 (Ildefonse et al., 2010; Teagle et al., 2006). Shown MORB (data from Atlantic, Indian, and Pacific ocean ridges), non-HIMU (EMI- and EMII-type basalts: Pitcairn, Tristan da Cunha, Kerguelen Islands, Walvis ridge, Society, Samoa, and Marquesas Islands), and HIMU (St. Helena, Austral-Cook archipelago [Tubuai, Rurutu, Mangaia, Rurutu, Tubuai, and Rimatara Islands]) oceanic island basalt fields are derived from the data compilation of Stracke et al. (2003). Crustal input parameters are given in supplementary Table A.4. See Appendix I Section A.2 for the outline of the modeling approach. The detailed calculation procedure is given in Stracke et al. (2003).

Figure 1

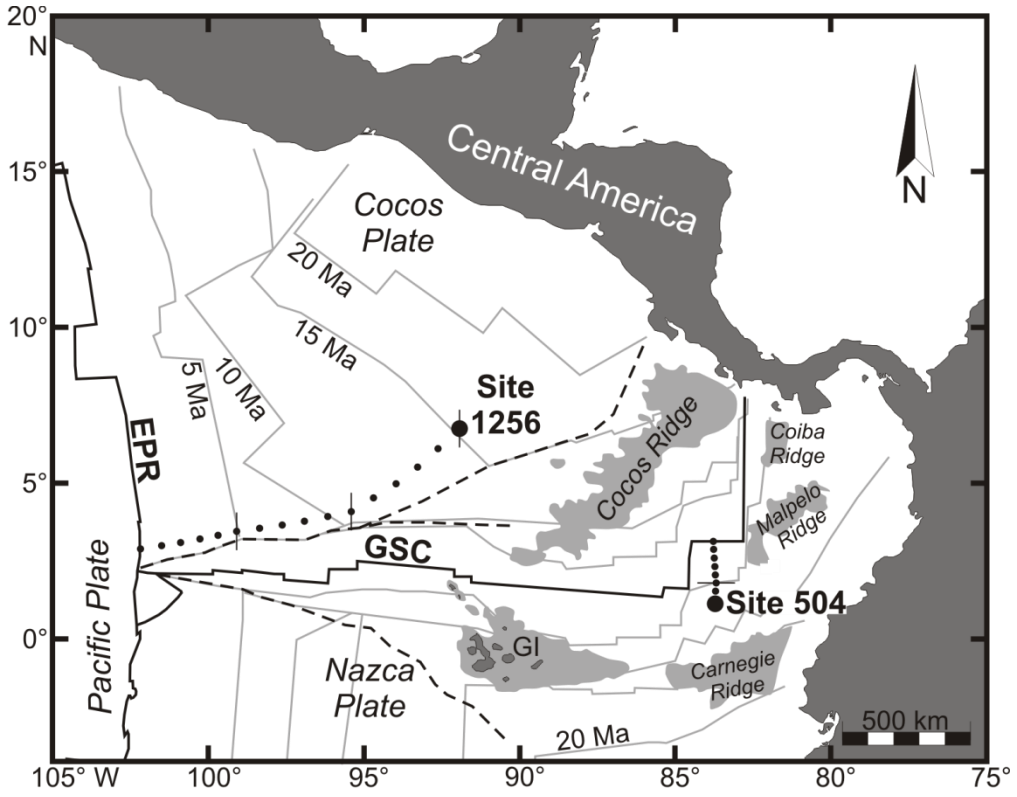
20° N
15°
10°
5°
0°
105° W
100°
95°
90°
85°
80°
75°
Central America
N
Cocos Plate
20 Ma
15 Ma
10 Ma
5 Ma
Site 1256
EPR
Pacific Plate
GSC
Cocos Ridge
Coiba Ridge
Malpelo Ridge
Site 504
GI
Nazca Plate
Carnegie Ridge
20 Ma
500 km

Figure 2

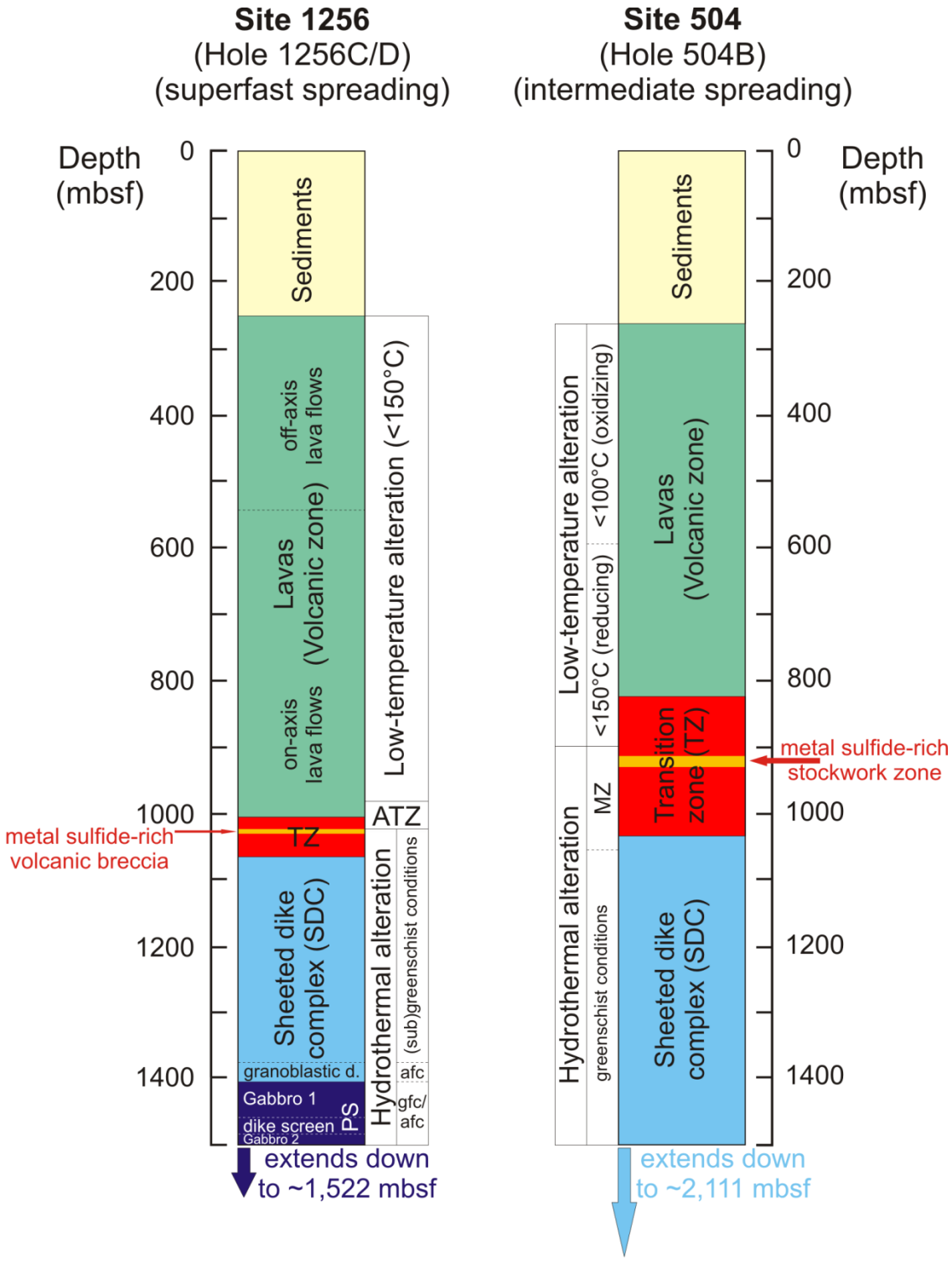
Site 1256
(Hole 1256C/D)
(superfast spreading)
Site 504
(Hole 504B)
(intermediate spreading)
Depth (mbsf)
0
200
400
600
800
1000
1200
1400
Sediments
off-axis lava flows
Lavas (Volcanic zone)
on-axis lava flows
Low-temperature alteration (<150°C)
ATZ
TZ
metal sulfide-rich volcanic breccia
Sheeted dike complex (SDC)
granoblastic d.
Gabbro 1
dike screen
PS
Gabbro 2
Hydrothermal alteration
(sub)greenschist conditions
afc
gfc/ afc
extends down to ~1,522 mbsf
Low-temperature alteration
<100°C (oxidizing)
<150°C (reducing)
Hydrothermal alteration
MZ
greenschist conditions
Transition zone (TZ)
metal sulfide-rich stockwork zone
extends down to ~2,111 mbsf

Figure 3

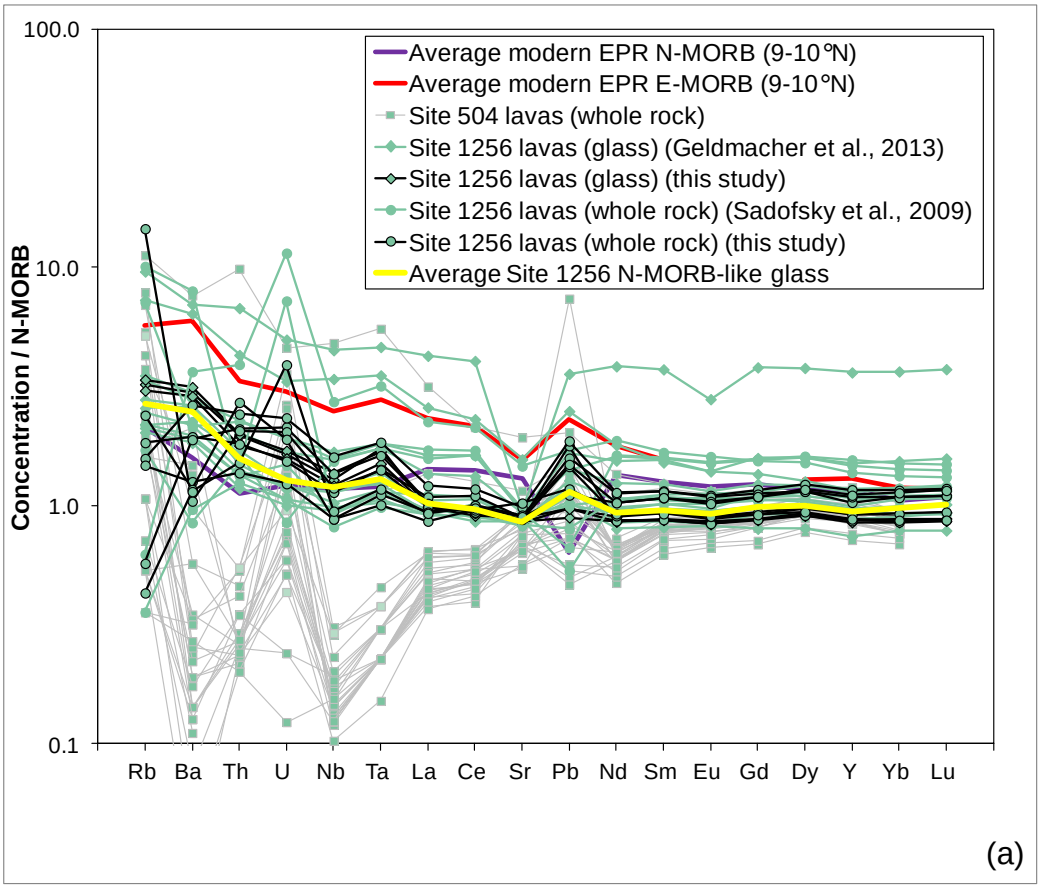
100.0
10.0
1.0
0.1
Concentration / N-MORB
Average modern EPR N-MORB (9-10°N)
Average modern EPR E-MORB (9-10°N)
Site 504 lavas (whole rock)
Site 1256 lavas (glass) (Geldmacher et al., 2013)
Site 1256 lavas (glass) (this study)
Site 1256 lavas (whole rock) (Sadofsky et al., 2009)
Site 1256 lavas (whole rock) (this study)
Average Site 1256 N-MORB-like glass
Rb Ba Th U Nb Ta La Ce Sr Pb Nd Sm Eu Gd Dy Y Yb Lu
(a)

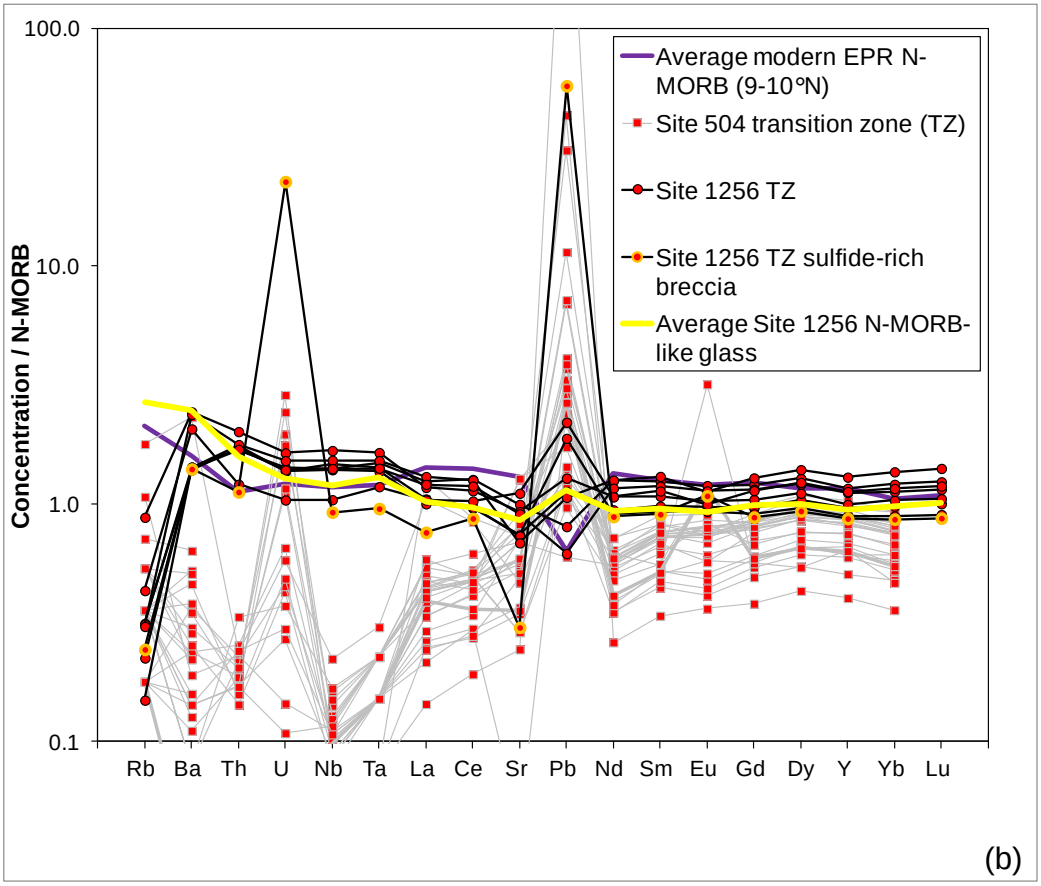
100.0
10.0
1.0
0.1
Concentration / N-MORB
Average modern EPR N-MORB (9-10°N)
Site 504 transition zone (TZ)
Site 1256 TZ
Site 1256 TZ sulfide-rich breccia
Average Site 1256 N-MORB-like glass
Rb Ba Th U Nb Ta La Ce Sr Pb Nd Sm Eu Gd Dy Y Yb Lu
(b)

Figure 3 (*continued*)

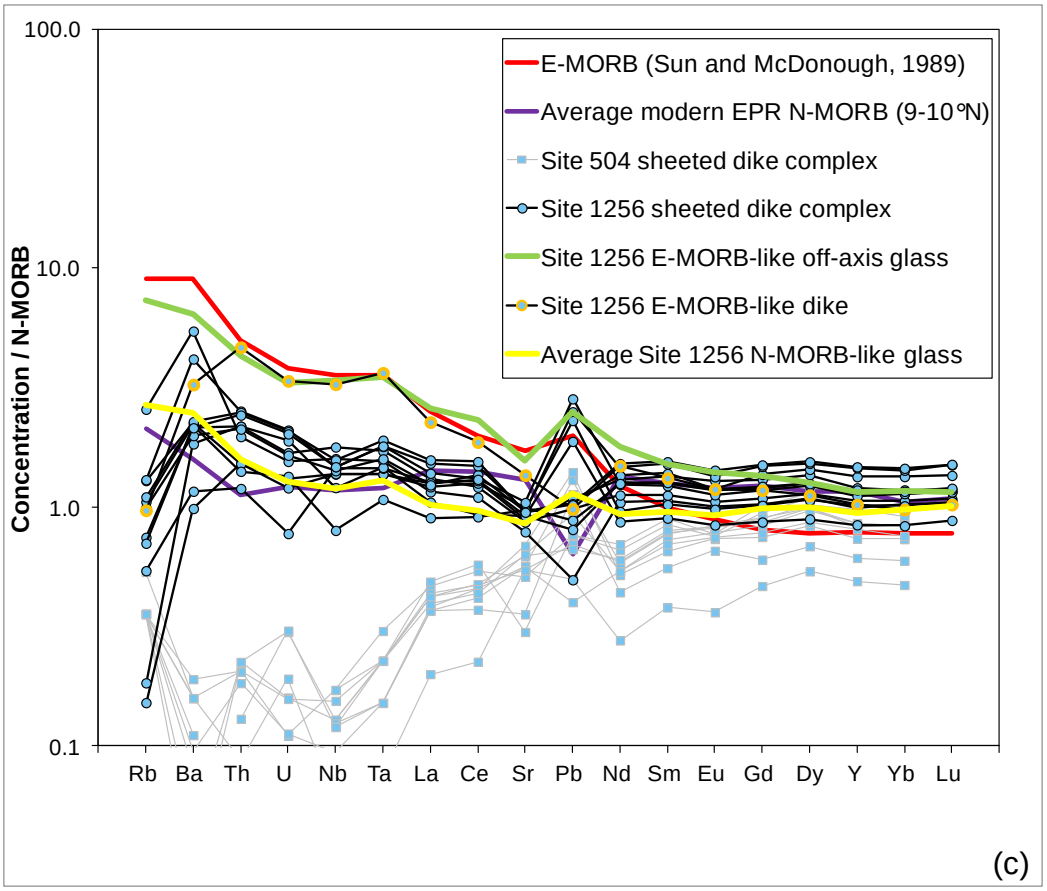

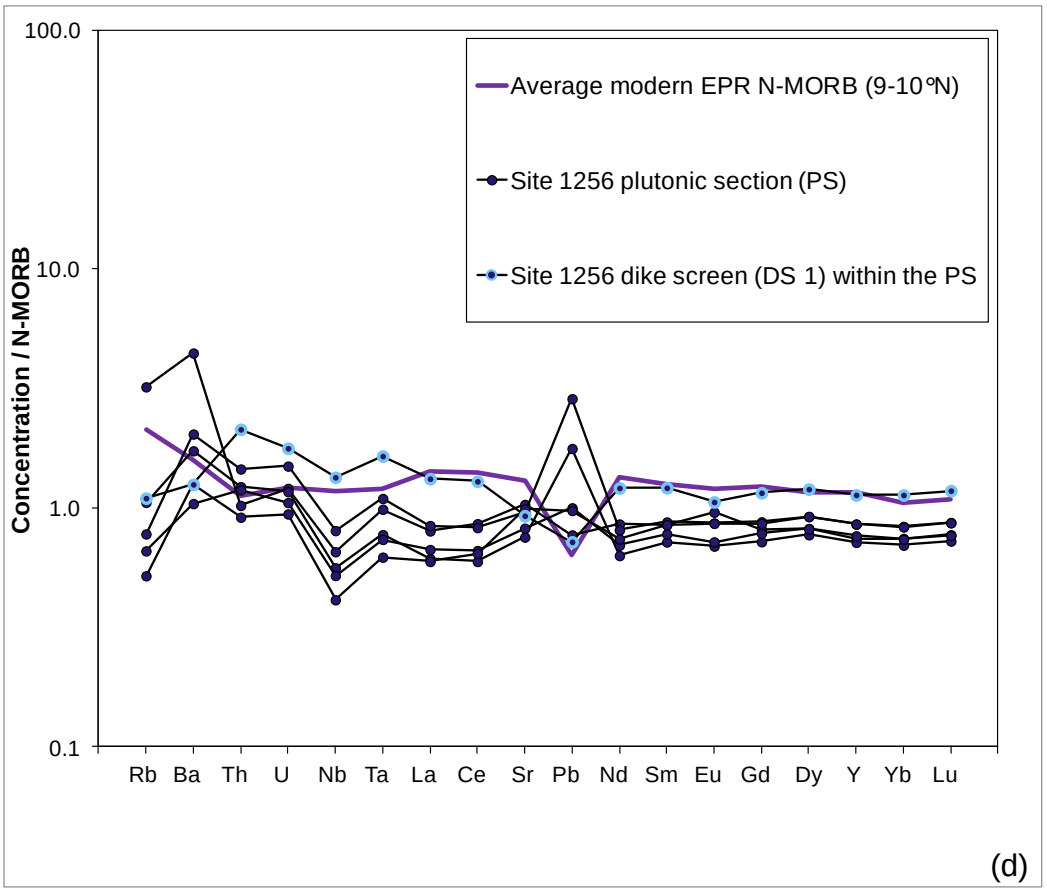

Figure 4

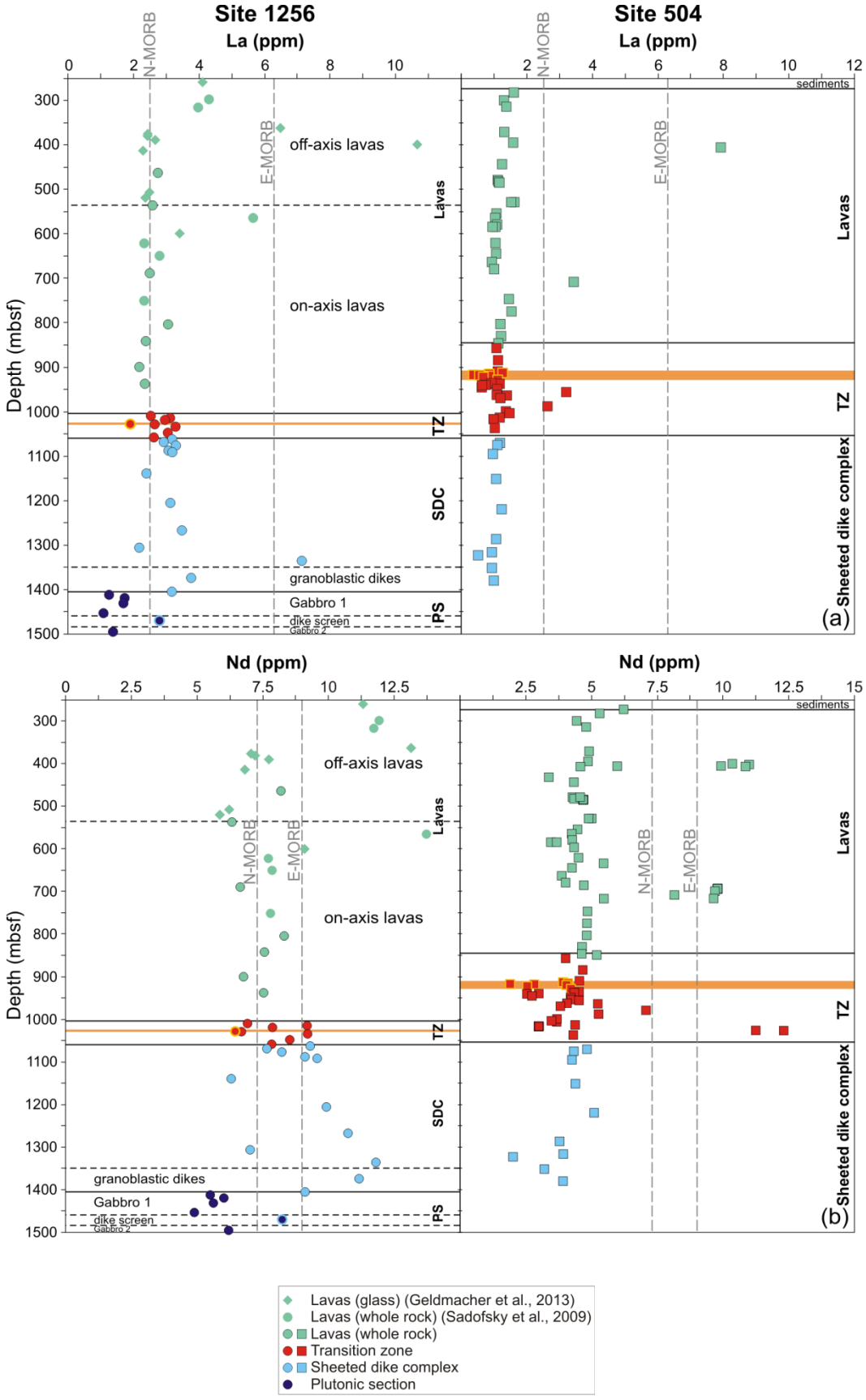
Site 1256
Site 504
La (ppm)
Nd (ppm)
N-MORB
E-MORB
off-axis lavas
on-axis lavas
granoblastic dikes
Gabbro 1
dike screen
Gabbro 2
sediments
Lavas
TZ
SDC
PS
Sheeted dike complex
Depth (mbsf)
(a)
(b)
Lavas (glass) (Geldmacher et al., 2013)
Lavas (whole rock) (Sadofsky et al., 2009)
Lavas (whole rock)
Transition zone
Sheeted dike complex
Plutonic section

Figure 4 (*continued*)

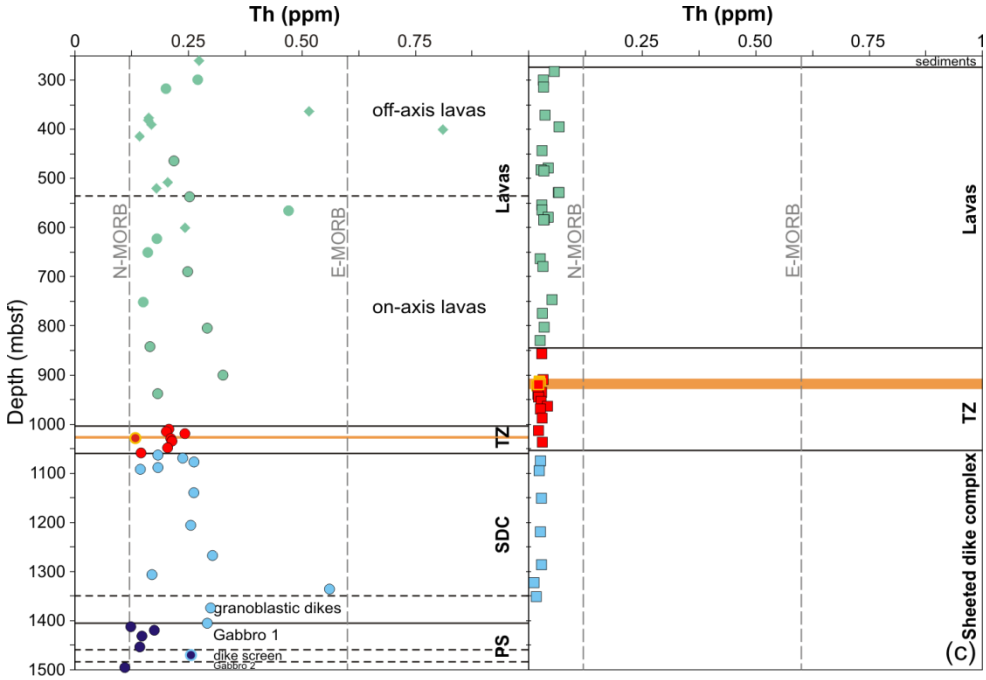

Figure 4 (*continued*)

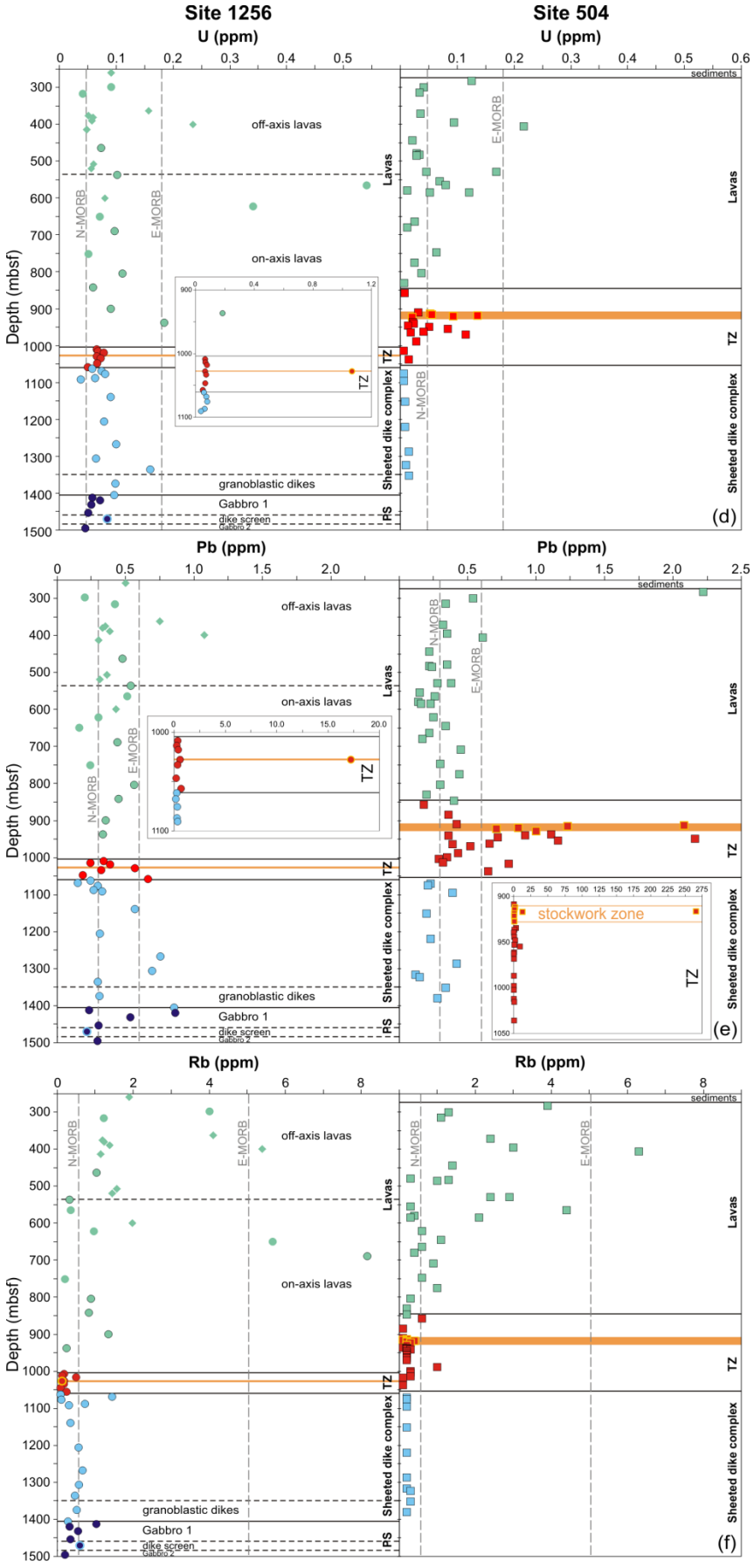

Figure 4 (*continued*)

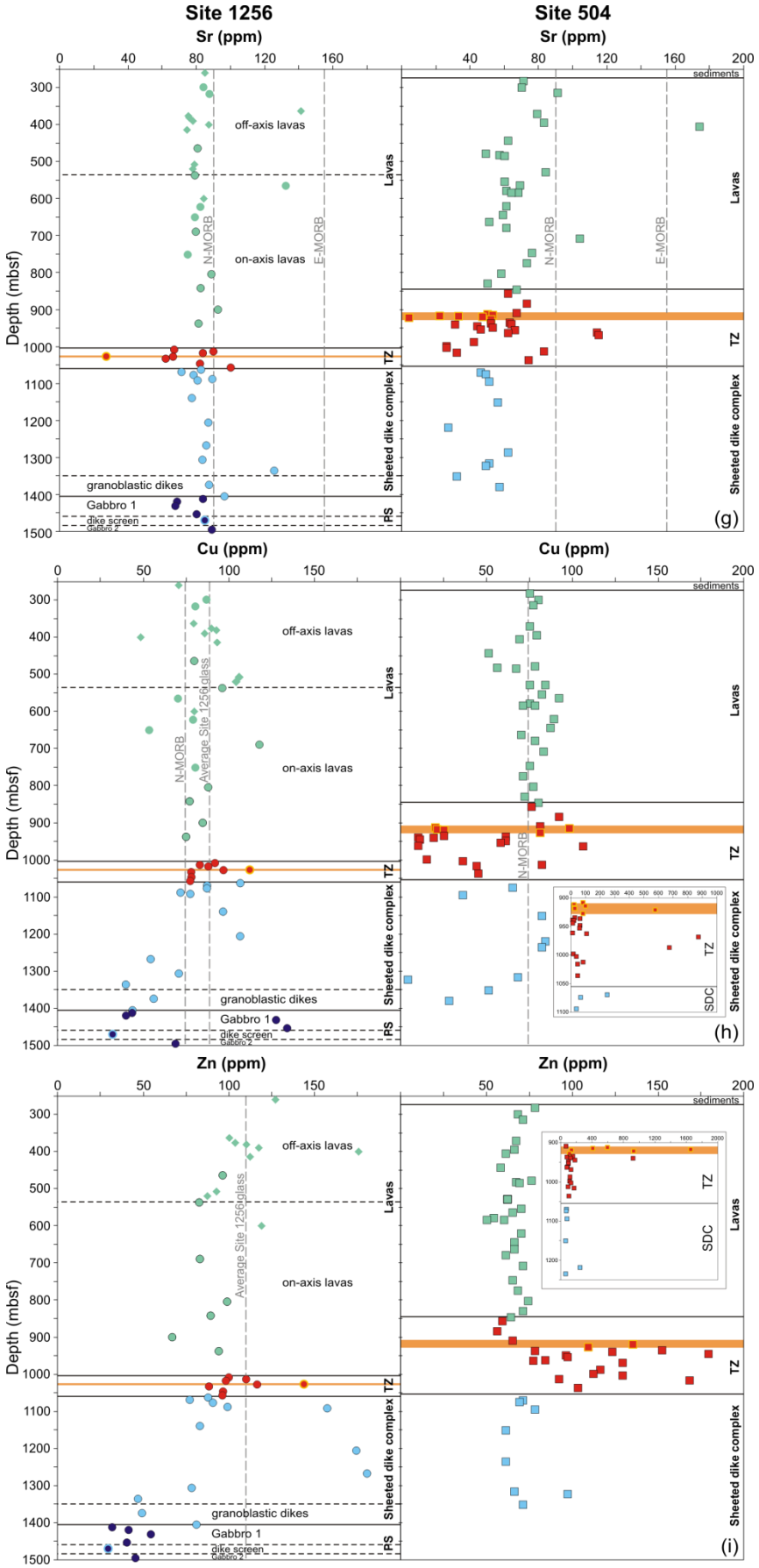

Figure 5

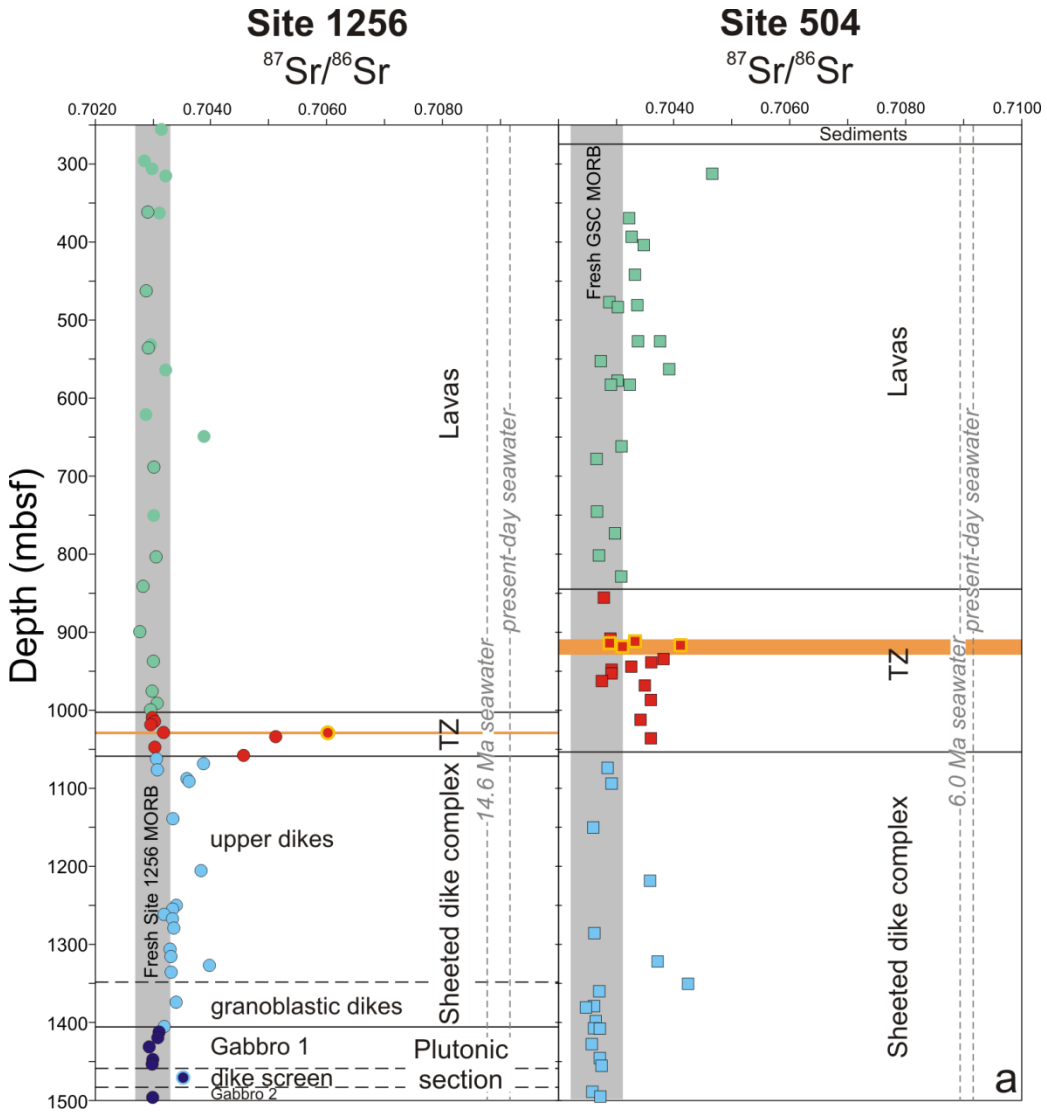
Site 1256
87Sr/86Sr
0.7020
0.7040
0.7060
0.7080
Depth (mbsf)
300
400
500
600
700
800
900
1000
1100
1200
1300
1400
1500
Lavas
TZ
Sheeted dike complex
14.6 Ma seawater
present-day seawater
Fresh Site 1256 MORB
upper dikes
granoblastic dikes
Gabbro 1
dike screen
Gabbro 2
Plutonic section
Site 504
87Sr/86Sr
0.7040
0.7060
0.7080
0.7100
Sediments
Fresh GSC MORB
Lavas
TZ
Sheeted dike complex
6.0 Ma seawater
present-day seawater
a

Figure 5 (*continued*)

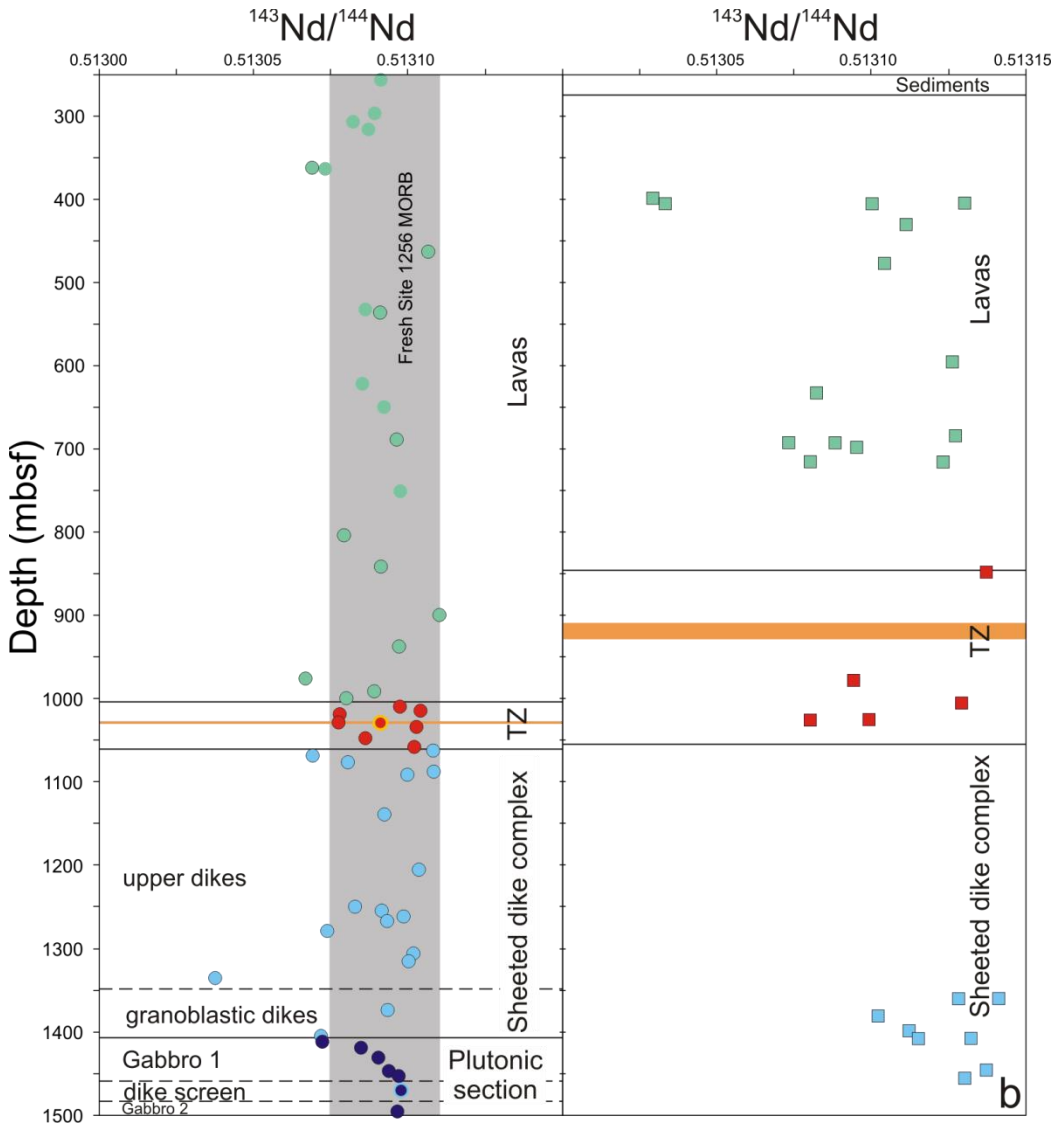

Figure 6

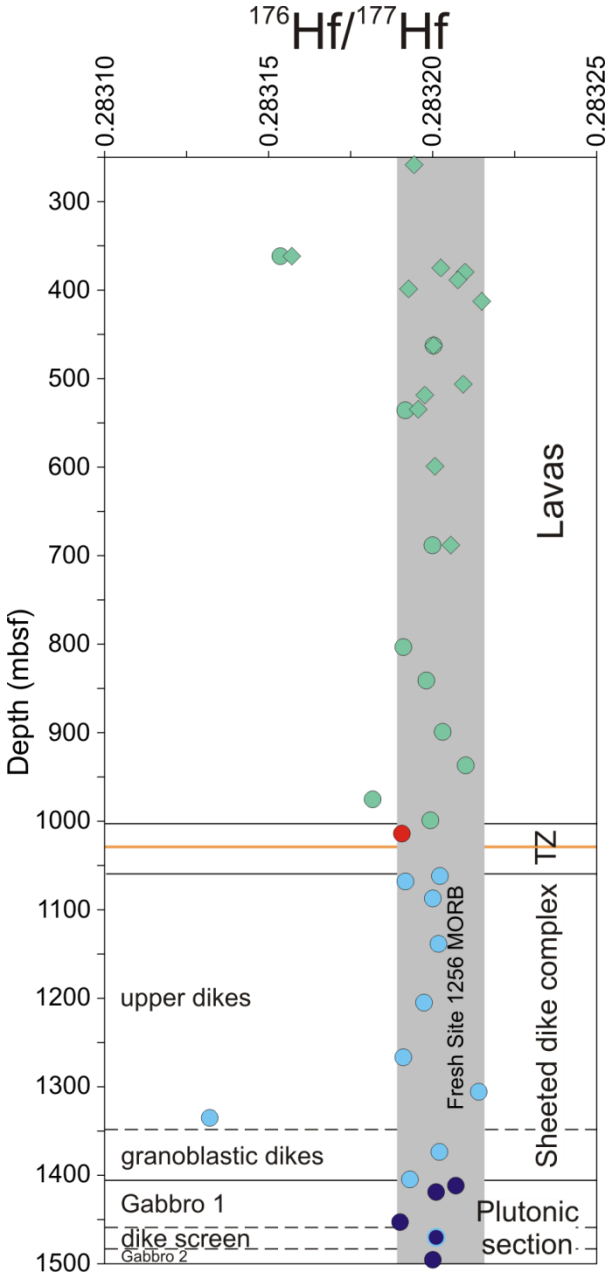
176Hf/177Hf
0.28310
0.28315
0.28320
0.28325
Depth (mbsf)
300
400
500
600
700
800
900
1000
1100
1200
1300
1400
1500
Lavas
TZ
Sheeted dike complex
Fresh Site 1256 MORB
upper dikes
granoblastic dikes
Gabbro 1
dike screen
Gabbro 2
Plutonic section

Figure 7

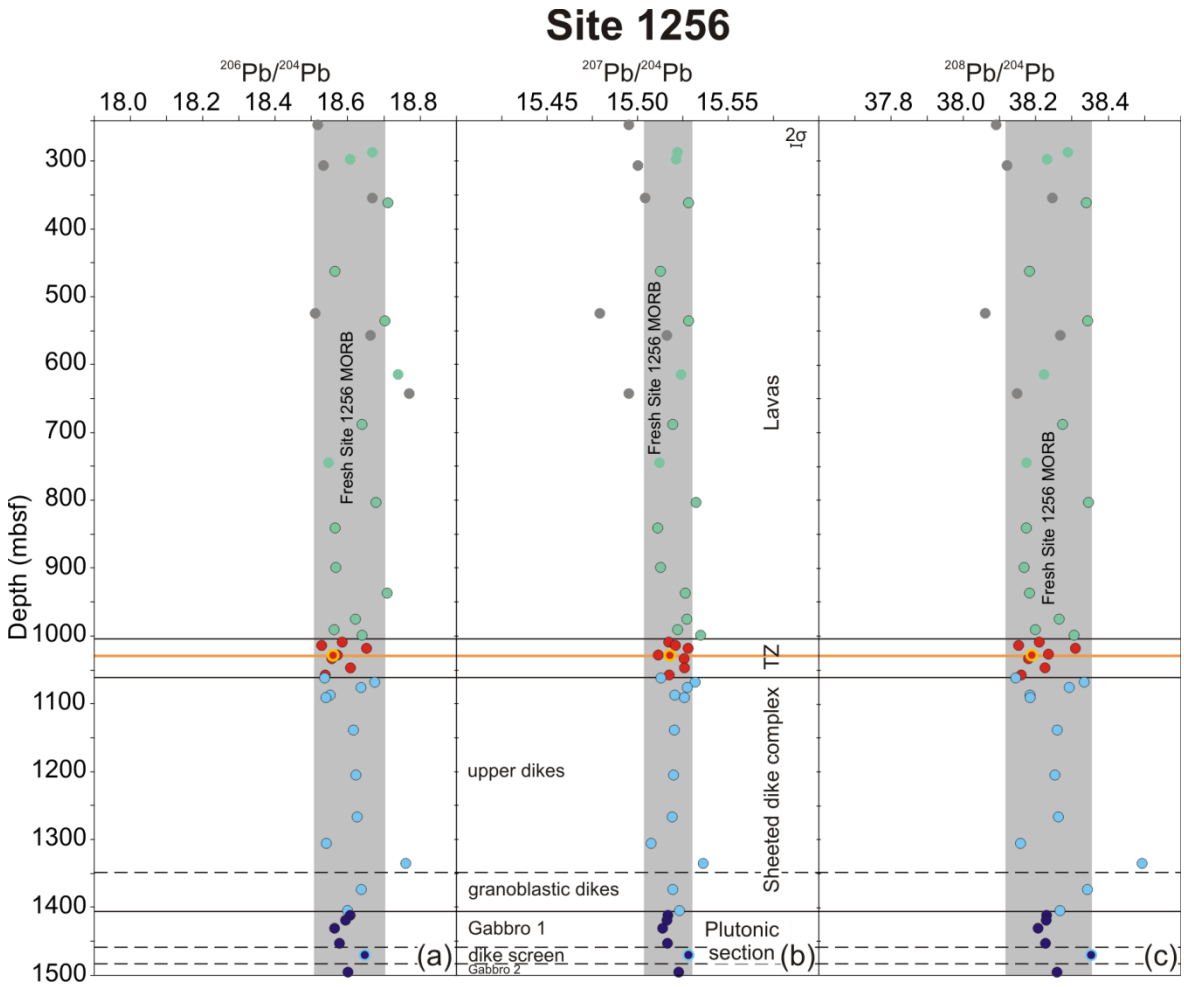
Site 1256
206Pb/204Pb
18.0 18.2 18.4 18.6 18.8
207Pb/204Pb
15.45 15.50 15.55
208Pb/204Pb
37.8 38.0 38.2 38.4
2σ
Depth (mbsf)
300 400 500 600 700 800 900 1000 1100 1200 1300 1400 1500
Fresh Site 1256 MORB
Lavas
TZ
Sheeted dike complex
upper dikes
granoblastic dikes
Gabbro 1
dike screen
Gabbro 2
Plutonic section
(a)
(b)
(c)

Figure 7 (*continued*)

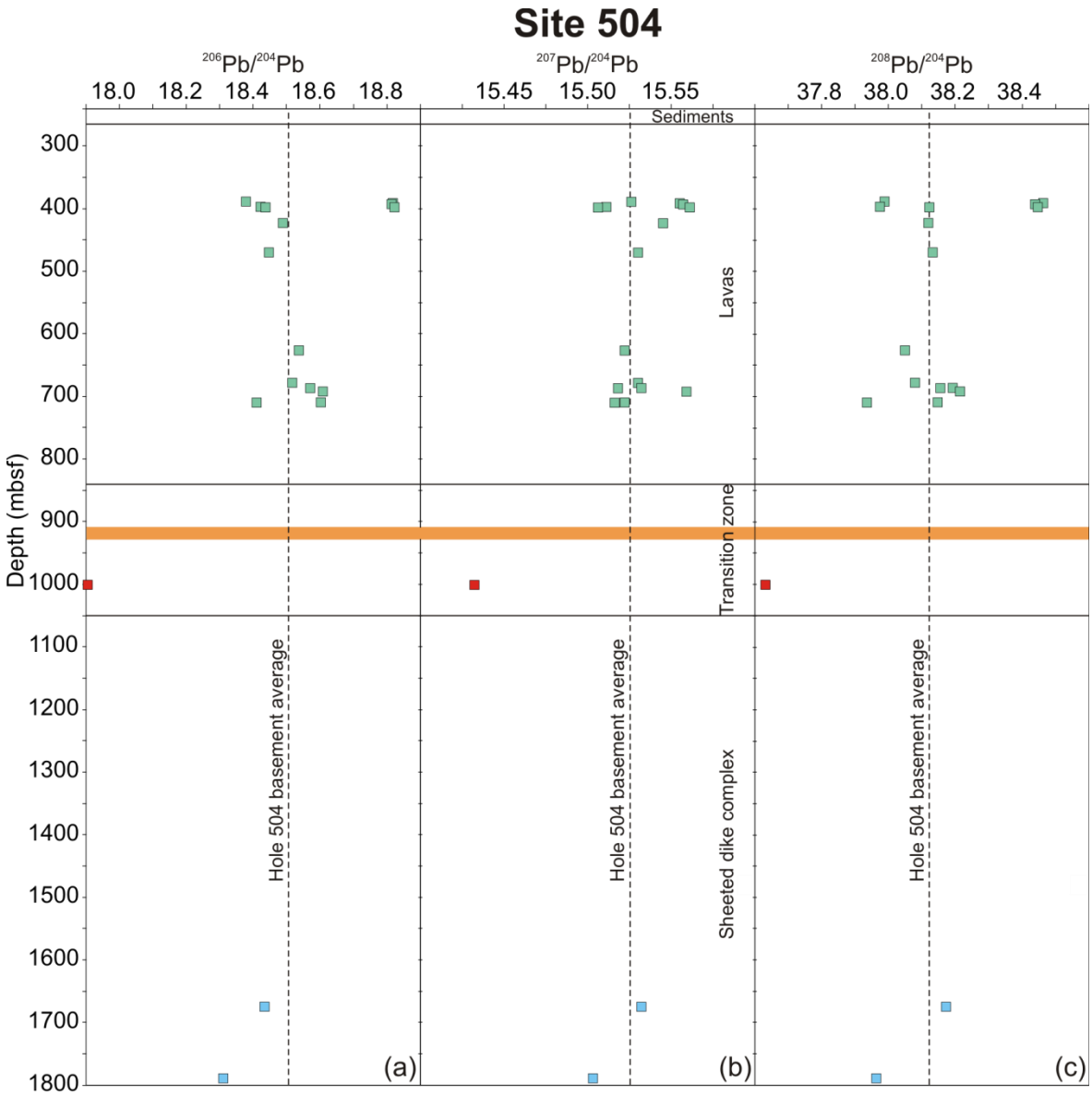

Figure 8

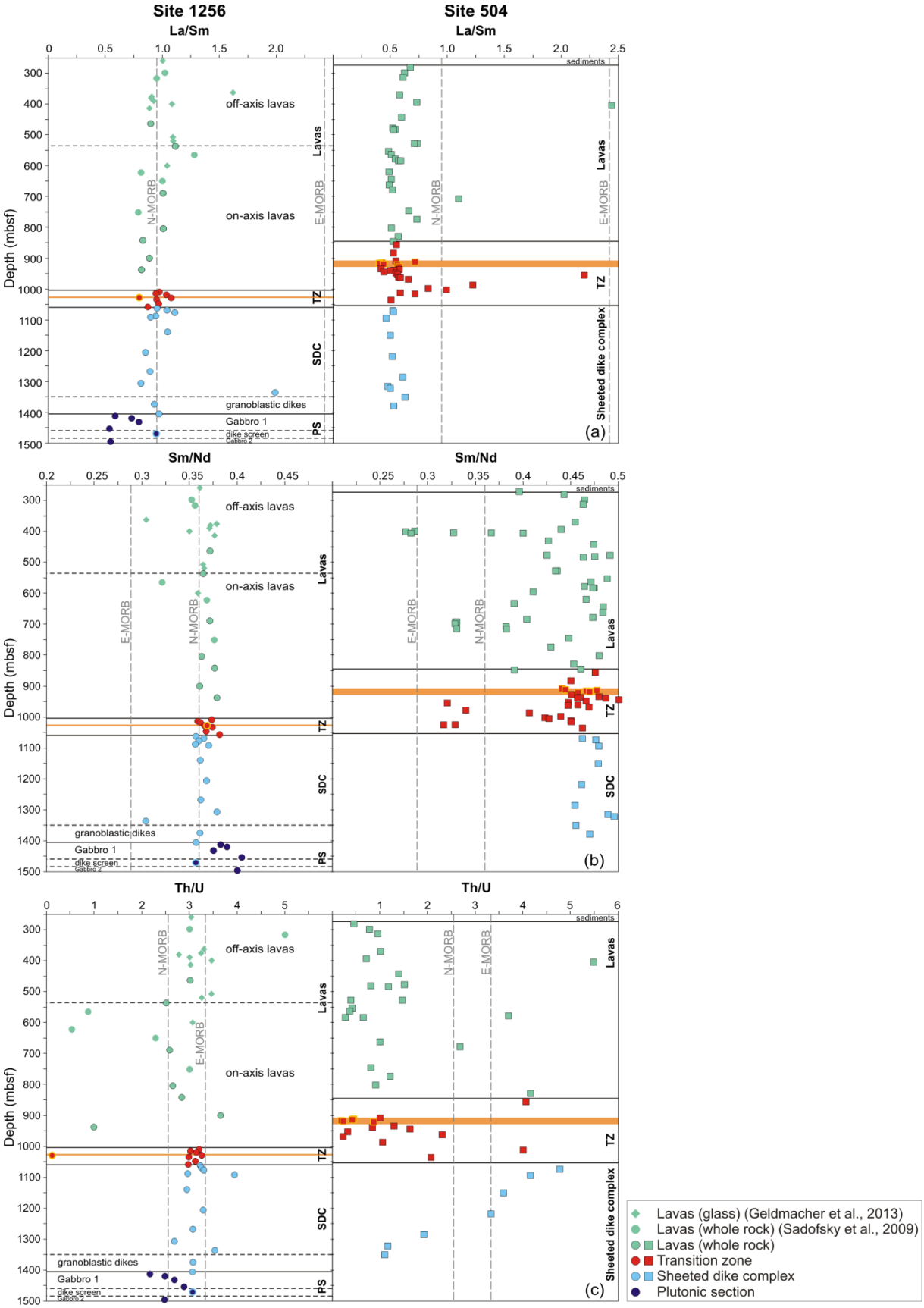
Site 1256
Site 504
La/Sm
Sm/Nd
Th/U
Depth (mbsf)
off-axis lavas
on-axis lavas
N-MORB
E-MORB
Lavas
TZ
SDC
Sheeted dike complex
granoblastic dikes
Gabbro 1
dike screen
Gabbro 2
PS
sediments
(a)
(b)
(c)
Lavas (glass) (Geldmacher et al., 2013)
Lavas (whole rock) (Sadofsky et al., 2009)
Lavas (whole rock)
Transition zone
Sheeted dike complex
Plutonic section

Figure 8 (*continued*)

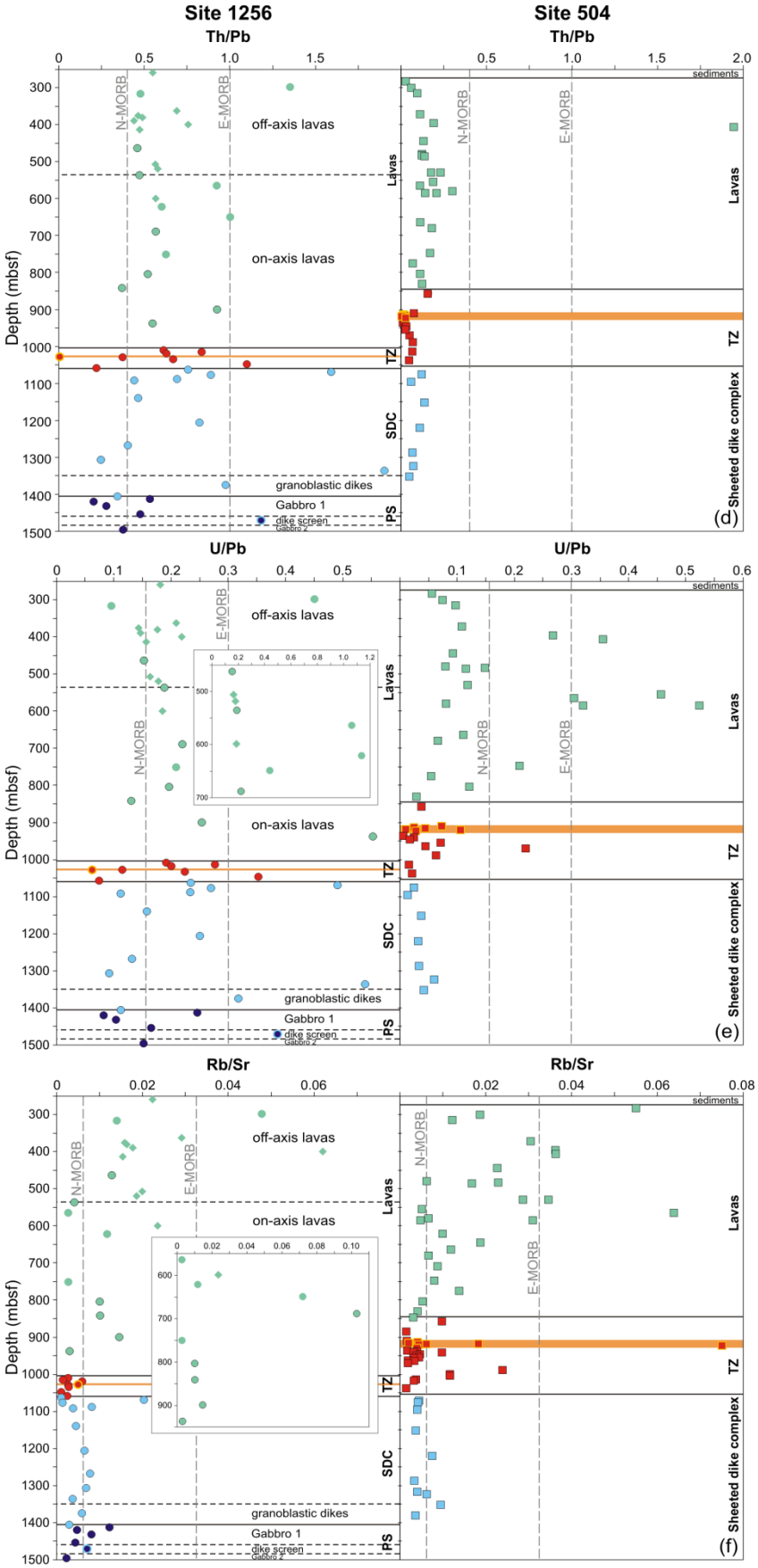

Figure 8 (*continued*)

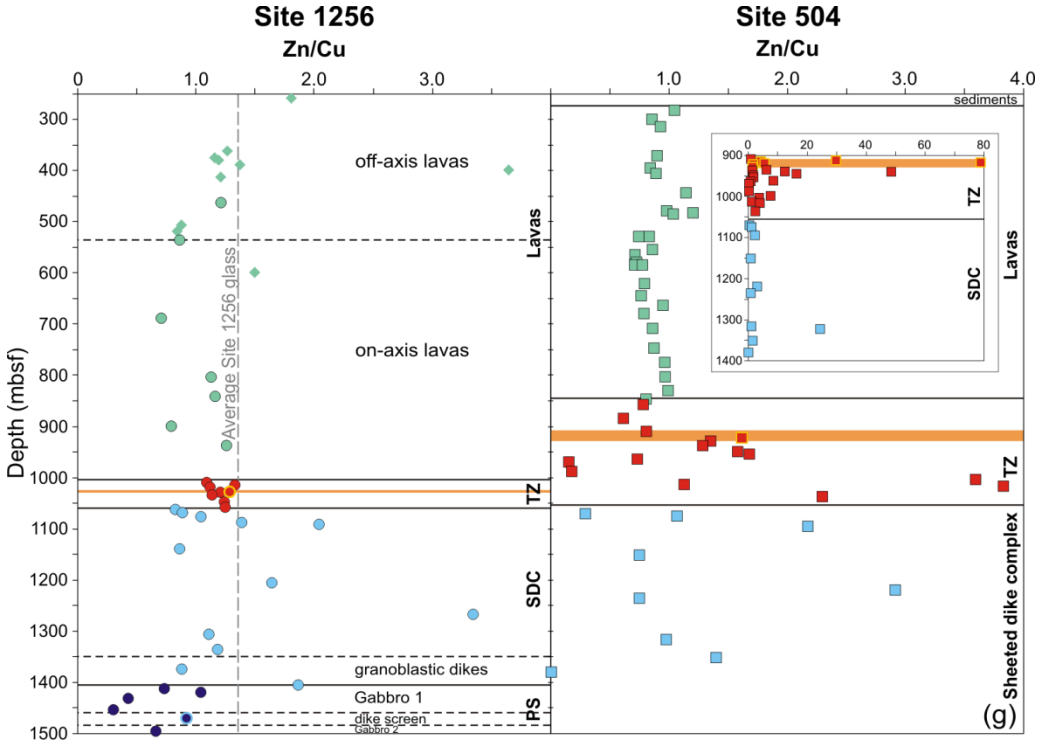

Figure 9

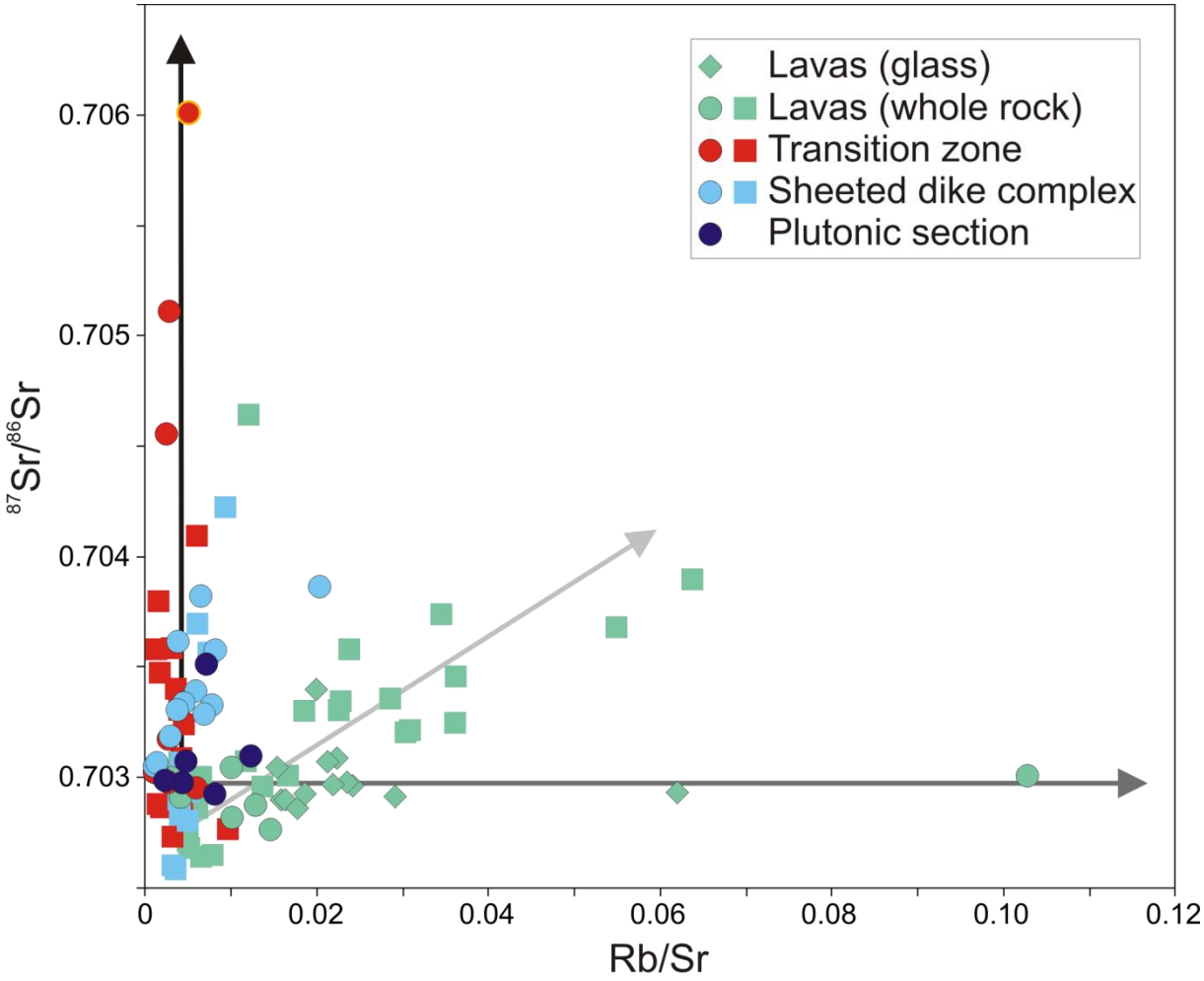
Lavas (glass)
Lavas (whole rock)
Transition zone
Sheeted dike complex
Plutonic section
0.706
0.705
0.704
0.703
87Sr/86Sr
0
0.02
0.04
0.06
0.08
0.10
0.12
Rb/Sr

Figure 10

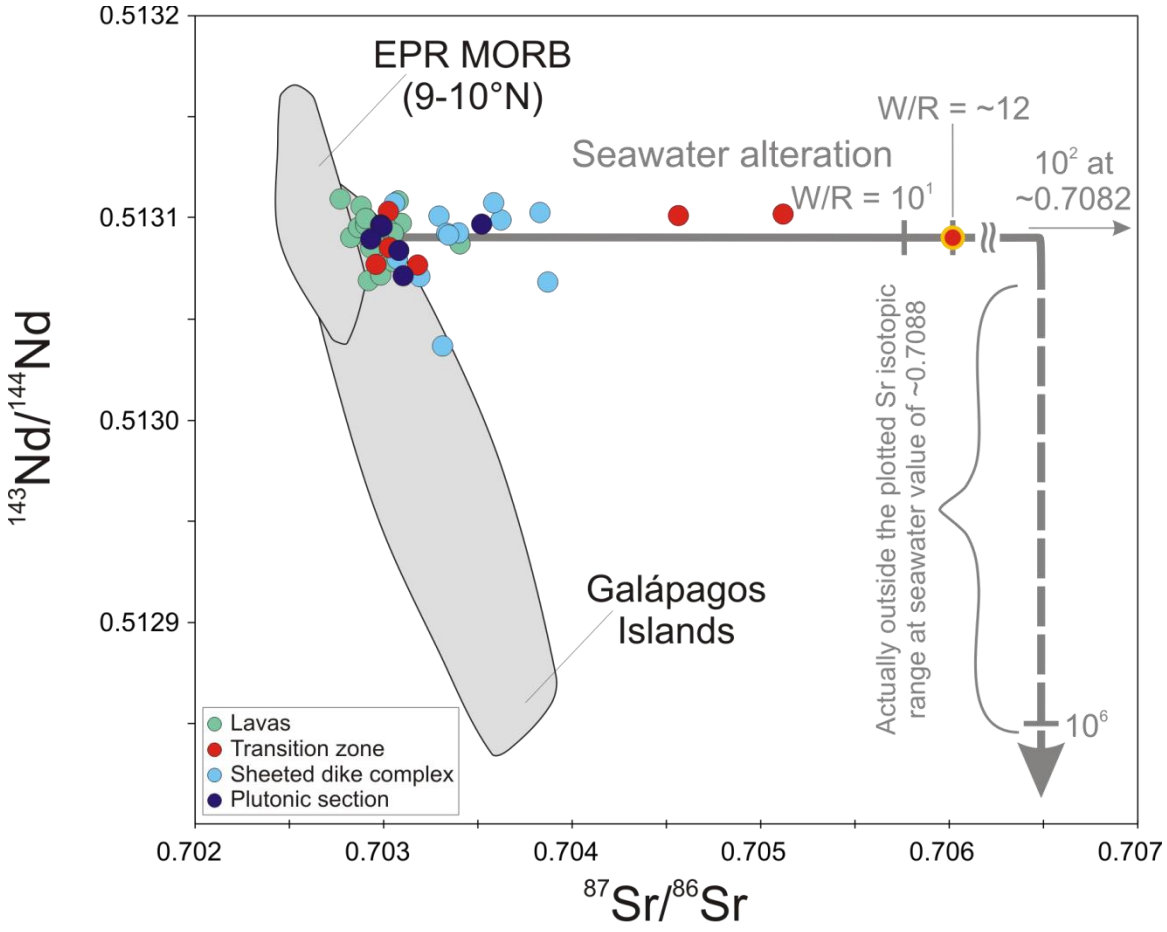
EPR MORB
(9-10°N)
Seawater alteration
W/R = ~12
W/R = 10¹
10² at
~0.7082
Actually outside the plotted Sr isotopic range at seawater value of ~0.7088
10⁶
Galápagos
Islands
Lavas
Transition zone
Sheeted dike complex
Plutonic section
0.5132
0.5131
0.5130
0.5129
143Nd/144Nd
0.702
0.703
0.704
0.705
0.706
0.707
87Sr/86Sr

Figure 11

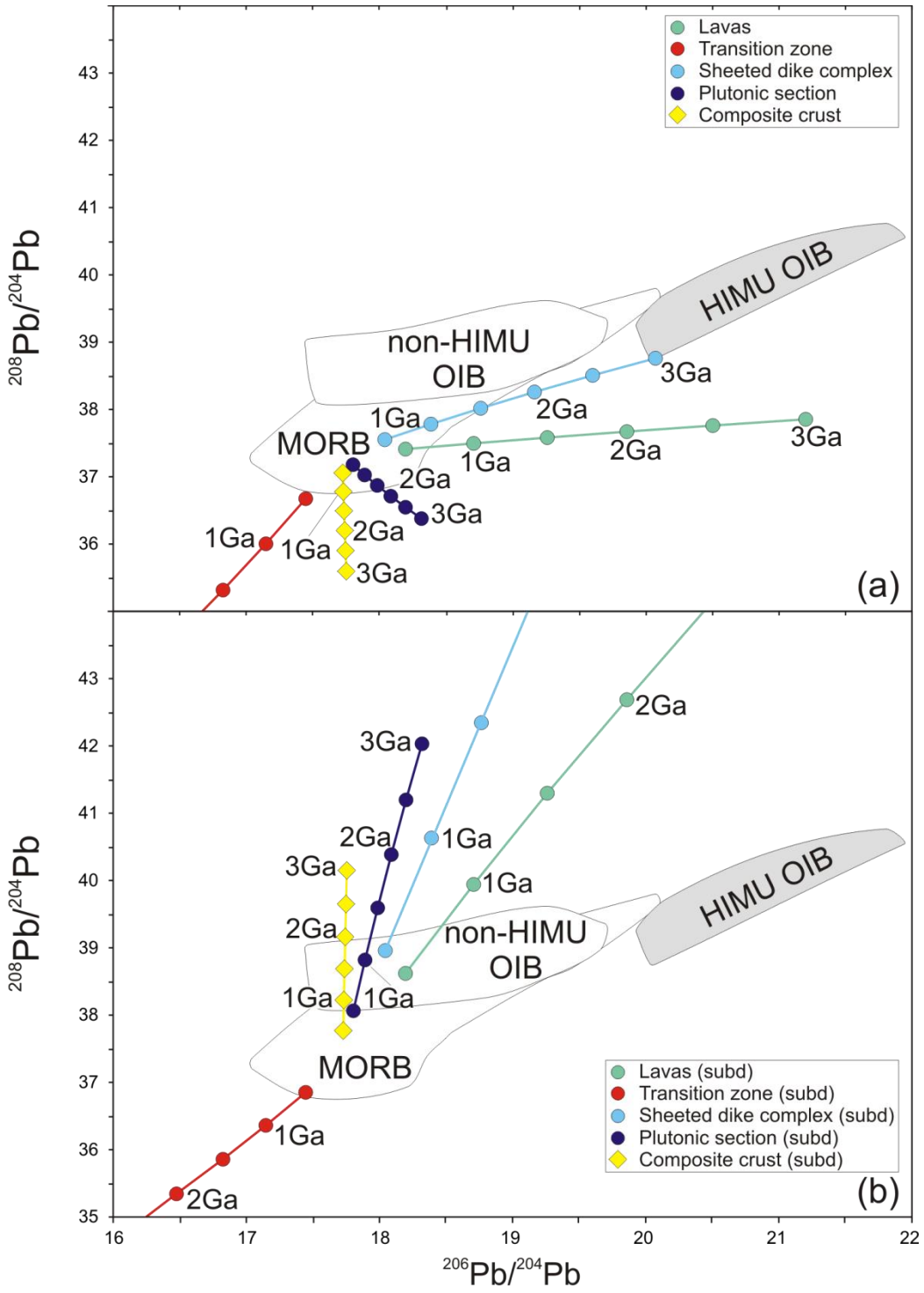
Lavas
Transition zone
Sheeted dike complex
Plutonic section
Composite crust
HIMU OIB
non-HIMU OIB
MORB
1Ga
2Ga
3Ga
(a)
Lavas (subd)
Transition zone (subd)
Sheeted dike complex (subd)
Plutonic section (subd)
Composite crust (subd)
(b)
208Pb/204Pb
206Pb/204Pb

Table 1.

Trace element concentrations (in µg/g [= ppm]) of studied ODP/IODP Site 1256 basement samples.
All concentrations (determined by ICP-MS) obtained from whole rocks, unless otherwise noted (g = glass). mbsf = meters below seafloor.

Core/ section	Interval (cm)	Depth (mbsf)	Li	Sc	V	Cr	Co	Ni	Cu	Zn	Ga	Rb	Sr	Y	Zr	Nb	Sn	Sb	Cs	Ba
Lavas (ODP Leg 206, Hole 1256C: 30R-1–62R-1; IODP Exp. 309, Hole 1256D: 84R-1–103R-1)																				
30R-1	41-58	461.81	6.16	43.9	371	66.6	48.4	47.7	79.4	96.0	16.2	1.03	80.4	32.7	74.9	2.65	0.884	0.033	0.018	12.3
30R-1 (g)	44-59	461.84	5.72	42.5	303	256	46.6	83.0	99.1	78.5	14.3	1.81	79.9	24.3	54.2	2.99	0.277	0.622	0.033	18.8
43R-1 (g)	09-12	533.99	5.57	41.0	299	226	45.5	84.0	97.7	75.6	14.0	1.89	77.6	23.9	54.0	3.19	0.601	0.027	0.032	19.8
43R-1	105-112	534.92	4.89	42.1	303	235	46.0	83.9	95.7	82.3	14.2	0.321	78.8	24.2	53.9	3.17	0.644	0.026	0.013	11.9
62R-1 (g)	10-12	687.30	5.98	41.3	308	159	45.7	72.1	91.6	81.0	14.3	1.703	76.2	25.8	57.9	2.83	0.654	0.028	0.034	18.1
62R-1	36-38	687.56	5.16	43.9	313	170	52.7	75.8	117	82.7	15.0	8.15	79.3	25.6	58.9	2.76	0.636	0.037	0.204	6.58
84R-1	79-85	802.59	6.32	43.5	334	76.3	66.2	59.0	87.5	98.6	15.5	0.883	88.4	28.9	75.5	3.73	0.858	0.037	0.024	16.6
88R-1	10-21	840.30	5.90	44.3	352	101	46.9	48.9	76.7	88.9	15.5	0.828	82.2	30.5	69.8	2.05	0.724	0.030	0.030	7.95
97R-1	61-70	898.41	6.07	43.1	282	314	42.9	108	84.3	66.5	15.2	1.34	92.3	24.6	59.3	2.05	0.599	0.023	0.096	7.37
103R-1	20-28	936.20	3.99	43.3	358	197	49.5	78.1	74.6	93.7	16.1	0.241	80.9	31.0	71.2	2.21	0.750	0.031	0.011	7.22
Transition zone (IODP Hole 1256D, Exp. 309)																				
118R-1	48-56	1008.48	3.64	44.3	342	298	48.4	103	91.5	99.6	14.2	0.176	66.7	27.0	68.5	3.24	0.397	0.006	0.004	8.75
119R-1	60-64	1013.40	1.96	47.2	374	145	45.4	60.4	82.7	110	16.3	0.126	89.6	32.6	92.4	3.26	0.149	0.004	0.004	8.87
120R-1	95-105	1017.60	2.73	44.4	355	66.6	47.3	51.4	87.6	97.8	15.9	0.492	83.5	27.9	75.0	3.91	0.349	0.005	0.006	15.4
122R-1	25-28	1027.55	3.17	41.8	335	237	48.7	100	96.4	116	14.0	0.175	66.0	25.0	60.7	3.41	0.360	0.005	0.005	9.00
122R-1	67-79	1027.97	4.30	28.0	249	37.9	27.4	24.8	112	144	12.8	0.137	27.2	24.3	58.5	2.15	1.13	0.223	0.003	8.83
123R-1	83-88	1032.88	1.59	49.0	438	65.6	43.8	47.4	77.6	88.0	11.7	0.171	61.7	36.3	92.4	3.56	0.207	0.011	0.002	15.0
126R-1	39-47	1046.39	2.06	46.3	362	50.5	48.1	51.9	77.7	96.2	16.0	0.084	81.8	31.2	81.1	3.28	0.294	0.007	0.003	9.00
128R-1	80-91	1056.90	3.20	47.6	377	171	48.9	73.5	77.0	95.8	9.71	0.242	99.8	31.6	76.2	2.43	0.293	0.007	0.002	13.0
Sheeted dike complex (IODP Hole 1256D, Exp. 309: 130R-2–159R-1, Exp. 312: 174R-1–212R-1)																				
129R-1	34-51	1061.24	2.12	46.3	369	188	46.7	78.1	106	87.5	16.5	0.085	82.4	31.8	84.2	3.20	0.497	0.009	0.003	6.22
130R-2	21-34	1067.41	4.92	48.4	348	79.0	45.5	54.9	86.9	76.8	14.3	1.44	70.9	27.9	71.4	3.72	0.151	0.003	0.006	34.4
132R-1	00-18	1075.30	2.65	48.9	366	83.1	47.6	53.8	86.8	90.3	15.3	0.103	78.0	29.8	78.0	4.16	0.413	0.007	0.002	11.6
134R-2	40-52	1086.60	2.60	41.1	376	188	44.8	76.8	71.4	98.8	15.4	0.724	89.0	31.2	88.5	3.22	0.118	0.004	0.006	14.2
135R-1	54-64	1090.24	2.59	46.8	424	50.8	50.3	43.3	77.0	157	17.4	0.303	80.4	33.7	47.5	3.39	0.261	0.008	0.006	7.34
145R-1	50-54	1138.00	2.11	41.6	279	235	42.72	77.9	101	95.2	14.6	0.419	82.7	23.6	55.7	2.81	0.566	0.091	0.024	13.6
159R-1	60-70	1204.40	3.58	48.6	407	63.1	40.5	46.0	106	174	15.3	0.558	86.7	37.6	91.1	3.31	0.701	0.021	0.007	12.6
174R-1	73-79	1266.13	1.63	45.1	393	53.8	44.80	40.3	57.6	184	17.8	0.730	86.1	40.9	102	3.44	0.910	0.095	0.024	26.3
182R-1	18-25	1305.08	0.82	42.5	319	213	45.30	76.5	72.9	87.0	16.0	0.590	87.6	28.4	64.1	1.86	0.788	0.091	0.022	13.8
189R-1	71-89	1334.61	1.11	31.9	247	234	40.50	125	54.7	46.7	16.6	0.543	123	28.7	100	7.62	0.854	0.095	0.020	20.5
202R-1	25-37	1373.05	0.74	45.3	417	41.6	47.18	36.8	69.1	48.8	18.6	0.618	85.7	41.3	102	3.67	1.14	0.088	0.021	14.4
212R-1	04-07	1404.14	0.65	43.2	332	161	42.61	54.6	48.7	87.3	17.1	0.395	94.1	33.0	85.4	3.44	0.926	0.089	0.023	13.5
Plutonic section (IODP Hole 1256D, Exp. 312)																				
214R-1	26-35	1411.16	1.54	42.2	219	482	35.74	105	28.3	36.1	14.4	1.80	93.1	20.9	40.2	1.53	0.817	0.081	0.022	28.1
216R-1	49-58	1418.39	0.84	50.6	280	385	44.48	96.0	126	56.5	13.3	0.436	86.9	24.0	47.1	1.87	0.685	0.085	0.024	12.9
219R-1	25-32	1430.25	1.65	54.3	261	843	42.98	126	94.9	50.7	11.5	0.591	68.0	20.1	40.6	1.31	0.526	0.087	0.024	10.9
223R-3	12-24	1452.40	1.08	47.8	233	563	44.82	134	132	45.7	12.2	0.370	74.1	21.4	44.0	1.21	0.520	0.081	0.021	6.57
227R-1	113-126	1469.63	1.53	44.4	440	131	42.42	79.2	28.4	31.5	16.5	0.616	83.5	31.7	83.2	3.13	1.39	0.087	0.020	7.91
232R-2	35-50	1494.93	2.01	48.1	302	454	44.20	101	95.1	53.9	15.2	0.291	89.2	24.0	32.0	0.96	0.598	0.088	0.022	7.93

Table 1. (*continued)*

Core/ section	Interval (cm)	Depth (mbsf)	La	Ce	Pr	Nd	Sm	Eu	Gd	Tb	Dy	Ho	Er	Tm	Yb	Lu	Hf	Ta	Pb	Th	U
Lavas (ODP Leg 206, Hole 1256C: 30R-1–62R-1; IODP Exp. 309, Hole 1256D: 84R-1–103R-1)																					
30R-1	41-58	461.81	2.72	8.26	1.46	8.17	3.03	1.13	4.30	0.806	5.59	1.21	3.46	0.525	3.54	0.537	2.06	0.187	0.475	0.218	0.072
30R-1 (g)	44-59	461.84	2.45	6.81	1.14	6.26	2.31	0.87	3.24	0.607	4.21	0.92	2.61	0.397	2.66	0.402	1.54	0.230	0.292	0.236	0.077
43R-1 (g)	09-12	533.99	2.59	6.99	1.16	6.27	2.29	0.85	3.20	0.597	4.12	0.89	2.53	0.390	2.60	0.393	1.52	0.223	0.268	0.239	0.080
43R-1	105-112	534.92	2.56	7.01	1.16	6.30	2.30	0.86	3.22	0.599	4.15	0.89	2.54	0.390	2.61	0.396	1.49	0.214	0.535	0.252	0.101
62R-1 (g)	10-12	687.30	2.48	7.02	1.19	6.54	2.44	0.90	3.40	0.638	4.43	0.96	2.73	0.417	2.80	0.427	1.60	0.198	0.291	0.214	0.074
62R-1	36-38	687.56	2.47	7.04	1.20	6.62	2.46	0.92	3.45	0.645	4.46	0.96	2.73	0.418	2.82	0.428	1.65	0.186	0.438	0.248	0.096
84R-1	79-85	802.59	3.03	8.81	1.49	8.29	3.01	1.11	4.11	0.760	5.23	1.11	3.16	0.485	3.33	0.501	2.02	0.244	0.561	0.291	0.110
88R-1	10-21	840.30	2.35	7.52	1.34	7.54	2.84	1.06	4.01	0.755	5.22	1.13	3.24	0.492	3.30	0.501	1.89	0.147	0.447	0.165	0.058
97R-1	61-70	898.41	2.15	7.19	1.23	6.74	2.43	0.92	3.37	0.630	4.29	0.93	2.63	0.399	2.65	0.396	1.69	0.133	0.353	0.326	0.089
103R-1	20-28	936.20	2.32	7.33	1.32	7.51	2.84	1.04	4.02	0.762	5.32	1.16	3.31	0.512	3.45	0.527	1.96	0.155	0.332	0.182	0.183
Transition zone (IODP Hole 1256D, Exp. 309)																					
118R-1	48-56	1008.48	2.50	7.20	1.25	6.89	2.57	0.99	3.54	0.684	4.71	1.03	2.93	0.449	2.98	0.456	1.90	0.181	0.338	0.207	0.065
119R-1	60-64	1013.40	3.09	9.50	1.67	9.16	3.28	1.22	4.44	0.849	5.83	1.28	3.61	0.554	3.69	0.564	2.50	0.196	0.241	0.201	0.067
120R-1	95-105	1017.60	2.93	8.52	1.44	7.85	2.83	1.05	3.84	0.733	5.05	1.10	3.09	0.475	3.15	0.478	2.06	0.217	0.385	0.242	0.077
122R-1	25-28	1027.55	2.62	7.26	1.23	6.66	2.44	0.95	3.34	0.639	4.38	0.95	2.70	0.406	2.71	0.411	1.68	0.187	0.566	0.211	0.065
122R-1	67-79	1027.97	1.90	6.52	1.17	6.46	2.38	1.10	3.24	0.621	4.25	0.93	2.63	0.396	2.63	0.396	1.67	0.126	17.2	0.135	1.067
123R-1	83-88	1032.88	3.26	9.45	1.65	9.18	3.43	1.15	4.73	0.916	6.34	1.39	4.01	0.620	4.16	0.642	2.61	0.201	0.320	0.213	0.071
126R-1	39-47	1046.39	3.02	8.91	1.55	8.50	3.12	1.16	4.24	0.806	5.51	1.20	3.39	0.518	3.45	0.525	2.25	0.187	0.186	0.204	0.065
128R-1	80-91	1056.90	2.60	7.71	1.38	7.82	2.98	1.01	4.18	0.810	5.60	1.23	3.50	0.534	3.54	0.541	2.19	0.156	0.662	0.145	0.049
Sheeted dike complex (IODP Hole 1256D, Exp. 309: 130R-2–159R-1, Exp. 312: 174R-1–212R-1)																					
129R-1	34-51	1061.24	3.15	9.74	1.71	9.28	3.31	1.19	4.43	0.840	5.70	1.23	3.47	0.527	3.48	0.528	2.29	0.181	0.242	0.182	0.057
130R-2	21-34	1067.41	2.90	8.25	1.41	7.63	2.78	1.03	3.77	0.723	4.96	1.08	3.06	0.468	3.12	0.474	2.01	0.205	0.149	0.237	0.073
132R-1	00-18	1075.30	3.27	9.09	1.53	8.20	2.95	1.08	4.01	0.759	5.18	1.13	3.20	0.486	3.24	0.492	2.13	0.226	0.295	0.262	0.079
134R-2	40-52	1086.60	3.04	9.45	1.66	9.08	3.23	1.15	4.33	0.821	5.59	1.21	3.44	0.525	3.47	0.527	2.35	0.182	0.265	0.182	0.062
135R-1	54-64	1090.24	3.16	9.68	1.71	9.54	3.53	1.32	4.81	0.913	6.22	1.33	3.66	0.545	3.60	0.539	1.48	0.192	0.326	0.144	0.036
145R-1	50-54	1138.00	2.62	6.97	1.17	6.33	2.37	0.86	3.19	0.600	4.06	0.88	2.50	0.379	2.55	0.400	1.62	0.194	0.565	0.262	0.089
159R-1	60-70	1204.40	3.10	10.3	1.78	9.90	3.64	1.21	5.04	0.952	6.55	1.41	4.01	0.611	4.09	0.618	2.62	0.210	0.310	0.255	0.077
174R-1	73-79	1266.13	3.82	11.2	1.94	10.8	3.99	1.37	5.45	1.01	6.94	1.50	4.29	0.648	4.35	0.684	2.87	0.237	0.752	0.303	0.099
182R-1	18-25	1305.08	2.26	6.83	1.22	7.00	2.70	1.00	3.74	0.707	4.87	1.05	2.99	0.459	3.09	0.481	1.86	0.142	0.691	0.170	0.063
189R-1	71-89	1334.61	5.68	14.0	2.14	10.9	3.48	1.21	4.33	0.776	5.09	1.07	3.01	0.448	2.98	0.466	2.59	0.482	0.295	0.560	0.159
202R-1	25-37	1373.05	3.94	11.6	2.01	11.1	4.07	1.46	5.53	1.03	7.04	1.53	4.35	0.654	4.43	0.687	2.88	0.252	0.307	0.299	0.097
212R-1	04-07	1404.14	3.46	9.81	1.67	9.17	3.33	1.21	4.50	0.833	5.70	1.23	3.48	0.525	3.55	0.546	2.40	0.238	0.852	0.291	0.095
Plutonic section (IODP Hole 1256D, Exp. 312)																					
214R-1	26-35	1411.16	2.00	6.45	1.13	6.25	2.24	0.98	3.00	0.547	3.73	0.80	2.26	0.339	2.27	0.351	1.23	0.130	0.231	0.123	0.057
216R-1	49-58	1418.39	2.11	6.21	1.07	5.90	2.30	0.88	3.22	0.612	4.19	0.91	2.55	0.386	2.55	0.396	1.43	0.145	0.860	0.175	0.070
219R-1	25-32	1430.25	1.53	4.48	0.80	4.61	1.90	0.71	2.66	0.511	3.51	0.76	2.13	0.321	2.13	0.331	1.22	0.102	0.532	0.147	0.055
223R-3	12-24	1452.40	1.67	4.97	0.89	5.10	2.05	0.74	2.88	0.544	3.72	0.80	2.27	0.340	2.26	0.349	1.32	0.097	0.300	0.143	0.050
227R-1	113-126	1469.63	3.32	9.70	1.63	8.85	3.20	1.08	4.26	0.804	5.46	1.18	3.39	0.515	3.46	0.538	2.31	0.218	0.216	0.256	0.084
232R-2	35-50	1494.93	1.49	4.84	0.92	5.41	2.24	0.88	3.17	0.610	4.19	0.90	2.56	0.379	2.54	0.394	1.12	0.082	0.293	0.110	0.044

Table 2.

Sr-Nd-Pb-Hf isotope ratios of ODP/IODP Site 1256 basement samples.
All isotopic compositions (determined by TIMS) obtained from whole rocks, unless otherwise noted (g = glass). mbsf = meters below seafloor.

Core/ section	Interval (cm)	Depth (mbsf)	$^{87}Sr/^{86}Sr$	2σ	$^{143}Nd/^{144}Nd$	2σ	$^{206}Pb/^{204}Pb$	2σ	$^{207}Pb/^{204}Pb$	2σ	$^{208}Pb/^{204}Pb$	2σ	$^{176}Hf/^{177}Hf$	2σ
Lavas (* $^{87}Sr/^{86}Sr$, $^{143}Nd/^{144}Nd$, Pb isotope ratios: Geldmacher et al. (2013); $^{176}Hf/^{177}Hf$: this study)														
(ODP Leg 206, Hole 1256C: 6R-1–62R-1; IODP Exp. 309, Hole 1256D: 84R-1–103R-1)														
06R-1* (g)	50-53	257.60	0.703089	3	0.513098	3	18.5895	14	15.5154	12	38.2084	34	0.283194	7
14R-1	139-142	360.89	0.702902	6	0.513069	2	18.7101	12	15.5279	12	38.3377	37	0.283154	6
17R-1* (g)	65-68	374.15	0.702900	2	0.513100	3	18.5443	17	15.5088	13	38.1574	34	0.283202	9
18R-1* (g)	81-84	378.81	0.702899	3	0.513097	3	18.5467	26	15.5116	23	38.1657	61	0.283210	8
20R-1* (g)	33-37	387.73	0.702862	3	0.513096	3	18.5599	14	15.5146	12	38.1861	28	0.283208	8
21R-1* (g)	116-119	397.96	0.702933	2	0.513093	3	18.6013	7	15.5186	6	38.2451	15	0.283193	6
23R-2* (g)	16-20	411.85	0.703047	3	0.513093	3	18.5519	47	15.5044	39	38.1560	96	0.283215	5
30R-1	41-58	461.81	0.702876	5	0.513106	3	18.5636	12	15.5124	11	38.1810	28	0.283200	8
30R-1* (g)	44-59	461.84	0.702968	3	0.513090	3	18.6793	88	15.5224	74	38.3180	190	0.283200	7
38R-1* (g)	121-124	505.51	0.703400	3	0.513088	2	18.6535	16	15.5252	14	38.2747	37	0.283209	8
40R-1* (g)	31-36	517.81	0.702927	3	0.513086	3	18.6209	17	15.5195	14	38.2615	38	0.283198	9
43R-1* (g)	09-12	533.99	0.702964	3	0.513087	2	18.6882	17	15.5265	16	38.3380	44	0.283196	8
43R-1	105-112	534.95	0.702912	6	0.513091	1	18.7019	16	15.5280	14	38.3415	34	0.283192	6
43R-1**	105-112	534.95											0.283192	6
51R-2* (g)	60-64	598.20	0.702980	3	0.513072	3	18.5991	11	15.5179	9	38.2435	23	0.283201	6
62R-1* (g)	10-12	687.30	0.703072	3	0.513109	3	18.6293	15	15.5181	13	38.2582	31	0.283205	7
62R-1	36-38	687.56	0.703009	5	0.513096	2	18.6383	15	15.5192	14	38.2723	37	0.283200	6
84R-1	79-85	802.59	0.703047	7	0.513079	2	18.6771	8	15.5321	8	38.3437	21	0.283191	6
88R-1	10-21	840.30	0.702820	7	0.513091	2	18.5642	14	15.5109	14	38.1723	40	0.283198	5
97R-1	61-70	898.41	0.702765	6	0.513110	2	18.5660	12	15.5125	11	38.1662	34	0.283203	5
103R-1	20-28	936.20	0.703000	6	0.513097	2	18.7083	11	15.5261	10	38.1811	28	0.283210	6
103R-1**	20-28	936.20	0.702969	6	0.513090	2	18.5996	12	15.5156	10	38.1701	25		
111R-1	26-32	974.66	0.702979	3	0.513066	3	18.6204	4	15.5270	4	38.2628	9	0.283182	5
114R-1	127-142	990.07	0.703064	3	0.513089	3	18.5613	9	15.5219	9	38.1973	30		
116R-1	00-15	998.40	0.702951	3	0.513080	3	18.6386	13	15.5346	14	38.3039	45	0.283199	9
Transition zone (IODP Hole 1256D, Exp. 309)														
118R-1	48-56	1008.48	0.702980	3	0.513097	3	18.5837	7	15.5170	6	38.2079	14		
119R-1	60-64	1013.40	0.703020	3	0.513104	2	18.5269	7	15.5207	6	38.1510	18	0.283191	6
119R-1**	60-64	1013.40	0.702955	2	0.513078	3	18.6510	10	15.5277	11	38.3076	35	0.283191	6
120R-1	95-105	1017.60	0.702955	2	0.513078	3	18.6510	10	15.5277	11	38.3076	35		
122R-1	25-28	1027.55	0.703175	3	0.513077	3	18.5703	42	15.5112	32	38.1872	83		
122R-1	67-79	1027.97	0.706013	6	0.513091	2	18.5584	10	15.5176	11	38.1850	34		
123R-1	83-88	1032.88	0.705114	3	0.513102	3	18.5553	7	15.5255	6	38.1784	16		
126R-1	39-47	1046.39	0.703025	3	0.513086	3	18.6064	15	15.5257	12	38.2238	31		
128R-1	80-91	1056.90	0.704558	3	0.513102	2	18.5368	9	15.5173	9	38.1581	23		
Sheeted dike complex (IODP Hole 1256D, Exp. 309: 130R-2–159R-1, Exp. 312: 174R-1–212R-1)														
129R-1	34-51	1061.24	0.703053	3	0.513108	2	18.5352	9	15.5127	7	38.1429	20	0.283202	7
130R-2	21-34	1067.41	0.703866	3	0.513069	2	18.6738	9	15.5316	8	38.3320	24	0.283192	5
132R-1	00-18	1075.30	0.703068	3	0.513080	2	18.6357	7	15.5273	8	38.2906	27		
134R-2	40-52	1086.60	0.703579	3	0.513108	2	18.5503	8	15.5204	7	38.1824	22	0.283200	7
135R-1	54-64	1090.24	0.703618	4	0.513099	2	18.5386	24	15.5256	20	38.1827	50		
145R-1	50-54	1138.00	0.703339	6	0.513092	1	18.6148	10	15.5201	8	38.2574	22	0.283202	5
159R-1	60-70	1204.40	0.703824	5	0.513103	2	18.6216	15	15.5197	12	38.2511	35	0.283197	4
169R-2	40-54	1248.90	0.703396	3	0.513082	3								
170R-2	130-144	1253.70	0.703334	2	0.513091	3								
173R-1	00-10	1260.60	0.703184	3	0.513098	2								
174R-1	73-79	1266.13	0.703330	5	0.513093	1	18.6249	20	15.5189	20	38.2607	63	0.283191	7
176R-2	42-55	1278.02	0.703352	3	0.513073	3								
182R-1	18-25	1305.08	0.703289	6	0.513101	2	18.5400	8	15.5073	7	38.1561	17	0.283214	5
184R-1	00-08	1314.50	0.703303	3	0.513100	3								
187R-2	21-31	1325.88	0.703968	3										
189R-1	71-89	1334.61	0.703308	5	0.513037	2	18.7596	10	15.5360	9	38.4916	24	0.283132	6
202R-1	25-37	1373.05	0.703393	6	0.513093	1	18.6365	22	15.5192	20	38.3408	53	0.283202	7
212R-1	04-07	1404.14	0.703188	6	0.513071	1	18.5984	15	15.5229	14	38.2651	38	0.283193	5
Plutonic section (IODP Hole 1256D, Exp. 312)														
214R-1	26-35	1411.16	0.703099	6	0.513072	1	18.6057	14	15.5165	13	38.2282	33	0.283207	6
216R-1	49-58	1418.39	0.703076	6	0.513084	3	18.5930	11	15.5160	10	38.2271	25	0.283201	6
219R-1	25-32	1430.25	0.702927	5	0.513090	2	18.5625	16	15.5137	15	38.2047	43		
222R-2	25-35	1446.35	0.702989	3	0.513093	3								
223R-3	12-24	1452.40	0.702978	6	0.513097	3	18.5762	14	15.5163	13	38.2252	31	0.283190	4
227R-1	113-126	1469.63	0.703515	5	0.513097	2	18.6460	25	15.5279	21	38.3509	54	0.283201	6
232R-2	35-50	1494.93	0.702988	6	0.513096	2	18.5996	16	15.5225	16	38.2569	46	0.283200	6
232R-2**	35-50	1494.93	0.703004	3	0.513093	3							0.283200	5

** Replicate analyses on separate sample dissolutions. Within run errors are reported for the last significant digit. σ = sigma internal analytical error.

CHAPTER II

23 Ma history of hydrothermal and active margin sediment supply to the eastern equatorial Pacific: Geodynamic and paleoceanographic implications

Tobias W. Höfig [a,b], Kaj Hoernle [a], Folkmar Hauff [a], and Martin Frank [a]

[a]*GEOMAR Helmholtz Centre for Ocean Research Kiel, Wischhofstr. 1-3, D-24148 Kiel, Germany*
[b]*New address: Department of Mineralogy, TU Bergakademie Freiberg, Brennhausgasse 14, D-09599 Freiberg, Germany*

in preparation

Abstract

We investigated the evolution of the Pb isotopic composition of bulk sediments from two Cocos Plate sediment cores at Deep Sea Drilling Project (DSDP) Site 495 and Ocean Drilling Program (ODP) Site 1256, encompassing the past 23 million years of depositional history. Our study is the first to characterize the Pb isotopic evolution of eastern equatorial Pacific sedimentation covering the entire tectonic pathway of the Cocos Plate from formation at the East Pacific Rise to arrival at the Central American subduction zone. A systematic trend toward more radiogenic Pb isotopic compositions from ~23 to ~6 Ma reflects a decrease in the contribution of hydrothermal particles from the East Pacific Rise and an increase in the contribution of mixed weathering products from the continental arcs of the Northern and south Central Andes as well as Mexico. Surprisingly, input from Central America did not have a significant influence on the Pb isotopic composition of the detrital fraction and of past seawater. Less radiogenic Pb isotope ratios in sediments younger than ~6–4 Ma reflect a reduction of the continental input from the South Central Volcanic Zone of the Andean Arc in favor of contributions from the Trans-Mexican Volcanic Belt as a consequence of changes of the atmospheric circulation. The eolian pathway has thus played a major role as supplier of detrital Pb over the entire Neogene and Quaternary. The delivery of hydrothermal Pb originating from the East Pacific Rise to the easternmost tropical Pacific has been a persistent feature, which is attributed to a stable central and eastern Pacific deep-water circulation.

1 Introduction

Lead (Pb) isotopes serve as a powerful tool for tracking the sources of oceanic water masses (e.g., O'Nions et al., 1978; von Blanckenburg et al., 1996; Abouchami et al., 1997; Frank et al., 1999; van de Flierdt et al., 2004; Ling et al., 2005; Haley et al., 2008) and sediments (e.g., Chow and Patterson, 1962; Jones et al., 2000; Pettke et al., 2000, 2002; Godfrey, 2002; Stancin et al., 2006; Xie and Marcantonio, 2012; Basak and Martin, 2013; Pichat et al., 2014) on different time scales. The importance of Pb isotopes as an

oceanographic tracer arises from the low mean deep-water Pb oceanic residence time of ~50 (Atlantic) to ~200–400 (Pacific) years in dissolved form (Schaule and Patterson, 1981; von Blanckenburg and Igel, 1999), being considerably shorter than the global mixing time of ~1500 years in the oceans (e.g., Broecker et al., 1982). Since there are three radiogenic Pb isotopes, they allow detailed reconstructions of complex mixing relationships between different isotopic source endmembers within the same isotopic system (reviewed by Frank, 2002; or Goldstein and Hemming, 2003). Variations in the Pb isotopic composition of different phases of marine sediments thus provide an important archive for reconstructing both changes in sediment provenance and in composition of water masses transporting the particulate or dissolved Pb through time.

In the eastern equatorial Pacific Ocean (EEP), possible sedimentary source materials include 1) tephras released from the Galápagos Hotspot and the Mexican, Central American, and Andean subduction zone volcanoes, 2) particulate matter originating from expelled hydrothermal fluids associated with areas of active submarine volcanism at the East Pacific Rise and at the Galápagos (or Cocos-Nazca) spreading centers, as well as Galápagos volcanoes, and 3) detrital (riverine and airborne) inputs derived from weathering and erosion of the surrounding active continental margins (Fig. 1). To date, only few Pb isotope studies have been carried out to shed light on the significance of these potential sources for sedimentation in the EEP. Following the pioneering work of Nakai et al. (1993), who made use of Sr-Nd isotopes on the eolian detrital fraction of Late Pleistocene EEP sediments, Jones et al. (2000) applied Pb isotopes and substantiated wind-controlled dust contribution of South American origin, which was not further constrained. Subsequently, based on statistical analysis, Sr-Nd-Pb isotopic mapping revealed that Pacific detritus of the past 5 Ma has principally been dominated by three continental components derived from Asia, North America, and Central/South America, with predominance of the latter source in the EEP east of c. 100°W (Stancin et al., 2006). Additionally, North Africa (Sahara area) and Australia could not be excluded as potential dust sources for young (≤ 25 ka) eolian sediments retrieved along ~110°W between ~7°N and ~3°S (Xie and Marcantonio, 2012). However, most recently, Pichat et al. (2014) found no significant Pb isotopic evidence for input from such distal sources in eolian-dominated bulk sediments of the same meridional transect during the past 160 ka. Instead, these authors provided unambiguous isotopic fingerprints which helped to further constrain distinct dust sources for the first time. Their data demonstrated that Late Pleistocene to Holocene equatorial dust deposition at ~110°W has been controlled by South American detrital input derived from erosion of volcanic arc segments of the central and southern Andes and has been supplied by the Southeast Trade Winds over the entire investigated period of time.

It remains to be shown how these inputs evolved on longer time scales of the past 23 million years covering major global and local climatic and tectonic changes such as the global cooling, the onset of northern hemisphere glaciation and the associated increase in wind speeds and wind transport (e.g., Rea 1994), or the northeastward movement of the Cocos Plate. In addition, it is not clear how this source-pathway system evolved in the easternmost

part of the tropical Pacific, i.e., more than 2000 km closer to Central America, an oceanic area with a most likely much stronger hemipelagic (i.e., continental shelf, riverine) influence (Rea, 1994, and references therein). Here we reconstruct the Pb isotopic evolution of bulk sediments from Deep Sea Drilling Project (DSDP) Site 495 and Ocean Drilling Program/Integrated Ocean Drilling Program (ODP/IODP) Site 1256, together covering ~23 million years of marine sedimentation on the Cocos Plate, which was formed by the break-up of the Farallon Plate ~23 Ma ago (Handschumacher, 1976). Thus, we document changes in detrital sedimentation along the entire pathway of the Cocos Plate from the spreading center at the East Pacific Rise to the Central American subduction zone. Our study provides the first continuous Pb isotope Neogene-Quaternary history of eastern equatorial Pacific sedimentation, which provides valuable insights into the long-term interaction of different sediment sources and into the extent of variations in provenance controlled by tectonic, oceanographic, and atmospheric changes. Moreover, the new Pb isotope data provide major constraints on EEP deep-water circulation through time linked to contributions of particles formed by mid-ocean ridge hydrothermal activity to marine sediments of the eastern tropical Pacific Ocean.

2 Background

2.1 Geological setting

DSDP Site 495 (12°29.8'N, 91°2.3'W) and ODP/IODP Site 1256 (6°44.2'N, 91°56.1'W) are located in the Guatemala Basin on the Cocos Plate ~700 km apart from each other (Fig. 1a). As inferred from marine magnetic anomalies, the oceanic basement at Site 495 formed 22.5–23 Ma ago (von Huene et al., 1982; Geldmacher et al., 2008, 2013) and the underlying seafloor of Site 1256 formed at ~15.2 Ma (Wilson, 1996).

The 428 m thick sediment succession at Site 495 was recovered during DSDP Leg 67 (Coulbourn et al., 1982) on a horst 22 km seaward of the Guatemala Trench axis in a water depth of 4140 m. The lower part of the Site 495 sediment column is characterized by a 251 m thick succession of Lower to Middle Miocene calcareous oozes and chalks with precipitates of Fe-Mn minerals and chert in the lower part of the section. The upper 177 m of the sediment column comprise Late Miocene to Quaternary hemipelagic mud, containing primarily diatoms and radiolarians with subordinate tephra particles and brown abyssal clays of Middle Miocene age (von Huene et al., 1982).

The 250 m thick sediment cover at Site 1256 was drilled at a water depth of 3635 m during ODP Leg 206 ~830 km to the WSW of Costa Rica (Wilson et al., 2003). The oceanic crust at Site 1256 was formed near the equator within the equatorial high-productivity zone leading to a high sedimentation rate of ~39 m/Ma in mid-Miocene times (Wilson et al., 2003; Jiang and Wise, 2007). The basal unit of the sediment section comprises 210 m of pelagic biogenic ooze, consisting of calcareous nannofossils with intercalations of diatom ooze (Wilson et al., 2003). As the site moved away from the equator, the amount of carbonate in the sediment

decreased, whereas the relative proportion of clastic material increased. Consequently, the upper unit at Site 1256 comprises 40 m of terrigenous silty clay with varying minor amounts of biogenic particles and disseminated volcanic glass shards (Wilson et al., 2003). The initiation of this terrigenously dominated sedimentation at ~5.5 Ma roughly corresponds to the Miocene-Pliocene boundary (Jiang and Wise, 2007).

Both sites have migrated toward Central America at rates of 7–9 cm/a (DeMets et al., 1990) as a result of northeastward plate motion of the Cocos Plate, which has been subducted beneath southern Mexico and Central America. The connection of plate tectonics and paleoceanographic processes in the study area is most pronouncedly evidenced by the evolution of the Central American Seaway, which formed a marine seaway linking the tropical western Atlantic and the eastern Pacific throughout most of the Cenozoic and began to close in the Early to Middle Miocene with final closure at ~4–3 Ma according to the standard model (reviewed by Molnar, 2008). This resulted from collision of NW South America (Farris et al., 2011) and the Cocos Ridge, a part of the Galápagos Hotspot track (Hoernle et al., 2002), with Central America. However, the timing of closure is still under debate in view of recent tectonic reconstructions favoring a new model, which suggests disappearance of the deep oceanic gateway by ~15 Ma (Farris et al., 2011; Montes et al., 2012a, 2012b). Most recently, Coates and Stallard (2013) have made an attempt to reconcile both scenarios of closure timing by proposing that they represent different angles of the Central American Volcanic Arc evolution, similar to the geotectonic, biogeographic, and oceanic settings developed along the present-day Indonesian Volcanic Arc.

2.2 Atmospheric circulation

The eastern equatorial Pacific has been governed by two different wind systems: the Northeast and Southeast Trade Winds (N/STW; Fig. 2a). They meet along a zonal atmospheric belt referred to as the Intertropical Convergence Zone (ITCZ; Fig. 2a), which is presently located at ~5°N on an annual average (Rea, 1994; Hovan, 1995). However, it experiences considerable latitudinal shifting (between ~4 and ~10°N; Fig. 2a) ultimately controlled by the changing seasonal vigor of atmospheric circulation and thus of the trade winds on each hemisphere, which are on average stronger in the south as a consequence of the higher pole-equator temperature gradient (e.g., Flohn, 1981; Hovan, 1995). As demonstrated by several studies (e.g., Rea, 1994; Hovan, 1995; Pettke et al., 2002; Hyeong et al., 2005), the paleo-ITCZ position above the Pacific was located considerably north of ~5°N prior to ~4 Ma (Fig. 2a) owing to a larger difference in temperature gradient between the hemispheres in the unipolar world of the Neogene (Flohn, 1981), and then migrated southward to the current location. Consequently, the studied drilling sites on the northeastward moving Cocos Plate have been affected by different wind systems through time. While Site 1256 passed the average ITCZ position at ~3 Ma, Site 495 probably already crossed the ITCZ at ~6–7 Ma and has been subject to the NTW since, as inferred from an ITCZ migration path estimate (Fig. 2b). In the study area, the wind pattern is, however, more

complex than in the westerly part of the eastern equatorial Pacific, particularly with respect to the NTW (Kessler, 2006), showing pronounced meridional patterns instead of strong latitudinal winds (see also Section 2.3).

The equatorial Pacific atmospheric circulation is weakest within the ITCZ and wind strength increases with distance from the ITCZ (Wyrtki and Kilonsky, 1984; Fig. 2a). However, despite the absence of strong winds, the ITCZ marks an area of enhanced eolian flux due to intense rainout of dust particles, thus efficiently preventing dust transfer between the hemispheres, particularly in the eastern Pacific (e.g., Rea, 1990, 1994; Hovan, 1995).

2.2 Oceanic circulation

The trade wind belts drive the oceanic surface circulation in the eastern equatorial Pacific. They force the equatorial waters in each hemisphere to flow westward (Fig. 2c), establishing the North Equatorial Current (NEC; north of the ITCZ) and the South Equatorial Current (SEC; south of the ITCZ), respectively (reviewed by Kessler, 2006). Between those, the North Equatorial Countercurrent (NECC) flows eastward in the zone of weak winds (i.e., the ITCZ; Fig. 2c). The SEC is fed by the Humboldt Current (Kessler, 2006), originating from offshore Chile and deflected northwestward by the STW (Garcia, 1994), which form close to the southern part of the Central Andes and are directed toward the equator (Fig. 1b). The NEC advects eastern Pacific surface water masses north of ~10°N (Fig. 2c). However, the actual zonal westward surface flow only starts west of ~120°W, since the easternmost tropical Pacific (i.e., the study area) is characterized by a more complex circulation pattern due to the collapse of the strictly zonal wind system and the establishment of weaker meridional (N-S directed) winds east of 110°W, which result in a gyre-like surface circulation and partially seasonally varying wind intensities (Kessler, 2006). This gives rise to a complex surface water circulation system in the Guatemala Basin, transporting water masses rather along N-S routes (Kessler, 2006), which contrasts with the fairly simple SEC current system operating south of ~5°N (Fig. 2c). There are two gyre-like surface water systems north of ~5°N, exchanging water masses and feeding the incoming NECC, which heads to the east toward southern Central America (Fig. 2c).

The abyssal circulation in the present-day central and eastern equatorial Pacific is most likely characterized by latitudinal deep water flow heading east toward the East Pacific Rise (reviewed by Lonsdale, 1976). It splits into two major bottom currents, apparently crossing the East Pacific Rise along transform faults just north of the Galápagos triple junction and at ~8°N (Fig. 2c). In addition, some of the deep water reservoir of the Guatemala Basin may be filled by diffuse overflow from the Pacific Basin across the ridge crest of the East Pacific Rise (Lonsdale, 1976). A second major flow direction is reflected by a southward bottom current originating offshore southern Mexico and moving along the eastern ridge flank of the East Pacific Rise (Lyle, 1992; Fig. 2c).

3 Sample preparation and analytical methods

The present study used 31 samples covering the entire sediment column drilled at Site 1256 and 16 samples from Site 495. These samples were obtained from the Gulf Coast Repository at Texas A&M University (College Station, Texas, USA). Distinct tephra layers were avoided during sampling in order to understand the long-term detrital source variations, not being obscured by short-term volcanic fallout derived from explosive events. Details of sample intervals, inferred ages, and lithology of the studied samples are provided in Table 1.

At GEOMAR, all 47 bulk sediment samples, consisting of both seawater- (e.g., calcareous ooze) and continent-derived (e.g., terrigenous clay) components in varying proportions, were dried over 48 hours at 50 °C. Afterwards, the dry sediment samples were filled into small glass tubes, each of which contained between 0.8 and 1.2 g of sediment. No further grinding of the sediments was performed. Five of the bulk samples of Site 1256 with weights of 1.5 to 2.6 g were subject to a leaching process in order to obtain both the detrital and the seawater-derived Pb isotope fractions contained in Fe-Mn coatings of the particles. The total blanks for the leaching procedure of 1.6 ng were relatively high but can nevertheless be considered negligible in the light of the total amount of Pb in the samples (1840 to 31209 ng Pb).

The leaching process followed the principles outlined in Gutjahr et al. (2007), modified by Stumpf et al. (2010), which encompassed a two-day procedure including several shaking and centrifugation steps. Firstly, carbonate was removed in 20 ml of a 15%-acetic acid/1M-Na acetate buffer solution (pH of ~4.1 for 1 h) followed by a triple rinse with deionized water followed by addition of another 10 ml of the same acetate solution together with 10 ml of MQ water for overnight shaking (125 rot/min). Subsequently, a 0.05 M-hydroxylamine hydrochloride/15%-acetic acid solution buffered to pH of 3.6 with NaOH was added to dissolve the ferromanganese (Fe-Mn) coatings. After shaking for 1 h, the supernatant was pipetted into 30 ml Teflon® vials for further ion-chromatographic separation. The residual detrital material was then dried over 48 hours at 50 °C. The bulk samples and the residues of the leaching process were dissolved in a 4:1 HF-HNO3 mixture at 150 °C for 48 hours. The ion-chromatographic separation and purification of Pb was conducted according to the procedures outlined in Hoernle et al. (2008).

Pb (double spike, DS) isotope analyses were obtained by thermal ionization mass spectrometry (TIMS) at GEOMAR on a Finnigan MAT 262 RPQ2+, operating in static multi-collection mode. Within run errors are reported as $2\sigma / \sqrt{n-1}$ (n = number of scans passing the outlier test) and all external errors, such as the reproducibility of standards, are shown as 2σ of the mean (Tab. 2). Pb isotope ratios were determined applying the Pb DS technique described in Hoernle et al. (2011). The long-term average double-spike corrected NBS981 values are $^{206}Pb/^{204}Pb = 16.9420 \pm 0.0030$, $^{207}Pb/^{204}Pb = 15.4998 \pm 0.0029$, $^{208}Pb/^{204}Pb = 36.7256 \pm 0.0072$, $^{207}Pb/^{206}Pb = 0.91487 \pm 0.00006$, $^{208}Pb/^{206}Pb = 2.16772 \pm 0.00010$ (n = 139) over the course of the project (2006–2012). Duplicate analyses of samples 206-1256B-3H-7, 23-24 cm, 206-1256B-24X-3, 79-81 cm, and 67-495-41R-6, 53-54 cm were identical within the external two sigma errors of the standard values (Tab. 2). Total chemistry blanks

are considered negligible as they typically ranged from 6 to 20 pg Pb, with one exception of 75 pg Pb.

Initial Pb isotope ratios were calculated using the algorithms outlined in Faure and Mensing (2005). The required Pb, Th, and U concentrations of Site 1256 sediments were obtained by inductively coupled plasma mass spectrometry (ICP-MS) on a ThermoFinnigan Element2 at the Department of Geosciences, University of Bremen. Sample digest and analyte solutions were prepared following the procedures outlined in Geldmacher et al. (2008). Pb, Th, and U concentrations for Site 495 sediments are from Patino et al. (2000).

4 Results

The initial Pb isotopic compositions of the bulk sediments of Site 495 ($^{206}Pb/^{204}Pb_{in}$ = 18.28–18.76; $^{207}Pb/^{204}Pb_{in}$ = 15.51–15.63; $^{208}Pb/^{204}Pb_{in}$ = 37.93–38.62) were on average somewhat less radiogenic than those of Site 1256 ($^{206}Pb/^{204}Pb_{in}$ = 18.58–18.80; $^{207}Pb/^{204}Pb_{in}$ = 15.56–15.63; $^{208}Pb/^{204}Pb_{in}$ = 38.34–38.71; see Tab. 2), but the two records generally overlap, thus essentially forming one remarkably consistent time series (Fig. 3) despite significant changes in sediment type. The bulk sediment Pb isotopic compositions increased continuously from ~22.5 Ma at Site 495 and from ~13.4 Ma at Site 1256 to maximum values of $^{206}Pb/^{204}Pb$ and $^{207}Pb/^{204}Pb$ at ~4 Ma, whereas $^{208}Pb/^{204}Pb$ apparently reached its maximum somewhat earlier at ~6 Ma (Fig. 3) Thereafter, a higher degree of Pb isotopic variability prevailed (Fig. 3), particularly between ~6 and ~2.8 Ma. The Pb isotope ratios have systematically become less radiogenic since ~2.8 Ma (Fig. 3). At ~1.8 Ma, they finally reached eastern equatorial Pacific seawater values (Fig. 3), as recorded by a Fe-Mn crust (GMAT 14D; Frank et al., 1999) from the northern Cocos Plate seafloor at a distance of ~1100 and ~2000 km, respectively, to the studied drill sites (Fig. 1a). Although being slightly offset to less radiogenic values prior to ~1.8 Ma, the seawater Pb isotopic evolution reflected by this Fe-Mn crust over the past ~7 million years shows a very similar variability in comparison to our bulk Pb isotopic composition (Fig. 3) as expected from the very short mean oceanic residence time of Pb, which is particularly low in the study area, where particle fluxes are high resulting in residence times of only ~5–10 years (Henderson and Maier-Reimer, 2002).

The Pb isotopic compositions obtained from both residues (reflecting detrital input) and leachates (reflecting past seawater) of five samples of Site 1256 closely follow the temporal evolution recorded by the bulk sediments (Fig. 3), which clearly indicates the same controlling factors. While $^{207}Pb/^{204}Pb$ generally shows no significant differences between the different sedimentary phases at all, the $^{206}Pb/^{204}Pb$ and $^{208}Pb/^{204}Pb$ signatures of the residues have been more radiogenic than the seawater-derived leachate compositions. For the samples older than ~5.5 Ma, the composition of which was dominated by biogenic oozes (Wilson et al., 2003), the residues were generally more radiogenic than the bulk Pb isotopic signal (Fig. 3), whereas they were rather less radiogenic than or identical to bulk Pb thereafter, referring to the section of the core dominated by terrigenous sediments (Wilson et al., 2003). Furthermore, after 6 Ma, the seawater Pb isotopic signal obtained from Site 1256 was similar to that of Fe-

Mn crust GMAT 14D, whereas the sediment leachates were more radiogenic prior to 6 Ma documenting a distinct water mass difference between the two locations.

5 Discussion

5.1 Identification of endmembers for eastern equatorial Pacific sediment compositions

The Pb isotope ratios for both sites are highly positively correlated (R^2 = 0.95 on uranogenic and R^2 = 0.98 on thorogenic Pb isotope diagrams; Figs. 4a and b, respectively) documenting well-defined mixing of two components: a depleted component with unradiogenic Pb and an enriched component with more radiogenic Pb isotopic composition. Notably, the mixing array formed by Site 495 and 1256 bulk sediments also includes the Fe-Mn crust GMAT 14D (Fig. 4), suggesting the same endmembers influencing the deep waters, which GMAT 14D has grown from.

The Pb isotopic space displays that basement formed at the Galápagos Spreading Center (GSC) can be ruled out as unradiogenic endmember, since it is significantly offset from the mixing array of our data on the uranogenic diagram (Fig. 4a). Thus, its contribution to the Pb supply is considered to be insignificant over time. It is, however, also clear that Cocos Plate mid-ocean ridge basalt (MORB) basement formed at the East Pacific Rise (EPR) represents the unradiogenic endmember of the two-component mixing line (Fig. 4). In this regard, the combined record points to a depleted endmember composition similar to the average Site 495/499 MORB basement, which is less radiogenic than Site 1256 MORB (Fig. 4). Therefore, it is evident that the dissolved and particulate deep water Pb isotopic composition of the Guatemala Basin has overall been strongly affected by contributions from a MORB source with an on average depleted composition over ~23 million years of sedimentation. The variable influence of the isotopically enriched Galápagos plume on the EPR spreading system lasting from ~22–11 Ma (Geldmacher et al., 2013) thus left no fingerprint on the overall unradiogenic Pb supply during the Neogene. Since only high-temperature fluids can leach major amounts of Pb from MORB oceanic crust, hydrothermal activity at the spreading center is an important mechanism for transferring dissolved Pb into the water column (e.g., Chen et al., 1986; Barrett et al., 1987). It is thus suggested that hydrothermal fluids from the underlying and nearby EPR oceanic crust were the ultimate source of the depleted endmember in the sedimentary successions (see Section 5.2 for discussion of the transport pathways).

Determining the enriched component of the sedimentary Pb isotopic mixing array is much more challenging. A number of volcanic and continental sources with radiogenic Pb isotopic signatures may have contributed to the depositional record (see Section A.1, Appendix II, and Tab. A.1 of the electronic appendix for databases of potential terrigenous sources). As demonstrated by Stancin et al. (2006), distant northern hemisphere continental rocks of central Asia and North America could have generally accounted for detrital input to the eastern equatorial Pacific. In the surroundings of the study area and to the south of it (see Fig. 1), apart from the continental basement of northern Central America (Chortís Block), all other

potential sources are volcanic in origin, representing either oceanic igneous complexes (Galápagos Islands (GI), including Cocos Island and associated aseismic ridges and seamounts; uplifted Caribbean Large Igneous Province (CLIP) fragments from Central and northern South America) or continental arcs (Trans-Mexican Volcanic Belt, Central American Volcanic Arc (CAVA), Andean Arc). The depositional impact of explosive volcanism on the Pb isotopic record is considered to be insignificant for the present study, since sampling of discrete tephra layers was avoided and disseminated tephra particles are present throughout the two studied sediment cores in minor to trace amounts only (von Huene et al., 1982; Wilson et al., 2003), accounting for, e.g., at maximum ~1–2 vol% of the terrigenous material at Site 1256 (Wilson et al., 2003). Thus, deposition of volcanic arc material has predominantly been associated with erosion and subsequent transport of detrital material to the studied sites. Supply of ocean island basalt-type Pb from submarine parts of the Galápagos hotspot track may have originated from hydrothermal activity.

However, as reflected by the Pb isotope diagrams, neither the on- and offshore volcanic complexes of the CLIP and GI, respectively, nor the CAVA can serve as the radiogenic endmember, because their Pb isotopic compositions are generally significantly beneath the mixing line formed by the bulk sediment data from the two cores. Specifically, they largely have lower $^{207}Pb/^{204}Pb$ and $^{208}Pb/^{204}Pb$ for a given $^{206}Pb/^{204}Pb$ isotope ratio (Fig. 4). This is likewise evident for the plotted Guatemala basement composition, representing a sampled part of the pre-Cenozoic Chortís Block (Heydolph et al., 2012), which essentially forms the continental basement of Central America regionally cropping out from Guatemala to Nicaragua, mainly behind the CAVA front (e.g., Rogers et al., 2007). Therefore, the geologic units most proximal to the studied sites of sedimentation are no suitable radiogenic endmember.

The eastern Pacific ITCZ represents a marked barrier for Asian dust (e.g., Rea, 1994; Jones et al., 2000; Pettke et al., 2000, 2002; Stancin et al., 2006). However, taking into account the northward migration of the studied sites and their apparent crossing of the ITCZ axis between ~6 Ma (Site 495) and ~3 Ma (Site 1256) (Fig. 2b), they have been subject to atmospheric circulation of the Northern Hemisphere thereafter. Therefore, contributions of continental sources on the Northern Hemisphere to the detrital sedimentation in the study area have been possible. Nevertheless, both highly radiogenic average central Asian dust (Pettke et al., 2000) and western North American hemipelagic clay (Stancin et al., 2006) overall deviate from the continuation of the sediment mixing line on Pb isotope diagrams (Fig. 4). Thus, they cannot serve as the radiogenic endmember. However, the main argument against a significant impact of these two source areas comes from the temporal trend of the sedimentary Pb isotopic record, showing highly fluctuating and decreasing values after 6 Ma (Fig. 3). In fact, the opposite pattern would be expected north of the ITCZ in view of the highly radiogenic composition of both distal continental Northern Hemisphere sources.

The Andean Arc has to be taken into account as potential radiogenic endmember as well, given that the studied sites have mostly been located south of the ITCZ during their NE migration (Figs. 2a/b). The Andean Arc, being Lower Jurassic to Quaternary in age, forms the

western continental margin of South America and has been grouped into four volcanic domains, referred to as Northern Volcanic Zone (NVZ: 5°N–2°S), Central Volcanic Zone (CVZ: 14.5°–27.5°S), Southern Volcanic Zone (SVZ: 33°–46°S), and Austral Volcanic Zone (AVZ: 49°–55°S) (reviewed by Stern, 2004). Applying the literature-based compositional subdivision of the CVZ (Faure, 2001, and references therein) used by Pichat et al. (2014), we have additionally subdivided the CVZ into three parts, termed the North (14.5°–19.5°S), Transitional (20.5°–21.5°S), and South CVZ (22°–27.5°S). A complex pattern is revealed through plotting the data fields and/or average values of all these Andean Arc segments in the Pb isotopic space. The AVZ can be excluded as radiogenic endmember for the sediments, since its average composition is too unradiogenic (Fig. 4). The SVZ is not appropriate either, as it is characterized by higher uranogenic and thorogenic ratios for a given $^{206}Pb/^{204}Pb$ close to the sediment mixing line (Fig. 4). Similarly, the isotopically variable North CVZ cannot account for the enriched compositions either given that they plot exclusively to the left of the sediment array (Fig. 4). The transitional sub-domain of the CVZ compositionally crosscuts the mixing array (not displayed) and partly overlaps with the SVZ and South CVZ data fields, however, its average Pb isotopic composition is too unradiogenic and, in addition, the uranogenic isotope ratio is considerably above that of the sediments (Fig. 4). Thus, it is unlikely that the comparatively small area of the Transitional CVZ has significantly contributed to the sedimentary Pb isotopic record over the past ~23 million years.

In contrast, the more extensive and volumetrically much larger South CVZ, geographically located next to the Transitional CVZ (see Fig. 1b), has sufficiently radiogenic $^{207}Pb/^{204}Pb$ and $^{208}Pb/^{204}Pb$ ratios to represent a significant radiogenic endmember for the Pb isotopic sediment array (Fig. 4). The South CVZ data field covers a substantial part of the sediment record and the radiogenic end of the sediment mixing line points to a composition very similar to that of the average South CVZ (Fig. 4). However, this cannot fully explain the entire mixing pattern of the isotopic sediment record, since the radiogenic end of the mixing lines differs between the uranogenic and thorogenic diagrams in terms of its proximity to the average composition of the South CVZ in that it deviates toward lower values to some extent on the thorogenic plot (Fig. 4). Taking additionally into account the inflection of the temporal isotopic trend after 6 Ma (Fig. 3), which is illustrated by shifts to less radiogenic compositions along the linear trend revealed on the Pb isotope diagrams (Fig. 4), it is unlikely that this solely mirrors a decreasing influence of the South CVZ compared to the unradiogenic endmember given the increasing distance to the EPR over time. We thus interpret these fluctuations to reflect a minor influence of other radiogenic Pb sources. An admixture of Pb from the NVZ most likely gave rise to the deflection of the trend to less radiogenic values in thorogenic space relative to the average South CVZ composition (Fig. 4b). The combined average composition of NVZ and South CVZ thus is the most likely endmember on the thorogenic Pb diagram. However, the impact of the NVZ on $^{207}Pb/^{204}Pb$ is not equally obvious, since the South CVZ – NVZ composition falls somewhat beneath the mixing line (Fig. 4a). This small-scale variation between the two plots likely reflects large age differences between the pre-Andean basement of the NVZ and CVZ, respectively. The NVZ basement

mainly consists of accreted Cretaceous mafic crustal slivers of the CLIP (e.g., Kerr et al., 1997) and Late Paleozoic to Early Mesozoic rock units (Stern, 2004, and references therein). In contrast, Proterozoic to Paleozoic crust forms the basement of the CVZ (Stern, 2004, and references therein), which has been demonstrated to notably affect the Pb isotopic composition of central Andean volcanic rocks (e.g., Wörner et al., 1992). It is therefore suggested that a greater abundance of radiogenic ^{207}Pb has been contributed to the Pacific from the South CVZ compared to NVZ, given the significantly older pre-Andean basement underlying the South CVZ, enabling enhanced generation of ^{207}Pb through time. This possibly explains the lack of a more pronounced NVZ impact on the uranogenic Pb isotopic mixing line (Fig. 4a). Besides, the Pb-Pb isotopic comparison reveals that the NVZ can be excluded as single radiogenic Pb source for the sediments, since it shows both lower $^{207}Pb/^{204}Pb$ and $^{208}Pb/^{204}Pb$ for a given $^{206}Pb/^{204}Pb$ isotope ratio with an average composition considerably different from the mixing trend (Fig. 4). The same conclusion can be applied to the more northerly located (between 18°N and 21.5°N) Trans-Mexican Volcanic Belt (TMVB) being too unradiogenic on average to serve as the enriched endmember. However, the combined average Pb isotopic composition of the South CVZ and the TMVB almost exactly lies on the 495-1256 linear regression line on both Pb isotope diagrams, showing a less radiogenic Pb isotopic composition compared to the South CVZ – NVZ endmember (Fig. 4). The impact of the TMVB on the detrital Pb input has been time-dependent, since it has mainly exerted influence on the sedimentary Pb isotopic composition after 6 Ma. This is expressed by Site 495 sediments of this time forming a cluster compositionally consistent with the South CVZ – TMVB mixed endmember. Moreover, the youngest Site 1256 samples (< 1.8 Ma) obtained are even less radiogenic than the average TMVB – South CVZ composition, plotting in the field of the EEP Fe-Mn crust GMAT 14D (Fig. 4). This, in turn, indicates diminished influence of the South CVZ on marine sedimentation in the EEP at certain ages younger than 6 Ma. In this regard, it is evident that virtually all time-dependent changes of the radiogenic Pb isotopic composition of the sediments (Fig. 2) are expressed as linear shifts along the mixing array (Fig. 4). In conclusion, it is thus strongly suggested that sedimentation on the Cocos Plate seafloor has taken place in a water column supplied by unradiogenic Pb from the EPR-related Cocos Plate basement and radiogenic Pb mainly derived from the continental arc of the southern Central Andes with time-dependent minor admixtures from the continental arcs of Mexico and the Northern Andes.

5.2 Constraining transport pathways of Pb to the studied sites of deposition

The majority of the metals leached from the oceanic crust and precipitated at spreading center high-temperature hydrothermal vents in contact with seawater is deposited close to the sites of fluid injection (Hannington et al., 2013, and references therein). However, a significant amount of the metalliferous matter is entrained in buoyant plumes, which may rise hundreds of meters above the venting sites (e.g., Lupton, 1995). During this ascent, they increasingly mix with the surrounding seawater, while being transformed to non-buoyant

plumes that may then expand laterally from the ridge crest over considerable distances of up to thousands of kilometers (e.g., Edmond et al., 1982; Lupton, 1995; Lupton et al., 2004). The hydrothermal plumes largely consist of Fe-oxyhydroxide particles and dissolved metals derived from disaggregation of sulfide minerals (Hannington et al., 2013, and references therein), which is also reflected by the composition of the resulting metalliferous sediments (e.g., Barrett et al., 1987). The Fe-oxyhydroxides continuously scavenge dissolved metals from the ambient water, while being transported in the non-buoyant plumes (Gurvich, 2006, and references therein). However, due to mixing with the surrounding seawater, the dilution of the hydrothermal signal increases with time (Gurvich, 2006, and references therein). Based on Pb isotopes, Barrett et al. (1987) demonstrated mid-ocean ridge (MOR) hydrothermal Pb to be present in minor amounts in the metalliferous component of Pacific Basin sediments at a distance of ~1000 km to the EPR at ~20°S. Such a distal advection of MOR hydrothermal Pb is also observed in the present study given the persistent EPR basement Pb isotopic signal affecting the non-metalliferous bulk sediments of the studied sites over time, even at a present-day distance of ~1300 km (Site 1256) and ~1500 km (Site 495), respectively, to the EPR ridge crest (Fig. 1a). Our data thus strongly suggest that hydrothermal particulate Pb must have continuously been transported to the core sites of our study by eastward-flowing deep waters from the EPR. It is therefore concluded that bottom currents, similar to those crossing the present-day EPR from the west (Lonsdale, 1976), most likely also transported the hydrothermal material to the study area in the past. This implies that eastward-deflected hydrothermal plumes must have represented a continuous phenomenon in eastern equatorial Pacific deep waters since the very beginning of marine sedimentation on the Cocos Plate at ~23 Ma. Our interpretation of eastward advection and deposition of MOR hydrothermal Pb is consistent with contour maps of metalliferous sediment (Boström and Peterson, 1969), which were later confirmed by Lyle (1992), showing northeastward extending sediment lobes in the Guatemala Basin with decreasing proportions of metalliferous matter as the distance to the EPR increases. Notably, it is inferred from the results of Pichat et al. (2014) that MOR hydrothermal Pb is insignificant for the Pb isotopic record of Site 849 sediments. This may be attributed to the deep-water flow pattern in the eastern equatorial Pacific described above, advecting hydrothermal Pb eastward. This implies that locations to the west of the EPR, such as Site 849 (Fig. 1a) do not receive any significant EPR basement signal.

While the unradiogenic Pb endmember of the sedimentary mixing array thus originated from the deep waters, the radiogenic Pb endmember is considered to have originally been derived from surface waters sourced by detrital input from a continental arc source. This supply has been dominated by the Andean South Central Volcanic Zone (CVZ) with minor contributions from both the Northern Volcanic Zone (NVZ) of the Andes and the Trans-Mexican Volcanic Belt (TMVB). At least for the latest Quaternary, the South CVZ source has served as the radiogenic endmember at more western equatorial ODP Site 849 (Fig. 1a), too, as shown by Pichat et al. (2014). This site has always been located south of the ITCZ, i.e., within the region governed by the Southeast Trade Winds (Fig. 2a). Today, it is located at ~110°W, hence, approximately 2000 km away from the next continental area and it has never

been located closer to any continental landmass, based on its paleo-track (Figs. 1a, 2a). Thus, Site 849 has always been remote from any hemipelagic influence, assumed to be important further east (Rea, 1994, and references therein). Indeed, Hovan (1995) demonstrated that EEP sites drilled along 110°W have been controlled by pelagic sedimentation, i.e., eolian supply has prevailed over time. In view of this result, Pichat et al. (2014) have invoked the Southeast Trade Winds (STW) as detrital Pb supplier for Site 849. Since Sites 495 and 1256 have revealed significant supply from the same radiogenic endmember over the entire Neogene and Quaternary, it is proposed that they have equally shared the direct impact of the STW transporting continental arc Pb from the South CVZ, at least as long as they were located within the ITCZ or south of it (see Section 5.3). Input via the STW is reasonable taking into account the low mean seawater residence time of Pb in the study area and the distance between the studied sites and the South CVZ source of ~4200–4600 km (Fig. 1b), ascribing a minor role to the South Equatorial ocean circulation for detrital Pb delivery from this fairly remote Andean Arc segment.

The origin of the atmospheric path of the STW is today located between 20°S and 30°S (Fig. 1b) in the coastal region occupied by the Atacama Desert, presently yielding the highest dust production rates in South America (e.g., Ginoux et al., 2012). Strong south-central Andean aridity commenced during the Early to Middle Miocene, coincident with orogenic uplift in this area (e.g., Alpers and Brimhall, 1988; Dunai et al., 2005; Rech et al., 2006). The transition of semiarid to extremely arid conditions in the region of the present-day Atacama Desert most likely took place between ~15 and ~25 Ma (e.g., Dunai et al., 2005; Rech et al., 2006, 2010; Evenstar et al., 2009). An Early Miocene onset of arid conditions in the southern Central Andes is consistent with our data, suggesting the onset of an important eolian dust contribution from this source area to the studied EEP sediment record at that time. Long-term aridity in the area of the South CVZ also explains why this source has predominated over other possible Andean sources during ~23 million years of eolian sedimentation in the EEP. It additionally suggests that the Southeast Trade Winds have consistently blown from essentially the same latitudes to the investigated area over time. The common eolian contribution to the study area also explains the reason for the insignificance of the Austral Volcanic Zone for the sedimentary Pb isotopic record, since this southernmost Andean arc segment has been located within the zone of persistent westerly winds (Garcia, 1994). The results of the present study also reveal that the Neogene-Quaternary sedimentation in the Guatemala Basin lacks any significant contribution of detrital Pb from the Southern Volcanic Zone (SVZ; see Section 5.1), in contrast to the results of Pichat et al. (2014), who demonstrated that the SVZ serves as the unradiogenic endmember for Site 849 bulk sediments, resulting from shifting wind patterns between glacials and interglacials in the Late Pleistocene southern South America. We assume that either such fluctuation did not play a major role in the pre-Quaternary eastern equatorial Pacific or the lower temporal resolution of our study does not allowed detecting provenance changes on a scale of tens of thousands of years, particularly in the Quaternary.

At present, northwestern South America, i.e., the region occupied by the Northern Volcanic Zone (NVZ) is characterized by high annual precipitation rates, leading to tropical climate with rainforests and subordinate savanna habitats at lower and temperate conditions at higher altitudes (e.g., Andriessen et al., 1993; Garcia, 1994). This gives rise to intense mass wasting to the trench of the Andean subduction zone in this area (Stern, 2004, and references therein). Both faunal and vegetational reconstructions have yielded similar climatic conditions throughout the Neogene and the Pliocene with mainly tropical forests and minor woodland savannas (reviewed and/or reconstructed by Webb, 1978; Janis, 1993; Pound et al., 2011, 2012). Eolian Pb input from the Northern Andes is unlikely, since there is a strong negative correlation of the humidity of an area and its potential to emit dust to the atmosphere (Rea, 1994, and references therein). It is therefore suggested that the Northern Andean Pb component may have principally been transported by pronounced continental runoff to the eastern equatorial Pacific and has then been advected by oceanic surface streams within the westward heading South Equatorial Current system toward the studied sites. The main uplift phase of the Northern Andes, which corresponds to the Northern Volcanic Zone, began after ~12 Ma (e.g., Gregory-Wodzicki, 2000; Hoorn et al., 2010). Milliman and Syvitski (1992) stressed that smaller mountainous rivers of active plate margins may supply greater proportions of their sediment loads compared to large streams straight to the ocean. However, a major riverine pathway may additionally have existed through the possible connection of the widespread proto-Amazon river and wetland system to the Pacific along the southern part of the Northern Andes (reviewed by Hovikoski et al., 2010), prior to establishment of the Amazon drainage toward the Atlantic between 10 and 12 Ma (Dobson et al., 2001; Figueiredo et al., 2009), but this is still under debate.

The formation of the Trans-Mexican Volcanic Belt (TMVB) began at ~22 Ma upon Upper Cretaceous to Oligocene subduction-related igneous complexes, which are, in turn, underlain by a Precambrian to Mesozoic terrane assemblage (Ferrari et al., 2012, and references therein). During the Early Miocene to Quaternary TMVB evolution, present-day Mexico has been subject to different climates. As shown by paleoecological studies, a rather humid climate of the Early to Middle Miocene, promoting tropical woodlands and forests, gradually transformed into a semiarid setting with rainy seasons, hosting subtropical savannas during the Latest Miocene and Pliocene (e.g., Webb, 1977; Janis, 1993; Pound et al., 2011, 2012; Eronen et al., 2012). Therefore, a mixture of riverine and eolian Pb supply to the eastern equatorial Pacific has been likely, presumably favoring an increasing contribution of eolian dust with time, in view of the declining average humidity in the area. Once the southward shifting paleo-ITCZ reached the latitudes of the study area prior to the Late Miocene (Hyeong et al., 2005; see Figs. 2a/b), zonal and meridional winds within the Northeast Trade Wind belt may have been atmospheric suppliers of a TMVB Pb component. The modern gyre-like oceanic surface circulation of the easternmost tropical Pacific has likely led to ubiquitous distribution of TMVB material within the Guatemala Basin. Mixing of different water masses may also dominate the present deep-water circulation as well, given the southward lobe of terrigenous material obviously entraining detritus from the Mexican continental slope (Lyle,

1992), which may subsequently be transported by eastward bottom flows to the studied sites of sedimentation (see Section 5.3).

5.3 Major drivers controlling Pb deposition in the Guatemala Basin through time

It has been shown that various pathways have supplied unradiogenic and radiogenic Pb components to the eastern equatorial Pacific over time. Different sources of Pb have interacted through these pathways and the relative importance of each provenance has apparently fluctuated during the examined period (see Section 5.1). It is thus concluded that tectonic, atmospheric, and/or oceanographic changes have controlled Pb input from the different isotopic endmembers.

First of all, the temporal evolution of Pb input into the Guatemala Basin (Fig. 3) has been a function of the distance to the East Pacific Rise that is driven by the tectonic movement of the Cocos Plate away from the spreading center, where the basement of the studied sites was formed, toward the subduction zone trenches of south Mexico and Central America. This migration has given rise to increasing inputs of the radiogenic endmember derived from the surrounding continental areas. As shown by Barrett et al. (1987) on metalliferous sediments, the Pb isotopic signal of the ambient seawater increases with distance from the spreading center, since gradually more of the non-hydrothermal Pb is taken up by the metalliferous matter. Such scavenging, in turn, results in dilution and weakening of the MOR hydrothermal isotopic signal. This mechanism provides the explanation for the increasing contributions of the radiogenic signal in Site 1256 leachate samples of the present study, representing the authigenic seawater-derived component of the record (including Fe-oxyhydroxide particles), concurrently to the corresponding residue samples. In addition, calcareous ooze, accumulated in high amounts during the onset of sedimentation at both sites studied (see Section 2.1), may have acquired a significant proportion of the continental Pb signal by scavenging of dissolved Pb from seawater.

However, the particulate terrigenous Pb has likely served as the major carrier of the continental arc signal from the South CVZ and NVZ, taking into account that the increasingly radiogenic supply continued even after the abrupt drop of the carbonate mass accumulation rates at ~11 Ma (Jiang and Wise, 2007). The onset of a significant increase in terrigenous mass accumulation rate (TMAR), which lasted for ~4 million years at Site 1256 (e.g., Jiang and Wise, 2007; Fig. 5b), roughly coincided with the carbonate decrease and correlated positively with an almost linear change in the Pb isotopic composition toward more radiogenic compositions between ~10 and ~6 Ma (Figs. 5a/b). As both Site 1256 and Site 495 were located south of the ITCZ, the Late Miocene increase in TMAR, which is similarly evident at other Guatemala Basin drilling sites (e.g., Site 845; Fig. 5c; Farrell et al., 1995), may have reflected a strengthening of the Southeast Trade Winds (and probably of the associated South Equatorial Current). This has been demonstrated by Hovan (1995) based on eolian sediment records of the 110°W drilling sites, which revealed the coarsest eolian dust grain sizes between ~8 and ~5 Ma. This interpretation has recently been supported by a

modeling study of McGee et al. (2010), who invoked the intensity of winds as a key driver of variations in dust emissions in the area. The eolian-controlled TMARs at Sites 852 and 853 (Farrell et al., 1995; Hovan, 1995) also increased and showed, respectively, the highest values between ~8 and ~5 Ma (Figs. 5d/e). Subsequently, a decline in the TMAR-driven terrigenous sedimentation at Site 1256 occurred and lower values between 0.4 and 0.5 g/cm^2 ka were maintained from ~5 to ~2 Ma with a slightly enhanced accumulation around 3 Ma (Fig. 5b). Decreasing values and the establishment of a comparatively low level of terrigenous deposition between ~6 and ~2 Ma exactly coincided with the timing of the inflection of the Pb isotopic trend at our study sites (Figs. 5a/b).

This pattern may also reflect a gradual weakening of the STW commencing at ~5–4 Ma (Hovan, 1995) followed by the time when Site 1256 passed the Intertropical Convergence Zone (ITCZ). The slight increase in TMAR at ~3–3.5 Ma possibly marked the time of crossing the ITCZ axis (Figs. 2a/b) causing enhanced deposition of aerosol particles (see Section 2.2) from different sources. Thus, the presence of two contrasting atmospheric and oceanic circulation systems supplying Pb from both hemispheres, is suggested to have caused the variable pattern in the vicinity of the ITCZ axis, favoring either the continental arc source of the Southern Hemisphere (South CVZ and subordinate NVZ) or allowing the Northern Hemisphere TMVB to be an important detrital sedimentary supply area. This suggests the first obvious influence of the TMVB on the Pb isotopic record at both sites studied, since it is assumed that Site 495 already entered and crossed the ITCZ between ~6 and ~7 Ma (Fig. 2b), marking the cessation of the previous isotopic trend at this location (Fig. 3). The particular influence of the TMVB for Site 495 thereafter is unclear, as these sediments show Pb isotopic compositions fairly similar to the combined South CVZ – TMVB composition (Fig. 4) in both Pb isotopic sediment core records.

After ~2 Ma, the TMAR at Site 1256 increased again, reaching the highest values of the entire terrigenous depositional record (Fig. 5b). Despite that, the Pb isotopic composition continued its trend with a further decrease to values similar to the more northerly located Fe-Mn crust GMAT 14D (Figs. 3, 5a). We interpret this apparent contradiction to reflect the ultimate establishment of the radiogenic endmember composition consisting of both the South CVZ and the TMVB. Therefore, the increasing terrigenous deposition was most likely associated with an increased supply of radiogenic Pb from this mixed endmember, which in turn implies an enhanced input from Mexico to the studied sites as reflected by the shift to less radiogenic values along the mixing array in Pb-Pb isotopic space (Fig. 4). This is not surprising, given that the Sites 495 and 1256 have been north of the average ITCZ position after ~6 Ma (495) and ~2 Ma (1256). It is suggested that the considerable increase in TMAR at Site 1256 resulted from entering of the gyre-like oceanic surface circulation induced by the North Equatorial Countercurrent, which seems to efficiently distribute terrigenous material within the Guatemala Basin, leading to higher accumulation rates within the basin. A likewise significant increase in TMAR took also place at more northerly located Guatemala Basin Site 845 (Fig. 5c). However, there, the increase started about 1 Ma earlier during a time, when Site 845 was already located far north of the ITCZ axis. Therefore, the enhanced TMAR was not

related to the commencing exposure of Site 845 to Northern Hemisphere circulation. It is thus proposed that the significant increase of Site 845 terrigenous accumulation at ~2.8 Ma reflected the initiation of the oceanic surface gyre in the easternmost equatorial Pacific. The similarly enhanced terrigenous deposition at Site 1256 after ~1.8 Ma was thus most likely not related to stronger Northeast Trade Winds, as supposed by Wilson et al. (2003), since such an increase is not reflected by eolian-dominated Pacific Basin Site 853 (Fig. 5e), located north of the ITCZ since ~4 Ma and today at a latitude similar to Site 1256 (Fig. 2b). To conclude, it has thus been demonstrated that the first order driving factor of terrigenous sedimentation has been plate tectonic movement onto which effects of changes in atmospheric and/or oceanic circulation have been superimposed over time.

Continued input from the South CVZ is interpreted to have been facilitated by two different mechanisms since both studied sites have moved away from the Southern Hemisphere circulation. First, at present, Site 1256 is located within the northern part of the latitudinal zone of the annual shifts of the ITCZ (Fig. 2a). Therefore, minor contributions from the Southern Hemisphere cannot be completely excluded. Second, Lyle (1992) revealed a lobe of high terrigenous deposition extending from ~12°S to an area north of the Galápagos triple junction at ~5°N in a SE-NW direction, which he proposed to indicate sedimentary material transported and accumulated by the Southeast Trade Winds. Thus deep-water advection of this South American terrigenous matter by strong northeastward bottom currents to the studied sites of deposition appears reasonable. Supply of continental arc Pb of South American origin via the abyssal circulation is highly likely, since Site 495 has also been affected to some extent by the South CVZ, considerably after this site left the Southern Hemisphere circulation regime, as shown by the Pb isotope relationships (Fig. 4). This strongly suggests a deep-water connection of Site 495 not only to the EPR but also to Site 1256, given the common radiogenic endmembers over the entire sedimentation record. It has additionally been demonstrated that the seawater record of Fe-Mn crust GMAT 14D continuously shared the same Pb isotopic endmembers as the bulk sediments (Fig. 4), although it has most likely always been located north of the migrations of the ITCZ (Fig. 2b). Thus, for several millions of years, GMAT 14D and Site 1256 have not been exposed to the same atmospheric and oceanic surface circulation system. This points to a persistent deep-water connection between Site 1256, Site 495, and Fe-Mn crust GMAT 14D, at least since ~7 Ma marking the time of initial precipitation at the location of GMAT 14D. This is substantiated by the small temporal variability of the Pb isotopic evolution of the GMAT 14D record resembling that of the seawater data obtained at Site 1256, which indicates well-mixed deep waters supplied by Pb from all sources relevant to the study area (Figs. 3, 4, 5a).

In conclusion, the present data strongly suggest an abyssal gyre, which has been active in the Guatemala Basin at least since ~7 Ma connecting locations of Sites 1256, 495, and Fe-Mn crust GMAT 14D via deep-water currents, leading to a similarity of all Pb isotopic records even at times of different surface water and atmospheric circulation affecting the locations considered. The dissolved Pb isotopic signal was less radiogenic than the bulk signatures prior to ~2 Ma and essentially indistinguishable thereafter, most likely related to the establishment

of deep water mixing in the Guatemala Basin due to the additional onset of a surface gyre (north of the ITCZ) at the studied drilling sites, balancing the interplay of TMVB and South CVZ Pb supply in favor of the TMVB source. Consequently, the present-day data provide clear evidence for the deep-water advection of detrital Pb from the TMVB, as this source was already present in the record well before the time when all oceanic sites were located north of the ITCZ. We invoke the mapped present-day deep-water current running southward along the eastern flank of the EPR (Lyle, 1992) to represent a major supplier of TMVB material to the Guatemala Basin deep water since at least ~7 Ma. Lyle (1992) proposed transport of terrigenous material by this bottom current when encountering the currents crossing the EPR to the east, which have previously been suggested (Lonsdale, 1976, and references therein). The present study now provides a geochemical proof of the existence of this counter-clockwise deep-water flow not only for today but also for at least the past ~7 million years.

5.4 Paleoceanographic implications of continuous supply of hydrothermal Pb from the EPR

The present Pb isotopic study has proved the existence of a continuous eastward-directed transport of mid-ocean ridge hydrothemal plume particles, which have affected the studied sites more than 1000 km away from the East Pacific Rise hydrothermal systems. This implies that such plumes have formed an oceanographically and sedimentologically significant component in the eastern equatorial Pacific over at least ~23 million years. Furthermore, this suggests that the deep ocean current pattern did not change to an extent redirecting hydrothermal plumes away from the studied sites, indicating that the closure of the Central American Seaway (CAS) had no major impact on the deep circulation in the central and eastern Pacific. We therefore argue that the deep-water circulation in the Pacific was overall essentially stable for millions of years. However, CAS closure may have led to the establishment of the counter-clockwise abyssal circulation in the Guatemala Basin, preventing eastern Pacific deep water from flowing through the gateway toward the Caribbean Sea in favor of the onset of a continuous gyre at depth within the study area. Deep-water flow through the open CAS terminated about 10 Myr ago as reflected by sedimentary Nd and Pb isotopic records on both sides of the gateway (Frank et al., 1999; Newkirk and Martin 2009; Osborne et al., 2014). In addition, by using isotopic proxies, the present study confirms recent modeling results of Sumata et al. (2010), who suggested an eastward throughflow in case of a deep open CAS. This supports the location of past deep water production to be placed in the North Pacific Ocean, as indicated by modeling studies (Motoi et al., 2005; Sumata et al., 2010).

Steady eastward deep-water flow also has profound consequences for the interpretation of the cause of the severe reduction in eastern equatorial Pacific carbonate accumulation in mid- to late-Miocene times, referred to as “carbonate crash” (Lyle et al., 1995). This event has been interpreted to reflect a decreasing inflow of high-CO_3^{2-} Caribbean deep water as a consequence of deep-water restriction at the CAS, enhancing dissolution in the deep eastern

equatorial Pacific as a consequence of shoaling of the Carbonate Compensation Depth (Farrell et al., 1995; Lyle et al., 1995). However, an oppositely directed, eastward deep-water flow from the eastern equatorial Pacific Ocean to the Caribbean Sea contradicts such a scenario. Thus, a more recently suggested model invoking changes in EEP bioproductivity (Jiang et al., 2007) is supported by the present study.

5.5 Why has Central America been insignificant for Pb input into the Guatemala Basin?

It is a somewhat surprising result that Pb input from Central America to the eastern equatorial Pacific has been isotopically insignificant during the Neogene and Quaternary epochs. Prior to ~6–7 Ma, both sites were located south of the ITCZ, thus, an eolian input from Central America was unlikely at that time. However, as Central American input has obviously not been a persistent feature afterwards either, other reasons than tectonic migration must have been involved. It has been shown that Central America was subject to a tropical climate during the Miocene and Early Pliocene, mainly hosting rainforests and vegetation, in which humid conditions prevailed (see reviews by Webb, 1978; Janis, 1993; Woodburne, 2010; Pound et al., 2012). First drier savanna-like habitats have been suggested for the Early Pliocene (< 4 Ma) and savanna-like conditions predominated during the Pleistocene prior to the onset of the mainly tropical Holocene environment (Woodburne, 2010, and references therein). Given this climatic evolution, an eolian contribution of Pb from Central America has been unlikely during the Neogene. This may explain the insignificant impact of this region on the marine Pb isotopic record, since eolian Pb input appears to have been a major pathway in the study area. Furthermore, Central America generally had a lowland character during the Neogene (Webb, 1978, and references therein) and highland areas have likely resulted from very late tectonic uplift, such as the Pleistocene uplift in the isthmus region (O'Dea et al., 2012). Therefore, a substantial runoff affecting the study area did most likely not occur and has also considerably restricted the hemipelagic influence of Central America during most of the studied period.

6 Conclusions

Our study is the first to characterize the Pb isotopic evolution of detrital sediments in the eastern equatorial Pacific (EEP) over the past ~23 million years covering the entire Neogene-Quaternary tectonic movement of Cocos Plate basement from formation at the East Pacific Rise spreading center to arrival at the Central American subduction zone. The ~23 Ma bulk sediment Pb isotopic records from two drilling sites in the EEP form tightly constrained mixing arrays reflecting inputs from two major sources: depleted, mantle-derived Pb from East Pacific Rise (EPR) hydrothermal systems and enriched, continental arc Pb derived from a mixture of terrigenous material from the Andean Arc segments (South Central Volcanic Zone, Northern Volcanic Zone) and the Trans-Mexican Volcanic Belt. Potential input of Pb

from most proximal sources in Central America is demonstrated to have been insignificant over time.

The temporal evolution of the EEP Pb isotopic record has mainly been driven by the tectonic migration of the Cocos Plate, which has been superimposed by changes in atmospheric and oceanic surface circulation, mainly in response to the northward movement of the studied sites approaching the at the same time southward shifting Intertropical Convergence Zone. It is suggested that winds have represented the major pathway for the detrital Pb supply in the eastern equatorial Pacific, whereas continental runoff has likely played only a subordinate role.

Continuous delivery of EPR mid-ocean ridge hydrothermal Pb to the easterly located drilling sites strongly suggests far reaching lateral advection of hydrothermal plumes by deep-water currents over distances of more than 1000 km. In addition, deep-water currents are suggested to have played an important role in transporting terrigenous Pb through entrainment of detritus at depth. The general deep-water circulation system in the central and eastern Pacific has essentially been stable for at least ~23 million years, despite any paleoceanographic changes, which may have occurred as a consequence of Central American Seaway closure. Both oceanic surface and abyssal gyres are reflected by the well-mixed Pb isotopic signatures in the eastern equatorial Pacific over the past ~7 million years.

Acknowledgments

We are grateful to S. Hauff, J. Heinze, and A. Klügel for valuable analytical support, as well as to S. Duggen for fruitful discussions. This research used samples provided by IODP and was funded by the Deutsche Forschungsgemeinschaft (DFG) IODP priority program grants HO1833/16-1 and 18-1.

References

Abouchami, W., Goldstein, S.L., Gazer, S., Eisenhauer, A., Mangini, A., 1997. Secular changes of lead and neodymium in central Pacific seawater recorded by a Fe-Mn crust. Geochimica et Cosmochimica Acta 61 (18), 3957–3974. 10.1016/S0016-7037(97)00218-4.

Alpers, C.N., Brimhall, G.H., 1988. Middle Miocene climatic change in the Atacama Desert, northern Chile: Evidence from supergene mineralization at La Escondida. Geological Society of America Bulletin 100 (10), 1640–1656. 10.1130/0016-7606(1988)100<1640:MMCCIT>2.3.CO;2.

Andriessen, P., Helmens, K.F., Hooghiemstra, H., Riezebos, P.A., Van der Hammen, T., 1993. Absolute chronology of the Pliocene-Quaternary sediment sequence of the Bogota area, Colombia. Quaternary Science Reviews 12 (7), 483–501. 10.1016/0277-3791(93)90066-U.

Barrett, T.J., Taylor, P.N., Lugoqski, J., 1987. Metalliferous sediments from DSDP Leg 92: The East Pacific Rise transect. Geochimica et Cosmochimica Acta 51 (9), 2241–2253. 10.1016/0016-7037(87)90278-X.

Basak, C., Martin, E.E., 2013. Antarctic weathering and carbonate compensation at the Eocene–Oligocene transition. Nature Geoscience 6 (2), 121–124. 10.1038/ngeo1707.

Berggren, W.A., Hilgen, F. J., Langereis, C. G., Kent, D. V., Obradovich, J. D., Raffi, I., Raymo, M. E., Shackleton, N.J., 1995a. Late Neogene chronology: New perspectives in high-resolution stratigraphy. Geological Society of America Bulletin 107 (11), 1272–1287. 10.1130/0016-7606(1995)107<1272:LNCNPI>2.3.CO;2.

Berggren, W.A., Kent, D.V., Swisher, C.C., Aubry, M.-P., 1995b. A revised Cenozoic geochronology and chronostratigraphy: Geochronology, Time Scales, and Global Stratigraphic Correlation, in: Berggren (Ed.), Geochronology, vol. 54, pp. 129–212.

Boström, K., Peterson, M.N.A., 1969. The origin of aluminum-poor ferromanganoan sediments in areas of high heat flow on the East Pacific Rise. Marine Geology 7 (5), 427–447. 10.1016/0025-3227(69)90016-4.

Broecker, W., Peng, T.H., Beng, Z., 1982. Tracers in the Sea. Lamont-Doherty Geological Observatory, Columbia University, Palisades, NY.

Cande, S.C., Kent, D.V., 1995. Revised calibration of the geomagnetic polarity timescale for the Late Cretaceous and Cenozoic. Journal of Geophysical Research: Solid Earth 100 (B4), 6093–6095. 10.1029/94JB03098.

Castillo, P. R., Klein, E., Bender, J., Langmuir, C., Shirey, S., Batiza, R., White, W., 2000. Petrology and Sr, Nd, and Pb isotope geochemistry of mid-ocean ridge basalt glasses from the 11°45′N to 15°00′N segment of the East Pacific Rise. Geochemistry, Geophysics, Geosystems 1 (11), 1–40. 10.1029/1999GC000024.

Chen, J.H., Wasserburg, G.J., Damm, K.L. von, Edmond, J.M., 1986. The U-Th-Pb systematics in hot springs on the East Pacific Rise at 21°N and Guaymas Basin. Geochimica et Cosmochimica Acta 50 (11), 2467–2479. 10.1016/0016-7037(86)90030-X.

Chow, T.J., Patterson, C.C., 1962. The occurrence and significance of lead isotopes in pelagic sediments. Geochimica et Cosmochimica Acta 26 (2), 263–308. 10.1016/0016-7037(62)90016-9.

Coates, A.G., Stallard, R.F., 2013. How old is the Isthmus of Panama? Bulletin of Marine Science 89 (4), 801–813. 10.5343/bms.2012.1076.

Coulbourn, W.T., Hesse, R., Azema, J., Shiki, T., 1982. A summary of the sedimentology of DSDP Leg 67 sites: the Middle America trench and slope off Guatemala - an active margin transect, in: Orlofsky, S. (Ed.), Initial Reports of the Deep Sea Drilling Project covering Leg 67 of the cruises of the drilling vessel Glomar Challenger, Manzanillo, Mexico to Puntarenas, Costa Rica. Initial Reports of the Deep Sea Drilling Project, pp. 759–774.

DeMets, C., Gordon, R.G., Argus, D.F., Stein, S., 1990. Current plate motions. Geophysical Journal International 101 (2), 425–478. 10.1111/j.1365-246X.1990.tb06579.x.

Dobson, D.M., Dickens, G.R., Rea, D.K., 2001. Terrigenous sediment on Ceara Rise: a Cenozoic record of South American orogeny and erosion. Palaeogeography, Palaeoclimatology, Palaeoecology 165 (3-4), 215–229. 10.1016/S0031-0182(00)00161-9.

Dunai, T.J., González López, Gabriel A., Juez-Larré, J., 2005. Oligocene–Miocene age of aridity in the Atacama Desert revealed by exposure dating of erosion-sensitive landforms. Geol 33 (4), 321. 10.1130/G21184.1.

Edmond, J.M., Von Damm, K. L., McDuff, R.E., Measures, C.I., 1982. Chemistry of hot springs on the East Pacific Rise and their effluent dispersal. Nature 297 (5863), 187–191. 10.1038/297187a0.

Eronen, J.T., Fortelius, M., Micheels, A., Portmann, F.T., Puolamaki, K., Janis, C.M., 2012. Neogene aridification of the Northern Hemisphere. Geology 40 (9), 823–826. 10.1130/G33147.1.

Evenstar, L.A., Hartley, A.J., Stuart, F.M., Mather, A.E., Rice, C.M., Chong, G., 2009. Multiphase development of the Atacama Planation Surface recorded by cosmogenic 3He exposure ages: Implications for uplift and Cenozoic climate change in western South America. Geology 37 (1), 27–30. 10.1130/G25437A.1.

Farrell, J.W., Raffi, I., Janecek, T.C., Murray, D.W., Levitan, M., Dadey, K.A., Emeis, K.-C., Lyle, M., Flores, J.-A., Hovan, S., 1995. Late Neogene Sedimentation Patterns in the Eastern Equatorial Pacific, in: Pisias, N.G., Mayer, L.A., Janecek, T.R., Palmer-Julson, A., van Andel, T.H. (Eds.), Proceedings of the Ocean Drilling Program, 138 Scientific Results, vol. 138. Ocean Drilling Program.

Farris, D.W., Jaramillo, C., Bayona, G., Restrepo-Moreno, S.A., Montes, C., Cardona, A., Mora, A., Speakman, R.J., Glascock, M.D., Valencia, V., 2011. Fracturing of the Panamanian Isthmus during initial collision with South America. Geology 39 (11), 1007–1010. 10.1130/G32237.1.

Faure, G., 2001. Origin of igneous rocks: the isotopic evidence. Springer-Verlag, Berlin.

Faure, G., Mensing, T.M., 2005. Isotopes: Principles and applications, 3rd ed. Wiley, Hoboken, N.J.

Ferrari, L., Orozco-Esquivel, T., Manea, V., Manea, M., 2012. The dynamic history of the Trans-Mexican Volcanic Belt and the Mexico subduction zone. Tectonophysics 522-523, 122–149. 10.1016/j.tecto.2011.09.018.

Figueiredo, J., Hoorn, C., van der Ven, P., Soares, E., 2009. Late Miocene onset of the Amazon River and the Amazon deep-sea fan: Evidence from the Foz do Amazonas Basin. Geology 37 (7), 619–622. 10.1130/G25567A.1.

Flohn, H., 1981. A hemispheric circulation asymmetry during Late Tertiar. International Journal of Earth Sciences 70 (2), 725–736. 10.1007/BF01822146.

Frank, M., Reynolds, B.C., Keith O'Nions, R., 1999. Nd and Pb isotopes in Atlantic and Pacific water masses before and after closure of the Panama gateway. Geology 27 (12), 1147–1150. 10.1130/0091-7613(1999)027<1147:NAPIIA>2.3.CO;2.

Frank, M., 2002. Radiogenic isotopes: Tracers of past ocean circulation and erosional input. Reviews of Geophysics 40 (1). 10.1029/2000RG000094.

García, N.O., 1994. South American climatology. Quaternary International 21, 7–27. 10.1016/1040-6182(94)90018-3.

Geldmacher, J., Hoernle, K., van den Bogaard, Paul, Hauff, F., Klugel, A., 2008. Age and Geochemistry of the Central American Forearc Basement (DSDP Leg 67 and 84): Insights into Mesozoic Arc Volcanism and Seamount Accretion on the Fringe of the Caribbean LIP. Journal of Petrology 49 (10), 1781–1815. 10.1093/petrology/egn046.

Geldmacher, J., Höfig, T.W., Hauff, F., Hoernle, K., Garbe-Schönberg, D., Wilson, D.S., 2013. Influence of the Galápagos hotspot on the East Pacific Rise during Miocene superfast spreading. Geology 41 (2), 183–186. 10.1130/G33533.1.

Ginoux, P., Prospero, J.M., Gill, T.E., Hsu, N. Christina, Zhao, M., 2012. Global-scale attribution of anthropogenic and natural dust sources and their emission rates based on MODIS Deep Blue aerosol products. Reviews of Geophysics 50 (3), RG3005. 10.1029/2012RG000388.

Godfrey, L.V., 2002. Temporal changes in the lead isotopic composition of red clays: comparison with ferromanganese crust records. Chemical Geology 185 (3-4), 241–254. 10.1016/S0009-2541(01)00406-5.

Goldstein, S.L., Hemming, S.R., 2003. Long-lived Isotopic Tracers in Oceanography, Paleoceanography, and Ice-sheet Dynamics, in: Holland, H.D., Turekian, K.K. (Eds.), Treatise on Geochemistry. Pergamon [Imprint]; Elsevier Science & Technology Books, San Diego, pp. 453–489.

Goss, A. R., Perfit, M. R., Ridley, W. I., Rubin, K. H., Kamenov, G. D., Soule, S. A., Fundis, A., Fornari, D. J., 2010. Geochemistry of lavas from the 2005–2006 eruption at the East Pacific Rise, 9°46′N–9°56′N: Implications for ridge crest plumbing and decadal changes in magma chamber compositions. Geochemistry, Geophysics, Geosystems 11 (5), Q05T09. 10.1029/2009GC002977.

Gregory-Wodzicki, K.M., 2000. Uplift history of the Central and Northern Andes: A review. Geological Society of America Bulletin 112 (7), 1091–1105. 10.1130/0016-7606(2000)112<1091:UHOTCA>2.0.CO;2.

Gurvich, E.G., 2006. Metalliferous sediments of the World Ocean: Fundamental theory of deep-sea hydrothermal sedimentation; with … 38 tables. Springer, Berlin, Heidelberg [u.a.], XIII, 416 S.

Gutjahr, M., Frank, M., Stirling, C.H., Klemm, V., van de Flierdt, T., Halliday, A.N., 2007. Reliable extraction of a deepwater trace metal isotope signal from Fe–Mn oxyhydroxide coatings of marine sediments. Chemical Geology 242 (3–4), 351–370. 10.1016/j.chemgeo.2007.03.021.

Haley, B. A., Frank, M., Spielhagen, R. F., Fietzke, J., 2008. Radiogenic isotope record of Arctic Ocean circulation and weathering inputs of the past 15 million years. Paleoceanography 23 (1), PA1S13. 10.1029/2007PA001486.

Handschumacher, D. W., 1976. Post-Eocene plate tectonics of the Eastern Pacific, in: Sutton, G.H., Manghnani, M.H., Moberly, R., McAfee, E.U. (Eds.), The Geophysics of the Pacific Ocean Basin and Its Margin, vol. 19. AGU, Washington, DC, pp. 177–202.

Hannington, M.D., 2013. The role of black smokers in the Cu mass balance of the oceanic crust. Earth and Planetary Science Letters 374, 215–226. 10.1016/j.epsl.2013.06.004.

Hart, D., Miller, D.J., 2006. Analysis and Correlation of Volcanic Ash in Marine Sediments from the Peru Margin, Ocean Drilling Program Leg 201: Explosive Volcanic Cycles of the North-Central Andes, in: Jørgensen, B.B., D'Hondt, S.L., Miller, D.J. (Eds.), Proceedings of the Ocean Drilling Program, 201 Scientific Results, vol. 201. Ocean Drilling Program.

Henderson, G.M., Maier-Reimer, E., 2002. Advection and removal of ^{210}Pb and stable Pb isotopes in the oceans: a general circulation model study. Geochimica et Cosmochimica Acta 66 (2), 257–272. 10.1016/S0016-7037(01)00779-7.

Heydolph, K., Hoernle, K., Hauff, F., Bogaard, Paul van den, Portnyagin, M., Bindeman, I., Garbe-Schönberg, D., 2012. Along and across arc geochemical variations in NW Central America: Evidence for involvement of lithospheric pyroxenite. Geochimica et Cosmochimica Acta 84, 459–491. 10.1016/j.gca.2012.01.035.

Hoernle, K., Abt, D.L., Fischer, K.M., Nichols, H., Hauff, F., Abers, G.A., van den Bogaard, Paul, Heydolph, K., Alvarado, G., Protti, M., Strauch, W., 2008. Arc-parallel flow in the mantle wedge beneath Costa Rica and Nicaragua. Nature 451 (7182), 1094–1097. 10.1038/nature06550.

Hoernle, K., Hauff, F., Kokfelt, T.F., Haase, K., Garbe-Schönberg, D., Werner, R., 2011. On- and off-axis chemical heterogeneities along the South Atlantic Mid-Ocean-Ridge (5–11°S): Shallow or deep recycling of ocean crust and/or intraplate volcanism? Earth and Planetary Science Letters 306 (1-2), 86–97. 10.1016/j.epsl.2011.03.032.

Hoernle, K., van den Bogaard, Paul, Werner, R., Lissinna, B., Hauff, F., Alvarado, G., Garbe-Schönberg, D., 2002. Missing history (16–71 Ma) of the Galápagos hotspot: Implications for the tectonic and biological evolution of the Americas. Geology 30 (9), 795–798. 10.1130/0091-7613(2002)030<0795:MHMOTG>2.0.CO;2.

Hoorn, C., Wesselingh, F.P., ter Steege, H., Bermudez, M.A., Mora, A., Sevink, J., Sanmartín, I., Sanchez-Meseguer, A., Anderson, C.L., Figueiredo, J.P., Jaramillo, C., Riff, D., Negri, F.R., Hooghiemstra, H., Lundberg, J., Stadler, T., Särkinen, T., Antonelli, A.,

2010. Amazonia Through Time: Andean Uplift, Climate Change, Landscape Evolution, and Biodiversity. Science 330 (6006), 927–931. 10.1126/science.1194585.

Hovan, S.A., 1995. Late Cenozoic Atmospheric Circulation Intensity and Climatic History Recorded by Eolian Deposition in the Eastern Equatorial Pacific Ocean, Leg 138, in: Pisias, N.G., Mayer, L.A., Janecek, T.R., Palmer-Julson, A., van Andel, T.H. (Eds.), Proceedings of the Ocean Drilling Program, 138 Scientific Results, vol. 138. Ocean Drilling Program.

Hovikoski, J., Wesselingh, F.P., Räsänen, M., Gingras, M., Vonhof, H.B., 2010. Marine influence in Amazonia: Evidence from the Geological Record, in: Hoorn, C., Wesselingh, F.P. (Eds.), Amazonia: Landscape and Species Evolution. Wiley-Blackwell Publishing Ltd, Oxford, UK, pp. 143–161.

Hyeong, K., Park, S.-H., Yoo, C.M., Kim, K.-H., 2005. Mineralogical and geochemical compositions of the eolian dust from the northeast equatorial Pacific and their implications on paleolocation of the Intertropical Convergence Zone. Paleoceanography 20 (1), 1–11. 10.1029/2004PA001053.

Janis, C.M., 1993. Tertiary Mammal Evolution in the Context of Changing Climates, Vegetation, and Tectonic Events. Annual Review of Ecology and Systematics 24, 467–500.

Jiang, S., Wise, S.W., 2007. Upper Cenozoic calcareous nannofossil biostratigraphy and inferred sedimentation, ODP Leg 206, East Pacific Rise, in: Teagle, D.A.H., Wilson, D.S., Acton, G.D., Vanko, D. (Eds.), Proceedings of the Ocean Drilling Program, 206 Scientific Results, vol. 206. Ocean Drilling Program.

Jones, C.E., Halliday, A.N., Rea, D.K., Owen, R.M., 2000. Eolian inputs of lead to the North Pacific. Geochimica et Cosmochimica Acta 64 (8), 1405–1416. 10.1016/S0016-7037(99)00439-1.

Kerr, A.C., Marriner, G.F., Tarney, J., Nivia, A., Saunders, A.D., Thirlwall, M.F., Sinton, C.W., 1997. Cretaceous Basaltic Terranes in Western Columbia: Elemental, Chronological and Sr-Nd Isotopic Constraints on Petrogenesis. Journal of Petrology 38 (6), 677–702. 10.1093/petroj/38.6.677.

Kessler, W.S., 2006. The circulation of the eastern tropical Pacific: A review. Progress in Oceanography 69 (2–4), 181–217. 10.1016/j.pocean.2006.03.009.

Ling, H.-F., Jiang, S.-Y., Frank, M., Zhou, H.-Y., Zhou, F., Lu, Z.-L., Chen, X.-M., Jiang, Y.-H., Ge, C.-D., 2005. Differing controls over the Cenozoic Pb and Nd isotope evolution of deepwater in the central North Pacific Ocean. Earth and Planetary Science Letters 232 (3–4), 345–361. 10.1016/j.epsl.2004.12.009.

Lonsdale, P., 1976. Abyssal circulation of the southeastern Pacific and some geological implications. Journal of Geophysical Research: Oceans 81 (6), 1163–1176. 10.1029/JC081i006p01163.

Lourens, L., Hilgen, F., Shackleton, N.J., Laskar, J., Wilson, D.S., 2004. The Neogene Period, in: Gradstein, F., Ogg, J., Smith, A. (Eds.), A Geological Time Scale 2004, Camebridge University Press, pp. 409–440.

Lupton, J.E., 1995. Hydrothermal plumes: Near and far field, in: Humphris, S.E., Zierenberg, R.A., Mullineaux, L.S., Thomson, R.E. (Eds.), Seafloor Hydrothermal Systems: Physical, Chemical, Biological, and Geological Interactions, vol. 91. American Geophysical Union, Washington, D. C., pp. 317–346.

Lupton, J.E., Pyle, D.G., Jenkins, W.J., Greene, R., Evans, L., 2004. Evidence for an extensive hydrothermal plume in the Tonga-Fiji region of the South Pacific. Geochem. Geophys. Geosyst. 5 (1), n/a. 10.1029/2003GC000607.

Lyle, M., 1992. Composition Maps of Surface Sediments of the Eastern Tropical Pacific Ocean, in: Mayer, L., Pisias, N., Janecek, T. (Eds.), Proceedings of the Ocean Drilling Program, 138 Initial Reports, vol. 138. Ocean Drilling Program.

Lyle, M., Dadey, K.A., Farrell, J.W., 1995. The Late Miocene (11-8 Ma) Eastern Pacific Carbonate Crash: Evidence for Reorganization of Deep-Water Circulation by the Closure of the Panama Gateway, in: Pisias, N.G., Mayer, L.A., Janecek, T.R., Palmer-Julson, A., van Andel, T.H. (Eds.), Proceedings of the Ocean Drilling Program, 138 Scientific Results, vol. 138. Ocean Drilling Program.

Mayer, L., Pisias, N., Janecek, T. (Eds.), 1992. Proceedings of the Ocean Drilling Program, 138 Initial Reports. Ocean Drilling Program.

McGee, D., Broecker, W.S., Winckler, G., 2010. Gustiness: The driver of glacial dustiness? Quaternary Science Reviews 29 (17-18), 2340–2350. 10.1016/j.quascirev.2010.06.009.

Milliman, J.D., Syvitski, J.P.M., 1992. Geomorphic/Tectonic Control of Sediment Discharge to the Ocean: The Importance of Small Mountainous Rivers. The Journal of Geology 100 (5), 525–544. 10.1086/629606.

Molnar, P., 2008. Closing of the Central American Seaway and the Ice Age: A critical review. Paleoceanography 23 (2), 1–15. 10.1029/2007PA001574.

Montes, C., Bayona, G., Cardona, A., Buchs, D. M., Silva, C. A., Morón, S., Hoyos, N., Ramírez, D. A., Jaramillo, C. A., Valencia, V., 2012b. Arc-continent collision and orocline formation: Closing of the Central American seaway. Journal of Geophysical Research: Solid Earth 117 (B4), 1–25. 10.1029/2011JB008959.

Montes, C., Cardona, A., McFadden, R., Morón, S.E., Silva, C. A., Restrepo-Moreno, S., Ramírez, D. A., Hoyos, N., Wilson, J., Farris, D., Bayona, G.A., Jaramillo, C. A., Valencia, V., Bryan, J., Flores, J.A., 2012a. Evidence for middle Eocene and younger land emergence in central Panama: Implications for Isthmus closure. Geological Society of America Bulletin 124 (5-6), 780–799. 10.1130/B30528.1.

Motoi, T., Chan, W.-L., Minobe, S., Sumata, H., 2005. North Pacific halocline and cold climate induced by Panamanian Gateway closure in a coupled ocean-atmosphere GCM. Geophysical Research Letters 32 (10), L10618. 10.1029/2005GL022844.

Nakai, S., Halliday, A.N., Rea, D.K., 1993. Provenance of dust in the Pacific Ocean. Earth and Planetary Science Letters 119 (1-2), 143–157. 10.1016/0012-821X(93)90012-X.

Newkirk, D.R., Martin, E.E., 2009. Circulation through the Central American Seaway during the Miocene carbonate crash. Geology 37 (1), 87–90. 10.1130/G25193A.1.

O'Dea, A., Hoyos, N., Rodríguez, F., Degracia, B., Gracia, C. de, 2012. History of upwelling in the Tropical Eastern Pacific and the paleogeography of the Isthmus of Panama. Palaeogeography, Palaeoclimatology, Palaeoecology 348-349, 59–66. 10.1016/j.palaeo.2012.06.007.

O'Nions, R.K., Carter, S. R., Cohen, R. S., Evensen, N. M., Hamilton, P. J., 1978. Pb, Nd and Sr isotopes in oceanic ferromanganese deposits and ocean floor basalts. Nature 273 (5662), 435–438. 10.1038/273435a0.

Osborne, A.H., Newkirk, D.R., Groeneveld, J., Martin, E.E., Tiedemann, R., Frank, M., 2014. The seawater neodymium and lead isotope record of the final stages of Central American Seaway closure. Paleoceanography, n/a. 10.1002/2014PA002676.

Patino, L.C., Carr, M.J., Feigenson, M.D., 2000. Local and regional variations in Central American arc lavas controlled by variations in subducted sediment input. Contributions to Mineralogy and Petrology 138 (3), 265–283. 10.1007/s004100050562.

Pettke, T., Halliday, A.N., Hall, C.M., Rea, D.K., 2000. Dust production and deposition in Asia and the north Pacific Ocean over the past 12 Myr. Earth and Planetary Science Letters 178 (3–4), 397–413. 10.1016/S0012-821X(00)00083-2.

Pettke, T., Halliday, A.N., Rea, D.K., 2002. Cenozoic evolution of Asian climate and sources of Pacific seawater Pb and Nd derived from eolian dust of sediment core LL44-GPC3. Paleoceanography 17 (3), 1–13. 10.1029/2001PA000673.

Pichat, S., Abouchami, W., Galer, S.J.G., 2014. Lead isotopes in the Eastern Equatorial Pacific record Quaternary migration of the South Westerlies. Earth and Planetary Science Letters 388, 293–305. 10.1016/j.epsl.2013.11.035.

Pound, M.J., Haywood, A.M., Salzmann, U., Riding, J.B., Lunt, D.J., Hunter, S.J., 2011. A Tortonian (Late Miocene, 11.61–7.25Ma) global vegetation reconstruction. Palaeogeography, Palaeoclimatology, Palaeoecology 300 (1-4), 29–45. 10.1016/j.palaeo.2010.11.029.

Pound, M.J., Haywood, A.M., Salzmann, U., Riding, J.B., 2012. Global vegetation dynamics and latitudinal temperature gradients during the Mid to Late Miocene (15.97–5.33Ma). Earth-Science Reviews 112 (1-2), 1–22. 10.1016/j.earscirev.2012.02.005.

Rea, D.K., 1990. Aspects of atmospheric circulation: the late Pleistocene (0–950,000 yr) record of eolian deposition in the pacific ocean. Palaeogeography, Palaeoclimatology, Palaeoecology 78 (3-4), 217–227. 10.1016/0031-0182(90)90215-S.

Rea, D.K., 1994. The paleoclimatic record provided by eolian deposition in the deep sea: The geologic history of wind. Reviews of Geophysics 32 (2), 159–195. 10.1029/93RG03257.

Rech, J.A., Currie, B.S., Michalski, G., Cowan, A.M., 2006. Neogene climate change and uplift in the Atacama Desert, Chile. Geol 34 (9), 761. 10.1130/G22444.1.

Rech, J.A., Currie, B.S., Shullenberger, E.D., Dunagan, S.P., Jordan, T.E., Blanco, N., Tomlinson, A.J., Rowe, H.D., Houston, J., 2010. Evidence for the development of the Andean rain shadow from a Neogene isotopic record in the Atacama Desert, Chile. Earth and Planetary Science Letters 292 (3-4), 371–382. 10.1016/j.epsl.2010.02.004.

Rogers, R.D., Mann, P., Emmet, P.A., 2007. Tectonic terranes of the Chortis block based on integration of regional aeromagnetic and geologic data, in: Special Paper 428: Geologic and Tectonic Development of the Caribbean Plate Boundary in Northern Central America, vol. 428. Geological Society of America, pp. 65–88.

Schaule, B.K., Patterson, C.C., 1981. Lead concentrations in the northeast Pacific: evidence for global anthropogenic perturbations. Earth and Planetary Science Letters 54 (1), 97–116. 10.1016/0012-821X(81)90072-8.

Sims, K. W. W, Goldstein, S.J., Blichert-Toft, J., Perfit, M. R., Kelemen, P., Fornari, D. J., Michael, P., Murrell, M.T., Hart, S.R., DePaolo, D.J., Layne, G., Ball, L., Jull, M., Bender, J., 2002. Chemical and isotopic constraints on the generation and transport of magma beneath the East Pacific Rise. Geochimica et Cosmochimica Acta 66 (19), 3481–3504. 10.1016/S0016-7037(02)00909-2.

Stancin, A.M., Gleason, J.D., Rea, D.K., Owen, R.M., Moore Jr. , T. C., Blum, J.D., Hovan, S.A., 2006. Radiogenic isotopic mapping of late Cenozoic eolian and hemipelagic sediment distribution in the east-central Pacific. Earth and Planetary Science Letters 248 (3–4), 840–850. 10.1016/j.epsl.2006.06.038.

Stern, C.R., 2004. Active Andean volcanism: its geologic and tectonic setting. Andean Geology (formerly Revista Geológica de Chile) 31 (2), 161–206. 10.5027/andgeoV31n2-a01.

Stumpf, R., Frank, M., Schönfeld, J., Haley, B.A., 2010. Late Quaternary variability of Mediterranean Outflow Water from radiogenic Nd and Pb isotopes. Quaternary Science Reviews 29 (19-20), 2462–2472. 10.1016/j.quascirev.2010.06.021.

Sumata, H., Minobe, S., Motoi, T., Chan, W.-L., 2010. A semi-analytical model of barotropic and baroclinic flows for an open Panama Gateway. Dynamics of Atmospheres and Oceans 50 (1), 55–77. 10.1016/j.dynatmoce.2009.10.001.

van de Flierdt, T., Frank, M., Halliday, A.N., Hein, J.R., Hattendorf, B., Günther, D., Kubik, P.W., 2004. Deep and bottom water export from the Southern Ocean to the Pacific over the past 38 million years. Paleoceanography 19 (1), PA1020. 10.1029/2003PA000923.

von Blanckenburg, F., Igel, H., 1999. Lateral mixing and advection of reactive isotope tracers in ocean basins: observations and mechanisms. Earth and Planetary Science Letters 169 (1-2), 113–128. 10.1016/S0012-821X(99)00070-9.

von Blanckenburg, F., O'Nions, R.K., Heinz, J.R., 1996. Distribution and sources of pre-anthropogenic lead isotopes in deep ocean water from FeMn crusts. Geochimica et Cosmochimica Acta 60 (24), 4957–4963. 10.1016/S0016-7037(96)00310-9.

von Huene, R., Aubouin, J., et al., 1982. Site 495: Cocos Plate Middle America Trench Outer Slope, in: Aubouin, J., von Huene, R. (Eds.), Initial Reports of the Deep Sea Drilling Project, 67, vol. 67. U.S. Government Printing Office, pp. 79–141.

Waters, C.L., Sims, Kenneth W. W., Perfit, M.R., Blichert-Toft, J., Blusztajn, J., 2011. Perspective on the Genesis of E-MORB from Chemical and Isotopic Heterogeneity at 9–10°N East Pacific Rise. Journal of Petrology 52 (3), 565–602. 10.1093/petrology/egq091.

Webb, S.D., 1977. A History of Savanna Vertebrates in the New World. Part I: North America. Annual Review of Ecology and Systematics 8, 355–380.

Webb, S.D., 1978. A History of Savanna Vertebrates in the New World. Part II: South America and the Great Interchange. Annual Review of Ecology and Systematics 9 (1), 393–426. 10.1146/annurev.es.09.110178.002141.

Wilson, D.S., 1996. Fastest known spreading on the Miocene Cocos-Pacific Plate Boundary. Geophysical Research Letters 23 (21), 3003–3006. 10.1029/96GL02893.

Wilson, D.S., Teagle, D.A.H., Acton, G.D., et al., 2003. Site 1256, Preliminary Results, in: Wilson, D., Teagle, D., Acton, G. (Eds.), Proceedings of the Ocean Drilling Program, 206 Initial Reports, vol. 206. Ocean Drilling Program.

Woodburne, M.O., 2010. The Great American Biotic Interchange: Dispersals, Tectonics, Climate, Sea Level and Holding Pens. Journal of Mammalian Evolution 17 (4), 245–264. 10.1007/s10914-010-9144-8.

Wörner, G., Moorbath, S., Harmon, R.S., 1992. Andean Cenozoic volcanic centers reflect basement isotopic domains. Geology 20 (12), 1103–1106. 10.1130/0091-7613(1992)020<1103:ACVCRB>2.3.CO;2.

Wyrtki, K., Kilonsky, B., 1984. Mean Water and Current Structure during the Hawaii-to-Tahiti Shuttle Experiment. Journal of Physical Oceanography 14 (2), 242–254. 10.1175/1520-0485(1984)014<0242:MWACSD>2.0.CO;2.

Xie, R.C., Marcantonio, F., 2012. Deglacial dust provenance changes in the Eastern Equatorial Pacific and implications for ITCZ movement. Earth and Planetary Science Letters 317–318 (0), 386–395. 10.1016/j.epsl.2011.11.014.

Figure captions

Figure 1. (a) Map of the eastern equatorial Pacific and adjacent continental areas, showing the locations of the studied ocean drilling sites 495 and 1256 together with other oceanic locations referred to in the text (Fe-Mn crust GMAT 14D; drilling sites 499, 845, 849, 852, 853). Indicated oceanic crustal ages of drilling site locations are based on magnetic lineations (Sites 495, 499: von Huene et al., 1982; Geldmacher et al., 2013; Sites 845, 849, 1256: Wilson, 1996; Sites 852, 853: Mayer et al., 1992) according to the geomagnetic polarity time scale of Cande and Kent (1995). The age of Fe-Mn crust GMAT 14D is derived from Frank et al. (1999). Reconstructed tectonic tracks were calculated with the software GPlates (http://www.gplates.org; version 1.1.1). Small dots along the tracks mark 1 Ma and small ticks label 5 Ma increments. Spreading ridges: EPR = East Pacific Rise, CSC = Galápagos Spreading Center (Cocos-Nazca Spreading Center). Other oceanic/continental geologic entities: CAVA = Central American Volcanic Arc, CLIP = Caribbean Large Igneous Province (uplifted parts), GI = Galápagos Islands, NVZ = Northern (Andean) Volcanic Zone, TMVB = Trans-Mexican Volcanic Belt. Chortís Block tectonic boundaries after Rogers et al. (2007). (b) Map of the easternmost tropical and southeastern Pacific (Site 1256 location marked by a black star) and adjacent western part of South America [adapted from Hart and Miller (2006), including oceanic circulation data from Kessler (2006)], depicting major present-day ocean surface (turquoise arrows) and wind (black arrows) currents affecting this area: HC = Humboldt Current, SEC = South Equatorial Current, STW = Southeast Trade Winds. In addition, major volcanic zones of the Andes are displayed: NVZ = Northern Volcanic Zone, CVZ = Central Volcanic Zone (north, transitional (trans.), south; cf. Pichat et al., 2014), SVZ = Southern Volcanic Zone. Note that the Austral Volcanic Zone, being the southernmost Andean Arc segment, follows south of the SVZ (i.e., from 49° to 55°S), thus outside the shown map.

Figure 2. (a) Map of the eastern equatorial Pacific, schematically showing simplified prevailing wind currents [adapted from Hovan (1995); STW = Southeast Trade Winds, NTW = Northeast Trade Winds] and the (present-day and Late Miocene) location of the Intertropical Convergence Zone (ITCZ). However, note that the wind pattern has a strong meridional component east of 110°W and is far more complex and varying than indicated in the present figure (see Kessler, 2006). True paleopositions of considered drilling sites (and Fe-Mn crust GMAT 14D) are shown in 1 Ma increments from 10 (7) Ma to the present (calculated with the software GPlates; http://www.gplates.org; version 1.1.1), encompassing the time frame characterized by continuous terrigenous flux records available from drill cores in both the Pacific and Guatemala Basins (see Fig. 5). Paleopositions represented by black dots (0–4 Ma) mark the period of time with the ITCZ being located at its average present-day latitude of c. 5°N, showing an annual shift between ~4°N and ~10°N (dashed gray vertical line) (Rea, 1994; Hovan, 1995). The Late Miocene (~8–10 Ma) ITCZ location (Hyeong et al., 2005) is indicated by a dashed gray horizontal line. Declining relative wind strength with

shorter distance to the ITCZ is schematically represented by decreasing length of simplified trade wind arrows in either atmospheric hemisphere (according to Wyrtki and Kilonski, 1984). Note that the true paleopositions of oceanic sites depicted here may deviate from the locations along the tectonic tracks shown in Fig. 1a, since the latter ones illustrate the backtrack path to the present-day location of that ridge segment where the underlying oceanic crust was formed, being part of the same tectonic plate. In contrast, the reconstruction of true paleopositions at a given age has taken into account that the associated ridge segment has been subject to ridge jumps through time, referring to the true position of the corresponding ridge segment at a given point of time, which may be different to its present-day location. Abbreviations are the same as in Fig. 1a. (b) Age (Ma) versus latitude (°N), reflecting the northward migration of eastern tropical Pacific drilling sites (Pacific Basin: 852, 853; Guatemala Basin: 495, 845, 1256) and Fe-Mn crust GMAT 14D through time, focusing on the past 10 million years. The northward movement is more pronounced in the Guatemala Basin, since the Cocos Plate has been moving within the stress field of two spreading ridges: N-S-trending EPR and E-W-trending GSC. Note that equatorial Site 849 has not been plotted, as it has exclusively been located south of the equator prior to ~0.5 Ma. The assumed path of the southward shift of the average ITCZ axis (dashed gray line) during the Late Neogene is estimated from interpolation between paleolocation of ~12 ± 2°N around 9 Ma (Hyeong et al., 2005) and current location of ~5°N established at ~4 Ma (Rea, 1994; Hovan, 1995). Note that the ITCZ was located even further north during the Early Neogene and Late Paleogene, respectively, probably being around 22°N at ~25 Ma (Rea, 1994). (c) Map of the eastern equatorial Pacific, schematically displaying major lobes of the oceanic surface [turquoise arrows; after Kessler (2006)] and abyssal [dark blue arrows; as suggested by Lonsdale (1976) and Lyle (1992)] current circulation affecting the eastern equatorial Pacific (CRCC = Costa Rica Coastal Current, NEC = North Equatorial Current, NECC = North Equatorial Countercurrent, SEC = South Equatorial Current, TB = Tehuantepec Bowl, WMC = West Mexican Current). Pale blue, transparent marine areas delineate the latitudinal extent of the westward flowing NEC (north of ~10°N) and SEC (south of ~5°N) surface circulation system, respectively (Hovan, 1995). The structural boundaries of the Guatemala Basin (GB) are highlighted in light gray (Cocos Ridge and part of the EPR and GSC crests). PB = Pacific Basin. Abbreviations are the same as in Fig. 1a.

Figure 3. Sites 495/1256 $^{206}Pb/^{204}Pb_{in}$ (a), $^{207}Pb/^{204}Pb_{in}$ (b), and $^{208}Pb/^{204}Pb_{in}$ (c) isotope ratios ($_{in}$ = initial) versus age (Ma) (left y-axis) and distance of Site 1256 to the East Pacific Rise (EPR; right y-axis) in kilometer (km). Data from eastern equatorial Pacific Fe-Mn crust GMAT 14D (Frank et al., 1999) are also shown for comparison. Distances of Site 1256 to the EPR were calculated with the software GPlates (http://www.gplates.org, version 1.1.1). Black dots placed on distinct blue and yellow circles refer to those Site 1256 samples from which the coeval leachate (white squares) and residual data (black squares) were obtained. Errors are within symbol sizes.

Figure 4. $^{206}Pb/^{204}Pb_{in}$ versus $^{207}Pb/^{204}Pb_{in}$ (a) and $^{208}Pb/^{204}Pb_{in}$ (b) ($_{in}$ = initial), respectively, constituting a narrowly defined linear two-component mixing array ($R^2 = 0.95$ on uranogenic and $R^2 = 0.98$ on thorogenic Pb isotopes, respectively, associated with the corresponding linear regression line shown in black) between East Pacific Rise (EPR) mid-ocean ridge basalt (MORB) and active continental margins of Mexico (Trans-Mexican Volcanic Belt) and the south Central Andes (south Central Volcanic Zone). Abbreviations are the same as in Figs. 1a/b. Errors are smaller than symbol sizes. Data sources: GMAT 14D (Frank et al., 1999); MORB (mid-ocean-ridge basalt) from Site 1256 (Geldmacher et al., 2013), Sites 495/499 (Geldmacher et al., 2008, 2013; Heydolph et al., 2012) (fields for both sites based on initial isotope data) and EPR (9–15°N) (Castillo et al., 2000; Sims et al., 2002; Goss et al., 2010; Waters et al., 2011); average Guatemala basement (Chortís Block part) composition (Heydolph et al., 2012); Asian dust endmember (Pettke et al., 2000); North American endmember (Stancin et al., 2006). All other data fields and calculated average compositions (GSC, CAVA, GI (including Cocos Island and associated seamounts), CLIP (uplifted fragments of the Pacific part), NVZ, north/transitional/ south CVZ, SVZ, AVZ, and TMVB), respectively, are based on Pb isotope data from either the GEOROC database (http://georoc.mpch-mainz.gwdg.de/georoc/) or the PetDB database (http://www.earthchem.org/petdb) retrieved in May/June 2014 and provided in the electronic appendix (Tab. A1). See electronic appendix section A.1 for criteria of Pb isotopic database construction.

Figure 5. $^{206}Pb/^{204}Pb$ (a) and terrigenous mass accumulation rate (TMAR; g/cm^2 ka) (b-f) versus age (past 10 Ma), respectively, for drilling sites east [1256 (a/b) and 845 (c)] and west of the East Pacific Rise (EPR) [852 (d) and 853 (e)]. Both Guatemala and Pacific Basin sites are ordered according to their latitudinal location from south to north; present-day coordinates are given in brackets. Fe-Mn crust GMAT 14D is shown for comparison in the Pb isotope versus age plot (a) with the same symbols as in Fig. 3; errors are within symbol sizes. Inset of different scale is used to show comparatively high Site 1256 TMAR since ~1 Ma (b). Polynomial regression lines of Sites 845, 852, and 853 TMAR records (c-f) are derived from fourth-order polynomial equations. TMAR data sources: Site 1256 (Jiang and Wise, 2007) and Sites 845, 852, 853 (Farrell et al., 1995).

Figure 1

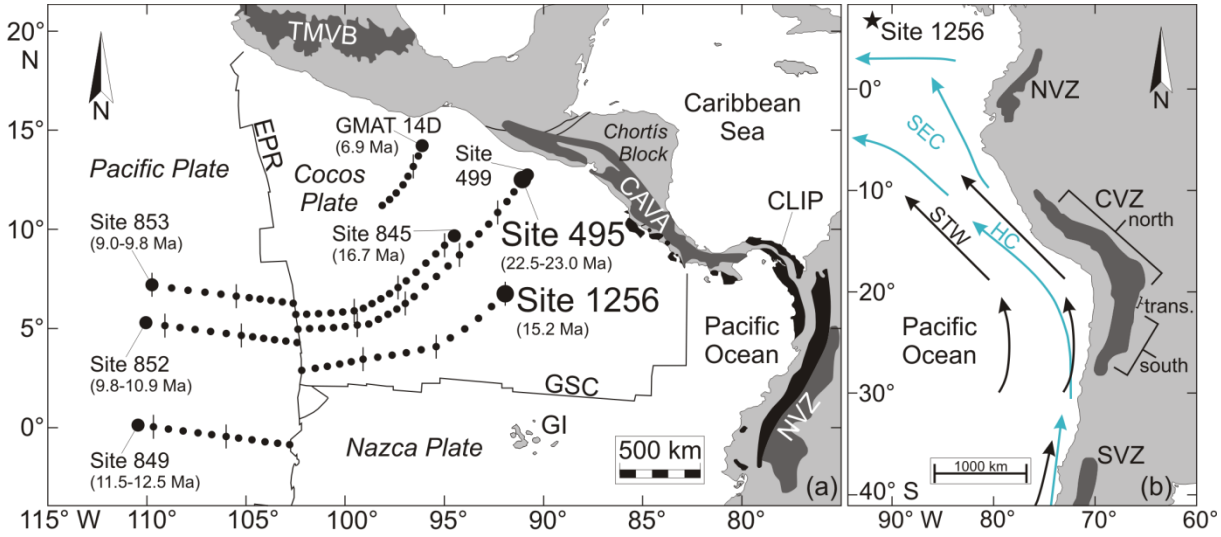
TMVB
EPR
Pacific Plate
Cocos Plate
GMAT 14D
(6.9 Ma)
Site 499
Site 853
(9.0-9.8 Ma)
Site 845
(16.7 Ma)
Site 495
(22.5-23.0 Ma)
Site 1256
(15.2 Ma)
Site 852
(9.8-10.9 Ma)
Site 849
(11.5-12.5 Ma)
Nazca Plate
GSC
GI
Chortís Block
CAVA
Caribbean Sea
CLIP
Pacific Ocean
NVZ
500 km
(a)
20° N
15°
10°
5°
0°
115° W
110°
105°
100°
95°
90°
85°
80°
Site 1256
0°
10°
20°
30°
40° S
NVZ
SEC
STW
HC
CVZ
north
trans.
south
Pacific Ocean
SVZ
1000 km
(b)
90° W
80°
70°
60°

Figure 2

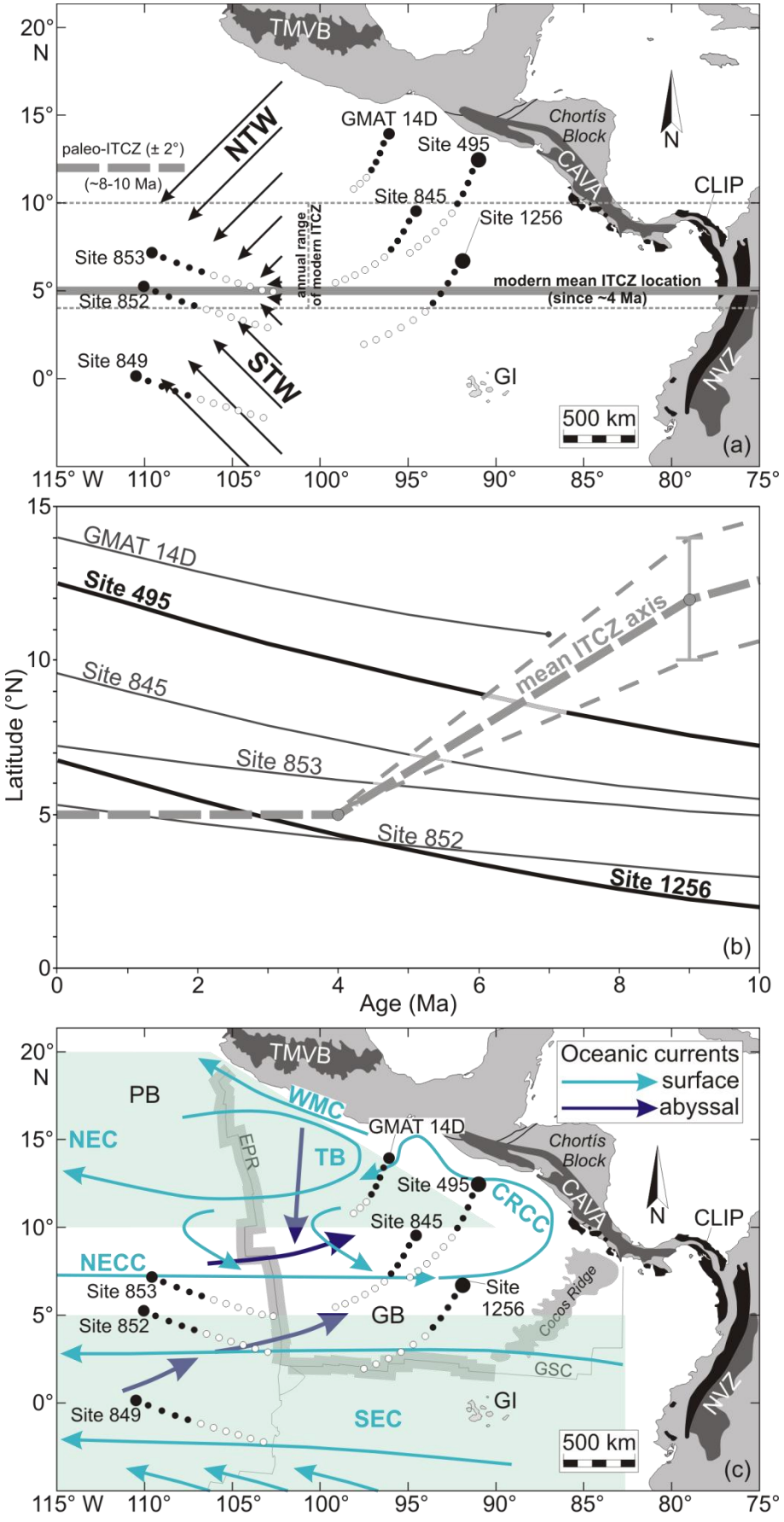
TMVB
GMAT 14D
Site 495
Chortís Block
CAVA
CLIP
N
paleo-ITCZ (± 2°)
(~8-10 Ma)
NTW
annual range of modern ITCZ
Site 845
Site 1256
Site 853
Site 852
modern mean ITCZ location (since ~4 Ma)
Site 849
STW
GI
NVZ
500 km
(a)
115° W
110°
105°
100°
95°
90°
85°
80°
75°
20° N
15°
10°
5°
0°
GMAT 14D
Site 495
Site 845
Site 853
Site 852
Site 1256
mean ITCZ axis
Latitude (°N)
Age (Ma)
(b)
Oceanic currents
surface
abyssal
PB
WMC
NEC
EPR
TB
CRCC
NECC
GB
Cocos Ridge
GSC
SEC
(c)

Figure 3

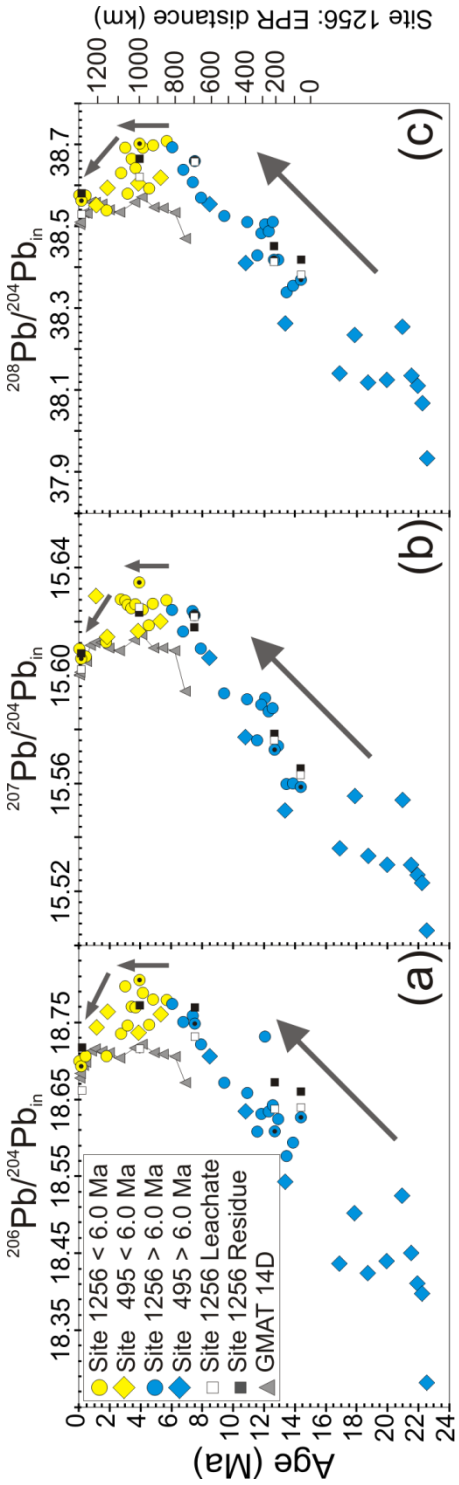
Site 1256: EPR distance (km)
0
200
400
600
800
1000
1200
(a)
(b)
(c)
$^{206}Pb/^{204}Pb_{in}$
$^{207}Pb/^{204}Pb_{in}$
$^{208}Pb/^{204}Pb_{in}$
Age (Ma)
Site 1256 < 6.0 Ma
Site 495 < 6.0 Ma
Site 1256 > 6.0 Ma
Site 495 > 6.0 Ma
Site 1256 Leachate
Site 1256 Residue
GMAT 14D

Figure 4

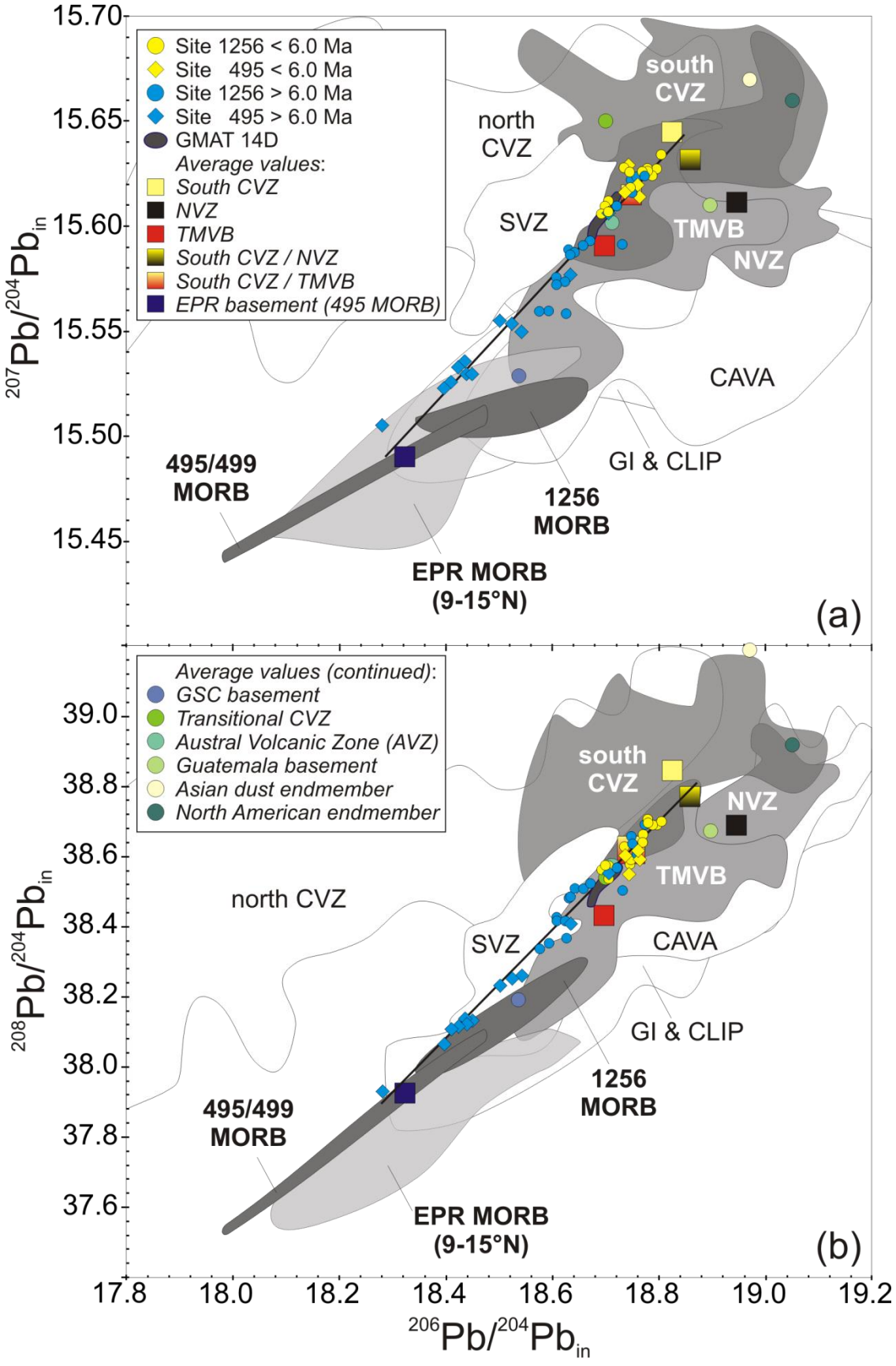
Site 1256 < 6.0 Ma
Site 495 < 6.0 Ma
Site 1256 > 6.0 Ma
Site 495 > 6.0 Ma
GMAT 14D
Average values:
South CVZ
NVZ
TMVB
South CVZ / NVZ
South CVZ / TMVB
EPR basement (495 MORB)
south CVZ
north CVZ
SVZ
TMVB
NVZ
CAVA
GI & CLIP
495/499 MORB
1256 MORB
EPR MORB (9-15°N)
(a)
Average values (continued):
GSC basement
Transitional CVZ
Austral Volcanic Zone (AVZ)
Guatemala basement
Asian dust endmember
North American endmember
south CVZ
NVZ
TMVB
north CVZ
SVZ
CAVA
GI & CLIP
1256 MORB
495/499 MORB
EPR MORB (9-15°N)
(b)
15.70
15.65
15.60
15.55
15.50
15.45
207Pb/204Pbin
39.0
38.8
38.6
38.4
38.2
38.0
37.8
37.6
208Pb/204Pbin
17.8
18.0
18.2
18.4
18.6
18.8
19.0
19.2
206Pb/204Pbin

Figure 5

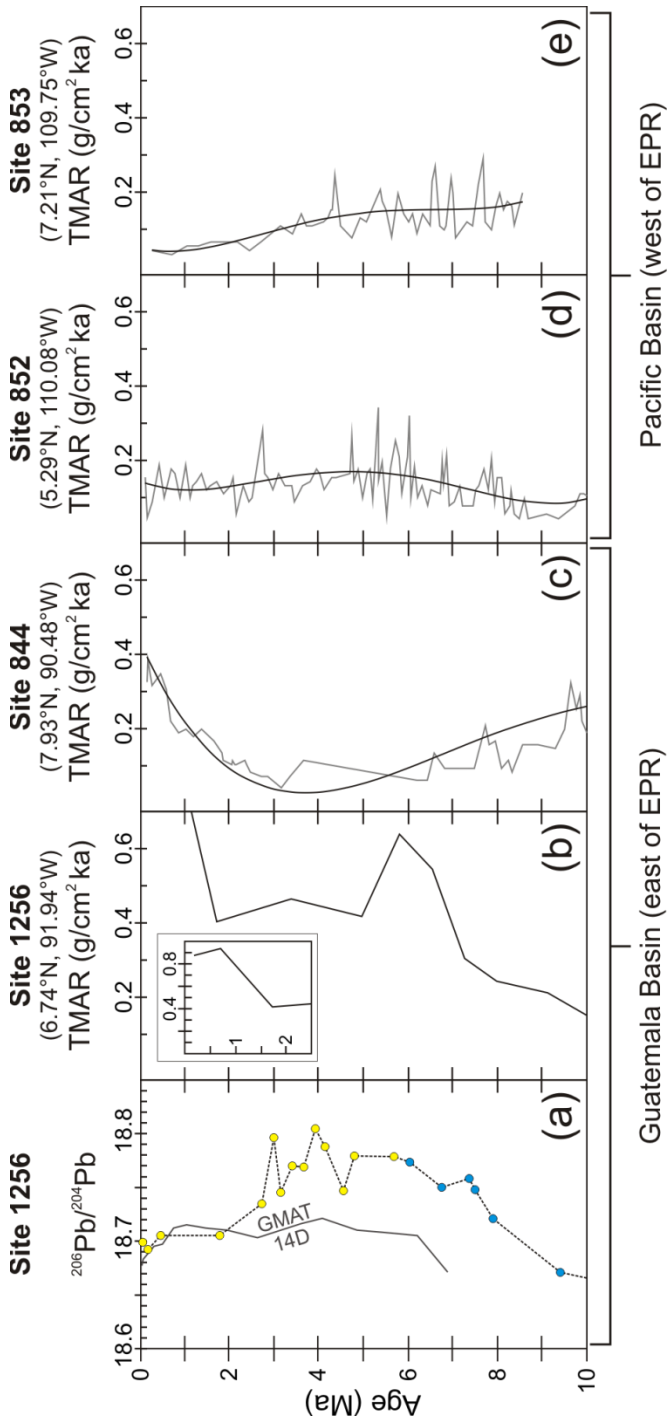
Site 1256
(6.74°N, 91.94°W)
Site 844
(7.93°N, 90.48°W)
Site 852
(5.29°N, 110.08°W)
Site 853
(7.21°N, 109.75°W)
TMAR (g/cm² ka)
$^{206}Pb/^{204}Pb$
GMAT
14D
Age (Ma)
(a)
(b)
(c)
(d)
(e)
Guatemala Basin (east of EPR)
Pacific Basin (west of EPR)

Table 1

Sample interval details, inferred biostratigraphic ages, lithology, and appropriate microfossil species used for age determinations of studied samples from both sediment cores. mbsf = meters below seafloor, FO = first occurrence, LO = last occurrence.

Site/hole	Core/ section	Interval (cm)	Depth (mbsf)	Biostrati-graphic age estimate (Ma)	Appropriate linear sedimentation rate (m/Ma)*	Lithology†	Appropriate biohorizon, with mean depth and age, used for calculation of biostratigraphic ages	Reference for microfossil species	Reference for microfossil datum level
1256A	1H-1	32–34	0.32	0.04	11.8	Nannofossil silty clay with diatoms	LO *Pseudoemiliania lacunosa* (5.28 mbsf, 0.46 Ma)	Jiang and Wise, 2007	Berggren et al., 1995a
1256A	1H-2	19–21	1.69	0.16	11.8	Nannofossil silty clay with diatoms			
1256B	1H-4	56–58	5.06	0.44	11.8	Nannofossil silty clay			
1256B	3H-2	34–36	17.44	1.76	6.1	Clayey nannofossil ooze with major abundance of colorless volcanic glass, quartz & feldspar	LO *Calcidiscus macintyrei* (16.38 mbsf, 1.59 Ma)	Jiang and Wise, 2007	Berggren et al., 1995a
1256B	3H-6	09–10	23.19	2.71	6.1	Clayey nannofossil ooze			
1256B	3H-7	23–24	24.83	2.98	6.1	Clayey nannofossil ooze			
1256B	4H-1	67–68	25.77	3.13	6.1	Sandy silty clay			
1256B	4H-2	75–76	27.35	3.39	6.1	Sandy silty clay			
1256B	4H-3	83–84	28.93	3.65	6.1	Sandy silty clay			
1256B	4H-4	90–92	30.50	3.90	6.1	Sandy silty clay			
1256B	4H-5	72–73	31.82	4.12	6.1	Sandy silty clay			
1256B	4H-7	24-25	34.34	4.53	6.1	Sandy silty clay			
1256B	5H-1	124–126	35.84	4.78	6.1	Sandy silty nannofossil ooze			
1256B	5H-6	92–94	43.02	5.67	13.2	Nannofossil ooze with diatoms	LO *Discoaster quinqueramus* (42.13 mbsf, 5.60 Ma)	Jiang and Wise, 2007	Berggren et al.,1995b
1256B	6H-3	59–61	47.69	6.02	13.2	Nannofossil ooze with diatoms			
1256B	7H-3	54–56	57.14	6.74	13.2	Diatom nannofossil ooze			
1256B	8H-2	66–68	65.26	7.35	13.2	Nannofossil ooze with diatoms			
1256B	8H-5	89–91	66.99	7.48	13.2	Nannofossil ooze with diatoms			
1256B	9H-2	79–81	74.89	7.89	8.4	Clayey nannofossil ooze with silt	FO *Discoaster berggrenii* (80.88 mbsf, 8.60 Ma)	Jiang and Wise, 2007	Berggren et al.,1995b
1256B	10H-4	95–97	87.55	9.39	8.4	Sandy silty nannofossil diatom ooze			

Table 1. (*continued*)

Site/hole	Core/ section	Interval (cm)	Depth (mbsf)	Biostrati-graphic age estimate (Ma)	Appropriate linear sedimentation rate (m/Ma)*	Lithology†	Appropriate biohorizon, with mean depth and age, used for calculation of biostratigraphic ages	Reference for microfossil species	Reference for microfossil datum level
1256B	12H-5	51–53	107.61	10.88	39.1	Nannofossil ooze	LO *Sphenolithus heteromorphus* (213.78 mbsf, 13.60 Ma)	Jiang and Wise, 2007	Berggren et al.,1995b
1256B	15H-3	37–39	132.97	11.53	39.1	Nannofossil ooze			
1256B	16H-3	132–134	143.42	11.80	39.1	Clayey nannofossil ooze			
1256B	17H-3	111–113	152.71	12.04	39.1	Nannofossil ooze			
1256B	19X-2	53–55	162.13	12.28	39.1	Nannofossil ooze with diatoms and silty clay			
1256B	20X-5	101–103	172.21	12.54	39.1	Clayey nannofossil ooze with silt			
1256B	21X-2	95–97	177.25	12.67	39.1	Nannofossil ooze with diatoms			
1256B	22X-2	45–47	185.95	12.89	39.1	Nannofossil ooze			
1256B	24X-3	79–81	207.19	13.43	39.1	Nannofossil ooze			
1256B	26X-1	89–91	223.59	13.85	39.1	Nannofossil ooze			
1256B	28X-2	54–56	243.64	14.36	39.1	Nannofossil ooze			
495	3R-5	76-77	25.76	1.11	37	Diatomaceous hemipelagic mud	LO *Discoaster brouweri* (57.0 mbsf, 1.95 Ma)	von Huene et al., 1982	Berggren et al., 1995a
495	6R-4	34–35	52.34	1.82	37	Biogenic silty mud			
495	9R-5	40–41	82.40	3.83	20	Diatomaceous silty mud	FO *Ceratolithus acutus* (112.60 mbsf, 5.34 Ma)	von Huene et al., 1982	Berggren et al., 1995a
495	12R-5	63–64	111.13	5.27	20	Siliceous mud			
495	15R-6	102–103	141.52	8.44	7	Diatomaceous mud	FO *Globorotalia plesiotumida* (142.50 mbsf, 8.58 Ma)	von Huene et al., 1982	Lourens et al., 2004
495	18R-7	61–62	171.11	10.77	11	Siliceous mud	LO *Discoaster kugleri* (179.10 mbsf, 11.50 Ma)	von Huene et al., 1982	Berggren et al.,1995b
495	21R-7	29–30	199.29	13.34	11	Nannofossil ooze			
495	24R-7	20–21	227.70	16.89	27	Nannofossil-foraminiferal ooze	LO *'Paragloborotalia' kugleri* (342.0 mbsf, 21.12 Ma)	von Huene et al., 1982	Lourens et al., 2004
495	27R-5	115–118	254.15	17.87	27	Nannofossil ooze			
495	30R-2	41–42	277.41	18.73	27	Foraminiferal-nannofossil ooze and chalk			
495	33R-5	41–42	310.41	19.95	27	Nannofossil ooze			
495	36R-4	50–51	337.50	20.95	27	Nannofossil ooze–chalk			
495	39R-3	108–109	365.08	21.50	58	Nannofossil-foraminiferal chalk			
495	41R-6	53–54	388.03	21.91	58	Foraminiferal-nannofossil chalk			
495	43R-5	24–25	405.24	22.21	58	Foraminiferal-nannofossil chalk with dendritic manganese			
495	45R-4	25–26	422.75	22.51	58	Foraminiferal-nannofossil chalk with dendritic manganese			

Table 2

Table 2
Pb, Th, U concentrations (in µg/g [= ppm]) and Pb (double spike) isotope analyses of studied samples including bulk sediment, residue (res), and leachate (lea) Pb isotope ratios. Displayed age estimates are biostratigraphic ages determined from calculations involving appropriate biohorizons of microfossil species and corresponding linear sedimentation rates. Details are provided in Tab. 1.

Hole/core/section, interval (cm)	Age (Ma)	Pb	Th	U	$^{206}Pb/^{204}Pb$	2σ	$^{207}Pb/^{204}Pb$	2σ	$^{208}Pb/^{204}Pb$	2σ	$^{206}Pb/^{204}Pb_{in}$	$^{207}Pb/^{204}Pb_{in}$	$^{208}Pb/^{204}Pb_{in}$
ODP Leg 206, Site 1256													
1256A-1H-1, 32-34	0.04	13.3	3.06	1.06	18.6988	0.0006	15.6097	0.0007	38.5755	0.0016	18.6988	15.6097	38.5754
1256A-1H-2, 19-21	0.16	15.1	3.08	0.84	18.6921	0.0007	15.6061	0.0006	38.5631	0.0012	18.6921	15.6061	38.5630
1256A-1H-2, 19-21_res	0.16				18.7167	0.0008	15.6080	0.0008	38.5792	0.0026			
1256A-1H-2, 19-21_lea	0.16				18.6609	0.0006	15.6020	0.0006	38.5281	0.0018			
1256B-1H-4, 56-58	0.44	13.4	2.50	0.73	18.7053	0.0005	15.6071	0.0005	38.5746	0.0024	18.7051	15.6070	38.5743
1256B-3H-2, 34-36	1.76	1.64	0.93	0.30	18.7083	0.0008	15.6123	0.0009	38.5407	0.0016	18.7051	15.6122	38.5374
1256B-3H-6, 09-10	2.71	17.5	3.26	0.92	18.7360	0.0004	15.6281	0.0004	38.6304	0.0010	18.7345	15.6280	38.6288
1256B-3H-7, 23-24	2.98	13.8	3.08	0.89	18.7980	0.0004	15.6276	0.0004	38.6929	0.0013	18.7961	15.6275	38.6907
1256B-3H-7, 23-24*	2.98				18.7980	0.0004	15.6280	0.0004	38.6938	0.0009			
1256B-4H-1, 67-68	3.13	17.7	3.11	0.84	18.7466	0.0005	15.6260	0.0005	38.5802	0.0011	18.7451	15.6260	38.5784
1256B-4H-2, 75-76	3.39	10.7	2.02	0.58	18.7716	0.0005	15.6249	0.0006	38.6655	0.0017	18.7697	15.6248	38.6634
1256B-4H-3, 83-84	3.65	16.1	3.03	0.76	18.7704	0.0005	15.6263	0.0004	38.6431	0.0011	18.7687	15.6262	38.6409
1256B-4H-4, 90-92	3.90	1.26	0.30	0.08	18.8065	0.0005	15.6344	0.0005	38.7033	0.0012	18.8043	15.6343	38.7004
1256B-4H-4, 90-92_res	3.90				18.7714	0.0005	15.6231	0.0004	38.6665	0.0012			
1256B-4H-4, 90-92_lea	3.90				18.7151	0.0005	15.6250	0.0005	38.6221	0.0016			
1256B-4H-5, 72-73	4.12	13.8	2.83	0.73	18.7898	0.0010	15.6243	0.0012	38.6931	0.0039	18.7876	15.6242	38.6904
1256B-4H-7, 24-25	4.53	14.1	5.64	1.87	18.7526	0.0005	15.6189	0.0005	38.5973	0.0013	18.7467	15.6186	38.5914
1256B-5H-1, 124-126	4.78	14.6	2.77	0.68	18.7812	0.0008	15.6265	0.0006	38.6992	0.0016	18.7790	15.6264	38.6964
1256B-5H-6, 92-94	5.67	10.4	2.63	1.39	18.7858	0.0007	15.6281	0.0007	38.7114	0.0022	18.7784	15.6277	38.7068
1256B-6H-3, 59-61	6.02	7.66	1.29	1.61	18.7855	0.0007	15.6247	0.0006	38.6948	0.0016	18.7732	15.6241	38.6916
1256B-7H-3, 54-56	6.74	8.43	1.89	1.01	18.7577	0.0008	15.6164	0.0009	38.6416	0.0025	18.7498	15.6161	38.6367
1256B-8H-2, 66-68	7.35	3.47	0.84	0.32	18.7645	0.0009	15.6240	0.0009	38.6122	0.0025	18.7580	15.6237	38.6064
1256B-8H-5, 89-91	7.48	6.35	1.47	0.46	18.7530	0.0007	15.6225	0.0006	38.6636	0.0016	18.7476	15.6222	38.6580
1256B-8H-5, 89-91_res	7.48				18.7688	0.0009	15.6176	0.0008	38.6629	0.0024			
1256B-8H-5, 89-91_lea	7.48				18.7308	0.0013	15.6215	0.0014	38.6616	0.0044			
1256B-9H-2, 79-81	7.89	4.24	0.86	0.30	18.7263	0.0007	15.6100	0.0007	38.5738	0.0021	18.7207	15.6098	38.5685
1256B-10H-4, 95-97	9.39	11.5	1.30	0.43	18.6743	0.0009	15.5934	0.0010	38.5275	0.0028	18.6708	15.5932	38.5239
1256B-12H-5, 51-53	10.88	3.40	0.45	1.43	18.7025	0.0007	15.5931	0.0006	38.5138	0.0014	18.6575	15.5910	38.5091
1256B-15H-3, 37-39	11.53	1.93	0.16	0.25	18.6221	0.0007	15.5765	0.0006	38.4308	0.0016	18.6073	15.5758	38.4278
1256B-16H-3, 132-134	11.80	1.81	0.12	0.21	18.6440	0.0013	15.5896	0.0013	38.4846	0.0040	18.6303	15.5890	38.4820
1256B-17H-3, 111-113	12.04	1.89	0.11	0.32	18.7516	0.0009	15.5924	0.0008	38.5061	0.0020	18.7312	15.5915	38.5039
1256B-19X-2, 53-55	12.28	1.93	0.15	1.20	18.7087	0.0006	15.5900	0.0006	38.4893	0.0015	18.6334	15.5865	38.4863
1256B-20X-5, 101-103	12.54	1.05	0.08	0.48	18.6987	0.0006	15.5903	0.0005	38.5128	0.0012	18.6416	15.5877	38.5096
1256B-21X-2, 95-97	12.67	2.61	0.11	0.64	18.6382	0.0009	15.5737	0.0008	38.4190	0.0021	18.6077	15.5723	38.4172
1256B-21X-2, 95-97_res	12.67				18.6715	0.0012	15.5782	0.0011	38.4522	0.0028			
1256B-21X-2, 95-97_lea	12.67				18.6367	0.0020	15.5758	0.0019	38.4139	0.0052			
1256B-22X-2, 45-47	12.89	2.84	0.14	0.32	18.6377	0.0010	15.5743	0.0010	38.4192	0.0025	18.6235	15.5737	38.4171
1256B-24X-3, 79-81	13.43	2.05	0.09	0.17	18.5864	0.0006	15.5601	0.0006	38.3397	0.0017	18.5755	15.5596	38.3377
1256B-24X-3, 79-81*	13.43				18.5880	0.0006	15.5612	0.0007	38.3444	0.0023			
1256B-26X-1, 89-91	13.85	1.76	0.13	0.07	18.5980	0.0006	15.5601	0.0005	38.3571	0.0012	18.5930	15.5598	38.3537
1256B-28X-2, 54-56	14.36	5.22	0.21	0.09	18.6282	0.0008	15.5587	0.0007	38.3701	0.0021	18.6258	15.5585	38.3682
1256B-28X-2, 54-56_res	14.36				18.6595	0.0009	15.5654	0.0010	38.4190	0.0029			
1256B-28X-2, 54-56_lea	14.36				18.6387	0.0008	15.5630	0.0007	38.3820	0.0018			
DSDP Leg 67, Site 495[†]													
495-3R-5, 76-77	1.11	5.86	2.15	5.87	18.7543	0.0007	15.6298	0.0009	38.5514	0.0030	18.7433	15.6293	38.5501
495-6R-4, 34-35	1.82	8.61	2.73	7.36	18.7791	0.0010	15.6148	0.0011	38.5942	0.0036	18.7637	15.6141	38.5923
495-9R-5, 40-41	3.83	9.69	3.03	5.50	18.7579	0.0012	15.6173	0.0012	38.6071	0.0034	18.7363	15.6163	38.6032
495-12R-5, 63-64	5.27	11.2	4.30	4.46	18.7811	0.0008	15.6208	0.0008	38.6240	0.0020	18.7604	15.6198	38.6174
495-15R-6, 102-103	8.44	9.76	2.51	4.18	18.7414	0.0008	15.6080	0.0010	38.5599	0.0030	18.7056	15.6064	38.5528
495-18R-7, 61-62	10.77	12.4	3.25	1.97	18.6509	0.0009	15.5778	0.0011	38.4180	0.0035	18.6339	15.5770	38.4087
495-21R-7, 29-30	13.34	3.26	0.22	0.16	18.5488	0.0008	15.5501	0.0009	38.2642	0.0028	18.5422	15.5498	38.2613
495-24R-7, 20-21	16.89	5.85	0.38	0.16	18.4400	0.0009	15.5360	0.0010	38.1426	0.0035	18.4355	15.5358	38.1390
495-27R-5, 115-118	17.87	6.13	0.44	0.13	18.5049	0.0007	15.5553	0.0009	38.2371	0.0027	18.5013	15.5551	38.2330
495-30R-2, 41-42	18.73	4.47	0.25	0.10	18.4271	0.0008	15.5331	0.0007	38.1200	0.0022	18.4230	15.5330	38.1167
495-33R-5, 41-42	19.95	1.55	0.08	0.13	18.4545	0.0005	15.5304	0.0004	38.1265	0.0012	18.4387	15.5297	38.1232
495-36R-4, 50-51	20.95	1.45	0.06	0.13	18.5428	0.0010	15.5546	0.0011	38.2559	0.0036	18.5239	15.5537	38.2529
495-39R-3, 108-109	21.50	7.57	0.01	0.08	18.4515	0.0007	15.5297	0.0009	38.1335	0.0028	18.4493	15.5296	38.1334
495-41R-6, 53-54	21.91	1.13	0.09	0.20	18.4471	0.0006	15.5276	0.0005	38.1146	0.0016	18.4097	15.5259	38.1090
495-41R-6, 53-54*	21.91				18.4493	0.0005	15.5284	0.0004	38.1175	0.0010			
495-43R-5, 24-25	22.21	2.20	0.09	0.08	18.4041	0.0008	15.5233	0.0008	38.0693	0.0025	18.3964	15.5230	38.0662
495-45R-4, 25-26	22.51	8.32	0.19	0.36	18.2899	0.0008	15.5057	0.0010	37.9331	0.0035	18.2803	15.5053	37.9315

Sample numbers with * are replicate analyses on separate sample dissolutions. [†]Pb, Th, U concentrations of DSDP Site 495 are taken from Patino et al. (2000). σ = sigma internal analytical error.

CHAPTER III

The geochemical evolution of Cocos Plate sedimentation and its paleoceanographic implications

Tobias W. Höfig [a,*], Kaj Hoernle [a], Martin Frank [a], Folkmar Hauff [a], and Andreas Klügel [b]

[a] *GEOMAR Helmholtz Centre for Ocean Research Kiel, Wischhofstr. 1-3, D-24148 Kiel, Germany*
[b] *University of Bremen, PO box 330440, D-28334 Bremen, Germany*
[*] *Current address: Department of Mineralogy, TU Bergakademie Freiberg, Brennhausgasse 14, D-09599 Freiberg, Germany*

in preparation

Abstract

Here we present a combined major and trace element and Sr-Nd-Hf isotopic record of Ocean Drilling Program (ODP) Site 1256, which is complemented by new Sr-Nd data from Deep Sea Drilling Project (DSDP) Site 495, together covering the history of eastern equatorial Pacific (EEP) Cocos Plate sedimentation in the Guatemala Basin of the past ~23 Ma. The Sr-Nd isotope data of bulk sediments of both cores reveal distinct isotopic trends and a major change at ~10.8 Ma, reflecting the transition from carbonate- to terrigenous sediment-dominated deposition. The inflections of the isotopic trend are interpreted to reflect changes in deep-water circulation related to the closure of the Central American Seaway for deep-water exchange, which led to establishment of a deep-water gyre circulating in the Guatemala Basin. These changes at depth also gave rise to changes in source provenance of the particles reflected by Nd and Sr isotopes, favoring southern Mexican, Central American, and northern South American continental arc sources after 10.8 Ma and more southern Andean Arc sediment input prior to that time. Eolian supply is shown to have been an insignificant pathway for the delivery of particles to the studied sites. In addition, exchange processes at the continental margin are invoked to be a major pathway of dissolved Nd input into the eastern equatorial Pacific.

1 Introduction

For more than three decades, radiogenic isotopic compositions of elements such as Nd, Sr, or Hf that occur in differing amounts in seawater have extensively been used to decipher the chemical history of the oceans. Given the global mixing time of the ocean of ~1500 years (e.g., Broecker et al., 1982), metals having short to intermediate residence times in seawater on the order of 10^3 years or less, such as Nd and Hf, have particularly been proven to be important tools for the investigation of large-scale paleoceanographic and continental

weathering processes (Frank, 2002, and references therein). The vast Pacific Ocean has been subject of studies focusing on the reconstruction of water mass compositions as a function of ocean circulation and water mass mixing (e.g., Abouchami et al., 1997; Lee et al., 1999; van de Flierdt et al., 2004a; Zimmermann et al., 2009; Jeandel et al., 2013; Noble et al., 2013), as well as circum-Pacific sources and input pathways of detrital sediments supplied to the marine realm (e.g., Nakai et al., 1993; Jones et al., 1994; Lacan and Jeandel, 2001; Pettke et al., 2002; Ling et al., 2005; Stancin et al., 2006) on various time-scales. For the latter, Sr isotopes have been combined with Nd isotopes to track sediment sources (e.g., Nakai et al., 1993; Dou et al., 2012; Jiang et al., 2013), whereas tracking of waters masses is not possible with Sr isotopes given its long oceanic residence time of several million years (cf. Frank, 2002).

While the western, central, and northern parts of the Pacific Ocean are relatively well understood in terms of source provenance of detrital inputs including Asian dust (e.g., Stancin et al., 2006, and references therein), distinct sources and input modes for the eastern equatorial Pacific (EEP) have long remained poorly studied. However, by means of bulk sediment Pb isotope ratios, Pichat et al. (2014) and Höfig et al. (in preparation; see Chapter II) have recently shed light on short- and long-term changes in sources and pathways in the EEP, demonstrating the predominant role of Andean Arc sources and eolian input for terrigenous Pb and the major impact of atmospheric changes on the temporal evolution of Pb isotopic signatures. Höfig et al. (in preparation) have also revealed the importance of hydrothermal material as the ultimate source of the unradiogenic Pb component in the Guatemala Basin over the past ~23 million years. In addition, they showed that changes in Pb isotopic composition took place irrespective of variations in sediment type through time.

To assess the impact of sedimentation on other radiogenic isotope systems, we have investigated the Neogene to Quaternary Sr-Nd-Hf isotopic evolution of EEP bulk sediments recovered from Deep Sea Drilling Project (DSDP) Site 495 and Ocean Drilling Program/Integrated Ocean Drilling Program (ODP/IODP) Site 1256 and document the ~23 Ma history of Cocos Plate sedimentation. By adding major and trace element data of Site 1256, the present study is the first to provide a comprehensive geochemical data set for the sedimentary evolution of this location in the EEP. The new Sr-Nd-Hf isotope data provide clear constraints on the variable contributions of different sediment sources through time, which most likely reflects changes in EEP deep-water circulation.

2 Geological and oceanographic background

Approximately ~700 km apart from each other, both DSDP Site 495 (12°29.8’N, 91°2.3’W) and ODP/IODP Site 1256 (6°44.2’N, 91°56.1’W) are located in the Guatemala Basin on the Cocos Plate (Fig. 1a), which formed by the break-up of the Farallon Plate ~23 Ma ago (Handschumacher, 1976). The age of the oceanic basement at Site 495 roughly coincides with the initial phase of Cocos Plate crustal accretion, as its formation has been dated at 22.5–23 Ma, based on marine magnetic anomalies (von Huene et al., 1982; Geldmacher et al., 2008, 2013). Using the same method, the seafloor hosting Site 1256

formed at ~15.2 Ma (Wilson, 1996). Resulting from northeastward tectonic migration of the Cocos Plate, which is subject to subduction beneath southern Mexico and Central America, both studied sites have moved toward Central America at rates of 7–9 cm/a (DeMets et al., 1990) since the beginning of sedimentation immediately after formation of the oceanic crust.

The sediment package of Site 495 amounts to a total thickness of 428 m and was recovered during DSDP Leg 67 (Coulbourn et al., 1982), and the bore hole was positioned on a horst at a seaward distance of only 22 km to the Guatemala Trench axis at a water depth of 4140 m. There are two distinct sedimentary successions at Site 495. The lower part, being Early to Middle Miocene in age, is 251 m thick and consists of calcareous ooze and chalk with Fe-Mn precipitates and chert in the basal core sections. In contrast, Middle Miocene brown abyssal clay and Late Miocene to Quaternary terrigenous mud, including diatoms and radiolarians with subordinate tephra particles, characterize the upper 177 m of the sediment column (von Huene et al., 1982).

About 830 km offshore Costa Rica in WSW direction, ODP Leg 206 penetrated the 250 m thick sediment succession at Site 1256 at a water depth of 3635 m (Wilson et al., 2003). The oceanic basement at Site 1256 formed close to the equator within the equatorial zone of high bioproductivity giving rise to a high bulk sedimentation rate of ~39 m/Ma during the Middle Miocene (Wilson et al., 2003; Jiang and Wise, 2007). Consequently, the basal unit of the sediment package is made up of 210 m of pelagic biogenic ooze, comprising calcareous nannofossils with intercalations of diatomaceous ooze (Wilson et al., 2003). As a consequence of the tectonic movement of the Cocos Plate, Site 1256 left the high-productivity zone and, consequently, the abundance of carbonate in the sediment decreased, whereas the relative proportion of clastic material increased. Therefore, the upper unit of the sediments at Site 1256 is characterized by a 40 m thick layer of terrigenous sandy to silty clay with varying minor amounts of biogenic particles (mainly calcareous nannofossils) and disseminated volcanic glass shards (Wilson et al., 2003). The onset of this strongly terrigenous sedimentation at ~5.5 Ma roughly corresponds to the Miocene-Pliocene boundary (Jiang and Wise, 2007). In summary, following the downhole sediment descriptions (Wilson et al., 2003), the terrigenous sediment package is subdivided into an upper Unit I (0–40.6 meters below seafloor, mbsf), consisting of Subunits IA (0–17.48 mbsf; nannofossil-rich silty clay) and IB (17.48–40.6 mbsf; generally sandy silty clay with a lower proportion of nannfossils compared to IA), whereas the predominantly biogenic ooze (with minor clay) below is referred to as Unit II (40.6–250.7 mbsf).

Surface currents in the study area, which potentially affect sediment supply, form in response to two prevailing wind systems. The Northeast and Southeast Trade Winds (N/STW) account for the present surface water circulation pattern in the EEP (Fig. 2). These wind systems meet at the Intertropical Convergence Zone (ITCZ; Fig. 2), which has an average annual location at ~5°N (Rea, 1994; Hovan, 1995). The trade winds force the equatorial waters in both hemispheres to flow westward (Fig. 2), establishing the North Equatorial Current (NEC; north of the ITCZ) and the South Equatorial Current (SEC; south of the ITCZ), respectively (reviewed by Kessler, 2006). Between them, the North Equatorial

Countercurrent (NECC) moves surface water eastward in the zone of light winds (i.e., the ITCZ; Fig. 2). The SEC is fed by the Humboldt Current (Kessler, 2006), originating from offshore SW South America and deflected northwestward by the STW (Garcia, 1994), which form close to the southern part of the Central Andes and are directed toward the equator (Fig. 1b). The NEC governs Pacific surface water masses north of ~10°N with strongly westward zonal flow commencing west of c. 120°W (Fig. 2). However, the eastern Central Pacific (i.e., the study area) is characterized by a complex circulation pattern due to the collapse of the strictly zonal wind system and the establishment of weaker meridional winds east of 110°W, showing a gyre-like character and revealing seasonally fluctuating intensities (Kessler, 2006). This leads to a complex surface water circulation system in the Guatemala Basin transporting water masses mainly along N-S routes (Kessler, 2006) and thus essentially in opposite direction to the comparatively simple SEC current system operating south of ~5°N (Fig. 2). There are two gyre-like surface water systems north of ~5°N, exchanging water masses and feeding the incoming eastward flowing NECC (Fig. 2). At depth in the water column, a latitudinal, eastward-directed deep water flow pattern likely characterizes the abyssal circulation in the modern central and eastern equatorial Pacific (Lonsdale, 1976, and references therein). It forms two major branches of bottom currents, which obviously cross the East Pacific Rise along transform faults immediately north of the Galápagos triple junction and at ~8°N (Fig. 2). Moreover, the deep water reservoir of the Guatemala Basin also receives some contributions by overflow dispersal from the Pacific Basin across the ridge crest of the East Pacific Rise (Lonsdale, 1976). In addition, a southward directed bottom current originates from offshore southern Mexico and moves adjacent to the parallel running eastern ridge flank of the East Pacific Rise (Lyle, 1992; Fig. 2), representing a second major flow direction in the present-day deep eastern Central Pacific.

3 Sample preparation and analytical methods

For the present study, 62 samples from Site 1256 and 16 samples from Site 495 were used, covering the entire sediment column intersected at each drilling location. All samples were recovered from the Gulf Coast Repository at Texas A&M University (College Station, Texas, USA). The sampling avoided distinct tephra layers to shed light on the long-lasting detrital processes and source variations. Details on lithology, depth intervals, and applied age models of the studied samples are given in Table 1.

Following an overnight drying step at 110 °C, a subset of 25 bulk samples from Site 1256 was selected for determination of major and some trace element concentrations (e.g., Sr, Ba) by X-ray fluorescence spectroscopy (XRF) on fused beads running a Philips X'Unique PW 1480 with Rh-tube at GEOMAR. Corresponding volatile contents (H_2O and CO_2) were analyzed in a Rosemount CSA 5003 infrared photometer. The obtained XRF data are provided in Table 2. Values (n = 6) of international rock standards (JA-2, JB-2, JB-3, and JR-1; see supplementary Tab. A.1, Appendix III) measured along with the sediment samples gave

an instrument reproducibility being better than 1 % (SiO_2, TiO_2, Al_2O_3, Fe_2O_3, MnO, CaO, Na_2O, K_2O, Sr), 2 % (MgO), 3 % (P_2O_5, Zn, Rb), 5 % (Co), and 10 % RSD (Ga, Ba).

Contents of 35 trace elements were determined on all 62 bulk samples from Site 1256 by inductively coupled plasma-mass spectrometry (ICP-MS) on a ThermoFinnigan Element2 at the Department of Geosciences, University of Bremen. Approximately 50 mg of powdered sample material were dissolved by pressurized digestion in a concentrated HF–aqua regia mixture in Teflon® beakers at 210 °C using a MLS Ethos microwave. The obtained analyte solution, which was spiked with 2.5 ng/ml indium as internal standard, contained 0.2 mg/ml of total dissolved solid corresponding to a final dilution factor of 1:5000. To avoid mass interferences, the middle through heavy REE and Hf were measured at high (10000), the transition metals at medium (4000), and all other trace elements at low (300) resolution. Data acquisition took place in nine passes with dwelling times ranging from 0.12 to 2.4 s for each element. Calibration of the instrument was done by using a mixture of pure element standards in a variety of dilutions. Determined trace element concentrations are displayed in Table 3. External precision as determined by repeated analyses of single aliquots is better than 5 % RSD for all elements and overall better than 3 % RSD for REE (see supplementary Tab. A.2, Appendix III). The results for the international rock standard BCR-2 (n = 9), processed and analysed along with the Site 1256 samples, can be compared to compiled and recommended values given in the GeoReM online database (http://georem.mpch-mainz.gwdg.de/ – June 30, 2014; Jochum et al., 2005; see supplementary Tab. A.3, Appendix III).

At GEOMAR, Sr-Nd isotope analyses were carried out on subsets of 38 and 16 bulk sediment samples from Site 1256 and Site 495, respectively, additionally including Hf isotope analysis, which was feasible on 9 of the Site 1256 bulk samples. All of these samples were dried over 48 hours at 50 °C. Subsequently, the dry sediment samples were packed in small glass tubes, each of which comprising between 0.8 and 1.2 g of sediment mass. No further grinding of the sediments was performed. Five of the bulk samples of Site 1256 with masses of c. 1.5 to 2.6 g were subject to a leaching process in order to obtain both the detrital fraction and the seawater-derived Sr-Nd fraction contained in Fe-Mn coatings of the particles.

The leaching process followed the procedure described in Gutjahr et al. (2007), modified by Stumpf et al. (2010), which covered a two-day procedure including a number of shaking and centrifugation steps in specific solutions. At first, carbonate was dissolved in 20 ml of a 15%-acetic acid/1M-Na acetate buffer solution (pH of ~4.1 for 1 h) followed by a triple rinse with deionized water. Afterwards, another 10 ml of the same acetate solution was added together with 10 ml of MQ water, introduced to overnight shaking (125 rot/min). Then, a NaOH-buffered (pH = 3.6) 0.05M-hydroxylamine hydrochloride/15%-acetic acid solution was put in to dissolve the ferromanganese (Fe-Mn) coatings. Subsequent to shaking for 1 h, the supernatant was pipetted into 30 ml Teflon® vials for further ion-chromatographic separation. The residual detrital material was then dried over 48 hours at 50 °C. Both bulk samples, which include all authigenic fractions and the residues obtained from the leaching process were dissolved in a 4:1 HF-HNO_3 mixture at 150 °C for 48 hours. The ion-chromatographic separation and purification of Sr, Nd, and Hf was implemented according to

the principles outlined in Hoernle et al. (2008) for Sr and Nd as well as in Geldmacher et al. (2006) for Hf.

Sr-Nd isotopic compositions were determined by thermal ionization mass spectrometry (TIMS) at GEOMAR using a Finnigan MAT 262 RPQ^{2+} (Sr, Nd) and Thermo Finnigan TRITON-TI (Nd), both of which operated in static multi-collection mode. Procedures for applied TIMS analyses are comprehensively described by Hoernle et al. (2011). Within-run errors are given as $2\sigma / \sqrt{n-1}$ (n = number of scans passing the outlier test) and all external errors, such as the reproducibility of standards, are displayed as 2σ of the mean (Tab. 4). Sr-Nd-Hf isotope analyses of selected samples were replicated by means of a separate digestion within the external two sigma errors of the standard values (Tab. 4). Mass bias correction of Sr and Nd isotope ratios took place within-run to $^{86}Sr/^{88}Sr = 0.1194$ and $^{146}Nd/^{144}Nd = 0.7219$, respectively. The Sr isotope data are reported relative to $^{87}Sr/^{86}Sr = 0.710250 \pm 0.000011$ (n = 49) for NBS987, while the Nd isotope data are given relative to $^{143}Nd/^{144}Nd = 0.511850 \pm 0.000007$ (n = 65) for La Jolla, yielded over the course of the project (2006–2012). Total chemistry blanks were <100 pg for Sr and Nd. Determination of Hf isotopic compositions was carried out on NU Instruments multi-collector ICP-MS at GEOMAR, running static multi-collection mode. Hf isotope ratios were mass bias corrected within-run to $^{179}Hf/^{177}Hf = 0.7325$. An in-house SPEX Hf ICP reference solution, normalized to JMC-475 ($^{176}Hf/^{177}Hf = 0.282163$; Blichert-Toft and Albarède, 1997), gave an average value of $^{176}Hf/^{177}Hf = 0.282170 \pm 0.000008$ (n = 51) during the measurement period (2011–2012). Since most of the carbonate-rich bulk sediment samples did not yield sufficient amounts of Hf to obtain reliable results, the Hf isotopic data set is mainly limited to siliciclastic bulk sediments.

All measured Sr-Nd-Hf isotope data are displayed in Table 4. Initial Sr-Nd-Hf isotopic compositions of the bulk sediments were calculated applying the algorithms outlined in Faure and Mensing (2005), while the leachate data were not decay corrected.

4 Results

The major and trace element data of the present study confirm previous shipboard and shore-based results from Wilson et al. (2003) and Ziegler and Murray (2007), respectively. The Site 1256 bulk sediment concentrations of major elements (expressed as wt% oxides) reflect the temporally varying proportions of the different sediment components (cf. Tabs. 1, 2). However, within the carbonate-rich Unit II, a clear chemical transition is revealed at ~10.8 Ma (Fig. 3), which has been termed a "chemical boundary" by Wilson et al. (2003). Whereas the CaO content abruptly dropped from almost 60 wt% to values being generally lower than 20 wt% (normalized; Fig. 3a), all other major element contents sharply increased at this point of time (e.g., Al_2O_3; Fig. 3c). This pattern is obviously related to the rapid decline in carbonate mass accumulation rate at ~10.8 Ma (Wilson et al., 2003; Jiang and Wise, 2007) and associated decrease in carbonate content (Fig. 3e), referred to as "carbonate crash" (Farrell et al., 1995; Lyle et al., 1995), which led to a corresponding increase in concentration

of terrigenous material (Fig. 3f) (Wilson et al., 2003). This is clearly exemplified by Al_2O_3 content versus age (Fig. 3c) with aluminum being virtually absent prior to ~10.8 Ma and showing values between 2 and 14 wt% thereafter, reflecting the enhanced clay-rich siliciclastic input. Notably, this is also true for Site 495 (Figs. 3a–d; Patino et al., 2000), pointing to a basin-wide chemical transition. Indeed, similar sedimentation patterns have also been demonstrated for other Guatemala Basin drilling sites (Farrell et al., 1995). The silica pattern is somewhat different from the terrigenously dominated major elements, since enrichment of silica is also associated with deposition of diatom mats at Site 1256 (Wilson et al., 2003). Therefore, prior to ~10.8 Ma, silica enrichments (and corresponding decreases in carbonate content) principally reflect intercalations of siliceous ooze, whereas, afterwards, the increase is mainly associated with the increasing amount of terrigenous material (Wilson et al., 2003). A hydrothermal contribution is likely reflected by the basal sample of the present study, showing an enhanced iron content of ~3.3 wt% Fe_2O_3, whereas the subsequent carbonate samples generally have iron contents < 1 wt% prior to ~10.8 Ma (Tab. 2). In general, all trace elements follow the chemical pattern reflected by the major elements, forming two distinct fractions being either enriched during carbonate-dominated deposition (e.g., Sr; Tab. 3, Fig. 3b) or during siliciclastic-dominated accumulation (e.g., Sc, Th, REE; Tab. 3; Fig. 3d). The only exceptions are two bulk siliciclastic samples (206-1256B-3H-2, 34–36 cm; 206-1256B-4H-4, 90–92 cm) reflecting contamination through disseminated volcanic glass particles (Tab. 3).

The initial Sr isotopic composition of the Site 495 bulk sediments ranged from 0.7067 to 0.7088, being fairly similar to Site 1256 with a range of 0.7061–0.7089 (Tab. 4, Fig. 4a). Bulk samples at both sites continuously followed the Neogene Sr isotopic seawater evolution prior to 10.8 Ma, being indistinguishable at the same age (Fig. 4a). However, after the chemical transition, bulk Sr isotopic compositions at both sites abruptly left the seawater curve and highly oscillated (Fig. 4a). This pattern reflects the high carbonate accumulation and carbonate content prior to 10.8 Ma as a consequence of the high seawater-derived Sr content of the carbonates and the decreasing and somewhat fluctuating carbonate concentration thereafter. On average, Site 495 Sr isotopic composition was somewhat less radiogenic during siliciclastic-dominated sedimentation but shows the same decreasing trend after 10.8 Ma (Fig. 4a). The least radiogenic Sr isotope ratio of Site 1256 corresponds to the sample with the highest content of volcanic glass, which deviates from the indicated trend (Fig. 4a). Leachate and residue samples obtained from Site 1256 follow the trend of the bulk samples, reflecting almost indistinguishable Sr isotopic compositions prior to 10.8 Ma and a pronounced divergence of seawater-derived (leachate) and detrital (residue) fractions afterwards (Fig. 4a). This shows that leachate samples of Site 1256 closely reflected the Sr isotopic seawater evolution over the entire sedimentary record and residue samples indicate a Sr isotope decrease during terrigenous deposition after 10.8 Ma. This is also reflected by the bulk samples, which, however, show a larger scatter, most likely due to variable contributions from carbonates.

The range in $^{143}Nd/^{144}Nd_{in}$ was generally larger for bulk samples of Site 495 (0.512352–0.512795) than for those of Site 1256 (0.512423–0.512681) (Tab. 4), but the two records overlapped prior to 10.8 Ma showing a common trend toward more radiogenic values (Fig. 4b). Expressing the initial Nd isotopic composition in terms of deviation from the Chondritic Uniform Reservoir (CHUR) at a given age of deposition, using a present-day CHUR value of 0.512638 (Jacobsen and Wasserburg, 1980), gives a range in $\varepsilon_{Nd}(T)$ from -5.04 to +3.11 (Fig. 4b inset). There was an abrupt increase in the bulk Nd isotopic composition at the chemical boundary between 10.88 and 10.77 Ma, based on the presented data set (Fig. 4b). Subsequently, the bulk Nd isotopic composition at Site 1256 rather showed a higher degree of variability compared with a nearby EEP Fe-Mn crust GMAT 14D (Fig. 4b). After 0.4 Ma, the bulk compositions approached the Fe-Mn crust data during the Late Pleistocene most likely due to higher carbonate contents, evident from the Site 1256 core descriptions (Wilson et al., 2003), and thus more seawater-like compositions. In contrast, the Site 495 bulk Nd isotope ratios show more radiogenic Nd isotopic compositions (Fig. 4b), which is supported by data from Vervoort et al. (2011). Site 1256 leachate and residue samples followed the evolution of the bulk samples (Fig. 4b). They displayed indistinguishable Nd isotope ratios prior to 10.8 Ma (Fig. 4b), suggesting that the seawater acquired the detrital sediment Nd isotopic composition through particle dissolution.

Site 1256 bulk sediment initial Hf isotopic compositions were obtained for sediments deposited after 10.8 Ma. During this period, they generally showed decreasing ratios with age ranging from 0.28306 to 0.28295 (Fig. 4c). However, this behavior is somewhat decoupled from both the Nd isotopic evolution of the same site and the Hf isotopic evolution shown by Site 495 bulk siliciclastic samples (Vervoort et al., 2011) (Figs. 4b/c). This is in contrast to the usual positive correlation of the Sm-Nd and Lu-Hf isotope systems along the terrestrial mantle-crust array (Vervoort et al., 1999, 2011). Furthermore, the decoupling in terms of Hf isotopes between Sites 495 and 1256 differs from the otherwise common bulk sediment isotopic evolution shown by the Nd isotope ratios. It is thus suggested that the Hf isotopic compositions revealed by Site 1256 bulk sediments most likely reflected incongruent weathering effects (e.g., van de Flierdt et al., 2007; Bayon et al., 2009) affecting the Hf isotopic signatures at Site 1256 but was less expressed at Site 495.

5 Discussion

The chemical transition during sedimentation in the Guatemala Basin, as revealed both by major and trace element concentrations and Sr-Nd isotope ratios, is also reflected on Pb-Nd and Sr-Nd isotope diagrams showing clear differences in isotopic patterns between samples older and younger than 10.8 Ma, being subject to mixing of different sources (Figs. 5a/b).

As shown by Höfig et al. (in preparation), submarine East Pacific Rise (EPR) mid-ocean ridge (MOR) hydrothermal and continental arc input from the Andes (Northern Volcanic Zone, South Central Volcanic Zone) and southern Mexico (Trans-Mexican Volcanic Belt) governed the Pb isotopic evolution of bulk sediments in the study area (see locations in Fig.

1). However, in contrast to the Pb isotope systematics, the local EPR MOR basement (Sites 495, 499, 1256) does not serve as an endmember for Nd in the record older than 10.8 Ma (Fig. 5a), supporting the insignificance of hydrothermal Nd input for the seawater budget due to near-vent scavenging, as demonstrated by previous studies (e.g., Michard et al., 1983; Rudnicki and Elderfield, 1993; van de Flierdt et al., 2004b). A direct delivery of hydrothermal Sr to the studied sites is not shown either by bulk samples on the isotope diagrams, since the older part of the sediment package, deposited closer to the EPR, was governed by the globally well-mixed Sr isotopic composition of seawater recorded by the carbonates (Fig. 5b).

As for Pb, the isotopic mixing relationships additionally exclude distant continental sources of North America (Figs. 5a/b) and central Asia (too unradiogenic in terms of Nd and too radiogenic with respect to Sr isotope systematics, plotting outside the present isotope diagrams) to play a role as supplier of continental Nd and Sr in the eastern equatorial Pacific (EEP). However, the Pb-Nd isotopic space indicates that the Andean Arc comes into consideration for input of Nd to the studied sites (Fig. 5a). Using the same latitudinal and isotopic subdivision of Andean Arc segments as applied by Pichat et al. (2014) and Höfig et al. (in preparation) (see Fig. 1b), it is conspicuous that both the Southern Volcanic Zone (SVZ) and adjacent South Central Volcanic Zone (South CVZ) did not significantly contribute to the Nd budget of the studied sediment successions. This is in partial contrast to the Pb isotopic evolution, which has revealed a major impact of the South CVZ on the detrital Pb input (Höfig et al., in preparation). In terms of Nd, the compositionally wide-ranging North Central Volcanic Zone (North CVZ) has exerted major influence (Fig. 5a). All samples deposited prior to the chemical transition at 10.8 Ma plot within the field of the North CVZ, showing a positive correlation of $^{206}Pb/^{204}Pb$ and $^{143}Nd/^{144}Nd$ with age revealing that younger Site 1256 samples are more radiogenic than older Site 495 samples. It is thus indicated that the North CVZ has formed the unradiogenic endmember prior to ~10.8 Ma. The combined record of Sites 495 and 1256 points to a radiogenic endmember derived from a source mixture of Central Pacific seawater (Fe-Mn crust VA13-2; Abouchami et al., 1997; Ling et al., 1997) and continental arc material from the Trans-Mexican Volcanic Belt (TMVB) and the Andean Northern Volcanic Zone (NVZ). Furthermore, a subordinate contribution of the Central American Volcanic Arc (CAVA) cannot be ruled out based on the Pb-Nd isotope systematics. This combined endmember is obviously represented by the EEP Fe-Mn crust GMAT 14D (Fig. 5a), located in the northern part of the Guatemala Basin (Fig. 1a). The fact that ≤ 7 Ma Fe-Mn crust GMAT 14D essentially serves as the radiogenic endmember for the > 10.8 Ma bulk sediment record in the EEP most likely indicates a presence of comparatively well-mixed EEP deep water as early as ~10.8 Ma. The decreasing influence of the North CVZ is likely a function of the northeastward migration of the studied sites implying an approach to other closer located continental arcs, such as NVZ and TMVB, as reflected by the course of the Pb-Nd isotopic mixing array of the sediments. Detrital and authigenic Nd isotopic compositions becoming more radiogenic from the Pacific area nearby the North CVZ to the latitudinal area of the NVZ have been demonstrated on ≤ 20 ka sediments of the Peru upwelling region reflecting compositional variations in the Andean geology (Ehlert et al., 2013). This is in

agreement with our results showing more radiogenic bulk signals with decreasing age, which may have been caused by the northeastward migration of the studied sites over time, being likely subject to an increasing impact of the NVZ in favor of the North CVZ.

The bulk samples deposited after 10.8 Ma, which form an inflected mixing array with considerably more radiogenic but variable $^{143}Nd/^{144}Nd$ values (compared to the period > 10.8 Ma) and rather narrowly ranging $^{206}Pb/^{204}Pb$ (Fig. 5a), indicated predominant mixing between an EEP seawater component reflected by GMAT 14D (still influenced by the North CVZ) and detrital Nd probably derived from an admixture of NVZ, TMVB, and CAVA material, when low carbonate and high terrigenous deposition established in the study area. Both the impact of Central Pacific seawater and continental arc sources, surrounding the Guatemala Basin, on the sediment deposition are confirmed by the Sr-Nd isotopic space (Fig. 5b). The continuous influence of the Central Pacific seawater corroborates the eastward heading deep-water circulation, demonstrated by Höfig et al. (in preparation) for the past ~23 million years in the study area. Central Pacific seawater plots close to the unradiogenic samples of the studied sediment record, indicating to be a likely source for the supply with well-mixed Pacific deep water in terms of Nd isotopic compositions. Moreover, the Sr-Nd isotope diagram nicely display that small but significant differences are indicated regarding the terrigenous endmember of both Sr and Nd. After 10.8 Ma, Site 1256 samples have rather pointed to an endmember dominated by the TMVB and possibly minor admixture of NVZ detritus, whereas the higher Nd isotope ratios at a given Sr isotopic composition of Site 495 samples reflect a stronger influence of terrigenous material derived from the CAVA and spatially closely associated uplifted fragments of the Caribbean Large Igneous Province (CLIP), being part of the basement along the southern Central American forearc (e.g., Hauff et al., 2000). The Sr-Nd isotopic plot additionally suggests that Nd from the North CVZ likely mainly reached the studied sites in dissolved form, since there is no isotopic relationship apparent from the plot indicating a significant particulate detrital input from the North CVZ (Fig. 5b).

Although showing a displacement away from the mantle-crust array, Hf isotopic compositions of Site 495 samples also indicate an influence of a combined CAVA-CLIP source, revealing a mixture between Site 1256 sediments and the Central American sources on the Nd-Hf isotope diagram (Fig. 5c). The likely effect of incongruent weathering on the Lu-Hf isotope system (i.e., retaining isotopically unradiogenic, weathering-resistant, Hf-hosting minerals on the continents) (e.g., van de Flierdt et al., 2007; Bayon et al., 2009) is clearly visible in the Nd-Hf isotopic space, being stronger at Site 1256 compared to Site 495, as mentioned above. This may indicate that efficient sediment sorting during terrigenous particle transport and longer exchange time with seawater has prevented Site 1256 from receiving a clearer Hf continental signal in comparison to Site 495 being located considerably closer to the continental slope of the Central American active margin.

Taking into account the Pb isotopic evolution of the studied sediments (Höfig et al., in preparation), the Sr-Nd-Pb isotope systematics provide clear constraints on input pathways and paleoceanographic events. Höfig et al. (in preparation) demonstrated a major Pb isotopic

change, which took place around 6 Ma, thus, almost 5 million years later than the chemical transition indicated by major and trace elements as well as Sr-Nd isotopic compositions of the same sediments. Höfig et al. (in preparation) related the inflection of the Pb isotopic trend to atmospheric changes. Therefore, the input of Sr and Nd into the Guatemala Basin may have been relatively unrelated to major changes in atmospheric circulation, given the temporal differences of isotopic trend inflections between Pb and Sr-Nd. Furthermore, given the lack of a major Nd contribution from the South CVZ and the long-term aridity in this area since the Early Miocene (Rech et al., 2006, 2010), it is strongly suggested that eolian input has been insignificant in the Neogene-Quaternary EEP for the supply of detrital Nd. This conclusion substantiates results from Jones et al. (1994) who suggested that eolian input has been of minor significance for the dissolved Nd isotopic composition of the NW Pacific. Conversely, the insignificance of the North CVZ for the Pb isotopic record suggests an input mechanism different from eolian particle delivery. We therefore interpret the North CVZ signal, preserved in the bulk sediments, to be a consequence of exchange with material from the ocean margin (Lacan and Jeandel, 2001; 2005), resulting from interaction of water masses with continental slope sediments and land-derived particles (Grasse et al., 2012) and the subsequent leaching and advection of dissolved elements by advecting water masses and preservation of this signal as authigenic coatings in the carbonates. Apparently, Nd is particularly susceptible for this process (e.g., Jeandel et al., 2013). Most likely, water masses associated with the large northwestward Humboldt Current flowing offshore relatively close to the northern Central Andes, being an overall persistent feature along the western South American margin (Garcia, 1994), may have been the carriers of dissolved Nd from the North CVZ margin to the eastern equatorial Pacific.

The same exchange mechanisms with ocean margins have most likely been responsible for the transport of Nd from the Central American margin (CAVA and CLIP) to nearby Site 495 and maybe partly to Site 1256. For Site 495, it has previously been suggested that terrigenous material has been transported within nepheloid layers, which may spread out laterally as suspension currents at near-surface to intermediate water depths. These layers have been interpreted to represent detachments from continental slope turbidite currents and may transport continental particles across deep-sea trenches into the open ocean (Heinemann and Füchtbauer, 1982; Shiki et al., 1982). These nepheloid layers may have delivered both dissolved and detrital Nd to the open ocean. It has recently been demonstrated that leaching of detrital sediment particles may favor release of less reactive but more radiogenic sedimentary components, e.g., volcanic particles, to seawater from the bulk material (e.g., Tachikawa et al., 2004; Wilson et al., 2013). This process may explain why the post-10.8 Ma bulk Nd isotopic signal, reflecting both terrigenous and minor carbonate components, is fairly radiogenic, particularly at Site 495, which is situated closer to the Central American trench. Moreover, the generally more radiogenic Nd isotopic compositions of Site 495, compared to Site 1256, likely reflect the overall higher abundance of dispersed tephra particles in the bulk sediments (cf. Cadet et al., 1982; Wilson et al., 2003). The lack of considerable Central American Pb contribution to the studied sites (Höfig et al., in preparation), obviously reflects

that either ocean margin exchange does not significantly mobilize sedimentary Pb or the input of this element to the slope sediments has been of minor importance throughout the study period due to likely comparatively low runoff in an area characterized by a flat relief during most of the Neogene (Webb, 1978, and references therein).

Pb presumably enters the ocean via riverine input only in areas of high continental runoff, as exemplified by the common role of the Northern Volcanic Zone as a source for both Nd and Pb in the study area. Both South American climatic studies and paleoecological reconstructions have yielded similar climatic conditions prevailing throughout the Neogene and Pliocene to the Quaternary with mainly tropical forests and minor woodland savannas in the area of the NVZ (reviewed and/or reconstructed by Webb, 1978; Andriessen et al., 1993; Janis, 1993; Garcia, 1994; Pound et al., 2011, 2012), leading to high mass wasting rates at the margin of the NVZ (Stern, 2004, and references therein). A combination of continental runoff and release of Nd from particles in response to the interplay with surface and deep currents is also suggested for detrital and dissolved Nd input from southern Mexico, i.e., the Trans-Mexican Volcanic Belt. In addition to the present surface-gyre in the EEP, an ancient equivalent to the proposed deep-water flow from the Mexican margin to the south along the course of the EPR (Lyle, 1992) may have formed a pathway for transporting Nd to the open ocean, as suggested for Pb (Höfig et al., in preparation).

The model proposed for the Sr-Nd isotopic evolution of Sites 495 and 1256 bulk sediments prior to ~10.8 Ma invokes a mixture between North CVZ and EEP deep water being fed by Central Pacific seawater, which dominated the bulk sediment signal due to high Sr content of the marine carbonates (Fig. 3b) and the formation of seawater-derived early diagenetic ferromanganese coatings enriched in seawater Nd as well as a minor fraction of detrital Nd from the Trans-Mexican Volcanic Belt and the NVZ. The tendency to show more radiogenic compositions with decreasing age is interpreted to reflect the gradual closure of the Central American Seaway, which formed a marine portal linking the tropical western Atlantic and eastern Pacific throughout most of the Cenozoic, but began to close in the Early to Middle Miocene (reviewed by Molnar, 2008; Coates and Stallard, 2013) due to tectonic stress resulted from collision of NW South America (Farris et al., 2011) and the Cocos Ridge, a part of the Galápagos Hotspot track (Hoernle et al., 2002), with Central America. The gradual closure most likely successively kept eastward flowing deep water from leaving the Guatemala Basin. Around 10.8 Ma, deep-water closure of the Central American Seaway was completed leading to a change in deep-water circulation through establishment of a deep-water gyre system. Höfig et al. (in preparation) noted that this circulation began at least ~7 Ma ago. Based on the present Sr-Nd isotope data, we suggest that this onset took place between 10.77 and 10.88 Ma.

6 Conclusions

The present study provides major and trace element compositions, as well as radiogenic Nd, Sr, and Hf isotopes of Site 1256 bulk sediments, being complemented by new bulk sediment isotope data from Site 495. These data shed light on the long-term chemical evolution of Cocos Plate sedimentation in the eastern equatorial Pacific (EEP) on a deep-time scale of ~23 million years. Major and trace element data confirm the results obtained by previous studies and show a marked chemical transition at ~10.8 Ma, related to the abrupt drop of carbonate production and associated increase of the content of terrigenous material (Wilson et al., 2003; Ziegler and Murray, 2007). Sr-Nd isotopes reflect this chemical transition as well, demonstrating not only the inflection of isotopic trends but also changes in sediment sources contributing Nd and Sr to the EEP. This evolution is in sharp contrast to the Pb isotopic record, showing an inflection of the trend about 5 million years later connected to changes in atmospheric circulation (Höfig et al., in preparation). We interpret this discrepancy to reflect the insignificance of eolian input in terms of Nd and Sr and propose oceanic circulation, particularly deep-water flow, to be the most important pathway for the detrital supply of these two elements. A mixture of Andean Arc (North Central Volcanic Zone and Northern Volcanic Zone), Trans-Mexican Volcanic Belt, and Central American Volcanic Arc input governed the isotopic evolution of bulk Nd. Similar conclusions hold for Sr once the terrigenous deposition began after 10.8 Ma. Throughout the study period, Nd and Sr have most likely been transported to the oceanic environment via continental runoff, and, in case of Nd, exchange processes at the continental margin may have played a significant role as well.

The isotopic changes at ~10.8 Ma most likely reflect the complete deep-water closure of the Central American Seaway preventing eastward flowing EEP deep water from entering the Caribbean Sea and forcing them to form a gyre in the deep EEP, providing information on the paleoceanographic consequences of the Central American Seaway closure in the study area.

Acknowledgments

We are grateful to S. Hauff and J. Heinze for valuable analytical support, as well as to S. Duggen for fruitful discussions. This research used samples provided by IODP and was funded by the Deutsche Forschungsgemeinschaft (DFG) IODP priority program grants HO1833/16-1 and 18-1.

References

Abouchami, W., Goldstein, S.L., Gazer, S., Eisenhauer, A., Mangini, A., 1997. Secular changes of lead and neodymium in central Pacific seawater recorded by a Fe-Mn crust. Geochimica et Cosmochimica Acta 61 (18), 3957–3974. 10.1016/S0016-7037(97)00218-4.

Andriessen, P., Helmens, K.F., Hooghiemstra, H., Riezebos, P.A., Van der Hammen, T., 1993. Absolute chronology of the Pliocene-Quaternary sediment sequence of the Bogota area, Colombia. Quaternary Science Reviews 12 (7), 483–501. 10.1016/0277-3791(93)90066-U.

Bayon, G., Burton, K.W., Soulet, G., Vigier, N., Dennielou, B., Etoubleau, J., Ponzevera, E., German, C.R., Nesbitt, R.W., 2009. Hf and Nd isotopes in marine sediments: Constraints on global silicate weathering. Earth and Planetary Science Letters 277 (3–4), 318–326. 10.1016/j.epsl.2008.10.028.

Berggren, W.A., Hilgen, F. J., Langereis, C. G., Kent, D.V., Obradovich, J. D., Raffi, I., Raymo, M. E., Shackleton, N.J., 1995a. Late Neogene chronology: New perspectives in high-resolution stratigraphy. Geological Society of America Bulletin 107 (11), 1272–1287. 10.1130/0016-7606(1995)107<1272:LNCNPI>2.3.CO;2.

Berggren, W.A., Kent, D.V., Swisher, C.C., Aubry, M.-P., 1995b. A revised Cenozoic geochronology and chronostratigraphy: Geochronology, Time Scales, and Global Stratigraphic Correlation, in: Berggren (Ed.), Geochronology, vol. 54, pp. 129–212.

Blichert-Toft, J., Albarède, F., 1997. The Lu-Hf isotope geochemistry of chondrites and the evolution of the mantle-crust system. Earth and Planetary Science Letters 148 (1-2), 243–258. 10.1016/S0012-821X(97)00040-X.

Broecker, W., Peng, T.H., Beng, Z., 1982. Tracers in the Sea. Lamont-Doherty Geological Observatory, Columbia University, Palisades, NY.

Cadet, J.-P., Pouclet, A., Thisse, Y., Bardintzeff, J.M., Azema, J., 1982. Middle America Neogene Explosive Volcanism and Ash Layers: Evidence from the Middle America Trench Transect, Deep Sea Drilling Project Leg 67, in: Aubouin, J., von Huene, R. (Eds.), Initial Reports of the Deep Sea Drilling Project, 67, vol. 67. U.S. Government Printing Office.

Cande, S.C., Kent, D.V., 1995. Revised calibration of the geomagnetic polarity timescale for the Late Cretaceous and Cenozoic. Journal of Geophysical Research: Solid Earth 100 (B4), 6093–6095. 10.1029/94JB03098.

Coates, A.G., Stallard, R.F., 2013. How old is the Isthmus of Panama? Bulletin of Marine Science 89 (4), 801–813. 10.5343/bms.2012.1076.

Coulbourn, W.T., Hesse, R., Azema, J., Shiki, T., 1982. A summary of the sedimentology of DSDP Leg 67 sites: the Middle America trench and slope off Guatemala - an active margin transect, in: Orlofsky, S. (Ed.), Initial Reports of the Deep Sea Drilling Project covering Leg 67 of the cruises of the drilling vessel Glomar Challenger, Manzanillo,

Mexico to Puntarenas, Costa Rica. Initial Reports of the Deep Sea Drilling Project, pp. 759–774.

DeMets, C., Gordon, R.G., Argus, D.F., Stein, S., 1990. Current plate motions. Geophysical Journal International 101 (2), 425–478. 10.1111/j.1365-246X.1990.tb06579.x.

Dou, Y., Yang, S., Liu, Z., Shi, X., Li, J., Yu, H., Berne, S., 2012. Sr–Nd isotopic constraints on terrigenous sediment provenances and Kuroshio Current variability in the Okinawa Trough during the late Quaternary. Palaeogeography, Palaeoclimatology, Palaeoecology 365–366, 38–47. 10.1016/j.palaeo.2012.09.003.

Ehlert, C., Grasse, P., Frank, M., 2013. Changes in silicate utilisation and upwelling intensity off Peru since the Last Glacial Maximum – insights from silicon and neodymium isotopes. Quaternary Science Reviews 72, 18–35. 10.1016/j.quascirev.2013.04.013.

Farrell, J.W., Raffi, I., Janecek, T.C., Murray, D.W., Levitan, M., Dadey, K.A., Emeis, K.-C., Lyle, M., Flores, J.-A., Hovan, S., 1995. Late Neogene Sedimentation Patterns in the Eastern Equatorial Pacific, in: Pisias, N.G., Mayer, L.A., Janecek, T.R., Palmer-Julson, A., van Andel, T.H. (Eds.), Proceedings of the Ocean Drilling Program, 138 Scientific Results, vol. 138. Ocean Drilling Program.

Farris, D.W., Jaramillo, C., Bayona, G., Restrepo-Moreno, S.A., Montes, C., Cardona, A., Mora, A., Speakman, R.J., Glascock, M.D., Valencia, V., 2011. Fracturing of the Panamanian Isthmus during initial collision with South America. Geology 39 (11), 1007–1010. 10.1130/G32237.1.

Faure, G., Mensing, T.M., 2005. Isotopes: Principles and applications, 3rd ed. Wiley, Hoboken, N.J., xxvii, 897.

Frank, M., Reynolds, B.C., Keith O'Nions, R., 1999. Nd and Pb isotopes in Atlantic and Pacific water masses before and after closure of the Panama gateway. Geology 27 (12), 1147–1150. 10.1130/0091-7613(1999)027<1147:NAPIIA>2.3.CO;2.

Frank, M., 2002. Radiogenic isotopes: Tracers of past ocean circulation and erosional input. Reviews of Geophysics 40 (1). 10.1029/2000RG000094.

García, N.O., 1994. South American climatology. Quaternary International 21, 7–27. 10.1016/1040-6182(94)90018-3.

Geldmacher, J., Hoernle, K., Klügel, A., van den Bogaard, Paul, Wombacher, F., Berning, B., 2006. Origin and geochemical evolution of the Madeira-Tore Rise (eastern North Atlantic). Journal of Geophysical Research 111 (B9). 10.1029/2005JB003931.

Geldmacher, J., Hoernle, K., van den Bogaard, Paul, Hauff, F., Klugel, A., 2008. Age and Geochemistry of the Central American Forearc Basement (DSDP Leg 67 and 84): Insights into Mesozoic Arc Volcanism and Seamount Accretion on the Fringe of the Caribbean LIP. Journal of Petrology 49 (10), 1781–1815. 10.1093/petrology/egn046.

Geldmacher, J., Höfig, T.W., Hauff, F., Hoernle, K., Garbe-Schönberg, D., Wilson, D.S., 2013. Influence of the Galápagos hotspot on the East Pacific Rise during Miocene superfast spreading. Geology 41 (2), 183–186. 10.1130/G33533.1.

Grasse, P., Stichel, T., Stumpf, R., Stramma, L., Frank, M., 2012. The distribution of neodymium isotopes and concentrations in the Eastern Equatorial Pacific: Water mass

advection versus particle exchange. Earth and Planetary Science Letters 353–354 (0), 198–207. 10.1016/j.epsl.2012.07.044.

Gutjahr, M., Frank, M., Stirling, C.H., Klemm, V., van de Flierdt, T., Halliday, A.N., 2007. Reliable extraction of a deepwater trace metal isotope signal from Fe–Mn oxyhydroxide coatings of marine sediments. Chemical Geology 242 (3–4), 351–370. 10.1016/j.chemgeo.2007.03.021.

Handschumacher, D. W., 1976. Post-Eocene plate tectonics of the Eastern Pacific, in: Sutton, G.H., Manghnani, M.H., Moberly, R., McAfee, E.U. (Eds.), The Geophysics of the Pacific Ocean Basin and Its Margin, vol. 19. AGU, Washington, DC, pp. 177–202.

Hart, D., Miller, D.J., 2006. Analysis and Correlation of Volcanic Ash in Marine Sediments from the Peru Margin, Ocean Drilling Program Leg 201: Explosive Volcanic Cycles of the North-Central Andes, in: Jørgensen, B.B., D'Hondt, S.L., Miller, D.J. (Eds.), Proceedings of the Ocean Drilling Program, 201 Scientific Results, vol. 201. Ocean Drilling Program.

Hauff, F., Hoernle, K., van den Bogaard, Paul, Alvarado, G., Garbe-Schönberg, D., 2000. Age and geochemistry of basaltic complexes in western Costa Rica: Contributions to the geotectonic evolution of Central America. Geochemistry, Geophysics, Geosystems 1 (5), n/a. 10.1029/1999GC000020.

Heinemann, C., Füchtbauer, H., 1982. Insoluble Residues of the Fine-Grained Sediments from the Trench Transect South of Guatemala, Deep Sea Drilling Project Leg 67, in: Aubouin, J., von Huene, R. (Eds.), Initial Reports of the Deep Sea Drilling Project, 67, vol. 67. U.S. Government Printing Office.

Heydolph, K., Hoernle, K., Hauff, F., Bogaard, Paul van den, Portnyagin, M., Bindeman, I., Garbe-Schönberg, D., 2012. Along and across arc geochemical variations in NW Central America: Evidence for involvement of lithospheric pyroxenite. Geochimica et Cosmochimica Acta 84, 459–491. 10.1016/j.gca.2012.01.035.

Hodell, D.A., Mead, G.A., Mueller, P.A., 1990. Variation in the strontium isotopic composition of seawater (8 Ma to present): Implications for chemical weathering rates and dissolved fluxes to the oceans. Chemical Geology: Isotope Geoscience section 80 (4), 291–307. 10.1016/0168-9622(90)90011-Z.

Hodell, D.A., Mueller, P.A., McKenzie, J.A., Mead, G.A., 1989. Strontium isotope stratigraphy and geochemistry of the late Neogene ocean. Earth and Planetary Science Letters 92 (2), 165–178. 10.1016/0012-821X(89)90044-7.

Hodell, D.A., Woodruff, F., 1994. Variations in the strontium isotopic ratio of seawater during the Miocene: Stratigraphic and geochemical implications. Paleoceanography 9 (3), 405–426. 10.1029/94PA00292.

Hoernle, K., Abt, D.L., Fischer, K.M., Nichols, H., Hauff, F., Abers, G.A., van den Bogaard, Paul, Heydolph, K., Alvarado, G., Protti, M., Strauch, W., 2008. Arc-parallel flow in the mantle wedge beneath Costa Rica and Nicaragua. Nature 451 (7182), 1094–1097. 10.1038/nature06550.

Hoernle, K., Hauff, F., Kokfelt, T.F., Haase, K., Garbe-Schönberg, D., Werner, R., 2011. On- and off-axis chemical heterogeneities along the South Atlantic Mid-Ocean-Ridge (5–

11°S): Shallow or deep recycling of ocean crust and/or intraplate volcanism? Earth and Planetary Science Letters 306 (1-2), 86–97. 10.1016/j.epsl.2011.03.032.

Hoernle, K., van den Bogaard, Paul, Werner, R., Lissinna, B., Hauff, F., Alvarado, G., Garbe-Schönberg, D., 2002. Missing history (16–71 Ma) of the Galápagos hotspot: Implications for the tectonic and biological evolution of the Americas. Geology 30 (9), 795–798. 10.1130/0091-7613(2002)030<0795:MHMOTG>2.0.CO;2.

Hovan, S.A., 1995. Late Cenozoic Atmospheric Circulation Intensity and Climatic History Recorded by Eolian Deposition in the Eastern Equatorial Pacific Ocean, Leg 138, in: Pisias, N.G., Mayer, L.A., Janecek, T.R., Palmer-Julson, A., van Andel, T.H. (Eds.), Proceedings of the Ocean Drilling Program, 138 Scientific Results, vol. 138. Ocean Drilling Program.

Jacobsen, S.B., Wasserburg, G.J., 1980. Sm-Nd isotopic evolution of chondrites. Earth and Planetary Science Letters 50 (1), 139–155. 10.1016/0012-821X(80)90125-9.

Janis, C.M., 1993. Tertiary Mammal Evolution in the Context of Changing Climates, Vegetation, and Tectonic Events. Annual Review of Ecology and Systematics 24, 467–500.

Jeandel, C., Delattre, H., Grenier, M., Pradoux, C., Lacan, F., 2013. Rare earth element concentrations and Nd isotopes in the Southeast Pacific Ocean. Geochem. Geophys. Geosyst. 14 (2), 328–341. 10.1029/2012GC004309.

Jiang, F., Frank, M., Li, T., Chen, T.-Y., Xu, Z., Li, A., 2013. Asian dust input in the western Philippine Sea: Evidence from radiogenic Sr and Nd isotopes. Geochemistry, Geophysics, Geosystems 14 (5), 1538–1551. 10.1002/ggge.20116.

Jiang, S., Wise, S.W., 2007. Upper Cenozoic calcareous nannofossil biostratigraphy and inferred sedimentation, ODP Leg 206, East Pacific Rise, in: Teagle, D.A.H., Wilson, D.S., Acton, G.D., Vanko, D. (Eds.), Proceedings of the Ocean Drilling Program, 206 Scientific Results, vol. 206. Ocean Drilling Program.

Jochum, K.P., Nohl, U., Herwig, K., Lammel, E., Stoll, B., Hofmann, A.W., 2005. GeoReM: A New Geochemical Database for Reference Materials and Isotopic Standards. Geostandards and Geoanalytical Research 29 (3), 333–338. 10.1111/j.1751-908X.2005.tb00904.x.

Jones, C.E., Halliday, A.N., Rea, D.K., Owen, R.M., 1994. Neodymium isotopic variations in North Pacific modern silicate sediment and the insignificance of detrital REE contributions to seawater. Earth and Planetary Science Letters 127 (1–4), 55–66. 10.1016/0012-821X(94)90197-X.

Kessler, W.S., 2006. The circulation of the eastern tropical Pacific: A review. Progress in Oceanography 69 (2–4), 181–217. 10.1016/j.pocean.2006.03.009.

Lacan, F., Jeandel, C., 2001. Tracing Papua New Guinea imprint on the central Equatorial Pacific Ocean using neodymium isotopic compositions and Rare Earth Element patterns. Earth and Planetary Science Letters 186 (3–4), 497–512. 10.1016/S0012-821X(01)00263-1.

Lacan, F., Jeandel, C., 2005. Neodymium isotopes as a new tool for quantifying exchange fluxes at the continent–ocean interface. Earth and Planetary Science Letters 232 (3–4), 245–257. 10.1016/j.epsl.2005.01.004.

Lee, D.-C., Halliday, A.N., Hein, J.R., Burton, K.W., Christensen, J.N., Günther, D., 1999. Hafnium Isotope Stratigraphy of Ferromanganese Crusts. Science 285 (5430), 1052–1054. 10.1126/science.285.5430.1052.

Ling, H.F., Burton, K.W., O'Nions, R.K., Kamber, B.S., von Blanckenburg, F., Gibb, A.J., Hein, J.R., 1997. Evolution of Nd and Pb isotopes in Central Pacific seawater from ferromanganese crusts. Earth and Planetary Science Letters 146 (1–2), 1–12. 10.1016/S0012-821X(96)00224-5.

Ling, H.-F., Jiang, S.-Y., Frank, M., Zhou, H.-Y., Zhou, F., Lu, Z.-L., Chen, X.-M., Jiang, Y.-H., Ge, C.-D., 2005. Differing controls over the Cenozoic Pb and Nd isotope evolution of deepwater in the central North Pacific Ocean. Earth and Planetary Science Letters 232 (3–4), 345–361. 10.1016/j.epsl.2004.12.009.

Lonsdale, P., 1976. Abyssal circulation of the southeastern Pacific and some geological implications. Journal of Geophysical Research: Oceans 81 (6), 1163–1176. 10.1029/JC081i006p01163.

Lourens, L., Hilgen, F., Shackleton, N.J., Laskar, J., Wilson, D.S., 2004. The Neogene Period, in: Gradstein, F., Ogg, J., Smith, A. (Eds.), A Geological Time Scale 2004, Camebridge University Press, pp. 409–440.

Lyle, M., 1992. Composition Maps of Surface Sediments of the Eastern Tropical Pacific Ocean, in: Mayer, L., Pisias, N., Janecek, T. (Eds.), Proceedings of the Ocean Drilling Program, 138 Initial Reports, vol. 138. Ocean Drilling Program.

Lyle, M., Dadey, K.A., Farrell, J.W., 1995. The Late Miocene (11-8 Ma) Eastern Pacific Carbonate Crash: Evidence for Reorganization of Deep-Water Circulation by the Closure of the Panama Gateway, in: Pisias, N.G., Mayer, L.A., Janecek, T.R., Palmer-Julson, A., van Andel, T.H. (Eds.), Proceedings of the Ocean Drilling Program, 138 Scientific Results, vol. 138. Ocean Drilling Program.

Michard, A., Albarède, F., Michard, G., Minster, J.F., Charlou, J., 1983. Rare-earth elements and uranium in high-temperature solutions from East Pacific Rise hydrothermal vent field (13 °N). Nature 303 (5920), 795–797. 10.1038/303795a0.

Molnar, P., 2008. Closing of the Central American Seaway and the Ice Age: A critical review. Paleoceanography 23 (2), 1–15. 10.1029/2007PA001574.

Nakai, S., Halliday, A.N., Rea, D.K., 1993. Provenance of dust in the Pacific Ocean. Earth and Planetary Science Letters 119 (1-2), 143–157. 10.1016/0012-821X(93)90012-X.

Noble, T.L., Piotrowski, A.M., McCave, I. Nick, 2013. Neodymium isotopic composition of intermediate and deep waters in the glacial southwest Pacific. Earth and Planetary Science Letters 384, 27–36. 10.1016/j.epsl.2013.10.010.

Patino, L.C., Carr, M.J., Feigenson, M.D., 2000. Local and regional variations in Central American arc lavas controlled by variations in subducted sediment input. Contributions to Mineralogy and Petrology 138 (3), 265–283. 10.1007/s004100050562.

Pettke, T., Halliday, A.N., Rea, D.K., 2002. Cenozoic evolution of Asian climate and sources of Pacific seawater Pb and Nd derived from eolian dust of sediment core LL44-GPC3. Paleoceanography 17 (3), 1–13. 10.1029/2001PA000673.

Pichat, S., Abouchami, W., Galer, S.J.G., 2014. Lead isotopes in the Eastern Equatorial Pacific record Quaternary migration of the South Westerlies. Earth and Planetary Science Letters 388, 293–305. 10.1016/j.epsl.2013.11.035.

Pound, M.J., Haywood, A.M., Salzmann, U., Riding, J.B., Lunt, D.J., Hunter, S.J., 2011. A Tortonian (Late Miocene, 11.61–7.25Ma) global vegetation reconstruction. Palaeogeography, Palaeoclimatology, Palaeoecology 300 (1-4), 29–45. 10.1016/j.palaeo.2010.11.029.

Pound, M.J., Haywood, A.M., Salzmann, U., Riding, J.B., 2012. Global vegetation dynamics and latitudinal temperature gradients during the Mid to Late Miocene (15.97–5.33Ma). Earth-Science Reviews 112 (1-2), 1–22. 10.1016/j.earscirev.2012.02.005.

Rea, D.K., 1994. The paleoclimatic record provided by eolian deposition in the deep sea: The geologic history of wind. Reviews of Geophysics 32 (2), 159–195. 10.1029/93RG03257.

Rech, J.A., Currie, B.S., Michalski, G., Cowan, A.M., 2006. Neogene climate change and uplift in the Atacama Desert, Chile. Geol 34 (9), 761. 10.1130/G22444.1.

Rech, J.A., Currie, B.S., Shullenberger, E.D., Dunagan, S.P., Jordan, T.E., Blanco, N., Tomlinson, A.J., Rowe, H.D., Houston, J., 2010. Evidence for the development of the Andean rain shadow from a Neogene isotopic record in the Atacama Desert, Chile. Earth and Planetary Science Letters 292 (3-4), 371–382. 10.1016/j.epsl.2010.02.004.

Rudnicki, M.D., Elderfield, H., 1993. A chemical model of the buoyant and neutrally buoyant plume above the TAG vent field, 26 degrees N, Mid-Atlantic Ridge. Geochimica et Cosmochimica Acta 57 (13), 2939–2957. 10.1016/0016-7037(93)90285-5.

Shiki, T., Yamasaki, T., Hisatomi, K., 1982. Features of Grain-Size Distribution and Mineral Composition of Turbiditic Sediments from the Middle America Trench off Guatemala, in: Aubouin, J., von Huene, R. (Eds.), Initial Reports of the Deep Sea Drilling Project, 67, vol. 67. U.S. Government Printing Office.

Stancin, A.M., Gleason, J.D., Rea, D.K., Owen, R.M., Moore Jr. , T. C., Blum, J.D., Hovan, S.A., 2006. Radiogenic isotopic mapping of late Cenozoic eolian and hemipelagic sediment distribution in the east-central Pacific. Earth and Planetary Science Letters 248 (3–4), 840–850. 10.1016/j.epsl.2006.06.038.

Stern, C.R., 2004. Active Andean volcanism: its geologic and tectonic setting. Andean Geology (formerly Revista Geológica de Chile) 31 (2), 161–206. 10.5027/andgeoV31n2-a01.

Stumpf, R., Frank, M., Schönfeld, J., Haley, B.A., 2010. Late Quaternary variability of Mediterranean Outflow Water from radiogenic Nd and Pb isotopes. Quaternary Science Reviews 29 (19-20), 2462–2472. 10.1016/j.quascirev.2010.06.021.

Tachikawa, K., Roy-Barman, M., Michard, A., Thouron, D., Yeghicheyan, D., Jeandel, C., 2004. Neodymium isotopes in the Mediterranean Sea: comparison between seawater and

sediment signals. Geochimica et Cosmochimica Acta 68 (14), 3095–3106. 10.1016/j.gca.2004.01.024.

van de Flierdt, T., Frank, M., Halliday, A.N., Hein, J.R., Hattendorf, B., Günther, D., Kubik, P.W., 2004a. Deep and bottom water export from the Southern Ocean to the Pacific over the past 38 million years. Paleoceanography 19 (1), PA1020. 10.1029/2003PA000923.

van de Flierdt, T., Frank, M., Halliday, A.N., Hein, J.R., Hattendorf, B., Günther, D., Kubik, P.W., 2004b. Tracing the history of submarine hydrothermal inputs and the significance of hydrothermal hafnium for the seawater budget—a combined Pb–Hf–Nd isotope approach. Earth and Planetary Science Letters 222 (1), 259–273. 10.1016/j.epsl.2004.02.025.

van de Flierdt, T., Goldstein, S.L., Hemming, S.R., Roy, M., Frank, M., Halliday, A.N., 2007. Global neodymium–hafnium isotope systematics — revisited. Earth and Planetary Science Letters 259 (3–4), 432–441. 10.1016/j.epsl.2007.05.003.

Vervoort, J.D., Patchett, P.J., Blichert-Toft, J., Albarède, F., 1999. Relationships between Lu–Hf and Sm–Nd isotopic systems in the global sedimentary system. Earth and Planetary Science Letters 168 (1–2), 79–99. 10.1016/S0012-821X(99)00047-3.

Vervoort, J.D., Plank, T., Prytulak, J., 2011. The Hf–Nd isotopic composition of marine sediments. Geochimica et Cosmochimica Acta 75 (20), 5903–5926. 10.1016/j.gca.2011.07.046.

von Huene, R., Aubouin, J., et al., 1982. Site 495: Cocos Plate Middle America Trench Outer Slope, in: Aubouin, J., von Huene, R. (Eds.), Initial Reports of the Deep Sea Drilling Project, 67, vol. 67. U.S. Government Printing Office, pp. 79–141.

Webb, S.D., 1978. A History of Savanna Vertebrates in the New World. Part II: South America and the Great Interchange. Annual Review of Ecology and Systematics 9 (1), 393–426. 10.1146/annurev.es.09.110178.002141.

Wilson, D.J., Piotrowski, A.M., Galy, A., Clegg, J.A., 2013. Reactivity of neodymium carriers in deep sea sediments: Implications for boundary exchange and paleoceanography. Geochimica et Cosmochimica Acta 109, 197–221. 10.1016/j.gca.2013.01.042.

Wilson, D.S., 1996. Fastest known spreading on the Miocene Cocos-Pacific Plate Boundary. Geophysical Research Letters 23 (21), 3003–3006. 10.1029/96GL02893.

Wilson, D.S., Teagle, D.A.H., Acton, G.D., et al., 2003. Site 1256, Preliminary Results, in: Wilson, D., Teagle, D., Acton, G. (Eds.), Proceedings of the Ocean Drilling Program, 206 Initial Reports, vol. 206. Ocean Drilling Program.

Ziegler, C.L., Murray, R.W., 2007. Analytical sediment chemistry on board the JOIDES Resolution: a comparison of shipboard and shore-based sample preparation protocols, in: Teagle, D.A.H., Wilson, D.S., Acton, G.D., Vanko, D.A. (Eds.), Proceedings of the Ocean Drilling Program, 206 Scientific Results, vol. 206. Ocean Drilling Program.

Zimmermann, B., Porcelli, D., Frank, M., Rickli, J., Lee, D.-C., Halliday, A.N., 2009. The hafnium isotope composition of Pacific Ocean water. Geochimica et Cosmochimica Acta 73 (1), 91–101. 10.1016/j.gca.2008.09.033.

Figure captions

Figure 1. (a) Map of the eastern equatorial Pacific and surrounding continental areas, displaying the locations of the studied ocean drilling sites 495 and 1256 together with Fe-Mn crust GMAT 14D. Indicated oceanic crustal ages of drilling site locations are based on magnetic lineations (Sites 495, 499: von Huene et al., 1982; Geldmacher et al., 2013; Site 1256: Wilson, 1996) according to the geomagnetic polarity time scale of Cande and Kent (1995). The age of Fe-Mn crust GMAT 14D is derived from Frank et al. (1999). Reconstructed tectonic tracks were calculated with the software GPlates (http://www.gplates.org; version 1.1.1). Small dots along the tracks mark 1 Ma and small ticks label 5 Ma increments. Spreading ridges: EPR = East Pacific Rise, CSC = Galápagos Spreading Center (Cocos-Nazca Spreading Center). Other oceanic/continental geologic entities: CAVA = Central American Volcanic Arc, CLIP = Caribbean Large Igneous Province (uplifted parts), GI = Galápagos Islands, NVZ = Northern (Andean) Volcanic Zone, TMVB = Trans-Mexican Volcanic Belt. (b) Map of the easternmost tropical and southeastern Pacific (Site 1256 location marked by a black star) and adjacent western part of South America [adapted from Hart and Miller (2006), including oceanic circulation data from Kessler (2006)], depicting major present-day ocean surface (turquoise arrows) and wind (black arrows) currents affecting this area: HC = Humboldt Current, SEC = South Equatorial Current, STW = Southeast Trade Winds. In addition, major volcanic zones of the Andes are displayed: NVZ = Northern Volcanic Zone, CVZ = Central Volcanic Zone (north, transitional (trans.), south; cf. Pichat et al., 2014), SVZ = Southern Volcanic Zone.

Figure 2. Map of the eastern equatorial Pacific, schematically displaying major lobes of the oceanic surface [turquoise arrows; after Kessler (2006)] and abyssal [dark blue arrows; as suggested by Lonsdale (1976) and Lyle (1992)] current circulation affecting the eastern equatorial Pacific (CRCC = Costa Rica Coastal Current, NEC = North Equatorial Current, NECC = North Equatorial Countercurrent, SEC = South Equatorial Current, TB = Tehuantepec Bowl, WMC = West Mexican Current). Pale blue, transparent marine areas delineate the latitudinal extent of the westward flowing NEC (north of ~10°N) and SEC (south of ~5°N) surface circulation system, respectively (Hovan, 1995). The structural boundaries of the Guatemala Basin (GB) are highlighted in light gray (Cocos Ridge and part of the EPR and GSC crests). True paleopositions of studied drilling sites (and Fe-Mn crust GMAT 14D) are shown in 1 Ma increments from the corresponding time of formation to the present (calculated with the software GPlates; http://www.gplates.org; version 1.1.1). Paleopositions represented by black dots (0–4 Ma) mark the period of time with the ITCZ being located at its average present-day latitude of c. 5°N (Rea, 1994; Hovan, 1995), thus, implying establishment of the present latitudinal extent of NEC and SEC areas. Note that the true paleopositions of oceanic sites depicted here may deviate from the locations along the tectonic tracks shown in Fig. 1a, since the latter ones illustrate the backtrack path to the present-day location of that ridge segment where the underlying oceanic crust was formed,

being part of the same tectonic plate. In contrast, the reconstruction of true paleopositions at a given age has taken into account that the associated ridge segment has been subject to ridge jumps through time, referring to the true position of the corresponding ridge segment at a given point of time, which may be different to its present-day location. Abbreviations are the same as in Fig. 1a.

Figure 3. Site 1256 CaO (wt%) (a), Sr (ppm) (b), Al_2O_3 (wt%) (c), and Sc (ppm) (d) concentrations versus age (Ma) as well as Site 1256 carbonate (e) and terrigenous (f) contents (Wilson et al., 2003) versus depth (meters below seafloor, mbsf). Geochemical data from Site 495 (Patino et al., 2000) are also shown for comparison. Plots (e) and (f) after Wilson et al. (2003).

Figure 4. Sites 4951256 $^{87}Sr/^{86}Sr_{in}$ (a), $^{143}Nd/^{144}Nd_{in}$ (b), and $^{176}Hf/^{177}Hf_{in}$ (c) isotope ratios ($_{in}$ = initial) versus age (Ma). Black dots placed on distinct blue and yellow circles refer to those Site 1256 samples from which the coeval leachate (white squares) and residual data (black squares) were obtained. Fig. 4b inset shows the widely distributed $\varepsilon_{Nd}(T)$ notation, which expresses the deviation of the initial Nd isotope ratio from the Chondritic Uniform Reservoir (CHUR) composition at a given age of deposition, calculated by means of equation (9.9) of Faure and Mensing (2005) using a present-day CHUR value of 0.512638 (Jacobsen and Wasserburg, 1980). Data from eastern equatorial Pacific Fe-Mn crust GMAT 14D (Frank et al., 1999) are also shown for comparison in plot (b). Literature data for $^{176}Hf/^{177}Hf_{in}$ taken from Vervoort et al. (2011), applying the age model of the present study. Errors are within symbol sizes. The evolution of the Neogene seawater Sr isotopic composition (Fig. 4a) has been compiled from Hodell et al. (1989, 1990) and Hodell and Woodruff (1994) and represents a third-order polynomial regression line.

Figure 5. $^{206}Pb/^{204}Pb_{in}$ versus $^{143}Nd/^{144}Nd_{in}$ (a), $^{87}Sr/^{86}Sr_{in}$ versus $^{143}Nd/^{144}Nd_{in}$ (b), and $^{143}Nd/^{144}Nd_{in}$ versus $^{176}Hf/^{177}Hf_{in}$ (c) ($_{in}$ = initial). Abbreviations are the same as in Figs. 1a/b. Errors are smaller than symbol sizes. Initial Pb isotope ratios used for plot (a) are taken from Höfig et al. (in preparation; see CHAPTER II). Data sources: GMAT 14D (Frank et al., 1999); MORB (mid-ocean-ridge basalt) basement from Site 1256 (Geldmacher et al., 2013; Höfig et al., in review [see CHAPTER I]), Sites 495/499 (Geldmacher et al., 2008, 2013; Heydolph et al., 2012) (fields for both sites based on initial isotope data); North American endmember (Stancin et al., 2006); Site 495 Hf isotope data from Vervoort et al. (2011). Central Pacific seawater field accounts for Fe-Mn crust data of Abouchami et al. (1997) and Ling et al. (1997) obtained from VA13-2. All other data fields and calculated average compositions (CAVA, GI (including Cocos Island and associated seamounts), CLIP (uplifted fragments of the Pacific part), NVZ, north/transitional/ south CVZ, SVZ, and TMVB), respectively, have been constructed from the GEOROC (http://georoc.mpch-mainz.gwdg.de/georoc/) and PetDB database (http://www.earthchem.org/ petdb) compilation provided by Höfig et al. (in preparation; see CHAPTER II).

Figure 1

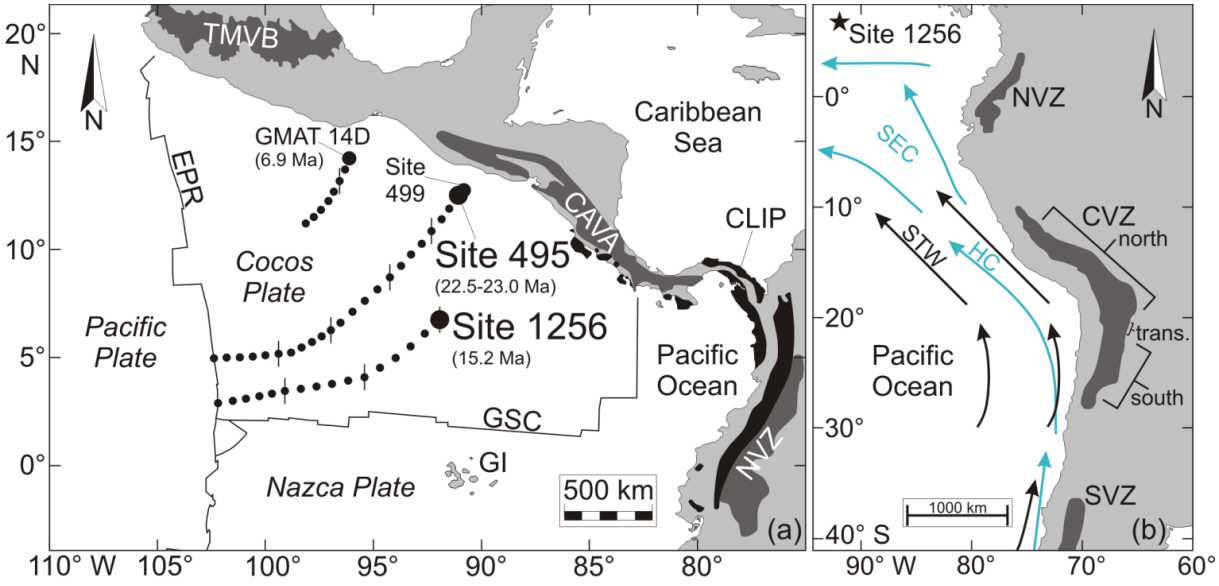
TMVB
Caribbean Sea
GMAT 14D
(6.9 Ma)
Site 499
EPR
CAVA
CLIP
Site 495
(22.5-23.0 Ma)
Cocos Plate
Pacific Plate
Site 1256
(15.2 Ma)
Pacific Ocean
GSC
GI
Nazca Plate
500 km
NVZ
(a)
20° N
15°
10°
5°
0°
110° W
105°
100°
95°
90°
85°
80°
Site 1256
NVZ
SEC
STW
HC
CVZ
north
trans.
south
Pacific Ocean
SVZ
1000 km
(b)
0°
10°
20°
30°
40° S
90° W
80°
70°
60°

Figure 2

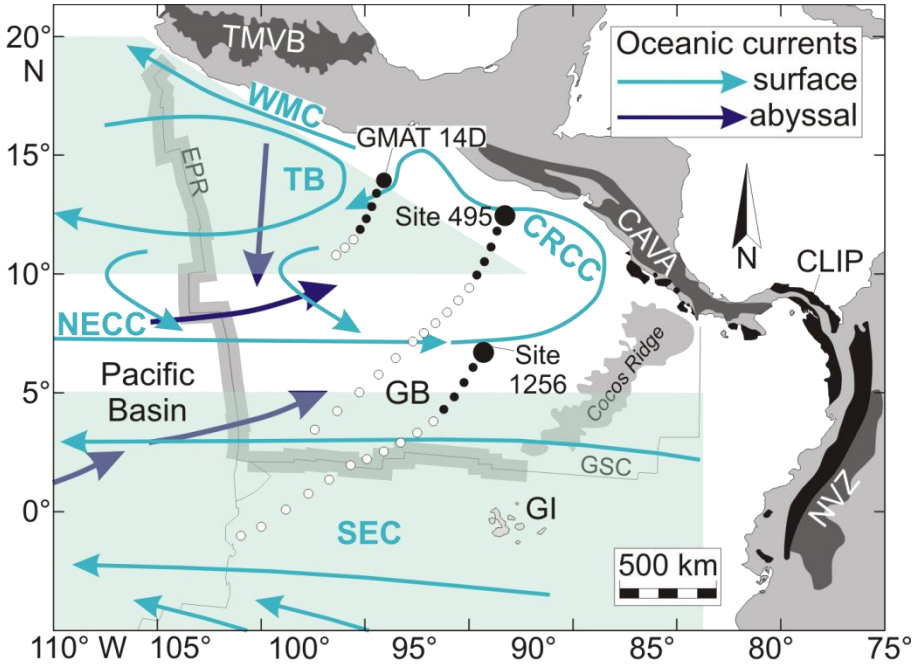
TMVB
WMC
GMAT 14D
EPR
TB
Site 495
CRCC
CAVA
N
CLIP
NECC
Site
1256
Pacific
Basin
GB
Cocos Ridge
GSC
GI
SEC
NVZ
500 km
Oceanic currents
surface
abyssal
20° N
15°
10°
5°
0°
110° W
105°
100°
95°
90°
85°
80°
75°

Figure 3

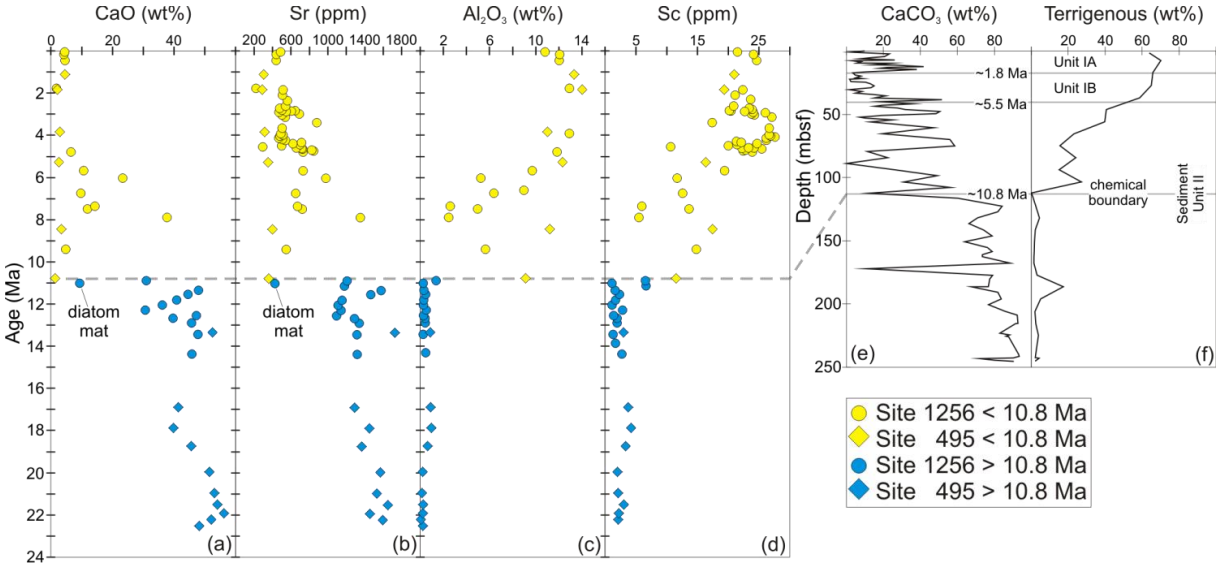
CaO (wt%)
Sr (ppm)
Al2O3 (wt%)
Sc (ppm)
Age (Ma)
diatom mat
diatom mat
(a)
(b)
(c)
(d)
CaCO3 (wt%)
Terrigenous (wt%)
Depth (mbsf)
~1.8 Ma
~5.5 Ma
~10.8 Ma
Unit IA
Unit IB
chemical boundary
Sediment Unit II
(e)
(f)
Site 1256 < 10.8 Ma
Site 495 < 10.8 Ma
Site 1256 > 10.8 Ma
Site 495 > 10.8 Ma

Figure 4

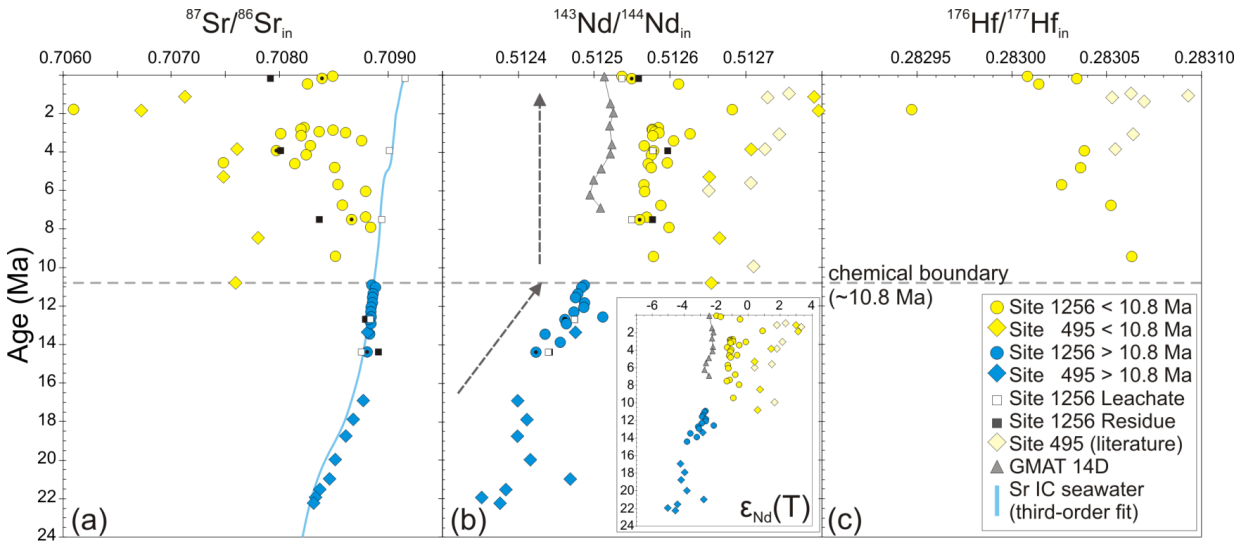
$^{87}Sr/^{86}Sr_{in}$
$^{143}Nd/^{144}Nd_{in}$
$^{176}Hf/^{177}Hf_{in}$
Age (Ma)
chemical boundary
(~10.8 Ma)
$\varepsilon_{Nd}(T)$
(a)
(b)
(c)
Site 1256 < 10.8 Ma
Site 495 < 10.8 Ma
Site 1256 > 10.8 Ma
Site 495 > 10.8 Ma
Site 1256 Leachate
Site 1256 Residue
Site 495 (literature)
GMAT 14D
Sr IC seawater
(third-order fit)

Figure 5

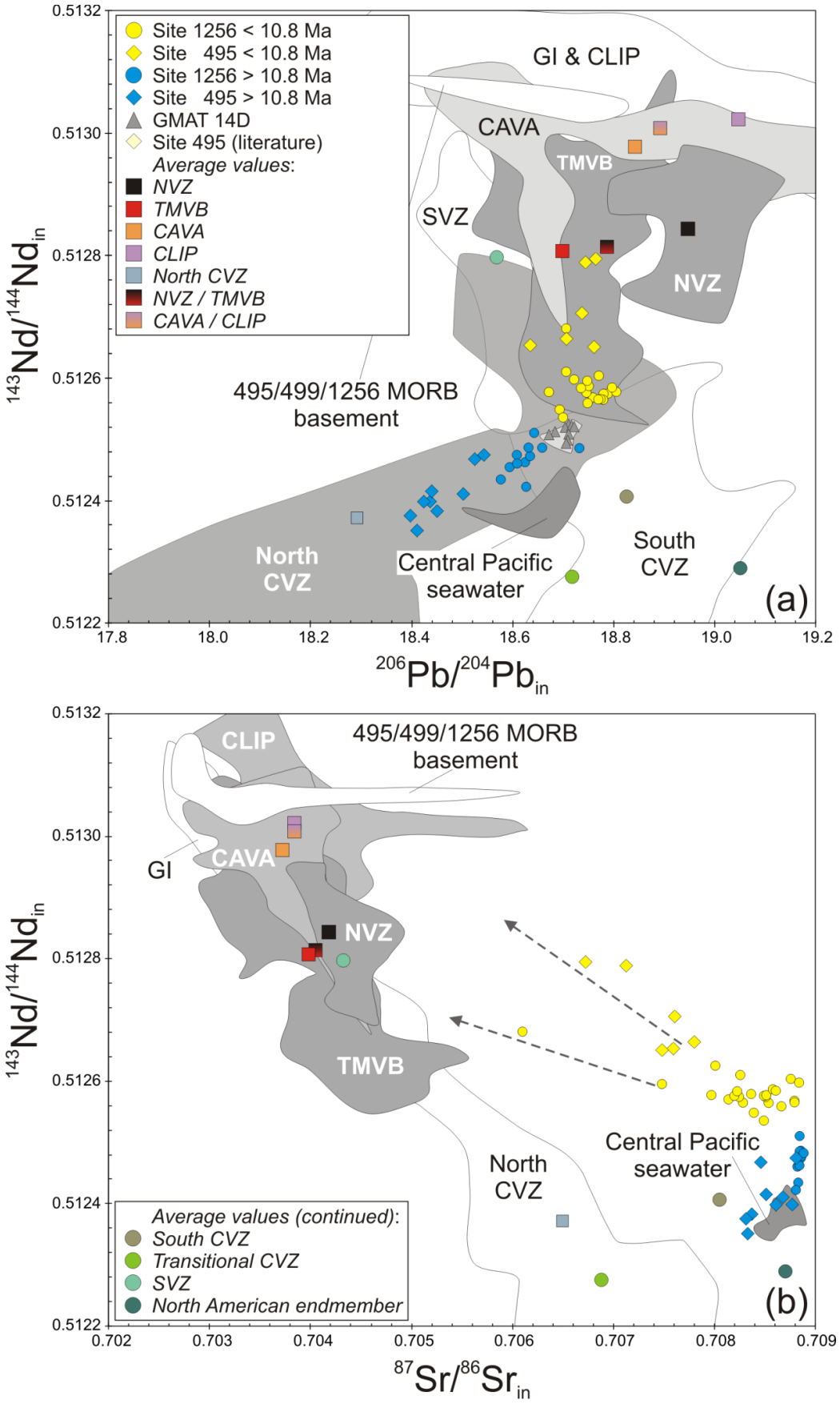
Site 1256 < 10.8 Ma
Site 495 < 10.8 Ma
Site 1256 > 10.8 Ma
Site 495 > 10.8 Ma
GMAT 14D
Site 495 (literature)
Average values:
NVZ
TMVB
CAVA
CLIP
North CVZ
NVZ / TMVB
CAVA / CLIP
GI & CLIP
CAVA
TMVB
SVZ
NVZ
495/499/1256 MORB basement
North CVZ
Central Pacific seawater
South CVZ
(a)
143Nd/144Nd in
206Pb/204Pb in
CLIP
495/499/1256 MORB basement
GI
CAVA
NVZ
TMVB
Central Pacific seawater
North CVZ
Average values (continued):
South CVZ
Transitional CVZ
SVZ
North American endmember
(b)
87Sr/86Sr in

Figure 5 (*continued*)

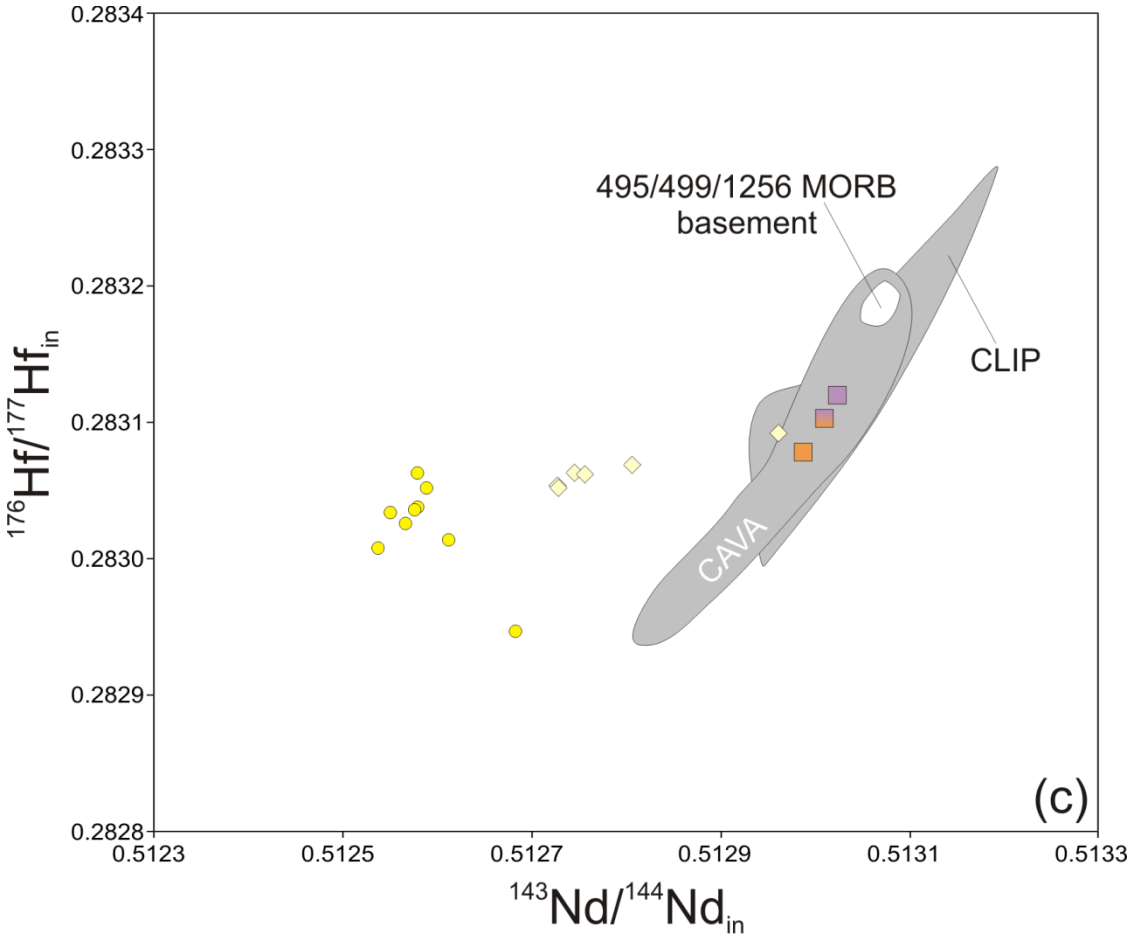

Table 1

Sample interval details, lithology, and age model of studied samples from both Site 1256 and Site 495. mbsf = meters below seafloor, FO = first occurrence, LO = last occurrence.

Site/hole	Core/ section	Interval (cm)	Depth (mbsf)	Biostrati-graphic age estimate (Ma)	Appropriate linear sedimentation rate (m/Ma)*	Lithology†	Appropriate biohorizon, with mean depth and age, used for calculation of biostratigraphic ages	Reference for microfossil species	Reference for microfossil datum level
1256A	1H-1	32–34	0.32	0.04	11.8	Nannofossil silty clay with diatoms	LO *Pseudoemiliania lacunosa* (5.28 mbsf, 0.46 Ma)	Jiang and Wise, 2007	Berggren et al., 1995a
1256A	1H-2	19–21	1.69	0.16	11.8	Nannofossil silty clay with diatoms			
1256B	1H-4	56–58	5.06	0.44	11.8	Nannofossil silty clay			
1256B	3H-2	34–36	17.44	1.76	6.1	Clayey nannofossil ooze with major abundance of colorless volcanic glass, quartz & feldspar	LO *Calcidiscus macintyrei* (16.38 mbsf, 1.59 Ma)	Jiang and Wise, 2007	Berggren et al., 1995a
1256B	3H-2	77–78	17.87	1.83	6.1	Clayey nannofossil ooze			
1256B	3H-3	81–82	19.41	2.09	6.1	Clayey nannofossil ooze			
1256B	3H-4	88–89	20.98	2.34	6.1	Clayey nannofossil ooze			
1256B	3H-5	96–97	22.56	2.60	6.1	Clayey nannofossil ooze			
1256B	3H-6	09–10	23.19	2.71	6.1	Clayey nannofossil ooze			
1256B	3H-6	40–41	23.50	2.76	6.1	Clayey nannofossil ooze			
1256B	3H-6	59–60	23.69	2.79	6.1	Clayey nannofossil ooze			
1256B	3H-6	78–79	23.88	2.82	6.1	Clayey nannofossil ooze			
1256B	3H-6	91–92	24.01	2.84	6.1	Clayey nannofossil ooze			
1256B	3H-6	103–104	24.13	2.86	6.1	Clayey nannofossil ooze			
1256B	3H-6	122–123	24.32	2.89	6.1	Clayey nannofossil ooze			
1256B	3H-6	141–142	24.51	2.92	6.1	Clayey nannofossil ooze			
1256B	3H-7	23–24	24.83	2.98	6.1	Clayey nannofossil ooze			
1256B	4H-1	04–05	25.14	3.03	6.1	Sandy silty clay			
1256B	4H-1	67–68	25.77	3.13	6.1	Sandy silty clay			
1256B	4H-2	75–76	27.35	3.39	6.1	Sandy silty clay			
1256B	4H-3	83–84	28.93	3.65	6.1	Sandy silty clay			
1256B	4H-4	90–92	30.50	3.90	6.1	Sandy silty clay (with minor volcanic glass and diatoms)			
1256B	4H-4	128–129	30.88	3.97	6.1	Sandy silty clay			
1256B	4H-5	11–12	31.21	4.02	6.1	Sandy silty clay			
1256B	4H-5	41–42	31.51	4.07	6.1	Sandy silty clay			
1256B	4H-5	72–73	31.82	4.12	6.1	Sandy silty clay			
1256B	4H-5	104–105	32.14	4.17	6.1	Sandy silty clay			
1256B	4H-5	135–136	32.45	4.22	6.1	Sandy silty clay			
1256B	4H-6	17–18	32.77	4.28	6.1	Sandy silty clay			

*Reference for linear sedimentation rate: Jiang and Wise, 2007 (Site 1256); von Huene et al., 1982 (Site 495).

† Reference for lithology: Wilson et al., 2003 (Site 1256); von Huene et al., 1982 (Site 495).

Table 1 (*continued*)

Site/hole	Core/ section	Interval (cm)	Depth (mbsf)	Biostrati-graphic age estimate (Ma)	Appropriate linear sedimentation rate (m/Ma)*	Lithology†	Appropriate biohorizon, with mean depth and age, used for calculation of biostratigraphic ages	Reference for microfossil species	Reference for microfossil datum level
1256B	4H-6	48–49	33.08	4.33	6.1	Sandy silty clay			
1256B	4H-6	80–81	33.40	4.38	6.1	Sandy silty clay			
1256B	4H-6	111–112	33.71	4.43	6.1	Sandy silty clay			
1256B	4H-6	143–144	34.03	4.48	6.1	Sandy silty clay			
1256B	4H-7	24–25	34.34	4.53	6.1	Sandy silty clay			
1256B	4H-7	56–57	34.66	4.59	6.1	Sandy silty clay	LO *Calcidiscus macintyrei* (16.38 mbsf, 1.59 Ma)	Jiang and Wise, 2007	Berggren et al., 1995a
1256B	4H-7	68–69	34.78	4.61	6.1	Sandy silty clay			
1256B	5H-1	04–05	34.64	4.58	6.1	Sandy silty nannofossil ooze			
1256B	5H-1	36–37	34.96	4.64	6.1	Sandy silty nannofossil ooze			
1256B	5H-1	67–68	35.27	4.69	6.1	Sandy silty nannofossil ooze			
1256B	5H-1	93–94	35.53	4.73	6.1	Sandy silty nannofossil ooze			
1256B	5H-1	124–126	35.84	4.78	6.1	Sandy silty nannofossil ooze			
1256B	5H-6	92–94	43.02	5.67	13.2	Nannofossil ooze with diatoms			
1256B	6H-3	59–61	47.69	6.02	13.2	Nannofossil ooze with diatoms	LO *Discoaster quinqueramus* (42.13 mbsf, 5.60 Ma)	Jiang and Wise, 2007	Berggren et al.,1995b
1256B	7H-3	54–56	57.14	6.74	13.2	Diatom nannofossil ooze			
1256B	8H-2	66–68	65.26	7.35	13.2	Nannofossil ooze with diatoms			
1256B	8H-5	89–91	66.99	7.48	13.2	Nannofossil ooze with diatoms			
1256B	9H-2	79–81	74.89	7.89	8.4	Clayey nannofossil ooze with silt			
1256B	10H-4	95–97	87.55	9.39	8.4	Sandy silty nannofossil diatom ooze	FO *Discoaster berggrenii* (80.88 mbsf, 8.60 Ma)	Jiang and Wise, 2007	Berggren et al.,1995b

*Reference for linear sedimentation rate: Jiang and Wise, 2007 (Site 1256); von Huene et al., 1982 (Site 495).

† Reference for lithology: Wilson et al., 2003 (Site 1256); von Huene et al., 1982 (Site 495).

Table 1 (*continued*)

Site/hole	Core/ section	Interval (cm)	Depth (mbsf)	Biostrati-graphic age estimate (Ma)	Appropriate linear sedimentation rate (m/Ma)*	Lithology†	Appropriate biohorizon, with mean depth and age, used for calculation of biostratigraphic ages	Reference for microfossil species	Reference for microfossil datum level
1256B	12H-5	51–53	107.61	10.88	39.1	Nannofossil ooze	LO *Sphenolithus heteromorphus* (213.78 mbsf, 13.60 Ma)	Jiang and Wise, 2007	Berggren et al.,1995b
1256B	13H-2	100–102	112.40	11.01	39.1	Diatomite with nannofossils			
1256B	13H-6	25–26	117.14	11.13	39.1	Nannofossil ooze			
1256B	14H-4	79–80	125.39	11.34	39.1	Nannofossil ooze			
1256B	15H-3	37–39	132.97	11.53	39.1	Nannofossil ooze			
1256B	16H-3	132–134	143.42	11.80	39.1	Clayey nannofossil ooze			
1256B	17H-3	111–113	152.71	12.04	39.1	Nannofossil ooze			
1256B	19X-2	53–55	162.13	12.28	39.1	Nannofossil ooze with diatoms and silty clay			
1256B	20X-5	101–103	172.21	12.54	39.1	Clayey nannofossil ooze with silt			
1256B	21X-2	95–97	177.25	12.67	39.1	Nannofossil ooze with diatoms			
1256B	22X-2	45–47	185.95	12.89	39.1	Nannofossil ooze			
1256B	24X-3	79–81	207.19	13.43	39.1	Nannofossil ooze			
1256B	26X-1	89–91	223.59	13.85	39.1	Nannofossil ooze			
1256B	28X-2	54–56	243.64	14.36	39.1	Nannofossil ooze			
495	3R-5	76–77	25.76	1.11	37	Diatomaceous hemipelagic mud	LO *Discoaster brouweri* (57.0 mbsf, 1.95 Ma)	von Huene et al., 1982	Berggren et al., 1995a
495	6R-4	34–35	52.34	1.82	37	Biogenic silty mud			
495	9R-5	40–41	82.40	3.83	20	Diatomaceous silty mud	FO *Ceratolithus acutus* (112.60 mbsf, 5.34 Ma)	von Huene et al., 1982	Berggren et al., 1995a
495	12R-5	63–64	111.13	5.27	20	Siliceous mud			
495	15R-6	102–103	141.52	8.44	7	Diatomaceous mud	FO *Globorotalia plesiotumida* (142.50 mbsf, 8.58 Ma)	von Huene et al., 1982	Lourens et al., 2004
495	18R-7	61–62	171.11	10.77	11	Siliceous mud	LO *Discoaster kugleri* (179.10 mbsf, 11.50 Ma)	von Huene et al., 1982	Berggren et al.,1995b
495	21R-7	29–30	199.29	13.34	11	Nannofossil ooze			
495	24R-7	20–21	227.70	16.89	27	Nannofossil-foraminiferal ooze	LO *'Paragloborotalia' kugleri* (342.0 mbsf, 21.12 Ma)	von Huene et al., 1982	Lourens et al., 2004
495	27R-5	115–118	254.15	17.87	27	Nannofossil ooze			
495	30R-2	41–42	277.41	18.73	27	Foraminiferal-nannofossil ooze and chalk			
495	33R-5	41–42	310.41	19.95	27	Nannofossil ooze			
495	36R-4	50–51	337.50	20.95	27	Nannofossil ooze–chalk			
495	39R-3	108–109	365.08	21.50	58	Nannofossil-foraminiferal chalk			
495	41R-6	53–54	388.03	21.91	58	Foraminiferal-nannofossil chalk			
495	43R-5	24–25	405.24	22.21	58	Foraminiferal-nannofossil chalk with dendritic manganese			
495	45R-4	25–26	422.75	22.51	58	Foraminiferal-nannofossil chalk with dendritic manganese			

*Reference for linear sedimentation rate: Jiang and Wise, 2007 (Site 1256); von Huene et al., 1982 (Site 495).

† Reference for lithology: Wilson et al., 2003 (Site 1256); von Huene et al., 1982 (Site 495).

Table 2

Major element concentrations (measured values) and (selected) trace element concentrations (not covered by ICP-MS) of Site 1256 samples, determined by XRF. The CO2 values of all carbonates (samples taken from a depth > 40.6 mbsf) were calibrated against the limestone standard KH (except for 206-1256B-19X-2, 53-55). b.d.l. = below detection limit.

Sample ID	Depth	SiO_2	TiO_2	Al_2O_3	Fe_2O_3	MnO	MgO	CaO	Na_2O	K_2O	P_2O_5	H_2O	CO_2	Sum	Sr	Ba
	(mbsf)	(wt%)	(wt%)	(wt%)	(wt%)	(wt%)	(wt%)	(wt%)	(wt%)	(wt%)	(wt%)	(wt%)	(wt%)	(%)	(ppm)	(ppm)
ODP Leg 206, Site 1256																
206-1256A-1H-1, 32-34 cm	0,32	43,4	0,45	9,36	5,11	2,52	2,91	3,78	7,50	1,54	0,36	5,71	4,14	86,8	487	7481
206-1256A-1H-2, 19-21 cm	1,69	46,2	0,56	10,9	6,63	0,64	3,08	3,71	6,67	1,58	0,33	6,57	3,93	90,8	440	7932
206-1256B-1H-4, 56-58 cm	5,06	47,7	0,58	11,0	6,73	0,61	3,39	4,10	6,20	1,67	0,32	6,32	3,18	91,8	439	7949
206-1256B-3H-2, 34-36 cm	17,44	64,5	0,25	12,4	2,40	0,55	1,09	1,61	4,46	3,83	0,14	4,21	0,64	96,1	220	3209
206-1256B-4H-4, 90-92 cm	30,50	48,6	0,58	11,6	5,97	0,95	3,65	2,64	6,04	1,64	0,44	5,94	1,72	89,7	490	12827
206-1256B-5H-1, 124-126 cm	35,84	43,9	0,51	10,39	4,87	2,20	3,16	5,62	5,27	1,43	0,48	5,40	4,62	87,9	731	17704
206-1256B-5H-6, 92-94 cm	43,02	44,6	0,41	8,68	4,30	0,50	3,00	9,43	5,30	1,52	0,36	4,89	6,73	89,7	731	15469
206-1256B-6H-3, 59-61 cm	47,69	35,0	0,23	4,77	2,41	0,44	2,02	21,2	4,42	0,87	0,30	3,72	15,9	91,3	978	9318
206-1256B-7H-3, 54-56 cm	57,14	51,8	0,24	5,72	2,76	0,36	2,29	8,64	5,55	1,28	0,28	4,84	6,21	90,0	651	11198
206-1256B-8H-2, 66-68 cm	65,26	53,5	0,11	2,37	1,26	0,33	1,51	13,0	4,87	0,64	0,12	4,36	9,86	92,0	671	7645
206-1256B-8H-5, 89-91 cm	66,99	51,0	0,23	4,49	2,54	0,44	2,20	10,7	4,91	0,96	0,25	4,78	8,19	90,6	722	13950
206-1256B-9H-2, 79-81 cm	74,89	18,6	0,11	2,35	1,44	0,84	1,11	36,1	2,81	0,57	0,20	2,15	29,8	96,0	1352	5142
206-1256B-10H-4, 95-97 cm	87,55	58,6	0,27	5,06	3,44	0,28	2,40	4,21	6,14	1,25	0,17	5,25	2,80	89,9	548	12541
206-1256B-12H-5, 51-53 cm	107,61	30,7	0,06	1,29	1,01	0,19	1,04	29,4	3,41	0,41	0,09	2,66	24,9	95,1	1208	5320
206-1256B-13H-2, 100-102 cm	112,40	67,8	b.d.l.	0,23	0,14	0,04	0,72	8,68	5,03	0,21	b.d.l.	4,46	6,77	94,1	426	1438
206-1256B-14H-4, 79-81 cm	125,39	8,48	0,02	0,30	0,36	0,32	0,47	47,0	1,58	0,12	0,10	1,08	38,4	98,3	1577	1600
206-1256B-15H-3, 37-39 cm	132,97	13,6	0,02	0,45	0,51	0,23	0,66	43,6	1,91	0,17	0,09	1,48	35,4	98,0	1465	2287
206-1256B-16H-3, 132-134 cm	143,42	16,4	b.d.l.	0,28	2,69	0,20	0,56	39,7	2,01	0,14	0,07	1,60	33,7	97,4	1154	2230
206-1256B-17H-3, 111-113 cm	152,71	26,5	b.d.l.	0,25	0,35	0,13	0,58	35,0	2,46	0,14	0,07	2,35	29,1	96,9	1110	2046
206-1256B-19X-2, 53-55 cm	162,13	35,6	0,02	0,47	0,42	0,06	0,59	28,5	2,91	0,17	0,08	2,80	21,6	93,1	1143	3197
206-1256B-20X-5, 101-103 cm	172,21	10,2	b.d.l.	0,26	0,26	0,12	0,47	46,5	1,39	0,09	0,10	1,17	38,1	98,7	1094	1732
206-1256B-21X-2, 95-97 cm	177,25	21,5	b.d.l.	0,39	0,47	0,13	0,53	38,6	1,93	0,13	0,07	1,82	32,0	97,5	1288	2381
206-1256B-22X-2, 45-47 cm	185,95	11,9	0,02	0,41	0,69	0,16	0,61	44,7	1,54	0,15	0,09	1,41	36,4	98,0	1340	2533
206-1256B-24X-3, 79-81 cm	207,19	9,17	b.d.l.	0,23	0,42	0,21	0,55	47,1	1,42	0,12	0,08	1,23	38,3	98,8	1315	1997
206-1256B-28X-2, 54-56 cm	243,64	9,31	0,03	0,51	3,27	0,36	1,29	45,6	0,73	1,52	0,10	1,16	36,0	99,9	1318	2854

Table 3

Trace element concentrations of Site 1256 samples in µg/g (= ppm).
All concentrations determined by ICP-MS with the exception of Sr and Ba for those samples marked by (*).

Sample ID	Li	Sc	V	Cr	Co	Ni	Cu	Zn	Ga	Rb	Sr	Y	Zr	Nb	Cs	Ba
ODP Leg 206, Site 1256																
206-1256A-1H-1, 32-34 cm*	36,5	21,4	151	45,4	57,8	569	426	518	14,7	36,5	487	62,1	112	5,46	1,94	7481
206-1256A-1H-2, 19-21 cm*	45,5	24,1	139	56,3	43,7	492	343	472	16,8	37,7	440	60,5	128	6,26	2,10	7932
206-1256B-1H-4, 56-58 cm*	50,2	24,6	106	50,4	67,4	760	442	464	17,5	35,4	439	57,1	113	5,84	1,87	7949
206-1256B-3H-2, 34-36 cm*	2,25	0,74	3,30	0,90	1,00	10,6	14,3	12,9	1,49	10,9	220	3,08	8,11	0,69	0,49	3209
206-1256B-3H-2, 77-78 cm	49,2	22,3	94,2	42,7	45,2	622	650	365	16,8	35,2	514	89,7	136	6,27	1,77	12158
206-1256B-3H-3, 81-82 cm	46,9	21,1	84,9	42,5	69,7	501	645	291	16,3	40,2	507	85,5	150	11,6	1,88	12245
206-1256B-3H-4, 88-89 cm	63,5	23,5	242	57,9	58,7	566	251	378	17,5	38,8	561	90,3	122	5,65	2,01	13073
206-1256B-3H-5, 96-97 cm	55,0	20,8	128	47,4	61,4	546	195	449	16,3	44,1	541	76,8	111	5,66	2,35	11244
206-1256B-3H-6, 09-10 cm	62,1	23,3	125	55,3	68,2	621	220	454	19,2	40,5	477	86,4	120	5,88	2,13	12596
206-1256B-3H-6, 40-41 cm	58,7	23,8	100	52,6	62,8	593	262	362	19,4	40,3	482	99,2	123	6,14	2,15	12853
206-1256B-3H-6, 59-60 cm	53,8	23,5	92,8	49,0	63,2	579	316	365	19,1	41,4	502	110	128	6,08	2,15	13269
206-1256B-3H-6, 78-79 cm	49,2	20,1	120	48,0	69,9	659	223	457	16,4	36,6	645	95,6	105	5,21	1,88	10693
206-1256B-3H-6, 91-92 cm	48,8	20,4	99,4	44,2	72,7	683	226	428	16,9	36,0	604	95,5	106	5,17	1,85	9757
206-1256B-3H-6, 103-104 cm	47,8	22,6	83,4	49,3	58,3	701	675	429	19,0	37,8	548	97,7	113	5,98	1,96	12256
206-1256B-3H-6, 122-123 cm	48,5	24,0	88,4	52,5	49,3	551	882	294	20,4	44,6	470	111	120	6,75	2,29	12552
206-1256B-3H-6, 141-142 cm	51,4	26,0	96,3	65,2	47,7	551	882	322	21,0	39,1	489	119	124	6,32	2,14	12919
206-1256B-3H-7, 23-24 cm	44,8	23,7	84,1	57,7	44,0	472	718	376	19,0	35,7	691	122	115	5,57	1,92	12900
206-1256B-4H-1, 04-05 cm	44,7	24,2	87,9	57,1	43,2	449	668	315	19,9	41,8	502	97,4	141	6,62	1,99	12703
206-1256B-4H-1, 67-68 cm	53,9	27,0	103	67,4	56,2	555	756	392	21,5	37,2	538	118	125	5,95	2,08	14286
206-1256B-4H-2, 75-76 cm	34,9	17,3	62,5	40,9	42,8	370	288	230	13,4	26,7	880	70,1	81,8	4,02	1,38	9554
206-1256B-4H-3, 83-84 cm	57,7	26,6	151	63,4	75,0	651	275	416	20,2	39,2	504	94,6	121	5,71	2,18	12417
206-1256B-4H-4, 90-92 cm*	5,06	2,64	9,31	5,58	6,49	65,5	55,6	36,7	2,03	3,82	490	10,3	11,6	0,59	0,20	12827
206-1256B-4H-4, 128-129 cm	57,1	26,6	89,8	63,4	49,5	538	563	298	19,9	39,0	513	102	115	6,02	2,00	10684
206-1256B-4H-5, 11-12 cm	59,9	26,8	93,3	58,8	57,0	611	571	306	19,7	39,9	479	107	114	5,97	2,03	10420
206-1256B-4H-5, 41-42 cm	67,9	27,5	104	64,0	73,8	727	353	363	20,8	41,0	499	112	118	6,18	2,13	11968
206-1256B-4H-5, 72-73 cm	70,2	26,1	170	67,2	74,5	715	261	377	19,8	39,7	468	108	112	5,85	2,09	10751
206-1256B-4H-5, 104-105 cm	61,7	26,1	95,0	61,2	63,6	654	494	299	19,6	38,1	507	121	114	5,85	2,04	10852

Table 3 (*continued*)

Sample ID	Li	Sc	V	Cr	Co	Ni	Cu	Zn	Ga	Rb	Sr	Y	Zr	Nb	Cs	Ba
ODP Leg 206, Site 1256																
206-1256B-4H-5, 135-136 cm	61,6	26,2	91,7	58,8	58,0	601	602	270	19,6	37,0	539	119	113	5,66	1,98	11444
206-1256B-4H-6, 17-18 cm	46,7	21,3	72,4	52,7	40,0	440	472	213	16,5	30,9	718	102	93,3	4,77	1,59	8409
206-1256B-4H-6, 48-49 cm	49,4	22,1	71,7	49,1	43,6	502	550	228	17,5	33,9	714	95,9	98,9	5,29	1,70	11411
206-1256B-4H-6, 80-81 cm	57,7	24,6	79,6	56,6	50,7	635	413	282	19,3	37,4	620	94,7	108	5,79	1,89	11335
206-1256B-4H-6, 111-112 cm	50,0	21,4	77,1	53,1	44,2	483	233	232	17,1	36,0	697	91,2	95,9	5,40	1,81	9320
206-1256B-4H-6, 143-144 cm	48,9	20,0	66,9	50,1	43,7	584	283	271	18,1	45,7	499	66,5	96,3	5,93	2,09	8388
206-1256B-4H-7, 24-25 cm	27,4	10,6	35,6	21,9	17,0	193	203	112	15,8	83,7	293	46,0	76,4	7,19	3,49	5519
206-1256B-4H-7, 56-57 cm	49,0	24,1	84,6	51,7	40,2	508	534	246	19,1	34,7	657	104	108	5,68	1,77	11103
206-1256B-4H-7, 68-69 cm	46,1	22,2	75,7	52,2	35,7	481	495	229	17,4	31,5	717	94,1	101	5,06	1,59	9805
206-1256B-5H-1, 04-05 cm	48,3	23,2	77,4	57,2	37,7	500	514	293	18,2	34,7	711	96,7	101	5,38	1,72	10385
206-1256B-5H-1, 36-37 cm	51,8	25,4	81,2	54,1	40,7	603	594	274	19,7	33,8	726	118	107	5,44	1,71	13910
206-1256B-5H-1, 67-68 cm	45,0	22,8	73,6	50,5	35,1	539	552	248	18,2	33,0	824	104	101	5,40	1,57	13478
206-1256B-5H-1, 93-94 cm	45,1	22,4	71,1	51,1	33,9	536	578	243	17,9	32,0	846	95,9	98,5	5,13	1,55	12817
206-1256B-5H-1, 124-126 cm*	42,6	23,9	80,8	48,7	65,1	751	829	311	20,5	33,9	731	111	108	5,44	1,72	17704
206-1256B-5H-6, 92-94 cm*	42,9	19,3	118,1	40,9	34,8	804	513	433	19,0	35,7	731	93,6	89,8	4,64	1,88	15469
206-1256B-6H-3, 59-61 cm*	26,5	11,6	40,2	23,9	26,7	506	190	268	10,8	18,4	978	66,7	57,2	2,51	0,89	9318
206-1256B-7H-3, 54-56 cm*	26,2	12,5	44,0	22,9	28,0	617	1837	406	13,6	28,0	651	58,7	67,8	2,84	1,25	11198
206-1256B-8H-2, 66-68 cm*	12,7	5,90	18,9	10,7	15,3	283	138	189	7,01	12,1	671	35,9	40,7	1,41	0,51	7645
206-1256B-8H-5, 89-91 cm*	22,8	13,6	60,9	22,6	55,7	776	395	472	13,0	19,3	722	71,1	79,4	2,92	0,83	13950
206-1256B-9H-2, 79-81 cm*	9,55	5,43	14,6	7,29	14,4	204	138	95	5,09	11,1	1352	41,5	37,8	1,83	0,39	5142
206-1256B-10H-4, 95-97 cm*	23,5	14,8	35,7	25,1	23,8	271	215	147	13,6	22,6	548	49,2	101	3,44	0,74	12541
206-1256B-12H-5, 51-53 cm*	10,7	6,49	57,5	8,78	7,89	93,74	281	109	6,17	7,13	1208	24,2	35,4	0,95	0,27	5320
206-1256B-13H-2, 100-102 cm*	2,59	1,05	16,2	3,19	0,89	17,76	55,58	27,5	1,62	1,38	426	3,48	9,19	0,14	0,04	1438
206-1256B-13H-6, 25-26 cm	16,8	6,58	25,3	8,49	5,09	74,5	87,1	80,6	5,74	7,25	1179	27,9	36,3	1,05	0,28	7251
206-1256B-14H-4, 79-81 cm*	4,40	1,55	7,20	1,76	1,74	13,66	14,92	15,2	1,20	1,73	1577	12,8	7,80	0,56	0,07	1600
206-1256B-15H-3, 37-39 cm*	9,87	2,27	6,19	2,20	1,41	13,29	33,83	24,7	2,02	2,83	1465	17,0	12,8	0,56	0,11	2287
206-1256B-16H-3, 132-134 cm*	8,61	1,64	6,17	2,89	1,69	11,62	31,30	42,5	1,63	1,83	1154	11,9	10,1	0,53	0,07	2230
206-1256B-17H-3, 111-113 cm*	6,48	1,06	6,03	3,74	1,18	10,48	48,05	41,1	1,67	1,47	1110	9,38	8,21	0,36	0,06	2046
206-1256B-19X-2, 53-55 cm*	6,34	2,77	16,2	3,18	3,16	60,01	97,54	88,3	3,01	1,62	1143	13,8	18,5	0,41	0,07	3197
206-1256B-20X-5, 101-103 cm*	6,82	1,31	10,2	1,98	1,37	11,21	14,48	24,1	1,25	1,28	1094	12,8	7,28	0,45	0,07	1732
206-1256B-21X-2, 95-97 cm*	7,16	1,87	15,5	3,78	3,39	29,86	100,7	65,7	2,09	1,54	1288	13,0	14,5	0,44	0,07	2381
206-1256B-22X-2, 45-47 cm*	8,06	1,88	18,6	5,57	1,71	18,83	25,20	38,5	1,45	2,46	1340	19,9	12,3	0,61	0,09	2533
206-1256B-24X-3, 79-81 cm*	5,02	1,22	9,30	1,99	1,74	11,45	27,52	28,5	1,12	1,80	1315	11,7	7,51	0,45	0,06	1997
206-1256B-26X-1, 89-91 cm	5,29	1,62	7,59	2,52	0,60	10,88	41,21	24,3	1,55	4,24		13,9	10,5	0,59	0,16	
206-1256B-28X-2, 54-56 cm*	5,65	2,66	15,3	7,48	2,21	14,73	75,00	49,3	1,60	32,2	1318	19,5	17,3	0,70	0,46	2854

Table 3 (*continued*)

Sample ID	La	Ce	Pr	Nd	Sm	Eu	Gd	Tb	Dy	Ho	Er	Tm	Yb	Lu	Hf	Ta	Pb†	Th†	U†
ODP Leg 206, Site 1256																			
206-1256A-1H-1, 32-34 cm*	29,1	31,8	6,49	27,4	6,29	1,74	7,67	1,13	7,56	1,71	5,21	0,72	5,38	0,87	2,10	0,52	13,3	3,06	1,06
206-1256A-1H-2, 19-21 cm*	29,7	34,6	6,69	27,9	6,39	1,72	7,65	1,11	7,46	1,66	4,96	0,69	5,18	0,82	2,46	0,57	15,1	3,08	0,84
206-1256B-1H-4, 56-58 cm*	26,1	31,6	5,65	23,8	5,57	1,56	6,71	0,99	6,74	1,54	4,63	0,65	4,91	0,78	2,28	0,56	13,4	2,50	0,73
206-1256B-3H-2, 34-36 cm*	2,89	4,39	0,58	2,11	0,41	0,09	0,43	0,06	0,42	0,09	0,28	0,04	0,30	0,05	0,24	0,08	1,64	0,93	0,30
206-1256B-3H-2, 77-78 cm	47,1	41,3	9,34	40,4	8,51	2,29	10,3	1,73	11,5	2,54	7,82	1,11	7,16	1,12	2,37	0,54	73,8	3,05	0,86
206-1256B-3H-3, 81-82 cm	45,8	44,2	9,52	40,2	8,62	2,21	9,98	1,70	11,2	2,40	7,35	1,05	6,66	1,04	2,84	0,87	16,7	3,75	1,04
206-1256B-3H-4, 88-89 cm	42,9	39,3	9,58	41,3	9,26	2,43	10,8	1,80	11,8	2,55	7,63	1,07	6,92	1,08	2,24	0,47	20,5	3,01	0,90
206-1256B-3H-5, 96-97 cm	37,9	38,7	8,91	38,3	8,61	2,22	9,64	1,66	10,6	2,27	6,79	0,97	6,17	0,95	2,18	0,46	16,3	3,73	1,15
206-1256B-3H-6, 09-10 cm	42,2	40,3	10,1	44,3	10,0	2,57	11,5	1,89	12,2	2,57	7,79	1,10	7,02	1,10	2,30	0,44	17,5	3,26	0,92
206-1256B-3H-6, 40-41 cm	47,5	42,1	11,2	48,9	11,1	2,92	12,9	2,08	13,6	2,98	8,98	1,25	8,18	1,27	2,50	0,45	16,5	3,38	0,92
206-1256B-3H-6, 59-60 cm	50,9	44,0	11,8	52,5	11,4	3,06	13,7	2,22	14,6	3,17	9,63	1,35	8,77	1,37	2,66	0,47	19,0	3,69	1,02
206-1256B-3H-6, 78-79 cm	45,4	37,3	10,7	47,4	10,5	2,73	12,2	1,96	13,0	2,81	8,30	1,16	7,45	1,16	2,09	0,41	16,4	3,06	0,87
206-1256B-3H-6, 91-92 cm	45,6	37,5	10,4	45,9	10,2	2,69	11,8	1,93	12,7	2,76	8,34	1,15	7,41	1,14	2,07	0,41	16,6	2,99	0,85
206-1256B-3H-6, 103-104 cm	48,8	40,0	11,2	49,2	10,6	2,82	12,6	2,00	13,2	2,84	8,58	1,19	7,74	1,19	2,22	0,43	15,7	3,44	0,94
206-1256B-3H-6, 122-123 cm	55,6	45,8	12,5	54,4	12,1	3,15	14,2	2,27	14,9	3,25	9,82	1,38	8,92	1,39	2,49	0,49	18,0	4,28	1,19
206-1256B-3H-6, 141-142 cm	56,2	43,5	12,7	55,9	12,3	3,22	14,4	2,36	15,5	3,38	10,2	1,42	9,15	1,43	2,39	0,45	18,0	3,55	1,01
206-1256B-3H-7, 23-24 cm	54,9	42,5	11,6	51,1	11,1	2,86	13,3	2,23	15,0	3,35	10,2	1,44	9,40	1,48	2,19	0,40	13,8	3,08	0,89
206-1256B-4H-1, 04-05 cm	49,0	48,4	10,6	45,9	10,0	2,52	11,6	1,90	12,7	2,75	8,37	1,20	7,88	1,23	2,85	0,46	27,4	3,80	1,11
206-1256B-4H-1, 67-68 cm	57,4	44,5	12,4	54,5	11,8	3,10	14,1	2,33	15,5	3,39	10,3	1,44	9,22	1,44	2,44	0,40	17,7	3,11	0,84
206-1256B-4H-2, 75-76 cm	34,0	27,6	7,16	31,4	6,91	1,80	8,14	1,34	8,93	1,99	6,06	0,85	5,46	0,84	1,55	0,29	10,7	2,02	0,58
206-1256B-4H-3, 83-84 cm	47,8	41,3	11,4	50,1	11,1	2,91	12,6	2,08	13,5	2,85	8,53	1,17	7,51	1,13	2,27	0,39	16,1	3,03	0,76
206-1256B-4H-4, 90-92 cm*	5,06	4,06	1,23	5,28	1,21	0,33	1,47	0,21	1,37	0,29	0,85	0,12	0,83	0,13	0,25	0,06	1,26	0,30	0,08
206-1256B-4H-4, 128-129 cm	50,0	39,4	11,3	47,5	10,9	2,78	12,2	2,05	13,4	2,85	8,44	1,16	7,37	1,14	2,29	0,55	11,0	2,91	0,72
206-1256B-4H-5, 11-12 cm	51,4	40,0	11,6	48,6	11,3	2,94	12,7	2,15	13,9	2,98	8,81	1,23	7,79	1,21	2,32	0,48	11,1	2,93	0,75
206-1256B-4H-5, 41-42 cm	53,6	40,9	12,2	51,8	11,9	3,14	13,7	2,25	14,7	3,11	9,41	1,31	8,22	1,27	2,35	0,49	13,4	2,93	0,74
206-1256B-4H-5, 72-73 cm	52,5	38,4	11,7	49,2	11,5	2,96	13,2	2,16	14,1	3,05	9,12	1,27	7,94	1,21	2,39	0,40	13,8	2,83	0,73
206-1256B-4H-5, 104-105 cm	57,3	38,4	12,3	52,3	12,0	3,12	14,0	2,28	15,1	3,27	9,85	1,36	8,59	1,34	2,38	0,49	13,9	2,86	0,76
206-1256B-4H-5, 135-136 cm	56,2	37,4	11,9	49,6	11,2	3,00	13,2	2,20	14,4	3,09	9,37	1,32	8,18	1,28	2,27	0,55	14,2	2,74	0,74
206-1256B-4H-6, 17-18 cm	47,8	33,6	10,3	43,4	9,9	2,57	11,5	1,88	12,6	2,75	8,21	1,15	7,23	1,10	1,84	0,39	10,5	2,29	0,63
206-1256B-4H-6, 48-49 cm	46,5	33,2	10,2	42,2	9,6	2,48	10,9	1,82	11,9	2,51	7,68	1,05	6,65	0,99	1,88	0,40	11,9	2,53	0,66
206-1256B-4H-6, 80-81 cm	47,3	33,5	10,5	42,9	10,0	2,54	11,0	1,88	11,9	2,49	7,47	1,02	6,22	0,95	1,96	0,44	12,8	2,58	0,67
206-1256B-4H-6, 111-112 cm	46,1	32,9	10,0	41,4	9,5	2,44	10,5	1,80	11,4	2,44	7,35	1,02	6,37	0,96	1,87	0,35	12,3	2,60	0,68

Table 3 (*continued*)

Sample ID	La	Ce	Pr	Nd	Sm	Eu	Gd	Tb	Dy	Ho	Er	Tm	Yb	Lu	Hf	Ta	Pb†	Th†	U†
ODP Leg 206, Site 1256																			
206-1256B-4H-6, 143-144 cm	36,2	30,4	8,2	33,1	7,8	1,97	8,45	1,41	9,11	1,90	5,48	0,76	4,80	0,73	1,97	0,44	12,0	3,01	0,83
206-1256B-4H-7, 24-25 cm	29,6	30,8	6,4	24,8	5,9	1,37	6,24	0,96	6,47	1,35	4,00	0,57	3,57	0,55	2,26	0,62	14,1	5,64	1,87
206-1256B-4H-7, 56-57 cm	52,9	36,6	12,2	51,3	11,6	3,01	13,2	2,10	13,7	2,91	8,64	1,19	7,37	1,13	2,22	0,43	11,3	2,90	0,70
206-1256B-4H-7, 68-69 cm	48,1	34,0	10,9	45,4	10,4	2,67	11,6	1,88	12,2	2,58	7,54	1,03	6,51	1,00	1,95	0,39	9,71	2,53	0,62
206-1256B-5H-1, 04-05 cm	48,8	34,1	11,0	45,4	10,6	2,69	11,7	1,93	12,4	2,63	7,64	1,07	6,49	1,01	1,97	0,43	25,3	2,63	0,66
206-1256B-5H-1, 36-37 cm	57,3	37,9	12,3	50,5	11,8	3,07	13,4	2,20	14,5	3,09	9,33	1,27	7,95	1,23	1,99	0,40	12,1	2,55	0,61
206-1256B-5H-1, 67-68 cm	51,4	36,0	11,2	47,0	11,0	2,77	11,9	1,97	12,9	2,77	8,19	1,11	7,14	1,09	1,95	0,38	12,3	2,54	0,62
206-1256B-5H-1, 93-94 cm	47,9	33,5	10,7	44,4	10,4	2,67	11,4	1,92	12,5	2,59	7,66	1,03	6,50	1,02	1,94	0,42	11,3	2,44	0,59
206-1256B-5H-1, 124-126 cm*	53,0	36,3	12,4	52,7	12,3	3,20	14,5	2,07	13,4	2,94	8,61	1,15	8,36	1,30	2,22	0,53	14,6	2,77	0,68
206-1256B-5H-6, 92-94 cm*	42,1	28,3	9,32	39,7	9,05	2,39	10,9	1,54	10,3	2,32	6,82	0,92	6,78	1,06	1,77	0,46	10,4	2,63	1,39
206-1256B-6H-3, 59-61 cm*	28,5	16,5	5,61	24,3	5,20	1,46	6,91	1,02	6,93	1,62	4,88	0,68	4,90	0,78	1,14	0,25	7,66	1,29	1,61
206-1256B-7H-3, 54-56 cm*	27,6	19,0	5,72	24,5	5,38	1,48	6,65	0,96	6,31	1,45	4,31	0,60	4,34	0,67	1,39	0,30	8,43	1,89	1,01
206-1256B-8H-2, 66-68 cm*	17,3	11,3	3,50	15,1	3,38	0,94	4,23	0,62	4,20	0,98	2,91	0,40	2,84	0,45	0,74	0,13	3,47	0,84	0,32
206-1256B-8H-5, 89-91 cm*	30,9	19,5	6,78	29,5	6,67	1,85	8,40	1,21	8,08	1,81	5,27	0,72	5,24	0,84	1,30	0,22	6,35	1,47	0,46
206-1256B-9H-2, 79-81 cm*	18,0	10,7	3,24	13,9	3,13	0,87	3,97	0,58	4,10	0,97	3,05	0,43	3,03	0,48	0,70	0,43	4,24	0,86	0,30
206-1256B-10H-4, 95-97 cm*	25,4	19,0	5,44	23,1	5,15	1,40	6,27	0,90	5,80	1,30	3,79	0,54	4,01	0,61	1,64	0,28	11,5	1,30	0,43
206-1256B-12H-5, 51-53 cm*	12,2	5,21	2,33	9,96	2,21	0,61	2,93	0,42	2,74	0,63	1,92	0,27	1,99	0,31	0,51	0,13	3,40	0,45	1,43
206-1256B-13H-2, 100-102 cm*	1,92	0,77	0,36	1,52	0,34	0,10	0,42	0,06	0,43	0,10	0,30	0,05	0,35	0,06	0,12	0,02	0,58	0,07	0,91
206-1256B-13H-6, 25-26 cm	14,2	6,51	2,81	12,7	2,71	0,73	3,44	0,54	3,64	0,81	2,47	0,35	2,30	0,36	0,56	0,07	4,97	0,51	1,53
206-1256B-14H-4, 79-81 cm*	5,91	1,51	0,97	4,24	0,90	0,25	1,26	0,18	1,25	0,30	0,93	0,13	0,92	0,15	0,12	0,68	1,17	0,10	0,36
206-1256B-15H-3, 37-39 cm*	8,22	2,25	1,48	6,42	1,49	0,39	1,90	0,28	1,88	0,44	1,33	0,19	1,37	0,22	0,18	0,56	1,93	0,16	0,25
206-1256B-16H-3, 132-134 cm*	5,47	1,67	0,96	4,23	0,94	0,26	1,30	0,19	1,36	0,32	0,98	0,15	1,00	0,16	0,14	0,60	1,81	0,12	0,21
206-1256B-17H-3, 111-113 cm*	4,36	1,21	0,71	3,20	0,68	0,20	0,97	0,14	1,01	0,25	0,77	0,11	0,73	0,12	0,11	0,47	1,89	0,11	0,32
206-1256B-19X-2, 53-55 cm*	7,06	2,04	1,26	5,61	1,14	0,33	1,60	0,23	1,61	0,37	1,11	0,15	1,06	0,18	0,24	0,26	1,93	0,15	1,20
206-1256B-20X-5, 101-103 cm*	5,94	1,44	0,91	4,07	0,82	0,24	1,21	0,19	1,34	0,32	1,01	0,15	0,97	0,16	0,11	0,68	1,05	0,08	0,48
206-1256B-21X-2, 95-97 cm*	6,78	1,77	1,15	5,09	1,11	0,30	1,50	0,22	1,51	0,36	1,09	0,15	1,04	0,17	0,20	0,52	2,61	0,11	0,64
206-1256B-22X-2, 45-47 cm*	10,2	2,35	1,70	7,52	1,57	0,45	2,28	0,33	2,39	0,54	1,70	0,23	1,59	0,25	0,19	0,67	2,84	0,14	0,32
206-1256B-24X-3, 79-81 cm*	6,10	1,39	0,97	4,31	0,91	0,25	1,24	0,18	1,34	0,31	0,91	0,13	0,93	0,14	0,10	0,69	2,05	0,09	0,17
206-1256B-26X-1, 89-91 cm	7,25	1,82	1,10	4,86	1,01	0,29	1,45	0,22	1,54	0,38	1,14	0,18	1,16	0,19	0,17	0,87	1,76	0,13	0,07
206-1256B-28X-2, 54-56 cm*	11,2	3,11	2,02	8,83	1,89	0,54	2,56	0,37	2,48	0,57	1,65	0,24	1,55	0,25	0,29	0,66	5,22	0,21	0,09

†Pb, Th, and U concentrations have already been published by Höfig et al. (in preparation, see CHAPTER II) in parts.

Table 4

Sr-Nd-Hf isotopic compositions of studied samples including bulk sediment, residue, and leachate data. εNd refers to the deviation of 143Nd/144Nd from the Nd isotopic composition of the present-day Chondritic Uniform Reservoir (CHUR = 0.512638; Jacobsen and Wasserburg, 1980).

Sample ID	$^{87}Sr/^{86}Sr$	2 sigma	$^{143}Nd/^{144}Nd$	2 sigma	ε_{Nd}	$^{176}Hf/^{177}Hf$	2 sigma
ODP Leg 206, Site 1256							
206-1256A-1H-1, 32-34 cm	0,708486	0,000005	0,512536	0,000004	-1,99	0,283014	0,000007
206-1256A-1H-2, 19-21 cm	0,708388	0,000004	0,512549	0,000005	-1,73	0,283009	0,000007
206-1256B-1H-4, 56-58 cm	0,708255	0,000005	0,512611	0,000005	-0,52	0,283034	0,000007
206-1256B-3H-2, 34-36 cm	0,706097	0,000004	0,512683	0,000002	0,87	0,282948	0,000005
206-1256B-3H-6, 09-10 cm	0,708231	0,000005	0,512587	0,000003	-1,00		
206-1256B-3H-6, 59-60 cm	0,708249	0,000003	0,512572	0,000002	-1,16		
206-1256B-3H-6, 91-92 cm	0,708498	0,000003	0,512580	0,000002	-1,15		
206-1256B-3H-6, 141-142 cm	0,708365	0,000003	0,512569	0,000002	-1,09		
206-1256B-3H-7, 23-24 cm	0,708611	0,000006	0,512588	0,000003	-0,98		
206-1256B-3H-7, 23-24 cm_Replicate	0,708615	0,000005	0,512585	0,000003	-1,03		
206-1256B-4H-1, 04-05 cm	0,708016	0,000006	0,512628	0,000003	-0,19		
206-1256B-4H-1, 67-68 cm	0,708203	0,000005	0,512579	0,000003	-1,14		
206-1256B-4H-2, 75-76 cm	0,708757	0,000005	0,512607	0,000003	-0,60		
206-1256B-4H-3, 83-84 cm	0,708291	0,000006	0,512569	0,000002	-1,35		
206-1256B-4H-4, 90-92 cm	0,707967	0,000004	0,512581	0,000002	-1,11	0,283044	0,000005
206-1256B-4H-5, 72-73 cm	0,708256	0,000006	0,512578	0,000002	-1,16		
206-1256B-4H-7, 24-25 cm	0,707530	0,000005	0,512600	0,000003	-0,74		
206-1256B-5H-1, 04-05 cm	0,708145	0,000005	0,512571	0,000000	-1,31		
206-1256B-5H-1, 124-126 cm	0,708513	0,000004	0,512576	0,000004	-1,15	0,283044	0,000006
206-1256B-5H-6, 92-94 cm	0,708545	0,000004	0,512570	0,000005	-1,32	0,283035	0,000005
206-1256B-6H-3, 59-61 cm	0,708795	0,000005	0,512571	0,000005	-1,30		
206-1256B-7H-3, 54-56 cm	0,708587	0,000005	0,512593	0,000005	-0,87	0,283061	0,000007
206-1256B-8H-2, 66-68 cm	0,708794	0,000005	0,512575	0,000005	-1,23		
206-1256B-8H-5, 89-91 cm	0,708668	0,000005	0,512566	0,000003	-1,40		
206-1256B-9H-2, 79-81 cm	0,708839	0,000004	0,512605	0,000005	-0,64		
206-1256B-10H-4, 95-97 cm	0,708527	0,000005	0,512586	0,000003	-1,02	0,283072	0,000006
206-1256B-12H-5, 51-53 cm	0,708850	0,000005	0,512496	0,000006	-2,77		
206-1256B-13H-2, 100-102 cm	0,708882	0,000004	0,512493	0,000019	-2,83		
206-1256B-14H-4, 79-81 cm	0,708860	0,000004	0,512488	0,000008	-2,93		
206-1256B-15H-3, 37-39 cm	0,708854	0,000005	0,512485	0,000004	-2,98		
206-1256B-16H-3, 132-134 cm	0,708854	0,000005	0,512498	0,000007	-2,74		
206-1256B-17H-3, 111-113 cm	0,708842	0,000004	0,512496	0,000005	-2,77		
206-1256B-19X-2, 53-55 cm	0,708839	0,000004	0,512483	0,000002	-3,03		
206-1256B-20X-5, 101-103 cm	0,708842	0,000005	0,512521	0,000010	-2,29		
206-1256B-21X-2, 95-97 cm	0,708820	0,000006	0,512472	0,000003	-3,23		
206-1256B-22X-2, 45-47 cm	0,708840	0,000006	0,512474	0,000003	-3,20		
206-1256B-24X-3, 79-81 cm	0,708828	0,000004	0,512447	0,000017	-3,73		
206-1256B-24X-3, 79-81 cm_Replicate	0,708824	0,000006					
206-1256B-26X-1, 89-91 cm	0,708830	0,000005	0,512467	0,000008	-3,34		
206-1256B-28X-2, 54-56 cm	0,708819	0,000005	0,512435	0,000002	-3,95		

Table 4 (*continued*)

Sample ID	$^{87}Sr/^{86}Sr$	2 sigma	$^{143}Nd/^{144}Nd$	2 sigma	ε_{Nd}	$^{176}Hf/^{177}Hf$	2 sigma
ODP Leg 206, Site 1256							
Residues							
206-1256A-1H-2, 19-21 cm_Res	0,707911	0,000005	0,512558	0,000002	-1,56		
206-1256B-4H-4, 90-92 cm_Res	0,708005	0,000006	0,512596	0,000003	-0,81		
206-1256B-8H-5, 89-91 cm_Res	0,708362	0,000005	0,512576	0,000002	-1,20		
206-1256B-21X-2, 95-97 cm_Res	0,708788	0,000005	0,512474	0,000002	-3,20		
206-1256B-28X-2, 54-56 cm_Res	0,708908	0,000006	0,512441	0,000002	-3,85		
Leachates							
206-1256A-1H-2, 19-21 cm_Leach	0,709153	0,000006	0,512536	0,000003	-1,99		
206-1256B-4H-4, 90-92 cm_Leach	0,709009	0,000006	0,512577	0,000002	-1,19		
206-1256B-8H-5, 89-91 cm_Leach	0,708938	0,000006	0,512549	0,000003	-1,74		
206-1256B-21X-2, 95-97 cm_Leach	0,708833	0,000006	0,512474	0,000002	-3,20		
206-1256B-28X-2, 54-56 cm_Leach	0,708751	0,000006	0,512439	0,000003	-3,88		
DSDP Leg 67, Site 495							
67-495-3R-5, 76-77 cm	0,707128	0,000005	0,512790	0,000002	2,97		
67-495-6R-4, 34-35 cm	0,706729	0,000005	0,512797	0,000003	3,10		
67-495-9R-5, 40-41 cm	0,707621	0,000005	0,512709	0,000002	1,39		
67-495-12R-5, 63-64 cm	0,707510	0,000006	0,512656	0,000003	0,35		
67-495-15R-6, 102-103 cm	0,707831	0,000006	0,512672	0,000003	0,67		
67-495-18R-7, 61-62 cm	0,707647	0,000005	0,512663	0,000003	0,49		
67-495-21R-7, 29-30 cm	0,708809	0,000005	0,512486	0,000002	-2,96		
67-495-24R-7, 20-21 cm	0,708772	0,000006	0,512413	0,000002	-4,38		
67-495-27R-5, 115-118 cm	0,708679	0,000006	0,512427	0,000009	-4,12		
67-495-30R-2, 41-42 cm	0,708610	0,000006	0,512415	0,000003	-4,36		
67-495-33R-5, 41-42 cm	0,708511	0,000005	0,512432	0,000013	-4,01		
67-495-36R-4, 50-51 cm	0,708458	0,000005	0,512486	0,000003	-2,96		
67-495-39R-3, 108-109 cm	0,708370	0,000005	0,512401	0,000005	-4,63		
67-495-41R-6, 53-54 cm	0,708332	0,000005	0,512369	0,000017	-5,24		
67-495-41R-6, 53-54 cm_Replicate	0,708327	0,000006	0,512386	0,000008	-4,92		
67-495-43R-5, 24-25 cm	0,708312	0,000006	0,512395	0,000007	-4,75		
67-495-45R-4, 25-26 cm	0,708293	0,000006	0,512366	0,000004	-5,30		

APPENDICES

Appendix I (CHAPTER I)

Appendix Section A.1:

Detailed summary on observed alteration at ODP/IODP Site 1256

Almost all Site 1256 lava flows were exposed to at least low-temperature alteration (<150 °C), which led to a slight overprint revealed by the presence of phyllosilicates and iron oxyhydroxides (Alt et al., 2010; Teagle et al., 2006). At ~981 mbsf, the first chlorite-smectite assemblage occurs representing the beginning of the hydrothermal alteration transition zone (see Fig. 2), which is characterized by a gradually increasing degree of alteration downhole, leading to (sub)greenschist-facies conditions in the upper dikes at ~1028 mbsf, where the first green background alteration is observed (Alt et al., 2010; Teagle et al., 2006). The identification of greenschist facies manifests the upper boundary of the high-temperature hydrothermal alteration zone and corresponds well with the top of the highly metal sulfide-mineralized hyaloclastic breccia encountered in the TZ at ~1028 mbsf (see Fig. 2). Primary glass shards in this breccia are replaced by chlorite, feldspar, and titanite, which are cemented by a dominantly quartz–pyritic assemblage (Alt et al., 2010).

Hydrothermal alteration predominates from the sulfide-mineralized layer downward through the sheeted dikes to the gabbros. According to Alt et al. (2010), the successive transformation to greenschist mineral assemblages along with minor metal sulfide mineralization in the upper dikes of the TZ is derived from the contact and mixing of ascending hydrothermal fluids and descending cooler seawater. Hydrothermal alteration predominates from the sulfide-mineralized layer downward through the sheeted dikes to the gabbros (Fig. 2) as evident by 1) an increase in the degree of alteration (with the first epidote grains at ~1095 mbsf and chlorite as a major alteration mineral at <1300 mbsf), 2) an increasing recrystallization of primary clinopyroxene to amphibole, the dominant alteration mineral below ~1300 mbsf, and 3) (partial) leaching of the base metals Cu, Zn, Pb, Ni, and Sn at significantly elevated temperatures of >300 to ~600 °C (Alt et al., 2010; Teagle et al., 2006).

Brecciation of chilled dike margins observed above 1350 mbsf in the SDC is linked to replacement of primary host-rock minerals by cross-cutting veins comprising an assemblage of greenschist-facies minerals and metal sulfides (common paragenesis: pyrite–chalcopyrite–sphalerite) (Alt et al., 2010). The lowermost ~58 m of the SDC are made up of highly to completely hydrothermally altered rocks, which were transformed to granoblastic hornfels to variable extent at high temperatures (850–900 °C) through contact metamorphism caused by the emplacement of gabbroic intrusive bodies below (Alt et al., 2010; Koepke et al., 2008; Teagle et al., 2006). The plutonic rocks are moderately to completely altered to a secondary

paragenesis of amphibole, chlorite, plagioclase, titanite ± laumontite and epidote showing a greater abundance of epidote and chlorite in Gabbro 2 (Teagle et al., 2012).

Appendix Section A.2:

On the applied isotopic modeling approach after Stracke et al. (2003)

Three parameters had to be determined in order to yield the present-day isotopic composition of recycled oceanic crust, being described in the following. First of all, this composition is a function of the recycling ages, which were chosen to range from 0.5 to 3 Ga for the present study, reflecting the likely spectrum of potential recycling ages pointed out by previous studies (e.g., Hanyu et al., 2011; Hauri and Hart, 1993). Secondly, the respective recycling age determines the initial isotopic composition of the recycled crust. This depends on the assumed differentiation age of the MORB source (the point of time referring to the derivation of the MORB source from the Bulk Earth (BE) reservoir), which has been set at 3 Ga for the present study. The simplified Pb isotopic evolution of the MORB source was determined by applying the initial Pb isotope ratios of Tatsumoto et al. (1973) to a single-stage evolution starting from BE at 4.55 Ga and using average $^{238}U/^{204}Pb$ (μ) = 8.2, $^{232}Th/^{204}Pb$ (ω) = 31.16, and $^{232}Th/^{238}U$ (κ) = 3.8 (Stracke et al., 2003), which gave the average present-day MORB composition ($^{206}Pb/^{204}Pb$ = 17.72, $^{207}Pb/^{204}Pb$ = 15.49, and $^{208}Pb/^{204}Pb$ = 37.34) and is used to back-calculate the initial (past) MORB compositions at a given time before the crust was modified by alteration/recycling. For the modeling of the initial Sr-Nd isotopic compositions, a two-stage evolution has been applied, accounting for a first period being equal to evolution of BE from 4.55 to 3 Ga and a subsequent evolution step from BE at 3 Ga (= differentiation/source age) to present-day MORB ($^{87}Sr/^{86}Sr$ = 0.7027 and $^{143}Nd/^{144}Nd$ = 0.5132; present-day BE: $^{87}Sr/^{86}Sr$ = 0.705 and $^{143}Nd/^{144}Nd$ = 0.512638) (Stracke et al., 2003). Furthermore, it is assumed that the initial Sr isotopic composition at a given recycling age was affected by seawater alteration (proportion of 25 % seawater Sr in altered MORB), using ratios for ancient seawater from Shields and Veizer (2002). Thirdly, by using average concentrations of parent and daughter elements (Rb, Sr, Sm, Nd, Pb, Th, U), the parent-daughter ratios (P/D) for each isotopic system were calculated, applying the algorithms outlined in Faure and Mensing (2005). Finally, the calculated initial isotope ratios and P/D ratios for the MORB crust were used to determine today's composition of the different Site 1256 crustal units (lavas without glasses, transition zone, sheeted dike complex and gabbros) at recycling increments of 0.5 Ga (Figs. 11, A.3, and A.4). Additionally, the evolution of a composite crust was modeled, consisting of 25 % altered MORB (average trace element contents for all igneous sections above the gabbros) plus 75 % plutonic section, respectively, according to the penetrated thicknesses of the extrusive segment (Teagle et al., 2006) and anticipated depth of the crust-mantle boundary at this location (~5500 mbsf) (Ildefonse et al., 2010). All input parameters for the crustal compositions used are shown in

supplementary Table A.4. The reader is referred to Stracke et al. (2003) for details of the calculations.

References cited in Appendix I

Alt, J.C., Laverne, C., Coggon, R.M., Teagle, D.A.H., Banerjee, N., Morgan, S., Smith-Duque, C.E., Harris, M., Galli, L., 2010. Subsurface structure of a submarine hydrothermal system in ocean crust formed at the East Pacific Rise, ODP/IODP Site 1256. Geochemistry, Geophysics, Geosystems 11 (10). 10.1029/2010GC003144.

Castillo, P., Klein, E., Bender, J., Langmuir, C., Shirey, S., Batiza, R., White, W.M., 2000. Petrology and Sr, Nd, and Pb isotope geochemistry of mid-ocean ridge basalt glasses from the 11°45′N to 15°00′N segment of the East Pacific Rise. Geochemistry, Geophysics, Geosystems 1 (11). 10.1029/1999GC000024.

Faure, G., Mensing, T.M., 2005. Isotopes: principles and applications. John Wiley & Sons, Inc., Hoboken, New Jersey.

Geldmacher, J., Höfig, T.W., Hauff, F., Hoernle, K., Garbe-Schönberg, D., Wilson, D.S., 2013. Influence of the Galápagos hotspot on the East Pacific Rise during Miocene superfast spreading. Geology 41 (2), 183–186. 10.1130/G33533.1.

Goss, A., Perfit, M., Ridley, W., Rubin, K., Kamenov, G., Soule, S.A., Fundis, A., Fornari, D., 2010. Geochemistry of lavas from the 2005-2006 eruption at the East Pacific Rise, 9°46′N-9°56′N: Implications for ridge crest plumbing and decadal changes in magma chamber compositions. Geochemistry, Geophysics, Geosystems 11 (5). 10.1029/2009GC002977.

Hanyu, T., Tatsumi, Y., Senda, R., Miyazaki, T., Chang, Q., Hirahara, Y., Takahashi, T., Kawabata, H., Suzuki, K., Kimura, J.-I., Nakai, S., 2011. Geochemical characteristics and origin of the HIMU reservoir: A possible mantle plume source in the lower mantle. Geochem. Geophys. Geosyst. 12 (2). 10.1029/2010GC003252.

Hart, S.R., 1984. A large-scale isotope anomaly in the Southern Hemisphere mantle. Nature 309 (5971), 753–757. 10.1038/309753a0.

Hauri, E.H., Hart, S.R., 1993. ReOs isotope systematics of HIMU and EMII oceanic island basalts from the south Pacific Ocean. Earth and Planetary Science Letters 114 (2-3), 353–371. 10.1016/0012-821X(93)90036-9.

Ildefonse, B., Abe, N., Blackman, D.K., Canales, J., Isozaki, Y., Kodaira, S., Myers, G., Nakamura, K., Nedimovic, M., Skinner, A.C., Seama, N., Takazawa, E., Teagle, D.A.H., Tominaga, M., Umino, S., Wilson, D.S., Yamao, M., 2010. The MoHole: A Crustal Journey and Mantle Quest, Workshop in Kanazawa, Japan, 3—5 June 2010. Scientific drilling (10), 56–63. 10.2204/iodp.sd.10.07.2010.

Koepke, J., Christie, D., Dziony, W., Holtz, F., Lattard, D., Maclennan, J., Park, S., Scheibner, B., Yamasaki, T., Yamazaki, S., 2008. Petrography of the dike-gabbro transition at IODP Site 1256 (equatorial Pacific): The evolution of the granoblastic dikes. Geochemistry, Geophysics, Geosystems 9 (7). 10.1029/2008GC001939.

Kogiso, T., Tatsumi, Y., Nakano, S., 1997. Trace element transport during dehydration processes in the subducted oceanic crust: 1. Experiments and implications for the origin of ocean island basalts. Earth and Planetary Science Letters 148 (1-2), 193–205. 10.1016/S0012-821X(97)00018-6.

Pedersen, R.B., Furnes, H., 2001. Nd- and Pb-isotopic variations through the upper oceanic crust in DSDP/ODP Hole 504B, Costa Rica Rift. Earth and Planetary Science Letters 189 (3-4), 221–235. 10.1016/S0012-821X(01)00349-1.

Saal, A., Kurz, M., Hart, S.R., Blusztajn, J.S., Blichert-Toft, J., Liang, Y., Geist, D., 2007. The role of lithospheric gabbros on the composition of Galapagos lavas. Earth and Planetary Science Letters 257 (3-4), 391–406. 10.1016/j.epsl.2007.02.040.

Shields, G., Veizer, J., 2002. Precambrian marine carbonate isotope database: Version 1.1. Geochemistry, Geophysics, Geosystems 3 (6), 1 of 12. 10.1029/2001GC000266.

Sims, K.W., Blichert-Toft, J., Fornari, D., Perfit, M., Goldstein, S., Johnson, P., DePaolo, D., Hart, S.R., Murrell, M., Michael, P.J., Layne, G., Ball, L., 2003. Aberrant youth: Chemical and isotopic constraints on the origin of off-axis lavas from the East Pacific Rise, 9°-10°N. Geochemistry, Geophysics, Geosystems 4 (10). 10.1029/2002GC000443.

Sims, K.W., Goldstein, S., Blichert-Toft, J., Perfit, M., Kelemen, P., Fornari, D., Michael, P.J., Murrell, M., Hart, S.R., DePaolo, D., Layne, G., Ball, L., Jull, M., Bender, J., 2002. Chemical and isotopic constraints on the generation and transport of magma beneath the East Pacific Rise. Geochimica et Cosmochimica Acta 66 (19), 3481–3504. 10.1016/S0016-7037(02)00909-2.

Stracke, A., Bizimis, M., Salters, V., 2003. Recycling oceanic crust: Quantitative constraints. Geochemistry, Geophysics, Geosystems 4 (3). 10.1029/2001GC000223.

Tatsumoto, M., Knight, R.J., Allegre, C.J., 1973. Time differences in the formation of meteorites as determined from the ratio of lead-207 to lead-206. Science 180 (4092), 1279–1283. 10.1126/science.180.4092.1279.

Teagle, D.A.H., Alt, J.C., Umino, S., Miyashita, S., Banerjee, N., Wilson, D.S., et al., 2006. Expedition 309/312 summary, in: Teagle, D.A.H., Alt, J.C., Umino, S., Miyashita, S., Banerjee, N., Wilson, D.S. (Eds.), Proceedings of the IODP, Volume 309/312. Integrated Ocean Drilling Program, Washington, DC, pp. 1–127.

Teagle, D.A.H., Ildefonse, B., Blum, P., 2012. IODP Expedition 335: Deep Sampling in ODP Hole 1256D. Scientific drilling 13, 28–34.

Waters, C., Sims, K.W., Perfit, M., Blichert-Toft, J., Blusztajn, J.S., 2011. Perspective on the Genesis of E-MORB from Chemical and Isotopic Heterogeneity at 9-10 N East Pacific Rise. Journal of Petrology 52 (3), 565–602. 10.1093/petrology/egq091.

Werner, R., Hoernle, K., Barckhausen, U., Hauff, F., 2003. Geodynamic evolution of the Galápagos hot spot system (Central East Pacific) over the past 20 m.y.: Constraints from morphology, geochemistry, and magnetic anomalies. Geochemistry, Geophysics, Geosystems 4 (12). 10.1029/2003GC000576.

White, W.M., McBirney, A.R., Duncan, R.A., 1993. Petrology and geochemistry of the Galápagos Islands: Portrait of a pathological mantle plume. Journal of Geophysical Research 98 (B11), 19533. 10.1029/93JB02018.

Figure captions for Appendix I

Figure A.1. Multielement plots showing three lava glass samples of different depths within the volcanic zone and their corresponding whole rock composition from the same lava flow (A, B, C). A general alteration-related whole rock enrichment of U and Pb and depletion of low field strength elements compared to the associated glass is obvious.

Figure A.2. $^{206}Pb/^{204}Pb$ versus $^{207}Pb/^{204}Pb$ (a), and $^{208}Pb/^{204}Pb$ (b), respectively, showing measured Site 1256 basement values from the present study and from Geldmacher et al. (2013). Note that initial data are not shown, since age correcting would only slightly shift some data points to less radiogenic values, similar to the shift of the Galápagos Islands field projected back in time to 15.2 Ma. The orange-rimmed red circle represents a highly sulfide-mineralized breccia of the Site 1256 TZ sampled at ~1028 mbsf. Errors are within symbol size for $^{206}Pb/^{204}Pb$ and $^{208}Pb/^{204}Pb$, whereas the $^{207}Pb/^{204}Pb$ error bar marks the 2σ external reproducibility. The dashed field contours the extent of the Site 504 data. There are few samples from this site plotting far outside the displayed range of Pb isotope ratios, however, they are not representative of the major compositional type at Site 504 (cf. Fig. 7). Data sources: Site 504 igneous rock values (Pedersen and Furnes, 2001), East Pacific Rise (EPR) mid-ocean-ridge basalt (MORB) (9–15°N) (Castillo et al., 2000; Goss et al., 2010; Sims et al., 2002, 2003; Waters et al., 2011), Galápagos Islands (Saal et al., 2007; Werner et al., 2003; White et al., 1993). Northern Hemisphere Reference Line (NHRL) after Hart (1984).

Figure A.3. Modeled present-day $^{206}Pb/^{204}Pb$ versus $^{87}Sr/^{86}Sr$ (a) and $^{143}Nd/^{144}Nd$ (b), respectively, of recycled igneous oceanic crust of Site 1256 basaltic rock composition as a function of the recycling age (0.5–3 Ga; with 0.5 Ga increments) and the age-dependent calculated initial isotopic composition of mid-ocean-ridge basalt (MORB). For example, the 3 Ga points show the modeled present-day isotopic compositions for a crustal segment that was modified (altered) 3 billion years ago. Modeling was implemented irrespective of any possible isotopic modification of the recycled oceanic crust during. Note that modeling included impact of seawater alteration on the initial $^{87}Sr/^{86}Sr$ of displayed crustal components assuming 25 % seawater Sr in altered MORB and applying ancient seawater $^{87}Sr/^{86}Sr$ ratios (0.5–3 Ga) from Shields and Veizer (2002) (resulting in non-linear evolution lines for the Sr isotopic modeling). Modeled crustal sections depicted: lavas (volcanic zone; whole rocks), dike-lava transition zone (TZ), sheeted dike complex (SDC), gabbros (plutonic section) and a composite crust. For further details and data sources, see Fig. 11 caption.

Figure A.4. Modeled present-day $^{206}Pb/^{204}Pb$ versus $^{87}Sr/^{86}Sr$ (a) and $^{143}Nd/^{144}Nd$ (b), respectively, of recycled igneous oceanic crust of Site 1256 basaltic rock composition as a function of the recycling age (0.5–3 Ga; with 0.5 Ga increments) and the age-dependent calculated initial isotopic composition of mid-ocean-ridge basalt (MORB). For example, the 3 Ga points show the modeled present-day isotopic compositions for a crustal segment that was modified (altered) 3 billion years ago. Modeling was implemented taking into account compositional modification during subduction processes ("subd") by applying element mobility coefficients from Kogiso et al. (1997) and Stracke et al. (2003). Note that modeling included impact of seawater alteration on the initial $^{87}Sr/^{86}Sr$ of displayed crustal components assuming 25 % seawater Sr in altered MORB and applying ancient seawater $^{87}Sr/^{86}Sr$ ratios (0.5–3 Ga) from Shields and Veizer (2002) (resulting in non-linear evolution lines for the Sr isotopic modeling). Modeled crustal sections depicted: lavas (volcanic zone; whole rocks), dike-lava transition zone (TZ), sheeted dike complex (SDC), gabbros (plutonic section) and a composite crust. For further details and data sources, see Fig. 11 caption.

Supplementary Figure A.1 (Appendix I)

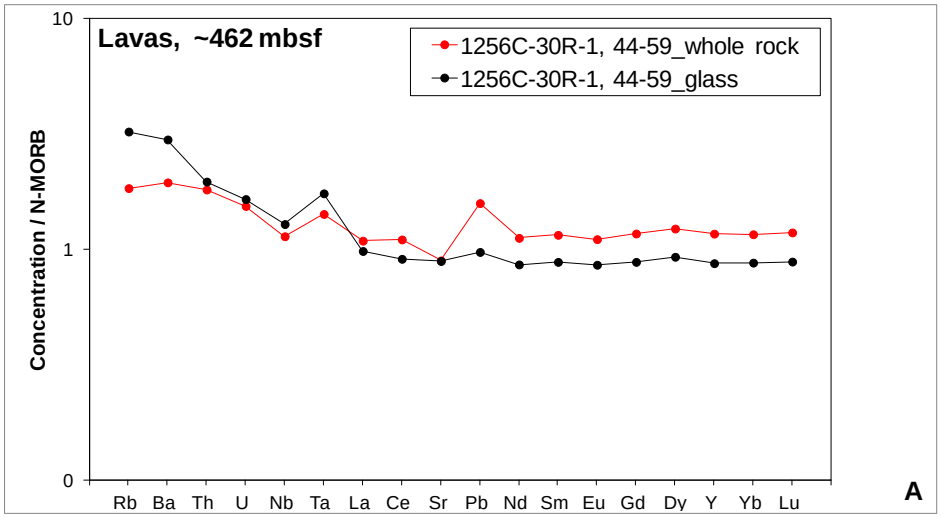

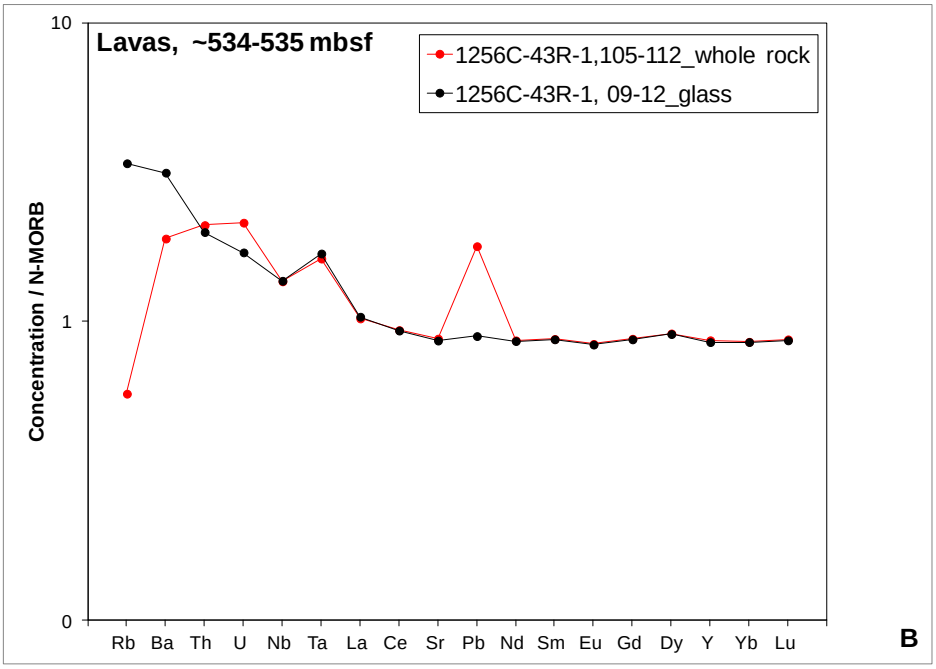

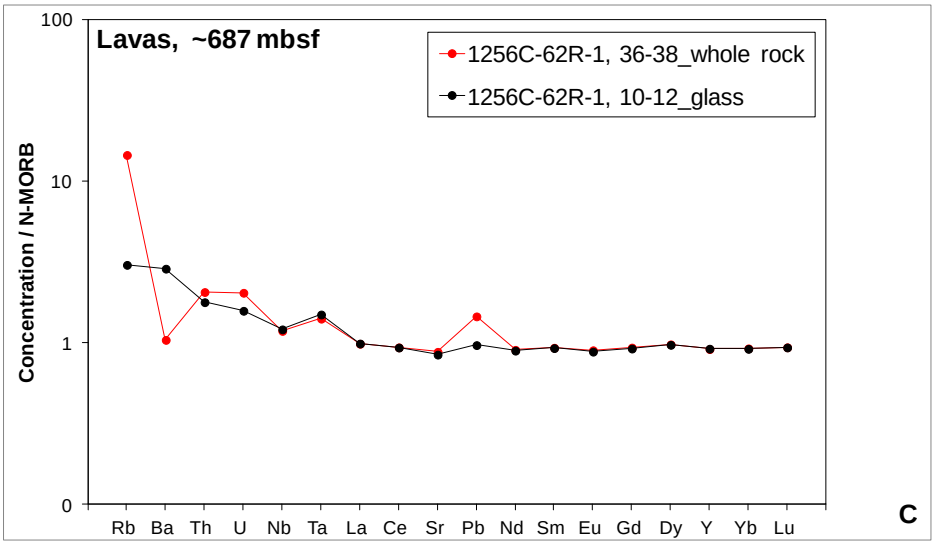

Supplementary Figure A.2 (Appendix I)

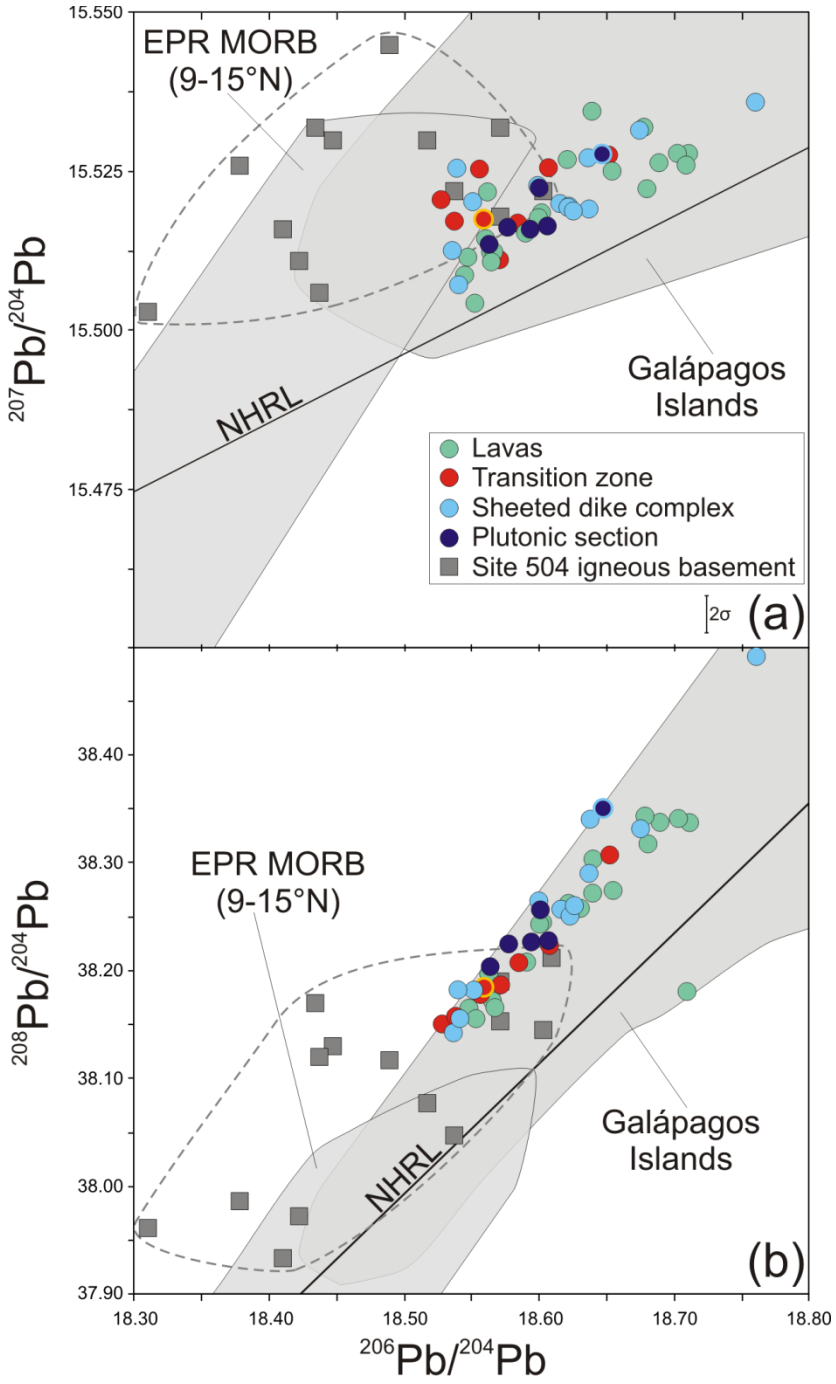

Supplementary Figure A.3 (Appendix I)

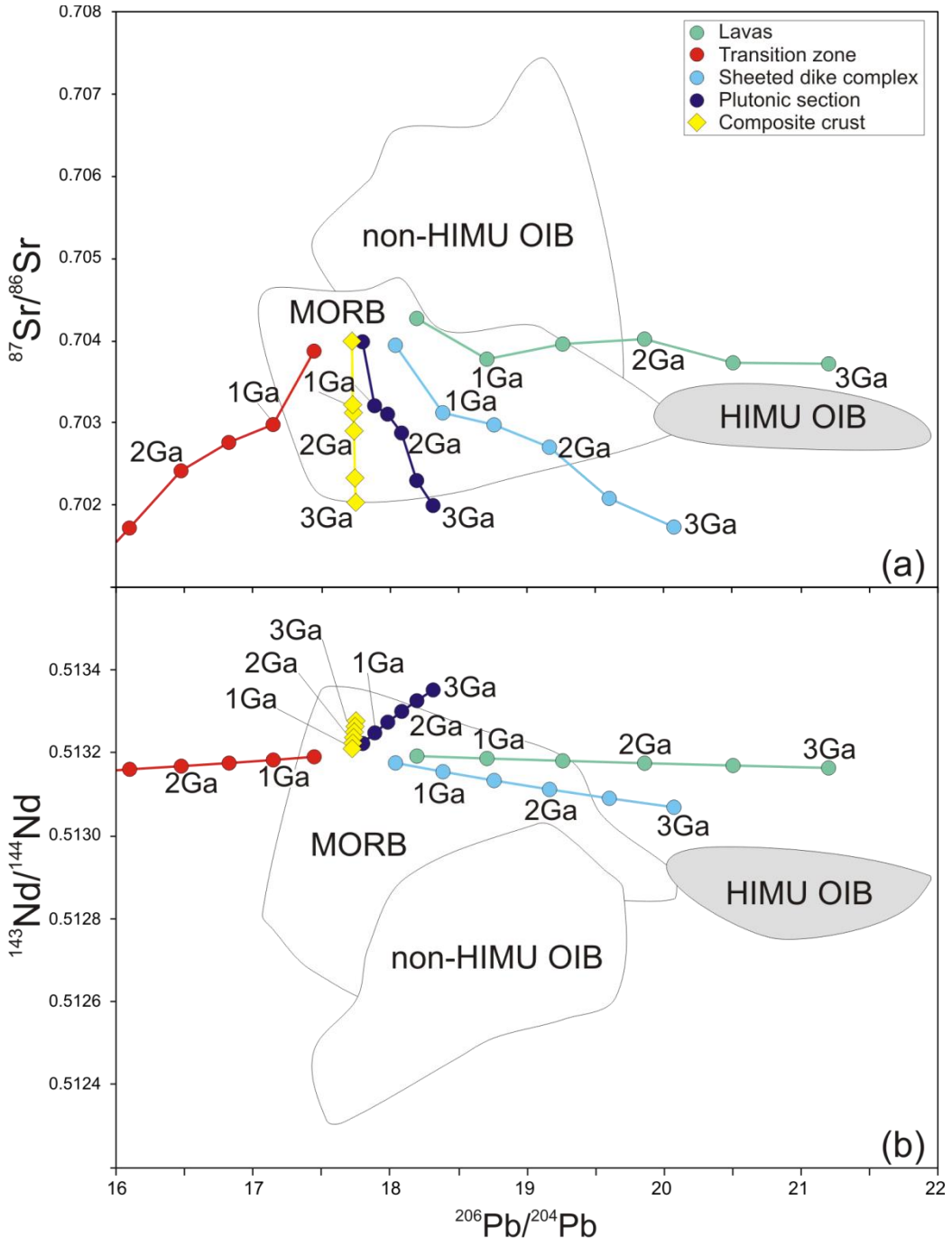

Supplementary Figure A.4 (Appendix I)

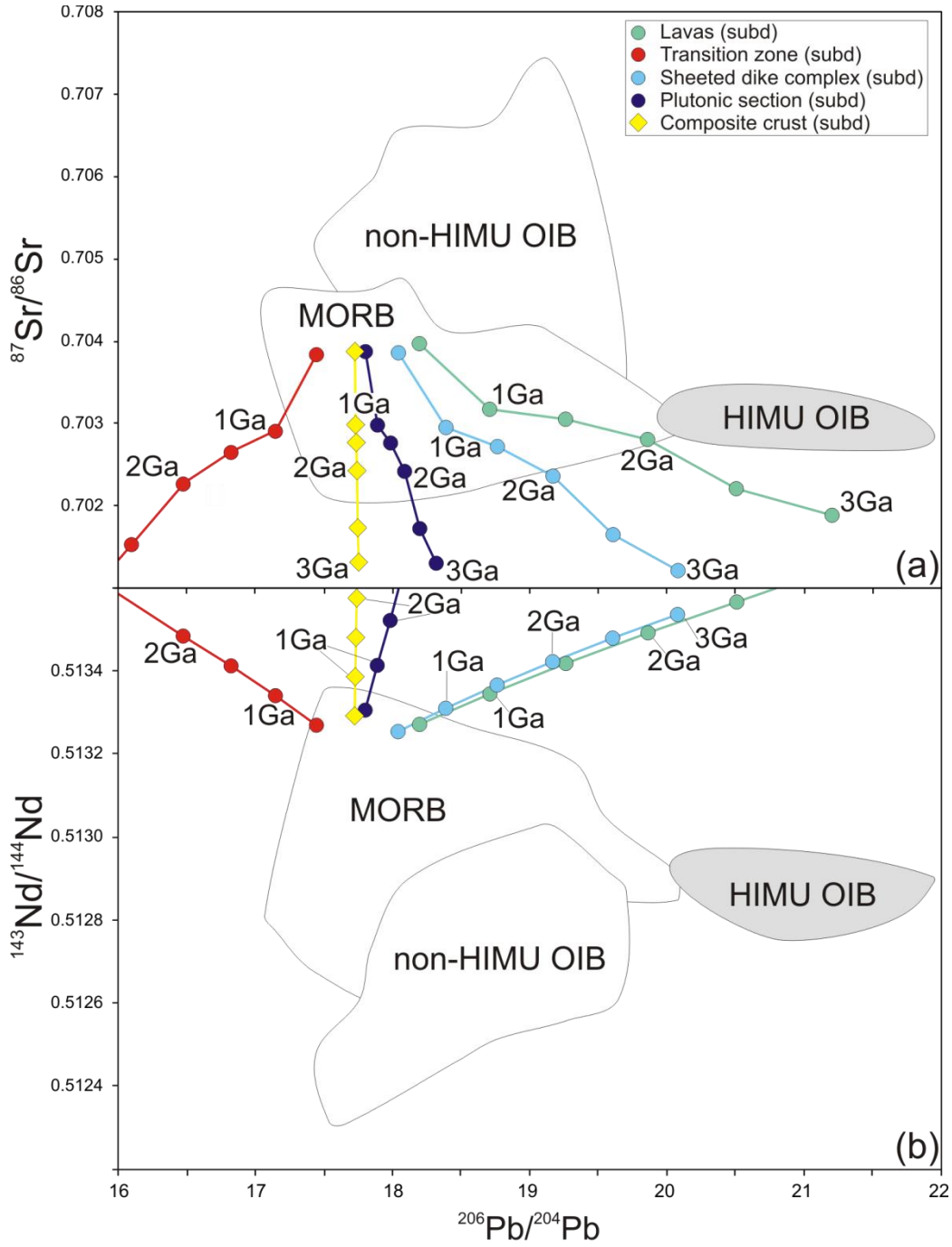

Supplementary Table A.1 (Appendix I)

Suppl. Table A.1	Reproducibility and accuracy of ICP-MS trace element data for BHVO-2								Reproducibility and accuracy of ICP-MS trace element data for AGV-2							
# Analysis/ Element	#1	#2	#3	#4	#5	Mean	Std. dev. (±1σ)	Relative std. dev. (±1σ %)	Reference value*	# Analysis/ Element	#1	#2	#3	#4	Mean	Std. dev. (±1σ)	Relative std. dev. (±1σ %)	Reference value*
Li (ppm)	4.56	4.62	4.58	4.76	4.70	4.65	0.07	1.60	4.60	Li (ppm)	10.2	10.1	10.8	10.8	10.5	0.32	3.09	11.0
Sc (ppm)	32.0	32.0	31.8	30.1	29.7	31.1	1.02	3.26	31.8	Sc (ppm)	13.4	12.7	12.2	12.1	12.6	0.53	4.18	13.0
V (ppm)	322	322	317	325	313	320	4.21	1.32	317	V (ppm)	119	119	121	121	120	1.24	1.04	120
Cr (ppm)	198	268	290	289	286	266	34.9	13.1	289	Cr (ppm)	13.3	13.5	17.2	17.8	15.5	2.06	13.4	17.0
Co (ppm)	44.9	45.3	45.0	44.7	43.9	44.8	0.49	1.10	45.0	Co (ppm)	14.4	14.1	14.4	14.4	14.3	0.12	0.82	16.0
Ni (ppm)	121	121	119	120	118	120	1.23	1.03	119	Ni (ppm)	16.7	16.3	17.1	17.1	16.8	0.34	2.01	19.0
Cu (ppm)	131	130	128	128	126	129	1.87	1.45	127	Cu (ppm)	50.8	49.5	50.1	50.2	50.1	0.44	0.88	53.0
Zn (ppm)	106	103	103	102	99	103	2.31	2.24	103	Zn (ppm)	87.2	86.8	86.0	87.9	87.0	0.69	0.80	86.0
Ga (ppm)	20.4	21.6	21.6	20.4	20.0	20.8	0.68	3.27	21.7	Ga (ppm)	20.8	20.7	19.7	19.8	20.3	0.49	2.42	20.0
Rb (ppm)	9.27	9.25	9.16	9.32	9.12	9.22	0.07	0.79	9.20	Rb (ppm)	65.9	66.0	69.0	68.7	67.4	1.46	2.17	68.6
Sr (ppm)	391	397	393	383	377	388	6.93	1.78	395	Sr (ppm)	651	648	643	646	647	2.91	0.45	658
Y (ppm)	25.7	25.0	25.0	25.6	25.3	25.3	0.32	1.25	25.5	Y (ppm)	18.9	18.7	19.5	19.3	19.1	0.32	1.70	20.0
Zr (ppm)	173	170	169	168	167	169	2.25	1.33	174	Zr (ppm)	230	229	232	229	230	1.23	0.53	230
Nb (ppm)	18.2	18.0	18.0	17.9	17.7	17.9	0.16	0.91	18.0	Nb (ppm)	13.8	13.6	13.7	13.7	13.7	0.09	0.62	15.0
Sn (ppm)	1.60	1.73	1.75	1.73	1.74	1.71	0.06	3.25	1.80	Sn (ppm)	1.86	1.90	1.94	1.85	1.89	0.03	1.83	2.30
Sb (ppm)	0.11	0.12	0.13	0.13	0.12	0.12	0.01	6.83	0.13	Sb (ppm)	0.53	0.59	0.51	0.43	0.51	0.06	10.7	0.60
Cs (ppm)	0.10	0.10	0.10	0.11	0.10	0.10	0.00	3.33	0.11	Cs (ppm)	1.16	1.15	1.20	1.19	1.18	0.02	1.59	1.16
Ba (ppm)	130	131	131	129	129	130	0.95	0.73	130	Ba (ppm)	1116	1110	1134	1128	1122	9.57	0.85	1140
La (ppm)	15.4	15.6	15.5	15.3	15.1	15.4	0.19	1.25	15.2	La (ppm)	39.3	39.0	38.5	38.5	38.8	0.36	0.93	38.0
Ce (ppm)	38.2	38.7	38.5	37.7	37.3	38.1	0.52	1.37	38.0	Ce (ppm)	68.0	67.6	67.4	67.3	67.6	0.27	0.39	68.0
Pr (ppm)	5.55	5.40	5.34	5.33	5.28	5.38	0.09	1.69	5.30	Pr (ppm)	8.17	8.08	8.27	8.22	8.18	0.07	0.83	8.30
Nd (ppm)	25.4	24.8	24.6	24.6	24.4	24.8	0.36	1.43	25.0	Nd (ppm)	30.7	30.3	31.2	30.9	30.8	0.32	1.03	30.0
Sm (ppm)	6.35	6.16	6.14	6.17	6.09	6.18	0.09	1.43	6.20	Sm (ppm)	5.52	5.51	5.62	5.62	5.57	0.05	0.93	5.70
Eu (ppm)	2.13	2.09	2.07	2.07	2.03	2.08	0.03	1.46	2.06	Eu (ppm)	1.51	1.50	1.52	1.51	1.51	0.01	0.43	1.54
Gd (ppm)	6.33	6.24	6.20	6.19	6.16	6.23	0.06	0.97	6.30	Gd (ppm)	4.72	4.65	4.72	4.76	4.71	0.04	0.83	4.69
Tb (ppm)	0.97	0.95	0.94	0.94	0.93	0.95	0.01	1.53	0.93	Tb (ppm)	0.65	0.64	0.65	0.65	0.65	0.01	0.79	0.64
Dy (ppm)	5.46	5.37	5.39	5.38	5.31	5.38	0.05	0.87	5.25	Dy (ppm)	3.53	3.49	3.59	3.57	3.55	0.04	1.09	3.60
Ho (ppm)	1.01	0.99	0.99	0.98	0.98	0.99	0.01	1.17	0.99	Ho (ppm)	0.66	0.66	0.68	0.68	0.67	0.01	1.13	0.71
Er (ppm)	2.48	2.45	2.45	2.44	2.42	2.45	0.02	0.78	2.50	Er (ppm)	1.77	1.74	1.80	1.79	1.77	0.02	1.22	1.79
Tm (ppm)	0.33	0.33	0.33	0.33	0.33	0.33	0.00	0.78	0.34	Tm (ppm)	0.25	0.25	0.26	0.26	0.25	0.00	1.62	0.26
Yb (ppm)	2.03	2.00	1.99	2.00	1.99	2.01	0.01	0.74	2.00	Yb (ppm)	1.64	1.62	1.67	1.66	1.65	0.02	1.20	1.60
Lu (ppm)	0.28	0.28	0.28	0.28	0.28	0.28	0.00	0.59	0.28	Lu (ppm)	0.25	0.25	0.25	0.25	0.25	0.00	1.04	0.25
Hf (ppm)	4.31	4.47	4.42	4.16	4.11	4.29	0.14	3.27	4.07	Hf (ppm)	5.14	5.06	4.90	4.90	5.00	0.10	2.03	5.08
Ta (ppb)	0.78	1.10	1.12	1.13	1.11	1.05	0.14	12.9	1.13	Ta (ppb)	0.80	0.79	0.83	0.83	0.81	0.02	2.06	0.89
Pb (ppm)	1.76	1.70	1.74	1.88	1.42	1.70	0.15	9.06	1.70	Pb (ppm)	12.8	12.9	13.1	13.0	13.0	0.10	0.74	13.0
Th (ppm)	1.21	1.21	1.21	1.21	1.20	1.21	0.00	0.36	1.21	Th (ppm)	6.05	5.98	6.17	6.15	6.09	0.08	1.29	6.10
U (ppm)	0.41	0.42	0.42	0.43	0.42	0.42	0.01	1.82	0.41	U (ppm)	1.87	1.84	1.90	1.92	1.88	0.03	1.57	1.88

*GeoReM preferred values from Jochum and Nehring (11/2006) [BHVO-2] & Jochum and Nehring (03/2007) [AGV-2]

Supplementary Table A.2 (Appendix I)

Suppl. Table A2	**Reproducibility of ICP-MS trace element data evaluated from sample duplicates (dup)***								
# Analysis/ Element	510-10R Dup1	510-10R Dup2	*Relative difference (%)*	K8-11 Dup1	K8-11 Dup2	*Relative difference (%)*	K8-36 Dup1	K8-36 Dup2	*Relative difference (%)*
Li (ppm)	4.50	4.62	*-2.52*	43.4	43.8	*-1.10*	11.2	11.2	*0.50*
Sc (ppm)	45.6	46.1	*-1.12*	8.63	8.52	*1.27*	19.1	19.2	*-0.28*
V (ppm)	286	291	*-1.75*	57.6	56.6	*1.73*	249	252	*-1.04*
Cr (ppm)	412	417	*-1.29*	1.73	1.70	*1.72*	148	149	*-0.61*
Co (ppm)	45.5	45.9	*-0.78*	0.36	0.31	*11.7*	28.4	28.7	*-0.77*
Ni (ppm)	90.8	92.2	*-1.46*	0.99	0.97	*2.76*	96.9	97.8	*-0.94*
Cu (ppm)	93.8	95.1	*-1.43*	325	307	*5.74*	119	117	*1.53*
Zn (ppm)	67.8	71.7	*-5.68*	19.4	18.9	*2.44*	79.1	78.2	*1.08*
Ga (ppm)	14.1	14.2	*-0.66*	8.90	8.79	*1.26*	20.2	20.4	*-1.05*
Rb (ppm)	0.25	0.26	*-2.53*	0.77	0.76	*1.80*	8.54	8.61	*-0.86*
Sr (ppm)	48.4	49.2	*-1.62*	140	138	*1.41*	1551	1553	*-0.13*
Y (ppm)	20.4	20.6	*-0.88*	33.2	32.9	*1.02*	11.26	11.35	*-0.75*
Zr (ppm)	30.3	30.3	*-0.16*	120	119	*1.38*	127	126	*0.47*
Nb (ppm)	0.34	0.33	*1.71*	1.93	1.91	*1.28*	9.00	9.05	*-0.60*
Sn (ppm)	0.39	0.39	*0.27*	0.80	0.79	*1.31*	0.82	0.81	*0.91*
Sb (ppm)	0.02	0.02	*-17.9*	0.14	0.14	*1.86*	0.06	0.06	*0.91*
Cs (ppm)	0.01	0.01	*-10.3*	0.02	0.02	*-1.91*	0.09	0.09	*1.28*
Ba (ppm)	< 1	< 1	*n/a*	82.0	82.3	*-0.39*	422	422	*-0.13*
La (ppm)	0.44	0.41	*5.28*	8.41	8.33	*0.96*	22.1	22.4	*-0.94*
Ce (ppm)	2.85	2.87	*-0.45*	20.6	20.4	*1.24*	50.7	51.0	*-0.69*
Pr (ppm)	0.62	0.62	*-0.30*	3.18	3.13	*1.48*	7.08	7.11	*-0.41*
Nd (ppm)	3.83	3.87	*-0.86*	14.6	14.5	*1.01*	29.8	30.0	*-0.73*
Sm (ppm)	1.64	1.64	*0.12*	3.81	3.75	*1.57*	5.53	5.56	*-0.60*
Eu (ppm)	0.66	0.66	*0.11*	1.05	1.03	*1.67*	1.64	1.64	*-0.41*
Gd (ppm)	2.50	2.53	*-0.94*	4.15	4.12	*0.77*	4.24	4.29	*-1.13*
Tb (ppm)	0.49	0.49	*-0.46*	0.73	0.72	*1.16*	0.53	0.53	*-0.41*
Dy (ppm)	3.48	3.50	*-0.62*	5.09	5.03	*1.07*	2.54	2.54	*-0.10*
Ho (ppm)	0.77	0.77	*-0.91*	1.16	1.15	*0.60*	0.42	0.43	*-1.52*
Er (ppm)	2.20	2.22	*-0.87*	3.42	3.37	*1.26*	1.02	1.02	*0.29*
Tm (ppm)	0.34	0.34	*-0.68*	0.51	0.51	*0.95*	0.13	0.13	*0.00*
Yb (ppm)	2.24	2.26	*-0.82*	3.30	3.24	*1.68*	0.81	0.80	*1.24*
Lu (ppm)	0.34	0.34	*-0.76*	0.49	0.49	*-0.16*	0.12	0.11	*0.56*
Hf (ppm)	1.06	1.07	*-0.64*	3.40	3.36	*1.23*	2.83	2.82	*0.06*
Ta (ppb)	0.03	0.03	*3.62*	0.14	0.14	*-0.09*	0.48	0.47	*1.00*
Pb (ppm)	0.28	0.28	*-0.15*	1.74	1.72	*0.78*	4.49	4.33	*3.41*
Th (ppm)	0.10	0.10	*-0.38*	1.06	1.05	*0.77*	1.46	1.45	*0.38*
U (ppm)	0.13	0.13	*0.25*	0.45	0.45	*0.35*	0.61	0.60	*1.16*

*Note that given replicate samples are not part of the studied sample set but account for different sample series. However, these samples, being of comparable textural basaltic composition, were digested and analyzed along with the samples of the present study.

Supplementary Table A.3 (Appendix I)

Suppl. Table A3	**Machine reproducibility of ICP-MS trace element data evaluated from same sample dissolution**									
# Analysis/ Element	309-1256D-128R-1, 80-91 (1)	309-1256D-128R-1, 80-91 (2)	309-1256D-128R-1, 80-91 (3)	309-1256D-128R-1, 80-91 (4)	309-1256D-128R-1, 80-91 (5)	*Relative std. dev. (±1σ %)*	206-1256D-30R-1, 44-59 (1)	206-1256D-30R-1, 44-59 (2)	206-1256D-30R-1, 44-59 (3)	*Relative std. dev. (±1σ %)*
Li (ppm)	3.20	3.23	3.05	3.12	3.16	*2.00*	5.72	5.70	5.75	*0.34*
Sc (ppm)	47.6	48.5	44.4	48.2	49.0	*3.43*	42.5	42.8	42.6	*0.25*
V (ppm)	377	380	349	382	382	*3.32*	303	310	309	*0.94*
Cr (ppm)	171	175	159	173	174	*3.57*	256	260	258	*0.55*
Co (ppm)	48.9	48.7	45.1	48.6	48.8	*3.02*	46.6	47.2	47.2	*0.58*
Ni (ppm)	73.5	73.1	67.2	71.0	71.5	*3.17*	83.0	83.8	84	*0.39*
Cu (ppm)	77.0	77.6	71.5	77.6	77.0	*3.06*	99.1	101	100	*0.65*
Zn (ppm)	95.8	96.7	91.2	93.7	94.3	*2.01*	78.5	79.0	79	*0.25*
Ga (ppm)	9.71	9.68	9.30	9.56	9.71	*1.61*	14.3	14.4	14.4	*0.31*
Rb (ppm)	0.24	0.25	0.24	0.25	0.25	*2.02*	1.81	1.76	1.74	*1.73*
Sr (ppm)	99.8	100	99.4	101	102	*0.97*	79.9	81.5	83	*1.31*
Y (ppm)	31.6	32.5	31.6	32.9	33.2	*2.02*	24.3	24.5	24.6	*0.43*
Zr (ppm)	76.2	77.9	75.2	77.8	78.3	*1.52*	54.2	54.1	54	*0.27*
Nb (ppm)	2.43	2.46	2.38	2.59	2.55	*3.11*	2.99	2.93	2.94	*0.98*
Sn (ppm)	0.29	0.30	0.30	0.30	0.29	*1.31*	0.62	0.62	0.62	*0.30*
Sb (ppm)	0.01	0.01	0.01	0.01	0.01	*5.81*	0.03	0.02	0.03	*6.08*
Cs (ppm)	0.00	0.00	0.00	0.00	0.00	*5.13*	0.03	0.03	0.03	*5.00*
Ba (ppm)	13.0	13.2	12.9	13.1	13.0	*0.65*	18.8	18.8	19.2	*1.02*
La (ppm)	2.60	2.60	2.58	2.61	2.61	*0.33*	2.45	2.46	2.47	*0.34*
Ce (ppm)	7.71	7.76	7.68	7.70	7.73	*0.37*	6.81	6.80	6.87	*0.45*
Pr (ppm)	1.38	1.39	1.39	1.39	1.38	*0.19*	1.14	1.15	1.15	*0.33*
Nd (ppm)	7.82	7.84	7.81	7.79	7.82	*0.21*	6.26	6.21	6.27	*0.42*
Sm (ppm)	2.98	2.99	2.99	2.98	2.98	*0.17*	2.31	2.30	2.31	*0.21*
Eu (ppm)	1.01	1.02	1.01	1.01	1.01	*0.40*	0.87	0.87	0.88	*0.27*
Gd (ppm)	4.18	4.18	4.13	4.15	4.14	*0.52*	3.24	3.25	3.25	*0.13*
Tb (ppm)	0.81	0.81	0.80	0.80	0.80	*0.41*	0.61	0.61	0.61	*0.10*
Dy (ppm)	5.60	5.62	5.55	5.57	5.55	*0.51*	4.21	4.21	4.21	*0.09*
Ho (ppm)	1.23	1.22	1.22	1.22	1.22	*0.39*	0.92	0.91	0.91	*0.57*
Er (ppm)	3.50	3.47	3.46	3.45	3.45	*0.53*	2.61	2.59	2.59	*0.33*
Tm (ppm)	0.53	0.53	0.53	0.53	0.53	*0.46*	0.40	0.39	0.40	*0.24*
Yb (ppm)	3.54	3.55	3.53	3.52	3.52	*0.34*	2.66	2.65	2.65	*0.18*
Lu (ppm)	0.54	0.54	0.54	0.54	0.54	*0.27*	0.40	0.40	0.40	*0.19*
Hf (ppm)	2.19	2.17	2.17	2.17	2.16	*0.35*	1.54	1.52	1.52	*0.61*
Ta (ppb)	0.16	0.15	0.15	0.17	0.16	*3.06*	0.23	0.20	0.20	*7.81*
Pb (ppm)	0.66	0.65	0.66	0.66	0.65	*0.57*	0.29	0.29	0.29	*0.33*
Th (ppm)	0.15	0.14	0.14	0.14	0.14	*1.34*	0.24	0.21	0.22	*4.36*
U (ppm)	0.05	0.05	0.05	0.05	0.05	*0.95*	0.08	0.07	0.07	*2.03*

Supplementary Table A.4 (Appendix I)

Table A.4. Site 1256 crustal input parameters (average trace element concentrations and calculated parent-daughter ratios [following the algorithms of Faure and Mensing (2005)] of relevant isotope systems) for modeling of present-day isotopic compositions as a function of the recycling age (0.5–3 Ga) without and with modification by subduction processing ("subd") according to the mobility coefficients (*) taken from Stracke et al. (2003), based on Kogiso et al. (1997). TZ = Transition zone, SDC = Sheeted dike complex, Comp. crust = composite crust (mixing of 25 % altered mid-ocean-ridge basalt [average composition of lavas + transition zone + sheeted dike complex] + 75 % gabbros [average composition]).

	Rb* (ppm)	Sr* (ppm)	Nd* (ppm)	Sm* (ppm)	Pb* (ppm)	Th* (ppm)	U* (ppm)	$^{238}U/^{204}Pb$	$^{232}Th/^{204}Pb$	$^{232}Th/^{238}U$	$^{87}Rb/^{86}Sr$	$^{147}Sm/^{144}Nd$
Lavas	1.83	83.2	7.31	2.70	0.45	0.24	0.10	14.1	34.4	2.45	0.06	0.22
Lavas (subd)	0.37	49.2	5.70	2.33	0.11	0.14	0.03	14.1	82.7	5.87	0.02	0.25
TZ	0.20	72.0	7.82	2.88	2.49	0.19	0.19	4.77	5.03	1.05	0.01	0.22
TZ (subd)	0.04	42.6	6.10	2.49	0.62	0.12	0.05	4.77	12.1	2.53	0.003	0.25
SDC	0.54	87.2	9.08	3.28	0.42	0.26	0.08	12.2	40.1	3.29	0.02	0.22
SDC (subd)	0.11	51.6	7.08	2.84	0.11	0.16	0.02	12.2	96.3	7.91	0.01	0.24
Gabbros	0.68	82.5	6.02	2.32	0.41	0.16	0.06	9.21	25.2	2.74	0.02	0.23
Gabbros (subd)	0.14	48.8	4.70	2.00	0.10	0.10	0.01	9.21	60.6	6.58	0.01	0.26
Comp. crust	0.71	82.3	6.58	2.49	0.56	0.18	0.07	8.25	20.3	2.46	0.02	0.23
Comp. Crust (subd)	0.14	48.7	5.13	2.15	0.14	0.11	0.02	8.25	48.8	5.91	0.01	0.25

*Mobility coefficients for the subduction environment, i.e., estimates of the fraction (in %) of each element extracted from the basaltic crust during subduction: Rb – 80 %, Sr – 41 %, Nd – 22 %, Sm – 14 %, Pb – 75 %, Th – 40 %, U – 75 % (taken from Stracke et al., 2003; based on Kogiso et al., 1997).

Appendix II (CHAPTER II)

Appendix Section A.1:

Details on Pb isotopic database construction applied to the present study

As numerous potential terrigenous sources from southern North America (Mexico), Central America, and South America may have accounted for the detrital Pb supplied to the eastern equatorial Pacific (EEP) study area (see Sections 1 and 5.1), construction of a variety of profound databases has been required to distinguish between the different possible continental source areas. We thus used the comprehensive GEOROC online database (http://georoc.mpch-mainz.gwdg.de/georoc/) to compile literature data for generating extensive data sets, which allowed us to shed light on the Neogene-Quaternary deposition history in the EEP.

The GEOROC database was retrieved in May and June, 2014. We compiled GEOROC-based data sets for the following potential sources: Central American Volcanic Arc; uplifted fragments of the Caribbean Large Igneous Province exposed in Central America and northern South America; Galápagos Islands and seamounts as well as associated features of the Galápagos hotspot track (Cocos Island and seamounts, Cocos Ridge); Trans-Mexican Volcanic Belt; Andean Arc, subdivided into Northern Volcanic Zone, North/Transitional/South Central Volcanic Zone, Southern Volcanic Zone, Austral Volcanic Zone. A spreadsheet (Tab. A.1) containing all data used for reconstruction is provided in the electronic version of the present thesis.

Filtering the extensive data sets yielded from GEOROC was done by principally following the procedure of Pichat et al. (2014). This facilitates comparison between different EEP studies with the same focus: deciphering distinct Pb sources to marine sediments. Our procedure thus covered the following points:

1. Incomplete data sets, lacking one or more Pb isotope ratios, were removed.
2. Any duplicate and triplicate analyses of the same paper or different publications using identical samples were not taken into account. In case, different studies used the same sample set over time, generating same kind of isotope data, the latest study was retrieved.
3. We considered whole rock data only, thus, leachate/residue data were excluded, since comparison of them is difficult. This also implies removing of data obtained from glasses, minerals, and inclusions.
4. Only whole rock data from volcanic rocks were used for database reconstruction, since they form those units in igneous complexes generally covering the largest areas and being most susceptible to any kind of erosion through time. In addition, they principally reflect the composition of the underlying basement as well. Thus, data from associated igneous intrusive bodies were not taken into account. Including them does not significantly affect the average values plotted, however, the data scattering is

considerably more pronounced. Xenoliths and ores were also excluded, since they represent only a fairly small part of the rock material exposed to erosion, in addition, such samples are often taken from underground.

5. Data from sedimentary and metamorphic rocks, being part of the basement, were also removed. They are mostly exposed locally only, thus, forming a minor proportion of erodible material.
6. Samples from historical eruptions were excluded as well, which further reduced data scattering. Their compositional range does not significantly contribute to help elucidating the long-term temporal evolution of a source area and its importance as Pb supplier to the marine realm in the EEP.

References cited in Section A.1

Pichat, S., Abouchami, W., Galer, S.J.G., 2014. Lead isotopes in the Eastern Equatorial Pacific record Quaternary migration of the South Westerlies. Earth and Planetary Science Letters 388, 293–305. 10.1016/j.epsl.2013.11.035.

Appendix III (CHAPTER III)

Supplementary Table A.1 (Appendix III)

Suppl. Table A.1	**Reproducibility and accuracy of XRF data for JA-2**			
# Analysis/ Element	#1	#2	Relative std. dev. (±1σ %)	Reference value*
SiO_2 (wt%)	56,3	56,01	*0,26*	56,2
TiO_2 (wt%)	0,67	0,67	*0*	0,67
Al_2O_3 (wt%)	15,4	15,4	*0*	15,3
Fe_2O_3 (wt%)	6,39	6,36	*0,24*	6,14
MnO (wt%)	0,11	0,11	*0*	0,11
MgO (wt%)	8,06	7,97	*0,56*	7,68
CaO (wt%)	6,24	6,24	*0*	6,48
Na_2O (wt%)	3,12	3,11	*0,16*	3,08
K_2O (wt%)	1,75	1,75	*0*	1,8
P_2O_5 (wt%)	0,17	0,16	*3,03*	0,15
Co (ppm)	31	31	*0*	30
Zn (ppm)	62	61	*0,81*	62,7
Ga (ppm)	21	16	*13,5*	16,4
Rb (ppm)	77	78	*0,65*	68
Sr (ppm)	240	240	*0*	252
Ba (ppm)	311	311	*0*	317

	Reproducibility and accuracy of XRF data for JB-2			
# Analysis/ Element	#1	#2	Relative std. dev. (±1σ %)	Reference value*
SiO_2 (wt%)	53,09	53,21	*0,11*	53,2
TiO_2 (wt%)	1,17	1,16	*0,43*	1,19
Al_2O_3 (wt%)	14,75	14,91	*0,54*	14,7
Fe_2O_3 (wt%)	14,42	14,45	*0,10*	14,3
MnO (wt%)	0,21	0,21	*0*	0,2
MgO (wt%)	4,78	4,78	*0*	4,66
CaO (wt%)	9,88	9,92	*0,20*	9,89
Na_2O (wt%)	2,16	2,19	*0,69*	2,03
K_2O (wt%)	0,42	0,41	*1,20*	0,42
P_2O_5 (wt%)	0,1	0,09	*5,26*	0,1
Co (ppm)	46	45	*1,10*	40
Zn (ppm)	104	106	*0,95*	110
Ga (ppm)	20	17	*8,11*	17
Rb (ppm)	11	10	*4,76*	6,2
Sr (ppm)	177	174	*0,85*	178
Ba (ppm)	234	226	*1,74*	208

Supplementary Table A.1 (Appendix III) (*continued*)

	Reproducibility and accuracy of XRF data for JB-3			
# Analysis/ Element	#1	#2	Relative std. dev. (±1σ %)	Reference value*
SiO_2 (wt%)	50,8	50,9	*0,10*	51,0
TiO_2 (wt%)	1,41	1,4	*0,36*	1,45
Al_2O_3 (wt%)	17,25	17,27	*0,06*	16,9
Fe_2O_3 (wt%)	11,98	11,97	*0,04*	11,9
MnO (wt%)	0,18	0,17	*2,86*	0,16
MgO (wt%)	5,25	5,21	*0,38*	5,2
CaO (wt%)	9,76	9,74	*0,10*	9,86
Na_2O (wt%)	2,88	2,91	*0,52*	2,82
K_2O (wt%)	0,77	0,77	*0*	0,78
P_2O_5 (wt%)	0,3	0,3	*0*	0,29
Co (ppm)	42	40	*2,44*	36,3
Zn (ppm)	101	105	*1,94*	106
Ga (ppm)	20	22	*4,76*	20,7
Rb (ppm)	20	19	*2,56*	13
Sr (ppm)	402	401	*0,12*	395
Ba (ppm)	233	246	*2,71*	251

	Reproducibility and accuracy of XRF data for JR-1				**All rock standards**
# Analysis/ Element	#1	#2	Relative std. dev. (±1σ %)	Reference value*	±1σ % (average)
SiO_2 (wt%)	74,8	75,17	*0,25*	75,4	*0,18*
TiO_2 (wt%)	0,11	0,11	*0*	0,1	*0,20*
Al_2O_3 (wt%)	12,72	12,77	*0,20*	12,9	*0,20*
Fe_2O_3 (wt%)	0,85	0,85	*0*	0,96	*0,10*
MnO (wt%)	0,11	0,11	*0*	0,1	*0,71*
MgO (wt%)	0,13	0,14	*3,70*	0,09	*1,16*
CaO (wt%)	0,69	0,69	*0*	0,63	*0,08*
Na_2O (wt%)	4,15	4,12	*0,36*	4,10	*0,43*
K_2O (wt%)	4,44	4,46	*0,22*	4,41	*0,36*
P_2O_5 (wt%)	0,02	0,02	*0*	0,02	*2,07*
Co (ppm)	6	5	*9,09*	0,65	*3,16*
Zn (ppm)	29	26	*5,45*	30	*2,29*
Ga (ppm)	19	20	*2,56*	17,6	*7,24*
Rb (ppm)	268	269	*0,19*	257	*2,04*
Sr (ppm)	25	24	*2,04*	30	*0,76*
Ba (ppm)	52	38	*15,6*	40	*5,00*

Supplementary Table A.2 (Appendix III)

Machine reproducibility of ICP-MS trace element data evaluated from repeated analyses of single aliquots.

Sample 1256B-			Li	Sc	V	Cr	Co	Ni	Cu	Zn	Ga	Rb	Sr	Y	Zr	Nb	Cs	Ba
3H2_77-78	RSD	[%]	1,25	1,58	2,59	1,45	1,81	1,20	1,06	1,78	1,28	0,55	0,97	0,90	1,80	1,12	0,58	1,60
3H3_81-82	RSD	[%]	0,93	1,55	1,82	1,28	1,61	1,51	1,70	1,75	0,81	0,73	1,02	0,87	1,06	0,89	1,32	1,64
3H4_88-89	RSD	[%]	1,40	1,28	2,96	1,39	2,74	0,74	1,00	1,43	0,65	1,16	1,43	0,72	1,33	0,92	1,03	1,39
3H5_96-97	RSD	[%]	1,37	0,85	1,87	0,74	1,68	0,73	1,17	1,46	0,91	0,55	1,02	0,86	0,92	1,02	1,04	1,24
3H6_9-10	RSD	[%]	0,80	0,88	1,24	0,63	1,19	1,25	1,34	0,97	1,41	0,41	0,84	0,44	3,65	0,84	1,09	1,25
3H6_40-41	RSD	[%]	1,00	1,41	1,68	1,36	1,90	0,79	0,74	1,36	0,85	0,55	0,63	0,78	0,35	0,76	0,70	1,23
3H6_59-60	RSD	[%]	0,87	1,36	1,58	0,92	2,28	1,01	1,03	1,81	1,28	1,00	0,88	0,72	0,63	0,94	0,66	1,74
3H6_78-79	RSD	[%]	0,74	1,11	2,02	1,02	1,11	0,96	0,90	0,91	1,02	1,07	0,76	0,57	1,51	0,64	0,53	1,84
3H6_91-92	RSD	[%]	0,77	0,71	0,70	0,63	1,12	0,64	0,73	0,37	0,92	0,95	0,55	0,58	1,77	0,85	0,50	1,55
3H6_103-104	RSD	[%]	0,58	0,67	1,20	0,77	1,16	0,87	1,35	1,28	0,97	0,45	0,69	0,68	0,76	0,65	0,48	0,67
3H6_122-123	RSD	[%]	0,94	0,97	1,00	1,12	1,18	0,74	0,94	0,82	0,70	0,83	0,72	0,95	1,23	0,76	0,84	1,16
3H6_141-142	RSD	[%]	0,73	0,97	1,06	1,05	1,15	0,97	0,62	0,72	0,83	1,17	1,05	0,86	0,82	0,53	0,78	0,66
3H7_23-24	RSD	[%]	0,70	0,90	1,48	1,02	1,32	0,88	0,94	1,00	0,74	0,86	0,49	0,53	0,72	0,41	0,70	1,54
4H1_4-5	RSD	[%]	0,48	0,59	1,07	0,89	1,44	0,69	0,30	1,14	0,98	0,46	0,68	0,48	1,39	0,40	0,53	1,43
4H1_67-68	RSD	[%]	0,56	0,59	1,09	0,83	1,40	0,87	1,32	0,83	0,88	0,66	0,84	0,61	1,11	0,80	0,52	1,50
4H2_75-76	RSD	[%]	0,85	1,29	1,39	1,47	1,08	0,99	0,96	0,73	1,22	0,74	0,72	0,94	3,84	0,74	1,04	1,06
4H3_83-84	RSD	[%]	0,89	0,78	1,60	1,25	1,53	1,33	0,90	0,72	0,79	0,81	0,65	0,77	0,92	0,91	0,63	1,12
4H4_128-129	RSD	[%]	1,80	1,09	1,49	1,03	1,19	0,85	0,84	1,36	0,92	1,64	1,46	1,29	3,07	1,65	1,37	2,03
4H5_11-12	RSD	[%]	1,23	0,68	1,47	0,84	1,84	0,93	0,85	1,28	0,70	1,58	1,27	1,26	0,91	1,13	1,27	1,07
4H5_41-42	RSD	[%]	0,60	1,17	0,89	1,15	1,40	1,34	0,80	1,00	1,05	0,69	1,04	0,53	0,73	0,67	0,84	1,37
4H5_72-73	RSD	[%]	0,65	1,28	1,53	1,21	1,61	1,25	1,32	1,04	1,38	1,02	0,88	0,96	1,10	1,04	0,98	2,21
4H5_104-105	RSD	[%]	1,49	1,08	0,86	0,74	1,11	0,60	0,88	0,95	0,79	1,34	1,01	1,47	2,26	1,09	1,29	1,31
4H5_135-136	RSD	[%]	0,99	1,03	1,30	1,02	1,60	0,97	1,36	1,43	1,19	0,63	0,81	0,68	1,39	0,88	1,12	1,29
4H6_17-18	RSD	[%]	0,84	1,47	1,33	1,21	1,66	1,39	1,02	1,26	1,69	0,72	0,97	0,87	2,45	1,03	0,81	0,98
4H6_48-49	RSD	[%]	1,47	0,82	1,46	0,89	1,56	0,83	0,87	0,97	0,68	1,18	1,20	1,41	2,46	1,20	1,02	1,13
4H6_80-81	RSD	[%]	0,62	0,69	1,18	0,81	0,77	1,27	1,22	1,01	0,80	1,16	1,20	0,98	0,98	1,40	1,61	1,12
4H6_111-112	RSD	[%]	1,31	1,40	1,92	1,63	0,82	1,03	1,01	0,64	1,26	0,80	1,09	1,01	1,65	0,96	1,04	1,85
4H6_143-144	RSD	[%]	0,90	1,35	1,64	1,25	1,61	1,28	0,95	0,93	0,79	1,21	1,39	0,99	1,88	1,04	0,74	1,14
4H7_24-25	RSD	[%]	0,78	0,88	1,10	1,31	0,97	0,79	0,68	0,82	0,87	0,94	1,01	1,02	7,14	1,27	0,59	2,36
4H7_56-57	RSD	[%]	0,64	1,00	1,21	0,97	1,20	0,93	0,80	1,05	1,06	1,75	1,40	0,94	2,04	1,22	1,00	1,68
4H7_68-69	RSD	[%]	0,97	1,54	0,99	1,08	1,17	0,92	0,74	0,71	0,99	1,98	1,12	1,01	6,01	1,25	0,83	1,35
5H1_4-5	RSD	[%]	1,37	1,65	2,11	0,93	1,29	0,92	1,14	1,02	1,09	1,40	1,23	0,91	1,92	1,25	1,30	1,91
5H1_36-37	RSD	[%]	0,79	1,91	2,23	1,76	1,67	1,56	1,82	1,43	1,54	0,93	0,87	1,11	0,93	0,99	0,97	2,05
5H1_67-68	RSD	[%]	1,14	1,04	1,40	1,01	2,03	1,11	1,42	1,12	1,66	0,94	0,83	0,90	1,09	1,27	1,23	1,67
5H1_93-94	RSD	[%]	1,34	0,78	0,55	1,13	1,92	1,28	0,93	0,87	1,17	1,09	1,11	1,18	1,78	1,33	1,52	1,89
13H6_25-26	RSD	[%]	0,98	1,29	1,22	1,51	1,79	1,64	1,06	1,48	2,07	0,98	0,68	0,79	0,80	0,99	1,26	1,25
	Mean RSD		***0,97***	***1,10***	***1,45***	***1,09***	***1,47***	***1,03***	***1,02***	***1,10***	***1,05***	***0,97***	***0,96***	***0,88***	***1,79***	***0,97***	***0,94***	***1,45***

Supplementary Table A.3 (Appendix III)

Suppl. Table A.3	**Reproducibility and accuracy of ICP-MS trace element data for BCR-2**												
# Analysis/ Element	#1	#2	#3	#4	#5	#6	#7	#8	#9	Mean	Std. dev. (±1σ)	Relative std. dev. (±1σ %)	Reference value*
Li (ppm)	10,9	11,0	10,8	10,5	10,5	10,3	12,3	12,1	12,2	11,2	0,74	*6,59*	9
Sc (ppm)	37,2	37,6	38,3	37,3	39,2	38,7	40,4	40,2	39,6	38,7	1,13	*2,92*	33
V (ppm)	445	443	459	453	465	459	440	449	451	452	7,86	*1,74*	416
Cr (ppm)	16,6	16,7	16,9	16,5	17,3	17,0	18,2	18,1	17,9	17,2	0,64	*3,72*	18
Co (ppm)	37,2	36,6	37,9	37,7	38,8	38,0	36,4	37,6	37,4	37,5	0,68	*1,80*	37
Ni (ppm)	12,5	12,5	12,7	12,5	12,9	12,7	13,8	13,5	13,4	13,0	0,48	*3,69*	18
Cu (ppm)	16,6	16,3	17,0	16,5	17,3	16,9	18,0	18,1	17,8	17,2	0,64	*3,71*	21
Zn (ppm)	129	128	136	135	138	137	130	132	130	133	3,67	*2,76*	127
Ga (ppm)	22,9	22,9	23,2	22,9	23,5	23,2	24,0	23,9	23,6	23,3	0,41	*1,74*	23
Rb (ppm)	51,0	50,6	51,0	49,8	51,0	50,0	53,2	53,3	53,7	51,5	1,40	*2,72*	46,9
Sr (ppm)	362	360	366	360	370	363	381	384	385	370	9,96	*2,69*	340
Y (ppm)	36,5	35,8	36,4	35,6	36,2	35,5	36,2	36,5	36,7	36,2	0,41	*1,15*	37
Zr (ppm)	204	198	203	200	204	200	200	203	204	202	2,14	*1,06*	184
Nb (ppm)	13,3	12,5	12,7	12,5	12,6	12,3	13,2	13,4	13,4	12,9	0,41	*3,22*	12,6
Cs (ppm)	1,29	1,23	1,21	1,20	1,21	1,18	1,21	1,21	1,22	1,22	0,03	*2,38*	1,1
Ba (ppm)	728	715	725	718	715	714	709	682	689	711	14,47	*2,04*	677
La (ppm)	26,5	25,7	26,0	25,9	26,1	25,7	25,8	26,3	26,5	26,1	0,31	*1,18*	24,9
Ce (ppm)	55,9	53,7	54,8	54,4	54,8	53,8	52,5	53,1	53,6	54,1	0,96	*1,77*	52,9
Pr (ppm)	7,11	6,86	6,95	6,91	6,86	6,76	6,53	6,61	6,69	6,81	0,17	*2,50*	6,7
Nd (ppm)	29,6	28,2	29,0	28,8	28,3	27,7	25,6	26,1	26,4	27,8	1,34	*4,82*	28,7
Sm (ppm)	6,72	6,36	6,65	6,62	6,51	6,55	6,19	6,44	6,52	6,51	0,15	*2,31*	6,58
Eu (ppm)	1,98	1,84	1,93	1,92	1,85	1,81	1,80	1,87	1,87	1,87	0,05	*2,89*	1,96
Gd (ppm)	6,62	6,32	6,58	6,58	6,24	6,19	6,01	6,08	6,44	6,34	0,22	*3,40*	6,75
Tb (ppm)	1,10	1,07	1,10	1,07	1,09	1,07	1,05	1,05	1,05	1,07	0,02	*1,80*	1,07
Dy (ppm)	6,68	6,49	6,75	6,52	6,55	6,60	6,29	6,45	6,55	6,54	0,12	*1,88*	6,41
Ho (ppm)	1,33	1,28	1,33	1,32	1,30	1,30	1,23	1,28	1,30	1,30	0,03	*2,26*	1,28
Er (ppm)	3,81	3,67	3,78	3,75	3,65	3,64	3,52	3,61	3,65	3,68	0,09	*2,32*	3,66
Tm (ppm)	0,53	0,50	0,53	0,53	0,51	0,51	0,49	0,50	0,52	0,51	0,01	*2,83*	0,54
Yb (ppm)	3,31	3,19	3,30	3,35	3,22	3,26	2,99	3,16	3,15	3,21	0,10	*3,16*	3,38
Lu (ppm)	0,49	0,47	0,49	0,49	0,47	0,47	0,44	0,47	0,47	0,48	0,01	*3,14*	0,503
Hf (ppm)	4,93	4,62	4,91	4,80	4,70	4,57	4,64	4,91	4,88	4,77	0,13	*2,80*	4,9
Ta (ppm)	2,02	1,20	1,11	0,98	1,05	0,93	1,10	0,99	0,99	1,15	0,32	*27,5*	0,74
Pb (ppm)	10,3	10,0	10,0	10,0	9,8	9,7	8,9	9,0	9,1	9,6	0,48	*4,95*	11
Th (ppm)	6,16	5,74	5,82	5,81	5,59	5,52	4,93	5,12	5,21	5,54	0,37	*6,67*	5,7
U (ppm)	1,69	1,58	1,59	1,58	1,51	1,47	1,32	1,39	1,40	1,50	0,11	*7,45*	1,69

*GeoReM preferred values from Jochum and Nehring (11/2006)